ROBUST HURRICANE SURGE RESPONSE FUNCTIONS

A Dissertation

by

IKPOTO ENEFIOK UDOH

Submitted to the Office of Graduate Studies of
Texas A&M University
in partial fulfillment of the requirements for the degree of

DOCTOR OF PHILOSOPHY

Approved by:

Co-Chairs of Committee,	Jennifer L. Irish
	James Kaihatu
Committee Members,	Francisco Olivera
	Steven Quiring
	Emily Zechman
Head of Department,	John Niedzwecki

December 2012

Major Subject: Ocean Engineering

ABSTRACT

To adequately evaluate risk associated hurricane flooding, numerous surge events must be considered, and the cost associated with high resolution numerical modeling for several storms is excessive. The Joint Probability Method with Optimal Sampling (JPM-OS) has been recently shown to be a reliable method in estimating extreme value probabilities of hurricane flooding – it relies heavily on a hurricane surge matrix comprised of surge values from several hurricane scenarios (with varying meteorological and climate change characteristics). Surge Response Functions (SRFs) are physics-based equations developed using scaling laws to adequately scale surge response in dimensionless space; they serve as surrogates to high resolution numerical models in estimating hurricane peak surge to populate the JPM-OS surge matrix.

Research presented in this dissertation is primarily focused on the development of dimensionless formulations using physics-based scaling laws to account for the contribution of forward speed (v_f), approach angle (θ) and Sea Level Rise (SLR). These parameters are incorporated into pre-existing SRFs for open coast locations and bays. For the bays, in addition to accounting for the effects of v_f and θ in the SRFs, a new dimensionless formulation for the influence of storm size (R_p) is included in the SRFs.

To account for the influence of v_f in the SRFs, the dimensionless formulations primarily consist of the time it takes for surge to build up (over the shelf, for open coast SRFs and within the bays, for bay SRFs). The formulation for the influence of θ primarily accounts for the rotation of the hurricane wind field as the storm makes landfall. For the influence of R_p in the bays, the new formulation scales R_p with the farthest distance through which water mass will move inside the bay, from its center of gravity. A simple correction based on a linear model is derived to account for the influence of SLR on surge response at open coast locations and in bays. The developed dimensionless formulations for v_f and θ (and R_p for bay SRFs) are incorporated into the SRFs to obtain revised versions of the response functions. For open coast locations, the revised SRFs estimate peak surge with an increased accuracy (based on root-mean-square errors of modeled versus SRF-estimated peak surge) of up to 12.5% reduction in root-mean-square errors. In addition, the new formulations improve the predictions of 65% of surge events of 2 m or greater. For the bays, the revised SRFs reduce the root-mean-square errors (by up to 54% in Matagorda Bay), when compared to the previous formulation. These results indicate that the new formulations, which include v_f and θ (and R_p for bay SRFs), significantly improve the accuracy of the SRFs. Application of the revised open coast SRFs to the JPM-OS framework shows only minor impacts of v_f and θ variation on surge versus return period curves (about 5.2% maximum increase in surge for θ varying from -80^{o} to +80^{o}, and a maximum of 6.7% for v_f varying from 1.54 m/s to 10.8 m/s). Climate change parameters however show a much more significant impact on the surge versus return period curves. SLR variation from 0.5 m to 2.0 m yields a maximum of 42.4% increase in surge, while hurricane intensification from 0.5^{o}C to 1.5^{o}C yields an increase of up to 11.3% in surge.

DEDICATION

This dissertation is dedicated to God for His love for me, and my family – My wife Agnes and my son Kentoro, for their patience and support during my Ph.D program.

ACKNOWLEDGEMENTS

I gladly acknowledge the support, advising and leadership of my committee chairs, Drs. Jennifer L. Irish and James Kaihatu throughout the course of my research. Their guidance was critical to my success, at every stage of my work. I thank my committee members, Dr. Francisco Olivera, Dr. Steven Quiring, and Dr. Emily Zechman for their advising and thoughtful contributions to this research.

Funding for this research was provided by the U.S. Department of Energy, and the Texas Sea Grant Program – I am deeply thankful to these agencies for their support and the opportunity to be a part of their projects.

I thank the Department of Civil Engineering at Texas A&M University for employing me as Graduate Research Assistant throughout the duration of my studies in TAMU. Specifically, I am thankful to the current Head of Department, Dr. John Niedzwecki for ensuring my continued employment in the Department, thus providing the stability I needed to complete this research. My sincere gratitude also goes Ms. Jane Reed of the Civil Engineering Department at Texas A&M University, for her remarkable support during the renewal of my employment.

I acknowledge Texas A&M University's (College Station, Texas) Supercomputing personnel, and the consultants at the National Energy Research Scientific Computing Center in Berkeley, California, for their effective support which was critical to the completion of numerical simulations in this research.

I also offer my thanks to my colleagues in graduate school: Kerri Whilden, Cristian Cifuentes, Amitava Guha, and Antonne Taylor, who were always willing to share helpful ideas with me during problem-solving. Lastly, I thank my parents, Hon. Justice Enefiok Udoh (Rtd.) and Barr. Bernadette E. Udoh, my siblings (Uddy, Nddie, Edidiong, Anyanya, Nsikak and Ifiok), my dear wife, Agnes Udoh, and my good friend, Akaninyene Ndey for their unwavering support and love throughout my years of study.

TABLE OF CONTENTS

Page

CHAPTER

CHAPTER Page

LIST OF FIGURES

FIGURE Page

FIGURE Page

FIGURE Page

FIGURE Page

FIGURE Page

FIGURE Page

FIGURE Page

FIGURE Page

FIGURE Page

LIST OF TABLES

TABLE Page

TABLE Page

CHAPTER I

INTRODUCTION AND OVERVIEW

Damage caused by hurricanes can be enormous, and storm surge among other factors is a primary component of storms intense enough to cause coastal damage. In recent years there have been significant improvements in the competence of hurricane surge estimation methods and models. Many of these efforts are directed not only towards increasing the accuracy of surge estimates, but also toward more efficient computing techniques aimed at minimizing the time associated with hazard assessment using extreme value statistics. In spite of these continuing developments, there still is plenty of improvement needed. To significantly reduce the risk of hurricane surge impacting life and property, efficient planning involving the locations of infrastructure in coastal areas must be based on accurate extreme value analyses. The derivatives of such analyses are also very beneficial to response and evacuation planning personnel.

Numerical simulation of storm surge, even with state-of-the-art computing facilities takes time and is quite expensive. Given the limited availability of efficient modeling and advanced computing resources, only a limited number of hurricane scenarios can be simulated at high resolutions within a small (i.e. on the order of a few days) time frame. Some storm surge modeling practices are directed at estimating possible flooding due to storm surge by an expected hurricane; for instance the application of SLOSH – Sea, Lake, and Overland Surge from Hurricanes model (Federal Emergency Management Agency [FEMA], National Oceanic and Atmospheric Administration [NOAA], 2003) for emergency evacuation plans by FEMA. For such applications, the extent of the numerical grid used may be reduced, and multiple simulations may be performed to obtain surge estimates at the location(s) of interest. This approach is not however efficient in obtaining surge estimates at spatially distant locations for a large number of scenarios for extreme value statistics, because it would possibly imply the use of multiple grids, many more simulations and an increased potential of modeling errors or inaccuracies. There is therefore a significant need in the storm surge modeling community, to develop new methods and improve on existing methods of accurately estimating hurricane surge for extreme value analysis, in a time-efficient fashion.

Accounting for the effects of global climate change (in addition to relevant hurricane meteorological parameters) on hurricane peak surges is one important way of making modeling tools more robust. The risk of coastal areas being flooded can be affected by climate change in two primary ways. First, a change in the frequency and intensity of hurricanes would lead to a direct change in the probabilities associated with the affected areas being flooded. Second, changes in sea level will produce a direct impact on coastal flooding. Several studies (Elsner et al. 2008; Knutson and Tuleya 2008; Emanuel et al. 2008; Vecchi and Soden 2007; Webster et al 2005) have indicated that future hurricanes in Category 3 or higher on the Saffir-Simpson scale (Simpson, 1974) may intensify in response to increasing sea surface temperatures (SSTs). Conflicting evidence on the increase/decrease of tropical cyclone frequencies have been reported recently in literature. Some studies (e.g. Webster et al., 2005; Holland and Webster, 2007; Mann et al, 2007) have suggested an increase in the frequency of future hurricanes, while some more recent research (e.g. Knutson et al., 2010,) show that this frequency will either remain unchanged or will decrease with increase in global warming. Regarding sea level rise, many studies (Church and White, 2006; *Rahmstorf, S., 2007; IPCC, 2007; *Pfeffer et al. 2008; *Horton et al., 2008; *Vermeer et al., 2009; *Jevrejeva et al., 2010) have affirmed that sea level will increase due to global warming. Taking these findings into consideration, this research attempts to incorporate the effects of climate change into the estimation of hurricane peak surge and inundation risk, by investigating and accounting for sea level rise influences on hurricane surge, and considering hurricane intensification in estimating extreme value statistics.

1.1 Basics of Hurricane Storm Surge

The development of hurricane storm surge is fundamentally dependent on surface wind stress, atmospheric pressure gradients, bottom friction developed by currents induced by the wind stress and the geometrical features (such as the continental shelf width, and its slope) of the location under consideration. Wave momentum induced by wind wave setup, long wave effects (e.g. tides), surface runoff, and land cover could also significantly affect fluctuations in water levels, especially for very intense storms. To characterize landfalling hurricanes adequately, their basic meteorological parameters namely, central pressure, radius of maximum winds (or scale radius), forward speed, approach angle, and landfall location must be known. A combination of the relative magnitudes of these important parameters and the geometric features of any location of interest, determine the extent to which a storm impacts such location in terms of maximum surge levels. Since hurricane events cannot be adequately scaled for physical modeling, numerical modeling is inevitable. The primary needs for numerical modeling of hurricanes are wind, pressure and wave fields. In this research, the contribution of waves, tides and river runoff to storm surge are not addressed.

As a first approximation, based on the principle of conservation of linear momentum (in one dimension, and depth integrated), a simple, linear, steady-state equation which encompasses the effect of geometry and wind stress is:

$$\zeta \propto \left(\frac{\tau_s}{gh} \right) L \tag{1.1}$$

and

$$\tau_s = c_d \rho_a U^2 \tag{1.2}$$

where:

τ_s = wind stress at the air-water interface

g = is gravitational acceleration

h = water depth

L = shelf width

c_d = drag coefficient

ρ_a = air density

U = wind speed

Equation (1.1) provides a basic idea of the proportionality of storm surge to primary driving mechanisms along the coast; it suggests that if the wind acts on the water surface for a sufficient duration, a stage will be reached in the surge development process where the water level is proportional to the term on the right hand side. A wide shelf, high wind stresses, and shallow water depths are conditions which enhance storm surge generation. In more complex regions (bays and estuaries), additional geometric parameters (discussed in Chapter IV) are needed to describe secondary influences that affect surge redistribution.

Throughout this dissertation, the terms surge, sea level rise and flood depth are used. For the benefit of the reader, Figure 1.1 is used to clarify the benchmark to which each of these measures of water level is referenced. As shown, surge is a measure of the water elevation due to hurricane action, with respect to the *mean sea level*. Sea level rise is considered a measure of the initial water level prior to any hurricane action or surge development, measured from the present-day mean sea level. Thus, if sea level rise is equal to zero, then the initial water level is the current-day mean sea level. The flood depth is a measure of the water elevation after hurricane action, measured from the sea bed.

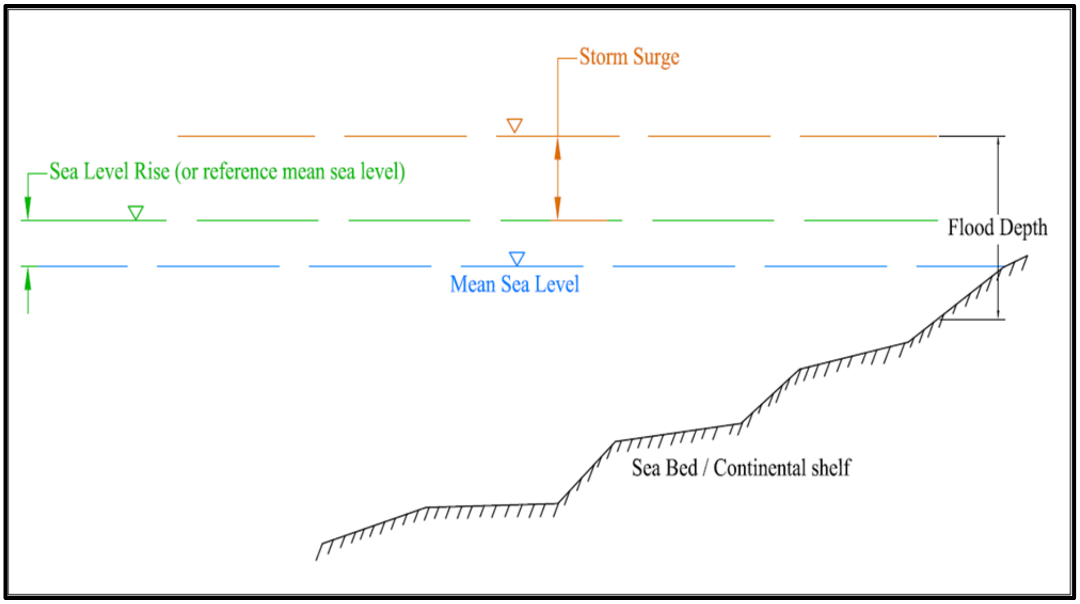

Figure 1.1: Definition sketch for flood depth, surge and sea level rise.

1.2 Motivation and Problem Statement

The risk of flooding or inundation of a coastal area may be defined as the product of the consequence of such flooding, and the estimated probability of such water levels occurring. To accurately quantify surge hazard on the coast, reliable methods for estimating the probabilities associated with hurricane surge are required. The probability of obtaining a specific peak surge value at a coastal location of interest is a function of the probability that the hurricane under consideration has specific meteorological parameters, namely its central pressure, size, forward speed and angle of approach at the coast. One of such methods recently introduced (Resio et al. 2009) is the joint probability method with optimal sampling, JPM-OS, which is a variation of the traditional joint probability methods, JPM (Myers 1975; Ho and Myers 1975). In the joint probability method, the surge probabilities depend strongly on the size of the domain comprising the individual probabilities of meteorological parameters. This dependence directly introduces a computational burden in the JPM, regarding the number of storm simulations required to generate the individual probabilities. Suppose for instance, that within a coastal segment of interest, it is desired that five hurricane tracks be simulated, with 4 values each of central pressure, storm size, forward speed and approach angle. A total of 1,280 storm simulations would be required to generate the discrete probabilities associated with these parameters. Clearly, the computational expense associated with such a large number of simulations is difficult to meet. It is pertinent, therefore, to use an optimal sampling technique to substantially reduce the required number of storms (hence the computational burden) for such extreme value analysis, while retaining great accuracy in peak surge estimates.

The optimal sampling technique adopted in this research involves two key steps, the first of which is to consider and model relatively small sets of representative storms to investigate and incorporate the effect of important parameters not yet considered in Surge Response Functions (SRFs). Introduced by Irish et al. (2009), SRFs are non-dimensional physics-based scaled equations which represent a continuous surface of peak surge response, parameterized by hurricane characteristics and spatial variables which play an important role in surge development and re-distribution. They serve as surrogates to complex high resolution surge models, and find great use in extreme value analyses where there is need to efficiently evaluate peak surge using many hurricane scenarios (or combinations of parameters).

In the second step, the revised or improved SRFs are used to (efficiently) generate the peak surge estimates, to which individual probabilities for extreme value analysis can be associated. The storm samples can be only be considered optimal, if they adequately represent larger populations of historical storms. Since the accuracy of the extreme probability is dependent on those of the joint probabilities of meteorological parameters, there is a strong need for the SRFs to be robust such that all important meteorological, spatial and climate change parameters related to hurricane storm surge are incorporated. The existing SRF formulations only account for the contributions of hurricane central pressure, size, landfall location, and the effects of the continental shelf width. Considering that hurricane forward speed, approach angle, and sea level rise are parameters that are known to influence surge generation, incorporating them correctly into the SRFs implies improving the accuracy of peak surge estimates obtained using the response functions.

1.3 Research Objectives

The ultimate goal of this work is to develop non-dimensional scaling laws that adequately account for the contributions of forward speed, approach angle and sea level rise in SRFs for open coast locations and in bays. A subsequent goal is to apply the resulting SRFs in extreme value analyses for select locations. We hypothesize that the effects of hurricane forward speed, approach angle and sea level rise on hurricane surge can be appropriately incorporated into SRFs using physics-based scaling laws; and that by increasing the parameter space covered in extreme value analysis due to the inclusion of these three parameters, inundation risk estimates obtained using these SRFs are more reliable. Consequently, this dissertation shows SRFs which include the three mentioned parameters as well as results of extreme value analysis at select open coast locations.

The remainder of this dissertation is organized as follows: discussions on related literature on hurricane parameters, numerical models, surge response functions, extreme value analysis, climate change, etc. are presented in Chapter II. In Chapter III, the study areas, and the approach (including models and data acquisition) to incorporate forward speed, approach angle and sea level rise into surge response functions are discussed. The results of the response functions and their application to extreme value analyses are discussed in Chapter IV. A summary of the major findings in this work, conclusions, and future related research are discussed in Chapter V.

CHAPTER II

LITERATURE REVIEW

2.1 Hurricane Storm Surge Modeling

The primary forcing for hurricane surge is wind and pressure fields; therefore the successful modeling of storm surge depends in large part to the accuracy of the parameterized wind and pressure fields. However, there are other forcing mechanisms like tide and river flow which are capable of altering the final water levels during and after a storm event. For completeness, both primary and secondary forcing mechanisms are discussed in this section, along with some basics of storm surge modeling.

As sustained winds act on the water surface, surface stresses are induced which transfer momentum into the water column inducing currents that in turn develop bottom stresses. For momentum to be conserved, the water surface responds with an increase in elevation due to the effects of both surface and bottom stresses. Being cyclonic in nature, hurricanes have a low central pressure which creates a strong pressure gradient from outside the storm vortex to inside the system. An increase in this pressure gradient leads to an increase in maximum wind speeds around the eye, causing additional rise in water levels. Waves contribute to water levels through wind wave momentum transferred into the water column via radiation stresses and during breaking. The presence of coastal vegetation may cause a reduction in water levels due to energy dissipation.

Tides and river runoff also contribute to peak surge levels. If the active surge generation stage of the storm coincides with high tide, surge magnitudes will increase (Rego and Li, 2009) and the oscillatory nature of the tides will impact the re-distribution of surge around the considered area. Regarding runoff, the associated river characteristics (such as discharge and average flow depth) will affect the extent to which overall water levels are affected by river outflows. A non-linear coupled modeling of additional influences (tides, river runoff and wind waves) with surge would offer a representation of the processes which affect final water levels that is very close to what is actually observed during storms. Simulating these coupled effects correctly at high resolution leads to surge estimates that are more accurate, than if they were omitted for simplification, as additional physics is used to capture their influences on water levels. It is, however, reasonable to expect that the additional accuracy achieved by accounting for the effects of tides and river runoff is dependent on location and time of occurrence of the storm(s), since for different regions and times their influences can vary. To appropriately capture the influence of river outflow, the resolution of the numerical grid needs to be adequately high (Bunya et al. 2010). Regarding waves, appropriate wave models need to be coupled to surge models, to allow the transfer of calculated radiation stresses which are then used to force the surge models at each simulation time step. It should be noted that for simplicity, this research does not consider the influence of tides, waves and river runoff on hurricane surge.

While it is common to model storm surge with only wind and pressure fields as input, recent studies (Westerink et al., 2008; Bunya et al., 2010; Dietrich et al., 2010) have demonstrated high-resolution numerical modeling of storm surge using coupled forcing comprising contributions of wind waves, tides, river runoff, and storm surge with satisfactory results. These studies have used the Advanced Coastal Circulation and Storm Surge Model (ADCIRC – Luettich and Westerink, 2004) which is discussed in greater detail in Chapter III, as it is the storm surge model used in this research. Other models which have been used in storm surge modeling include FVCOM (e.g. Chen et al., 2003) which solves the momentum, continuity, temperature, salinity and density equations, and SLOSH (FEMA, NOAA; 2003) which is not discussed as much as ADCIRC or FVCOM in available literature.

In modeling storm surge with numerical models, the governing equations (for conservation of mass and momentum) are typically solved for solutions in two or three dimensions (hereafter referred to as 2-D and 3-D respectively). The primary difference in capability between a 2-D and a 3-D storm surge model is that a 3-D model can incorporate the influence of vertical stresses and velocities in the water column (hence they are very useful for modeling the effects of salinity and/or temperature changes), whereas a 2-D model obtains depth-averaged solutions. Weaver and Luettich (2010) investigated the sensitivity of ADCIRC in estimating storm surge using the 2-D and 3-D versions of the model; they state that the major difference in water surface elevation output is due to difference in bottom stress calculations between the two versions of the model – the 2-D version computes the bottom stress using a depth-averaged velocity, while the 3-D version computes the bottom stress as a function of near-bottom velocity. There are advantages and challenges associated with each version of the model, but an important factor to consider in choosing which model to use is the primary output required from such modeling, and the capability of the model to produce such results without much loss in accuracy. Weaver and Luettich (2010) state that it would take the 3-D model 10 times the time required for a 2-D model, to complete one simulation with the same number of computing processors. Using hurricane Isabel as case study, the authors also report that the difference in surge elevations over most of the modeling domain is less that 5% when using realistic values of roughness.

Although it is possible to model storm surge at high resolution with coupled forcing using numerical models (e.g. Bunya et al., 2010; Dietrich et al., 2010), relying on such modeling efforts to generate sufficient surge data for direct application to extreme value analyses would be highly inefficient (given present computing resources). A great amount of time and computing resources would be required to complete such high resolution numerical simulations. Given the large number of scenarios that need to be considered for extreme value analysis, such approach is just not practical.

2.2 Estimating Hurricane Extreme Value Statistics

To emphasize the advantage of the JPM-OS method used in this research, it is important to discuss it in the context of other methods applied in previous research for extreme value studies. Discussions presented in section 2.3.1 on these methods are mostly derived from findings reported in Resio et al. (2009; 2007) – the latter contains a wealth of contributions, discussions, data and comments from academic researchers, a team of the U.S. Army Corps of Engineers, Federal Emergency Management Agency (FEMA), National Oceanic and Atmospheric Administration (NOAA), and consulting engineers in the private sector. Besides the JPM-OS method, four other methods are discussed in the cited studies. These are:

- Historical Storm Estimates Approach
- The Empirical Simulation Technique
- The Empirical Track Model
- Traditional Joint Probability Method

The next section briefly highlights the major difficulties associated with using the above-listed methods in extreme value probability analyses.

2.2.1 Challenges of Methods of Extreme Value Statistics

Relying on only historical storms to estimate risk or damage due to coastal inundation would be ideal if certain limitations were inexistent. Typically, the use of historical storms has been either through the determination of a “design storm” (Sorensen, 2006) event where one representative storm is adopted for analysis, or the “Peaks Over Threshold (POT)” approach in which storms with a specified parameter (e.g. storm size) over a selected threshold value are selected neglecting “smaller” storms, which may lead to inaccurate estimates of inundation risk (Resio et al. 2007). The design storm approach essentially allows the representation of the storm behavior by a significant parameter (e.g. R_p or c_p), and a deterministic dependence of all other parameters on the critical parameter (Sorensen, 2006); it implies that if the behavior of a given storm is strongly dependent on parameters other than the selected critical, then inundation estimates derived from that storm are significantly biased or inaccurate (Resio et al., 2007). The Empirical Simulation Technique (EST) is a variation of the POT approach, developed to obtain distributions of extreme surges of storms above some threshold (Borgman et al., 1992; Scheffner et al., 1996). Resio et al. (2007) highlight that the EST assumes a non-parametric distribution within its interior range of ranked points, emphasizing that this limitation restricts the non-parametric estimates to a record length spanned by hindcasts (which is typically short). Empirical Track Model (ETM, Vickery et al., 2000) is applied within a Monte Carlo construct which controls the sampling of storm parameters from a pool of empirically developed probability and joint probability functions. The challenge with the ETM is that a large number of storms must be simulated efficiently, to acquire sufficient data to span the sample space for coastal inundation risk analysis (Resio et al., 2007).

Myers (1975) and Ho and Myers (1975) discuss the traditional Joint Probability Method (JPM), which was applied to storm surge frequencies. Further extensions of the JPM (Schwerdt et al., 1979; Ho et al., 1987) were developed to obviate the discussed challenges associated with insufficient historical hurricane records. Five primary hurricane parameters were considered in the basic application of the JPM – the landfall location, central pressure, the radius of maximum wind speed, the forward speed and the approach angle of the storm relative to the shoreline or coast. In its basic form, the JPM used constant parametric wind fields obtained from simulations of straight-line tracks to define the peak surge for given combinations of these parameters. Probabilities were associated with these maximum surge values through the basic storm characteristics. If we denote the maximum surge value for a given storm as $\zeta_{\max}(x)$, then the probability of that surge value occurring as a result of the storm, as obtained from Resio et al. (2007) is:

$$p(\zeta_{\max}) = p(c_p, R_{\max}, v_f, \theta, x) \tag{2.1}$$

where:

c_p is the central pressure of the storm

R_p is the storm size

v_f is the forward speed of the storm

θ is the approach angle of the storm

x is the distance to a location of interest, from a known reference point

Considering the probabilities in equation (2.1) to be discrete increments, the cumulative distribution function for the probabilities is given as:

$$F(x) = \sum p_{ijklm} \mid x_{ijklm} < x \tag{2.2}$$

In Equation (2.2), p is the probability and the subscripts *ijklm* are the indices of the 5 parameters on which the probability in Equation (2.1) is dependent. Resio et al. (2007) pointed out two primary advantages of the JPM over methods that have a strong dependence on historical records:

- Though non-parametric, the conventional JPM covers a sufficient range of storm scenarios, such that extrapolations outside the range of simulations is not needed
- The JPM takes into account possible storm events, rather than only storm events that have already occurred

The authors also indicate that challenges of the JPM in the 1970's and 1980's included

- Insufficient data, which made the derivation of representative distributions (for say, radius of maximum wind speeds) significantly difficult
- The omission of a parameter to represent the variable peakedness of the hurricane wind fields
- Assuming that the values of central pressure, radius of maximum wind speed, forward speed, and approach angle varied only slowly in storms approaching the coast, and thus using parameter values at landfall to estimate the surge at the coast
- A lack of quantification of uncertainties associated with the expected extreme values

2.2.2 Joint Probability Method with Optimal Sampling (JPM-OS)

To address the previously-mentioned challenges associated with early (1970’s and 1980’s) applications of the JPM, Resio et al. (2009) emphasize the need to develop a method in which a smaller optimal sample of storms will be simulated, to characterize the storm population needed for inundation probability analysis – hence a JPM with optimal sampling technique. As of the time of this research, only few optimal sampling techniques have been published. Toro et al. (2010) and Niedoroda et al. (2008) discuss two optimization techniques that greatly reduce the number of storm simulations required in the JPM analysis. Their approach involves probabilistic descriptions of storm characteristics and storm occurrence to define a set of synthetic storms, followed by the use of a numerical method to calculate the coastal flood elevations that would be generated by those storms. A “quadrature” scheme is used to optimally select but minimize the number of synthetic storms, by assigning weights to each parameter combination. This is followed by a “response-surface” scheme which interpolates between the surges of the optimally selected storms. An alternative approach to optimal sampling is the use of SRFs, which is discussed in section 2.3; this approach involves estimating surge response as a function of physics-based scaled meteorological and spatial parameters that influence surge generation. Improving the robustness of this optimal sampling tool, and its application, is the focus of this research.

2.3 Surge Response Functions

2.3.1 Response Functions for Open Coast Locations

To address the need for accurate and robust surge estimation models that guarantee high computational efficiency in risk analysis, simplified models which capture the most relevant processes in surge generation must be developed. The use of surge response functions as surrogate models for the more complex numerical models was recently introduced (Irish et al. 2009). SRFs are non-dimensional physics-based scaled equations, comprising of the most important meteorological parameters for hurricanes, and spatial parameters that drive surge at the coast and in estuarine areas. The SRFs represent a continuous surface of surge response, parameterized by the hurricane characteristics. These storm parameters have the strongest influence on hurricane structure and intensity. Parameters accounted for in the SRFs prior to this research are hurricane central pressure, radius or size, landfall location and the influence of regional attributes namely, the continental shelf with.

Introducing an improved surge hazard scale for hurricanes, Irish and Resio (2010) presented a hydrodynamics-based surge scale that incorporates both meteorological characteristics of storms, and regional-scale spatial parameters into one equation that relates to storm surge potential. Storm parameters considered in the non-dimensional surge potential discussed in their work include central pressure, storm size and landfall location. Hence they demonstrated the possibility of producing a simplified but practical index of surge potential, while considering the effects of storm size, offshore depth profile, approach angle and forward speed. The authors report a satisfactory comparison of the surge scale to 28 historical storms in the United States. Using similar physical scaling laws, Irish et al. (2009) developed non-dimensional SRFs to relate surge response to storm size, central pressure and hurricane track. Here the authors show that these SRFs can reduce the computational burden of surge estimation by 75% for hurricane risk assessment. Their dimensionless alongshore and surge response expressions are given by equations (2.3) and (2.4):

$$x_1^{'} = \frac{x - x_o}{R_p} - \lambda - F(1 - R')H(1 - R') \qquad (2.3)$$

$$\zeta_1' = \frac{\gamma\zeta}{P_{far} - c_p} + m_x \frac{\left(P_{far} - c_p\right)}{\left(P_{far} - c_{p-\max}\right)} \qquad (2.4)$$

where:

x is the distance to the coastal location of interest

x_o is the hurricane landfall position along the shoreline

R_p is storm size

x_{eye} is the location of the storm eye at landfall

$x_{\zeta_{peak}}$ is the location of peak surge

c_p is the central pressure

P_{far} is the far-field barometric pressure

γ is specific weight of water

$c_{p\text{-}max}$ is a constant minimum possible central pressure based on a maximum possible intensity argument (e.g. Tonkin et al., 2000)

λ is a regional constant which describes a linear correlation between R_p and the alongshore distance between the storm eye at landfall (x_{eye}) and the as in Equation (2.5).

$$x_{\zeta_{peak}} - x_{eye} \cong \lambda R_p \tag{2.5}$$

In Equation (2.3), the third term was developed to modify the effects of the first two terms while correcting secondary influences due to relatively small storms that make landfall close to the location of interest. Irish et al. (2009) classify these small storms, for the Texas coast, as storms with R_p less than a threshold value, R_{thresh} = 25 km. They define the kernel in the third term of Equation (2.3), $F(1\text{-}R')$ and a Heaviside function, $H(1\text{-}R')$ as shown in Equations (2.6) and (2.7) respectively.

$$F(1-R') = \begin{cases} a_1(1-R') + b_1(\lambda \le x' \le 0) \\ a_2(1-R') + b_2(0 \le x' \le \lambda) \\ 0 \rightarrow (\lambda \le |x'|) \end{cases} \tag{2.6}$$

$$H(1-R') = \begin{cases} 0 \rightarrow (R' \ge 0) \\ 1 \rightarrow (otherwise) \end{cases} \tag{2.7}$$

where $R^{'}$ is the dimensionless hurricane size defined as $R^{'} = \left(\frac{R_p}{R_{thresh}} \right)$. Equation (2.4) is derived from the linear, depth-integrated, one-dimensional shallow water equation for conservation of momentum, with the assumptions that sustained winds blow long enough that a steady-state water surface profile is achieved, and that the only forces affecting water column are the surface wind stress and the pressure gradient force (Irish et al. 2010). The first term of Equation (2.4) accounts for the momentum transfer due to surface wind stress, while the second term accounts for additional wind-drag effects. Song et al. (2012) extended the work of Irish et al. (2009), by incorporating the effect of the varying continental shelf width along the Texas coast, relative to storm size. Surge generation is affected by the shelf width over which the sustained winds act. For a given storm size, wider shelf widths support the development of higher surges. The SRFs obtained after accounting for these regional influences are more robust relative to Irish et al. (2009), and are reported to have an improved accuracy (in terms of RMS-errors) of about 20 cm at open coast locations. This outcome demonstrates the potential of a more versatile parametric SRF to produce even more accurate peak surge estimates.

The current form (i.e. prior to this research) of open coast non-dimensional SRFs formulation for the Texas coast consisting contributions from Irish et al. (2009) and Song et al. (2012) is given in Equations (2.8) through (2.10). As can be noted, both the alongshore and surge axes of the SRFs have been modified to include the effects of geometric or regional attributes on peak surge distribution.

$$\zeta_1' = \frac{\zeta\gamma}{\Delta p} + m_2(x,x')\left(\frac{P_{far} - c_p}{P_{far} - c_{p-\max}} \right)^{\alpha(x,x')} \left(\frac{R_p / L_{30}(x_O)}{\left[R_p / L_{30} \right]_{ref}} \right)^{\beta(x,x')} \quad (2.8)$$

$$x' = \frac{(x - x_o)}{R_p} - \lambda(x_o) + cH\left(\frac{(x - x_o)}{R_p} - \lambda(x_o) \right)\left(\frac{R_p}{L_{30}} \right) - F(1 - R')H(1 - R') \quad (2.9)$$

The parameters in Equations (2.8) and (2.9) are defined as follows:

L_{30} is cross-shore distance from the shoreline to the 30-m depth contour, taken at the landfall location,

Δp_{MPI} is a regional constant taken as central pressure deficit evaluated for the Maximum Possible Intensity (MPI) for the region (taken as 870 mb based on Tonkin et al. [2000]),

$[R_p/L_{30}]_{ref}$ is a regional constant, defined as the maximum R_p/L_{30} in the region, taken as 3.5 for the Texas coast,

x is alongshore position measured on an axis which runs alongshore,

c is a dimensionless regional constant (taken as 0.75 for the Texas coast),

$\lambda(x_o)$ is a dimensionless landfall-location-dependent constant, and R' is dimensionless pressure radius, R_p/R_{thresh},

R_{thresh} is a regional constant, taken as 25 km for Texas coast,

m_2, α, and β are dimensionless fit coefficients varying by location and x' as follows:

$$\left[m_2\left(x,x'\right),\alpha\left(x,x'\right),\beta\left(x,x'\right)\right]=\begin{cases}\left[m_{2L}(x),\alpha_L(x),\beta_L(x)\right] & for\ x'<0\\ \left[m_{2R}(x),\alpha_R(x),\beta_R(x)\right] & for\ x'\geq 0\end{cases} \qquad (2.10)$$

Improvements to non-dimensional surge response functions for the open coast regarding v_f and θ stem from equations (2.8) through (2.10).

2.3.2 Response Functions for Bays

To develop SRFs for more complex regions such as coastal bays, Katyal (2009) considered three bays along the Texas coast; Corpus Christi, Matagorda and Galveston bays. The spatial parameters incorporated in the non-dimensional SRFs generated in his work are based on the characteristics of each bay, such as center of gravity and fetch distance – these parameters need to be considered because the proximity of the storm eye to the center of gravity affects the redistribution of water mass within bay**.** If the path and radius of a storm is such that the intense portion of its sustained winds acts over the bay, higher surge is generated within the bay due to corresponding high wind stresses, than if this is not the case. The author presents the dimensionless surge and spatial equations as given in Equations (2.11) and (2.12) respectively.

$$\zeta' = \frac{\gamma\zeta}{\Delta p} + m_x \Delta p + F_{\zeta'}\left(\Delta p, R_p, \zeta, S_b\right) \tag{2.11}$$

$$X' = \frac{X_{cg}}{R_p} + \frac{S_b}{X_C} - \lambda + F_{X'}\left(\Delta p, R_p, S_b\right) \tag{2.12}$$

where X_{cg} is the minimum distance from the center of gravity of a bay to the storm eye as it passes by the bay, m_x is a location dependent constant determined by linear regression at each station of interest and S_b is the characteristic size of the bay. The functions $F_{\zeta'}$ and $F_{X'}$ are given by Equations (2.13) and (2.14). In Equation (2.13), Katyal (2009) recommended values of 0.01 m^{-2} and 0.03 m^{-2} for the coefficient c, for Corpus Christi and Matagorda Bays respectively. Katyal (2009) used 3-term and 4-term (depending on the location considered) exponential functions of the form shown in Equation (2.15), to fit the non-dimensional surge distributions produced using Equations (2.11) and (2.12). Comparing simulated and predicted surge values, his work illustrated the accuracy of the SRFs in terms of RMS-errors which were, for most stations within the bays, less than 50 cm. It is desired that this uncertainty be much less than 50 cm, given that some uncertainty due to numerical modeling already exists, and the total uncertainty in the SRFs applied to extreme value will be cumulative. This work strives to reduce the uncertainties in the SRFs, by modifying the formulations developed by Katyal (2009) while including the effects of forward speed, approach angle and sea level rise.

$$F_{\zeta'}\left(\Delta p, R_p, \zeta, S_b\right)=\begin{cases}\zeta c R_p & for \quad \dfrac{\Delta p}{\gamma}<0.9m \,\&\, R_p>S_b \\ 1 & Otherwise\end{cases} \tag{2.13}$$

$$F_{X'}\left(\Delta p, R_p, \zeta, S_b\right)=\begin{cases}\dfrac{(\Delta p-82.5)}{(0.1\times S_b\times\gamma)} & for \quad R_p>S_b \\ \dfrac{(\Delta p-82.5)}{(0.1\times S_b\times\gamma)} & for \quad \Delta p>82.5mb \,\&\, R_p>S_b \\ \dfrac{(82.5-\Delta p)}{(0.1\times S_b\times\gamma)} & for \quad \Delta p<82.5mb \,\&\, R_p>S_b\end{cases} \tag{2.14}$$

$$\Phi = a_1 \exp\left(-\left(\frac{X'-b_1}{c_1}\right)^2\right)+..........a_3 \exp\left(-\left(\frac{X'-b_3}{c_3}\right)^3\right)+a_4 \exp\left(-\left(\frac{X'-b_4}{c_4}\right)^2\right) \tag{2.15}$$

While the results reported by Irish et al. (2009), Song et al. (2012), and Katyal (2009) are satisfactory, the contributions of variations in hurricane forward speed, approach angle and sea level rise were not accounted for in the SRFs. As these parameters have influences on surge generation along the coast and within bays, it is expected that accounting for their influences in the SRFs, using valid scaling laws, will lead to more accurate estimates of peak surge for extreme value analysis.

2.4 Hurricane Forward Speed and Approach Angle

Studies discussed here are useful in assessing the quality of surge data simulated in this research. Understanding the variation of surge as a function of forward speed and approach angle is useful in developing scaling laws to represent their effects. The following subsections review studies which offer insights on the effects of these parameters on surge response.

2.4.1 Forward Speed

In considering the effects of storm forward speed while developing hydrodynamic surge scales for hurricanes, Irish et al. (2008) mention that the duration over which surge is generated is affected by the storm's forward speed and the shelf characteristics (width and slope). Toro et al. (2010) assert (based on numerical sensitivity tests) that variations in forward speeds are found to produce fairly small variations in surge response, compared to storm size and central pressure. They further explain that the variations in storm speed are approximately linear, insensitive to the storm size (R_p) and central pressure deficit (Δp), and that only few storms are needed to characterize the variations in storm speed in surge response functions.

Rego and Li (2009) conducted a numerical study using a fully non-linear FVCOM (Chen, et al., 2003) model to assess the importance of the forward speed of hurricanes on surge. The authors used the Louisiana coast as study area and applied a range of forward speeds (2 m/s – 12 m/s), representing very slow to very fast moving storms respectively. Their study shows that hurricane forward speeds have a positive effect on peak surge heights, and a significant negative effect on flood volumes (flooded area times flood depth). It is reported in their work that increasing the forward speeds from a defined standard value decreases flood volumes (that is, the areal extent of flooding), while increasing peak surges for the range of forward speeds considered. The authors also showed that the effects of varying forward speeds on peak surge is less than the influence of central pressure and storm size.

Regarding the effects of hurricane forward speed on surge in estuarine (bay) areas as opposed to the open coast, Weisberg and Zheng (2006) performed storm surge simulations for Tampa Bay, also using FVCOM (Chen, et al., 2003). The authors assessed the sensitivity of storm surge to forward speed and found surge heights to be similar in Pinellas County beaches (representative of open coast locations) in spite of the fact that forward speeds varied – this was attributed to sufficiently-sustained winds causing similar equilibrium water levels to be achieved. Within Tampa Bay (representative of estuarine locations), their findings differ significantly from those obtained at the open coast locations; they found that slower storms induce higher surges within the bay, than faster storms. The effects of the leading and trailing edges of the storm on redistribution of mass within the bay are reported to be the major mechanisms through which the effect of forward speed manifests in surge heights.

2.4.2 Approach Angle

The angle with which a storm approaches the coast or an estuarine location influences the surge levels on the affected coastal area. Storms could approach the coast at an angle normal to it, one rotated clockwise or one rotated counter-clockwise from the shore-normal. Depending on the orientation of the shoreline (other factors held constant) one approach angle may have a significantly different effect on surge magnitudes than another, at specified coastal stations. Irish and Resio (2010) assert that for tropical storms in the northern hemisphere, storms which have a track rotated counterclockwise to shore-normal are expected to produce higher surges than those rotated clockwise. The authors explain that for the first group of storms (rotated counterclockwise), the continental shelf and coastline experience the impact of winds directed primarily onshore before those directed offshore, as opposed to the latter group.

Resio et al. (2009) show storm simulations using seven angles of approach, ranging from -15 to +45 degrees at 15 degree increments for a fairly straight shallow-sloping section of the Mississippi coast. The SLOSH (FEMA) model is used in their work to model storm surge, and the reported trends of surge versus angle of approach vary from fairly linear to weakly non-linear, depending on the location of coastal stations investigated. Signorini et al. (1992) used a 2-dimensional model to perform sensitivity analyses of storm surge height to bathymetry along the Texas-Louisiana shelf using historical storms of different approach angles. They found no critical dependence between surge and exact track angles for storms rotated within 20 degrees counterclockwise of shorenormal.

The influence of approach angle (among other parameters) on surge in bays was investigated by Weisberg and Zheng (2006) using Tampa Bay as case study; they found that the worst case of storm surge is of a storm moving from northwest, traveling parallel to the west coast of Florida, right past the bay entrance. The authors explain that winds for such storms are directed onshore ahead of the storm, causing a continuous increase in water levels, and they acknowledge that the opposite of their finding (i.e. southeast to northwest) would be the worst case for the east coast of Florida (which would be in agreement with Irish and Resio, 2010). Given the reported findings, the approach angle of a storm is obviously an important parameter to include in a model (SRFs) intended for peak surge estimation in coastal bays.

2.5 Potential Influences of Climate Change and Sea Level Rise on Storm Surge

By modeling carbon dioxide (CO_2) warming-induced intensification of hurricanes, Knutson et al. (2000) have showed that contrary to the notion that tropical storms may weaken due to their coupling with ocean response, the reduction in their intensity is quite mild and thus insufficient to significantly weaken tropical storms. In a similar work focusing on the sensitivity of future hurricane intensification and precipitation to the choice of climate models and convective parameterization used in modeling, Knutson and Tuleya (2004) conclude as part of their major findings based on all experiments conducted using 80-yr linear trends of +1% yr^{-1} CO_2 increase, that hurricane central pressures will reduce (by up to 14%). More recently, Knutson et al. (2010) stated that studies based on potential intensity theory and higher resolution (<20-km grid) models project mean global maximum wind speed increases of +2 to +11% (implied to be equivalent to +3 to +21% central pressure deficit). Villarini et al. (2011) used a statistical model to assess the disparity between dynamic model projections of hurricane frequency due to climate change, and they found that these disparities are an artifact of the differences in large-scale SST patterns from the different climate model projections. The authors concluded that their results do not support the notion of large increases in tropical storm frequency in the North Atlantic basin. Knutson et al. (2010) have also projected that hurricane frequency will either remain unchanged, or decrease with future climate change by the year 2100. It is important to note that Knutson et al. (2010) based their estimates on a review of several tropical cyclone frequency studies (including Zhao et al., 2009; Gualdi et al., 2008; Bengtsson et al., 2007 and Oouchi et al., 2006), which used statistical and dynamical models to estimate this parameter – their work gives an average range of tropical cyclone frequency of 6 – 34% with respect to the globally averaged frequency. While alternative opinions about the influence of climate change on hurricane intensities and frequency may exist, the consequence of omitting the evidence provided in literature may imply underestimating the risk associated with coastal inundation, hence poor coastal planning. To avoid this threat, this research assumes these effects to be important, and accounts for them in estimating extreme value analysis of coastal inundation.

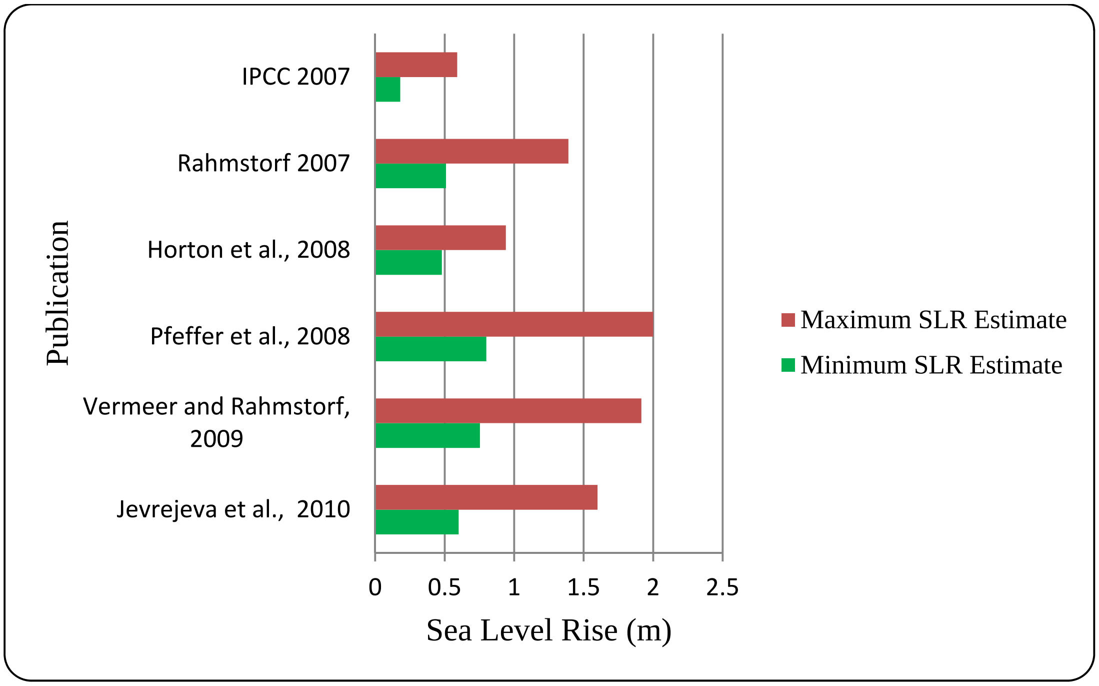

Figure 2.1: Estimates of sea level rise by 2100 (published within the past decade).

According to the International Panel on Climate Change (IPCC, 2007), model-based predictions of global sea level rise (SLR) shows a lower limit of 0.18 m and an upper limit of 0.59 m by the year 2099, corresponding to a range of temperature change (0.3 – 6.4^{o}C). This range spans the six climate scenarios (B1, A1T, B2, A1B, A2 and A1F1) defined in their report, and listed here in order of increasing greenhouse gas emissions. Other investigations/projections (Church and White, 2006; *Rahmstorf, S., 2007; IPCC, 2007; *Pfeffer et al. 2008; *Horton et al., 2008; *Vermeer et al., 2009; *Jevrejeva et al., 2010) of sea level rise have reported values higher than those in IPCC, 2007. The cited references with asterisks present estimates which include ice dynamics. Figure 2.1 shows minimum and maximum estimates of SLR projected for the year 2100, from some articles published within the past decade – it is similar to that shown in the "Sea-Level Change Considerations for Civil Works Programs" report by USACE, 2011, but with less references, and values are obtained directly from each publication listed. These reported estimates clearly suggest that SLR will play an important role in hurricane flooding in the future.

Studies have indicated the potential effects of climate change to increase hurricane flooding in estuarine areas (Frey et al., 2010; Irish et al., 2010; Mousavi et. al. 2009; Smith et. al., 2009). To date, no published works clearly indicate a universal trend relating hurricane surge change to changes in SLR, in estuaries and along the open coast. Not only is the understanding of such trends important to developing scaling laws for surge response estimation, this information is critical in the design of coastal structures. Smith et al. (2009) state that because surge generation and propagation processes are non-linear, (for locations where surge does not correlate linearly with SLR) the linear addition of relative sea level rise to design water levels is not appropriate for the region they studied (south-east Louisiana, USA) – the authors showed that the relationship between SLR and hurricane surge is non-linear at some locations within their study area. This research investigates these trends for the open coast and estuarine locations along the Texas coast.

The discussions covered throughout this chapter on previous research bolster the argument that hurricane forward speed, approach angle and sea level rise have significant influences on hurricane surge that should not be neglected in a tool intended for inundation risk analyses. Considering the significant advantage of using SRFs over complex numerical models for extreme value analyses, namely enormous savings in time and effort needed to complete such analyses, it is worth improving this tool by incorporating these important variables, thus extending its capability to evaluate more hurricane scenarios without loss of accuracy. Furthermore, the challenges associated with other methods of extreme value analysis make the JPM-OS a preferred approach to the other briefly discussed methods. Evidence of climate change as reported in the presented discussions is significant, hence the importance to account for hurricane intensification in estimating inundation risk. Efforts are made in this research to consider the contributions of these effects in SRFs, and their applications to risk analyses.

CHAPTER III

RESEARCH METHODOLOGY

3.1 Study Areas

3.1.1 Texas Coast - open coast locations

For the development of surge response functions for open coast locations, the region studied in this research is the Texas coast which borders the Gulf of Mexico (Fig. 3.1). The Texas coast is characterized by a continental shelf which gradually increases in width from south to north; also, several estuaries are located along the Texas shoreline. Located in the northwest part of the Gulf coast, historically, this area is susceptible to hurricanes. Hurricanes Carla (1961), Bret (1999), Rita (2005), and Ike (2008) are some of the storms which caused significant damage along the Texas coast.

Figure 3.1: Gulf of Mexico, highlighting the Texas coast (inner box).

Hurricane Rita made landfall near the Texas/Louisiana border as a category 3 hurricane, and caused widespread damage from eastern Texas to Alabama worth at least $5.6 billion; storm surge from Hurricane Rita is reported to have been as high as 4.5 m along the Louisiana coast (Knabb et al. / NOAA, 2006). Hurricane Ike hit Galveston, Texas as a category 2 storm, and is reported to be responsible for over 100 lives lost and about $10.0 billion in damages; the highest storm surge from Hurricane Ike was observed to be about 5.3 m on the Bolivar Peninsula and on the east side of Galveston Bay (Berg, R. / NOAA, 2008). In each of these cases of historical hurricanes, storm surge is strongly affiliated with the extensive devastations observed as a result of the event.

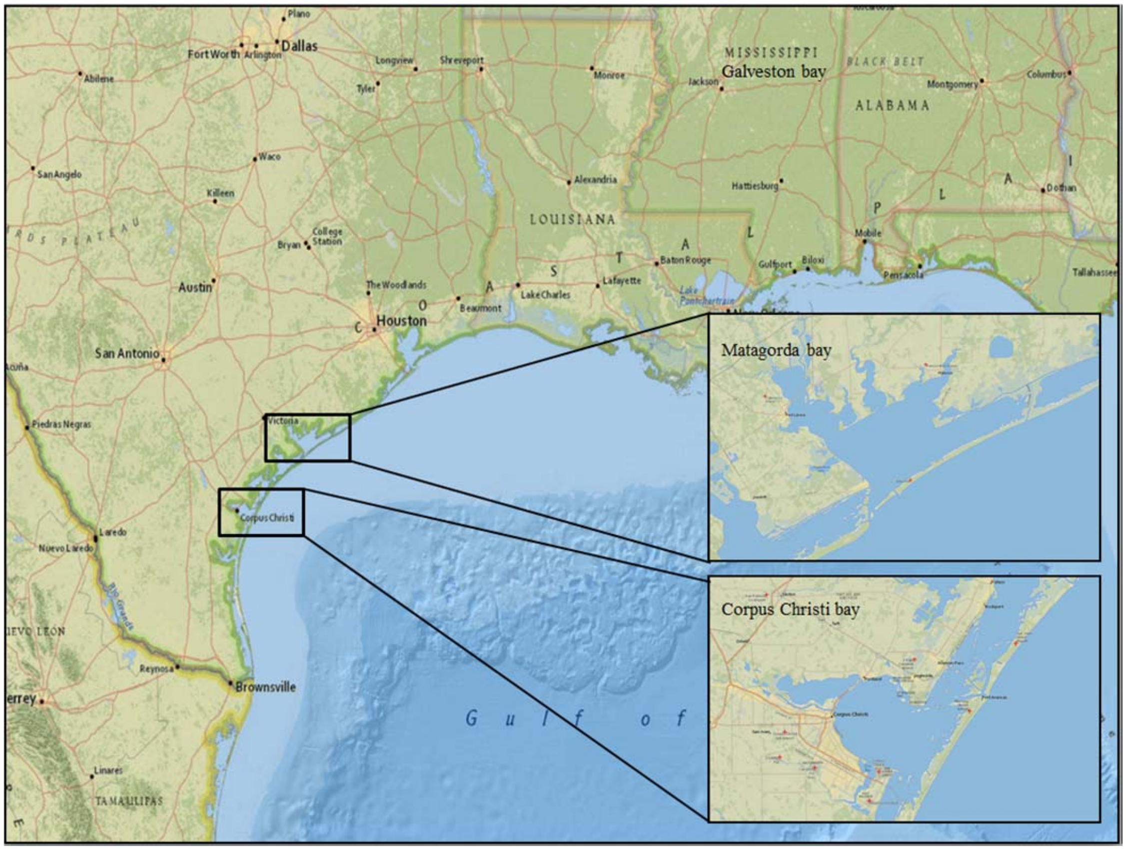

Figure 3.2: Corpus Christi and Matagorda, Texas.

Resio et al. (2007) found that all of the large storms affecting the U.S. Gulf of Mexico coastlines entered the Gulf either through the aperture between the Yucatan Peninsula and Cuba or through the gap between Cuba and southern Florida. Considering that the Texas coast is located north-west of these entrance points, the likelihood of hurricane impact to this part of the Gulf of Mexico can be considered significant. The occurrence and vast impacts of past hurricanes along the Texas coast has increased the interest of the coastal engineering community in risk and damage assessment in this area; hence the consideration of this study area for our research.

3.1.2 Corpus Christi and Matagorda Bays

Corpus Christi Bay (Fig. 3.2) is located along the Texas coast, at approximately 27.71^o latitude and -96.13^o longitude. The bay is about 3 m deep, has an industrial port and the surrounding city has a significant coastal population. The bay is also characterized by a barrier island, a navigation channel, an inlet (Aransas pass) and two adjoining bays (Oso Bay and Nueces Bay). Matagorda Bay located around 28.55^o latitude and -96.30^o longitude is a large bay (relative to Corpus Christi Bay) with an average depth of about 2.5 m. It is also characterized by a barrier island and a navigation channel, and has significant economic value. Matagorda Bay has a wide range of wildlife along its shores, which attracts agriculture and tourism in the area (Holtcamp, 2006) thus yielding significant revenue. Considering the population and economic importance of the areas surrounding these bays, it is essential to have efficient inundation risk analysis tools (e.g. SRFs) for these areas. Given the variety in characteristics (shape, size, width and elevation of their respective barrier Islands) of the two bays, response functions methodology developed for these areas will possibly be widely applicable.

3.2 ADvanced Circulation Model (ADCIRC)

Numerical simulations of synthetic storms are performed using the 2-dimensional depth-integrated (2DDI) version of the high resolution finite element model, ADCIRC (Luettich and Westerink, 2004). The domain of the finite element grid used in ADCIRC for this research spans the Gulf of Mexico (GOM), Atlantic Ocean and Caribbean Sea, with 1.3 million nodes over an area of 8.4 x 10^6 km^2 (Figure 3.3).

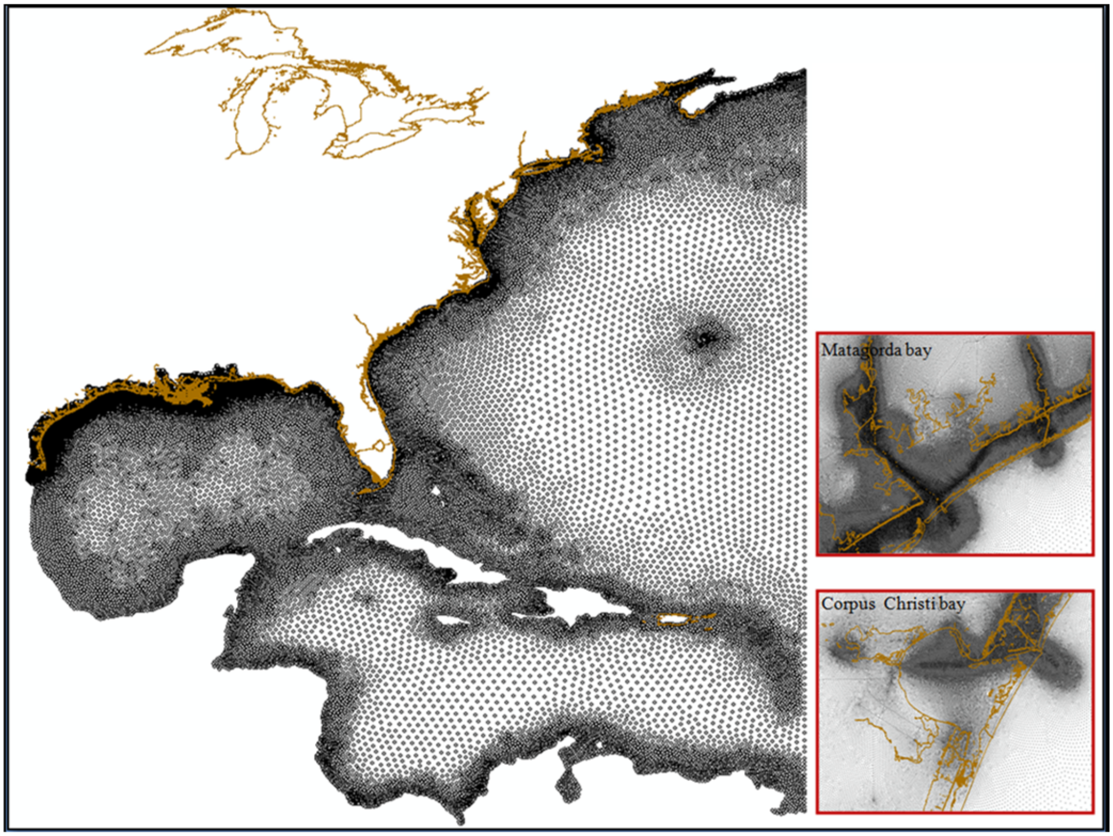

Figure 3.3: Numerical grid showing GOM, with Corpus Christi and Matagorda Bays.

Along the Texas coast, the resolution of this grid is as high as 80 m. Within the bays, the resolution is slight higher especially around the channels (about 50 m for Corpus Christi and Matagorda bays). The model solves the generalized wave continuity and momentum Equations (3.1) and (3.2) respectively, for water elevations and currents using meteorological and hydrodynamic parameters as input.

$$\frac{\partial H}{\partial t}+\frac{\partial}{\partial t}(UH)+\frac{\partial}{\partial y}(VH)=0 \qquad (3.1)$$

$$\frac{\partial U}{\partial t}+U\frac{\partial U}{\partial x}+V\frac{\partial U}{\partial y}-fV=-g\frac{\partial}{\partial x}\left[\zeta+{P_s}\big/{g\rho_o}-\alpha\eta\right]+\frac{\tau_{sx}}{H\rho_o}-\frac{\tau_{bx}}{H\rho_o}+\frac{M_x}{H}-\frac{D_x}{H}-\frac{B_x}{H}$$

$$\frac{\partial V}{\partial t}+U\frac{\partial V}{\partial x}+V\frac{\partial V}{\partial y}-fU=-g\frac{\partial}{\partial y}\left[\zeta+{P_s}\big/{g\rho_o}-\alpha\eta\right]+\frac{\tau_{sy}}{H\rho_o}-\frac{\tau_{by}}{H\rho_o}+\frac{M_y}{H}-\frac{D_y}{H}-\frac{B_y}{H}$$

(3.2)

where:

U and V are depth-averaged velocities in the x and y directions respectively,

H is the total water column thickness,

t is time,

f is the Coriolis parameter,

g is the acceleration due to gravity,

ζ is the free surface departure from the geoid,

P_s is atmospheric pressure at the sea surface,

ρ is the reference density of water,

η is the Newtonian equilibrium tide potential,

τ_{sx} and τ_{sy} are imposed surface stresses in x and y directions respectively,

τ_{bx} and τ_{by} are bottom stress components in x and y directions respectively,

M_x and M_y are vertically-integrated lateral stress gradients in x and y directions respectively,

D_x and D_y are momentum dispersion terms, and

B_x and B_y are vertically-integrated baroclinic pressure gradients (Luettich and Westerink, 2004).

3.3 Planetary Boundary Layer Model (PBL) for Hurricane Forcing

In modeling hurricanes in this research, the primary forcing are parametric wind and pressure fields, generated using the parametric Planetary Boundary Layer (PBL) model of Thompson and Cardone (1996). Many studies (Bunya et al., 2010; Smith et al., 2010; Westerink et al. 2008), have used the PBL model for surge modeling with satisfactory results. In this model, the wind and pressure fields are calculated using hurricane meteorological parameters (central pressure, forward speed, storm size, approach angle, and Holland B) by solving:

$$\frac{d\hat{V}}{dt} + fK \times \hat{V} = -\frac{1}{\rho}\nabla p + \nabla \cdot \left(K_H \nabla \hat{V}\right) - \frac{C_D}{h}\left|\hat{V}\right|\hat{V} \tag{3.3}$$

$$p_c(r) = p_o + \Delta p e^{-\left(\frac{Rp}{r}\right)^B} \tag{3.4}$$

where:

$\hat{V}$ is the vertically averaged horizontal velocity,

K is the unit vector in the vertical direction,

C_D is the drag coefficient,

f is the Coriolis parameter,

r is the radial distance from the storm center,

p_o is the central pressure, and

Δp is the difference in the central and far-field pressures.

Figure 3.4 shows an example wind field for a storm having central pressure of 900 mb, radius of 65 km and propagation speed of 5.6 m/s, created using the PBL wind model.

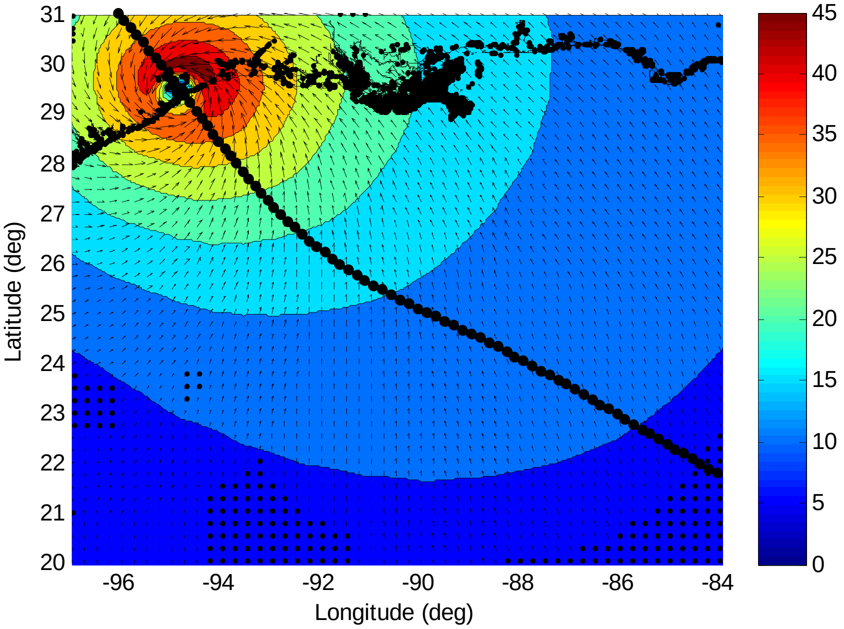

Figure 3.4: PBL wind field for storm with c_p = 900mb, R_p = 65km and v_f = 5.6m/s.

Equation (3.3) is the vertically averaged horizontal motion of the moving (hurricane) vortex, while Equation (3.4) gives the axisymmetric pressure field of the storm. Holland-B (Holland, 1980) is a parameter that controls the peakedness of the pressure profile relative to the radial distance from the center of the storm. In this PBL model, the range for this parameter is 0.5 - 2.5 (Thompson and Cardone, 1996), and the typical range for historical storms impacting the Gulf of Mexico is 0.9 – 1.6 (Resio et. al, 2007). The forcing fields are generated at an interval of 15 minutes, with resolution as high as 2.0 km in the inner nest of the grid. The model resolution is highest at the center of the storm to capture in great detail the strongest pressure gradients, and gradually reduces (4.0 km, 8.0 km, 16 km, etc.) away from the storm eye (Thompson and Cardone, 1996), to regions of relatively weaker pressure gradients.

3.4 Range of Meteorological Characteristics of Hurricanes in the Gulf of Mexico

To realistically generate subsets of synthetic hurricane data sets, it is important to review the characteristics of historical storms which have affected the defined study area. Over the years, technical advances in the methods of observing and recording tropical cyclone activity have evolved rapidly. Jarvinen et al. (1984) discussed various methods of hurricane data collection applied since the late 1800s to develop the best track database officially called HURDAT (NOAA). Hurricane wind speed estimates, central pressures and geographic storm trajectories are the most reported parameters in HURDAT. The National Hurricane Center (NHC) also has archives of maximum hurricane wind speeds and “most accepted” estimates of storm paths, in a database officially known as H*Wind (Powell et al., 1998, Powell and Houston, 1998). Although these two widely used archives contain several years (as far back as 1983 for H*Wind, and as early as 1955 for HURDAT) of hurricane central pressure and wind speed information for historical storms in the Gulf of Mexico (GOM), it has been suggested in literature that some of the data is inaccurate. Levinson et al. (2010) noted that the most reliable estimates are those recorded after the introduction of aircraft satellite and organized reconnaissance (which commenced in the 1950s).

With best track data, storm propagation speeds and approach angles can be easily calculated. However, estimates of radius of maximum winds ($R_{\max}$), and parameters which control the radial profile of hurricane wind speeds, e.g., Holland-B need to be obtained independent of the mentioned archives. The sensitivity of these parameters to hurricane wind fields depends strongly on the wind model used. For this research, best-track (historical) and synthetic hurricane data used in the PBL model are provided by Ocean Weather Inc. (OWI), to inform storm selection (see section 3.7) for surge modeling. The synthetic storms are derived from the historical storms, and represent possible future hurricane events. Table 3.1 gives approximate typical ranges of hurricane characteristics based on historical data of storms in the Gulf of Mexico; values are extracted from Tonkin et al. 2000 and Resio et al. 2007.

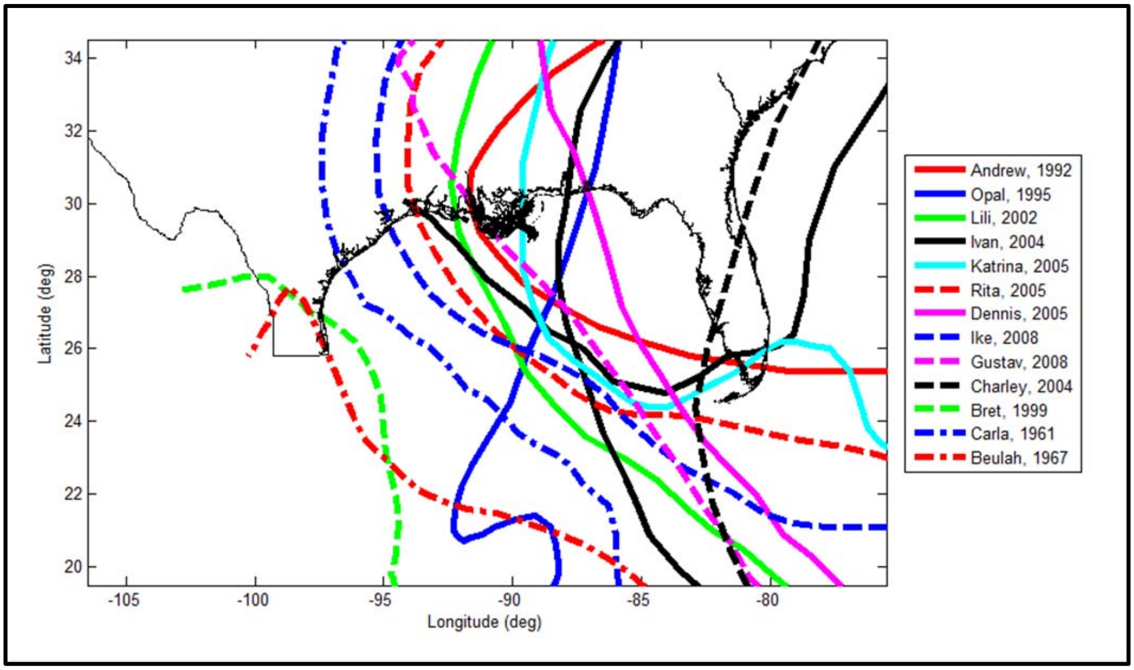

Figure 3.5: Tracks of historical storms for model validation.

Typical track paths of historical storms (Fig. 3.5) show most Gulf of Mexico hurricanes entering the region between Florida and Cuba, with a few storms entering the Gulf between Cuba and the Yucatan. The storms shown in Figure 3.5 are some of the major storms which had significant impacts along the coast in the GOM (National Hurricane Center, NOAA). Historically, the region from the northern end of the Texas coast through the coast of Florida seems to be the most impacted area of the GOM coastline. As may be observed above, most hurricanes in the Gulf of Mexico deflect to the right as they propagate toward the coast. Except for Hurricanes Opal (1995) and Bret (1999), the majority of these historical storms are generally oriented from southeast to northwest. Synthetic hurricane samples which are created to mimic historical samples in the Gulf of Mexico should therefore include this dominant track orientation, and more oblique orientations such as that of Hurricane Opal which produced storm surge of up to 4.2 m around Mobile Bay and Gulf Shores, Alabama, and the coast of Florida, with significant damage in these areas (Mayfield/NOAA, 1995).

Table 3.1: Range of storm characteristics for Gulf of Mexico storms.

Parameter	Minimum Value	Maximum Value	Notes
c_p	870 millibars	1010 millibars	+
R_p	9 km	74 km	*
vf	2.5 m/s	11.8 m/s	*
θ	-52 degrees	50 degrees	*
B	0.9	1.6	#

* Based on a subset of 22 historical storms in the GOM (Resio et al., 2007) spanning 1941 – 2005, which at some point in their history attained a central pressure of 955 mb or less prior to landfall.
\+ Deduced from Tonkin et al. (2000).
\# Obtained through sensitivity tests of wind fields and surges (Resio et al., 2007).

3.5 Range of Climate Change Parameters

The ranges for climate parameters, namely sea level rise and change in central pressure deficit, may be deduced from the literature summary presented in Chapter II (section 2.5). Sea level rise estimates range from 0.6 – 2.0 m (considering discussed literature), while hurricane central pressure deficits could go as high as 21% (Knutson et al, 2010). For hurricane frequency, a range of 6 – 34% with respect to the globally averaged frequency is deduced from Knutson et al. (2010). While the debate about realistic values of climate change parameters may be on-going in the literature, these reported values are useful in investigating the potential influence of climate change on extreme value probabilities of storm events.

3.6 Model Validation

The application of ADCIRC to model storm surge with input wind and pressure forcing generated by the PBL model has been tested and validated by Westerink et al. (2008), for hurricanes Betsy (1965) and Andrew (1992), which caused significant storm surge flooding in the southeastern region of Louisiana. Using 67 observations, the authors reported a mean error of -0.15 m, a mean absolute error of 0.30 m, and a standard deviation 0.37 m between the simulated and modeled peak surges. The model grid used in their work is very similar in extent and resolution (less than 100 m in coastal areas and channels), to that used in this research.

Irish et al. (2010) performed comparisons of SRF surges versus actual water levels for Hurricanes Carla (1961), Rita (2005), Bret (1999) and Ike (2008) using the same model set-up described in this research; these comparisons were proved to be satisfactory. Frey et al. (2010) also applied the discussed model set-up to hurricanes Carla (1961), Beulah (1967) and Bret (1999) in investigating the potential impacts of climate change on hurricane flooding; the authors satisfactorily quantified flood estimates based on ADCIRC output, and used these results in damage calculations.

Other applications (Bunya et al., 2010; Dietrich et al., 2010 – simulated hurricanes Katrina and Rita, 2005) of ADCIRC coupled with the STeady-state Spectral WAVE (STWAVE) model to include wave effects have been reported with satisfactory results. For 80 high water mark stations also within the southeastern region of Louisiana, Bunya et al. (2010) reported a match between simulated and observed peak surges of within 0.5 m and R^2 of 0.87 for Hurricane Rita; for Hurricane Katrina, 206 USACE high water marks were used, and the authors reported an average absolute difference of 0.40 m, a standard deviation of 0.48 m, and R^2 of 0.92. Kennedy et al. (2011) also applied a similar set-up to investigate the origin of the hurricane Ike forerunner surge; their work also demonstrates the competence of the ADCIRC model to accurately estimate forerunner surge which, as in hurricane Ike, can travel well in advance of the storm to cause major coastal flooding.

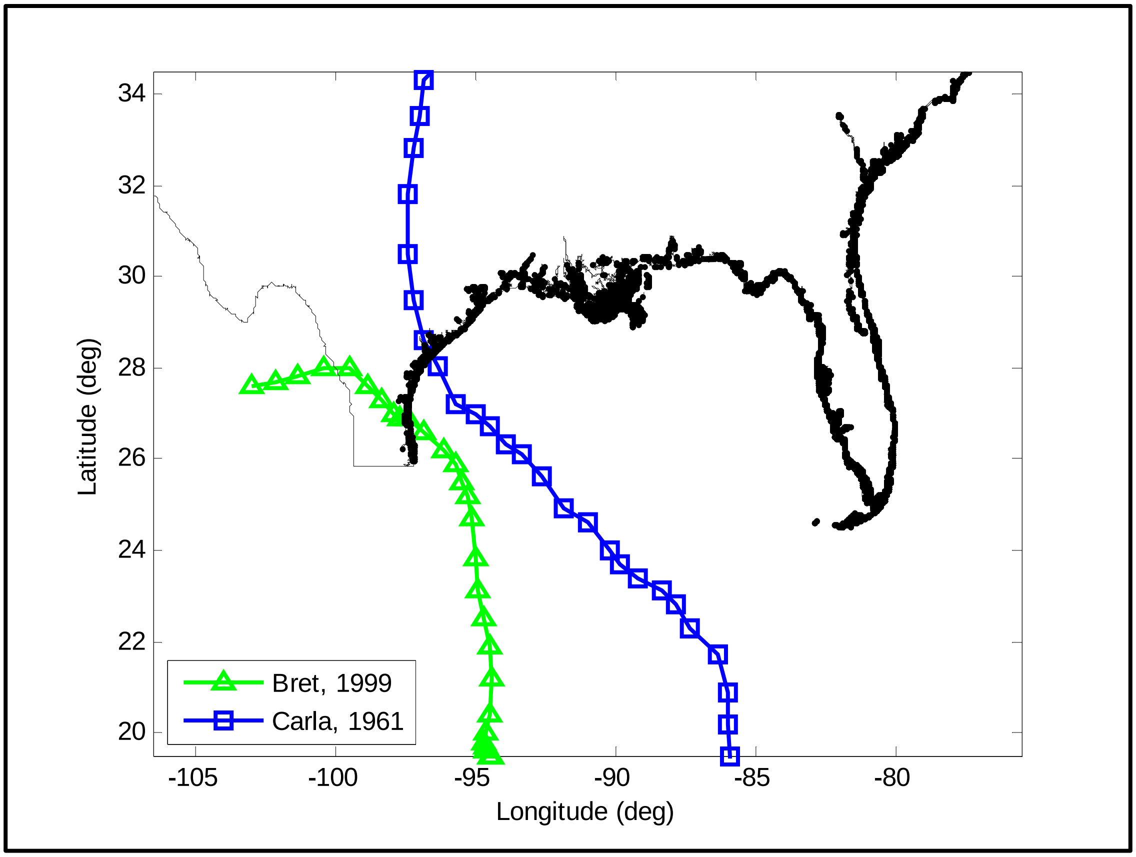

Figure 3.6: Tracks of historical storms Bret and Carla for model validation.

In the just-cited works related to model validation, more comparisons are made and more statistics are reported. For more details on the error statistics for such comparisons, the reader is referred to these publications; they are omitted here for brevity. Although the model set-up used in this research has been validated in other works, it is shown here that the performance is within the range reported in previous works. To demonstrate the model skill and the adequateness of the model grid's resolution, two historical hurricanes (Carla–1961 and Bret–1999) which made landfall in the Gulf of Mexico, are simulated; the tracks for these storms are shown in Figure 3.6. The meteorological information for all storms was obtained from OWI, and wind and pressure fields generated with the PBL model were used as forcing in ADCIRC for storm surge. Each storm was simulated using the ADCIRC model on the grid described in section 3.2. A total of 14 comparisons at 14 stations along the Texas coast, are made between peak surges from the ADCIRC-simulated storms and observed water level data (less tide estimates) from NOAA and the Texas Coastal Ocean Observation Network (TCOON). Most of the differences between the ADCIRC surges and the data are within 30 cm, as shown in Table 3.2. Figure 3.7 shows the recording stations used in the comparisons, while Figure 3.8 shows the plotted comparisons with respect to an exact-match line and regression fit. The locations selected for surge comparisons span the study area. With a linear fit, the observed and simulated surges correlate with an R^2 of 0.842 and a root mean error of 0.20 m and the mean absolute error is 0.179 m. Considering the magnitudes of these differences in the context of those earlier discussed, the model set-up is reliable for peak surge estimation.

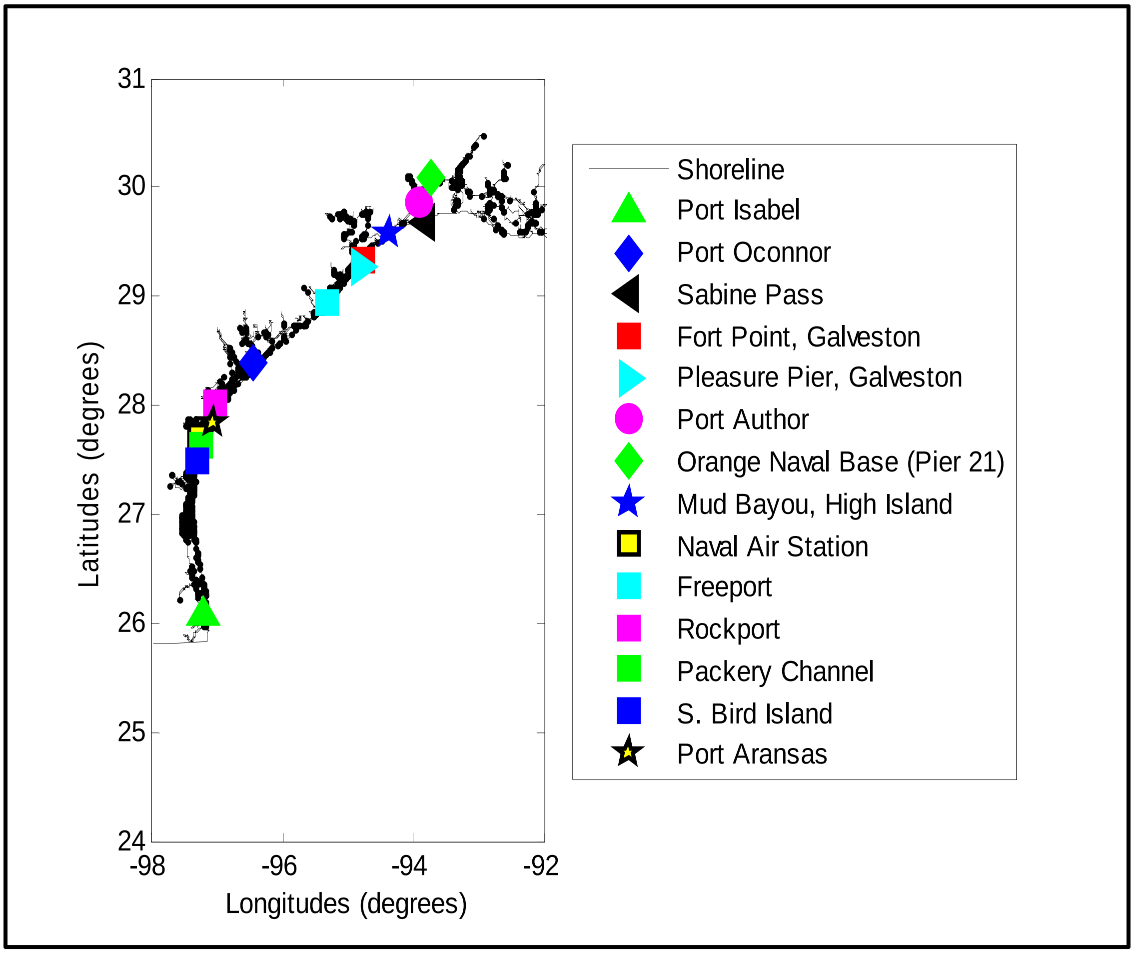

Figure 3.7: Recording stations used in peak surge comparisons for historical storms.

Table 3.2: Comparison of surges from historical storms in the Gulf of Mexico.

No.	Storm	Location	ADCIRC Surge (m)	Observed Data Level* (m)	Observed Data Source	Difference (m)
1	Carla	Port Isabel	1.19	1.00	NOAA	0.19
2	Carla	Port O'Connor	2.93	3.36	NOAA	-0.43
3	Carla	Sabine Pass	1.70	1.96	NOAA	-0.26
4	Carla	Fort Point, Galveston	1.95	2.35	NOAA	-0.40
5	Carla	Pleasure Pier, Galveston	2.16	2.41	NOAA	-0.25
6	Carla	Port Author	1.87	1.90	NOAA	-0.03
7	Carla	Orange Naval Base (Pier 21)	1.84	2.02	NOAA	-0.18
8	Carla	Mud Bayou, High Island	1.92	2.38	NOAA	-0.46
9	Bret	Naval Air Station, TX	0.28	0.64	TCOON	-0.36
10	Bret	Freeport, TX	0.30	0.70	NOAA	-0.40
11	Bret	Rockport, TX	0.29	0.48	NOAA	-0.19
12	Bret	Packery Channel	0.28	0.30	NOAA	-0.02
13	Bret	S. Bird Island, TX	0.29	0.34	TCOON	-0.05
14	Bret	Port Aransas, TX	0.29	0.41	TCOON	-0.12

*Tide estimates have been subtracted

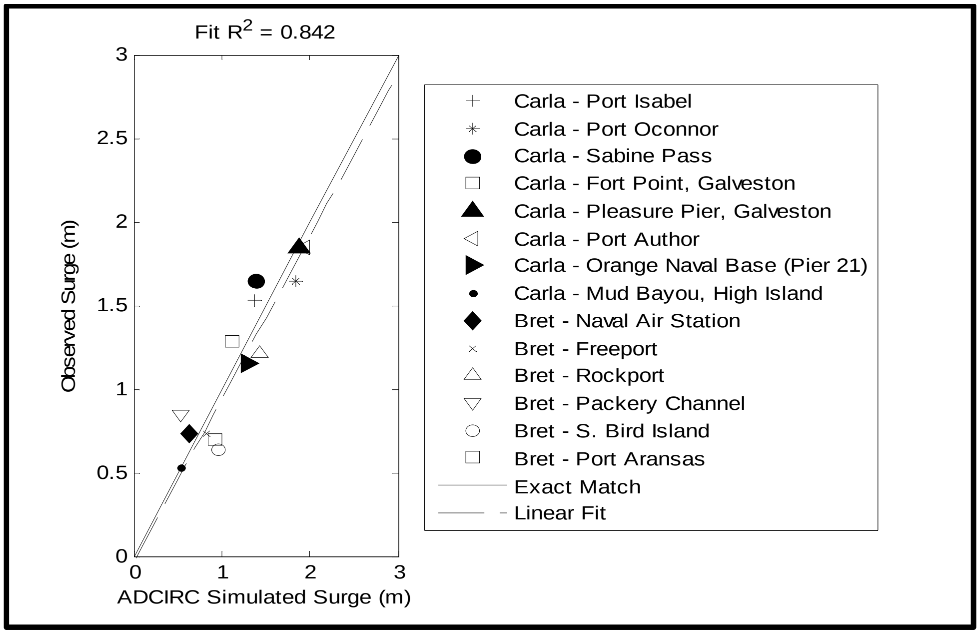

Figure 3.8: Comparison of simulated versus observed peak surges for historical storms.

3.7 Selection of Storm Samples, Hurricane Intensity Model and SRF Stations

3.7.1 Storm Set for Modeling

The storm set simulated in this research to investigate the effects of forward speed, approach angle and sea level rise (SLR) are synthetic storms. Storms selected for modeling are within recorded historical values (Tonkin et al. 2000; Resio et al. 2007) for hurricanes that have made landfall in the Gulf of Mexico. Regarding track spacing, Resio et al. (2007) used track spacing of about 57 km while developing a scale for alongshore distribution of surge in the New Orleans area; they found this to be adequate in describing the alongshore distribution of surge for a range of storm sizes similar to that considered in this research, and also found that this spacing introduced no bias in the probability estimates within the JPM framework. The track spacing used in this work is 30 km, and this is considered adequate as Irish et al. (2009) showed that SRF development from hurricane tracks separated by up to 90 km was as accurate as those separated by 30 km. Song et al. (2012) have also successfully applied similar track spacing to scale the alongshore distribution of surge for the Texas coast.

Simulations for the v_f effect cover slow (2.1 and 3.1 m/s) , medium (5.7 and 6.7 m/s) and fast-moving (8.7 and 10.3 m/s), storms combined with two values of central pressures, while keeping the hurricane size and the Holland B parameter constant at 32.78 km and 1.27 respectively. The storms are selected such that at a reference point for each track (X_{REF},Y_{REF} - approximately 166 km off the coast, Resio et al. 2007), the characteristics of the storms are as shown in Tables 3.3 through 3.5. Beyond this reference point, the structure of each hurricane undergoes deformation; the storm size increases with a corresponding reduction in peakedness (lower B values) while their intensity decays as it is approaches and crosses the coastline (OceanWeather Inc.). This weakening, or decay, of the storm toward landfall could be attributed to a number of effects, namely the impedance of the surface circulation by geomorphologic or frictional effects, and a reduction in the hurricane’s moisture as it makes landfall (NOAA, 1999).

Figure 3.9 shows the storm tracks for the simulated hurricanes. By orientation, the tracks are classified into A-tracks, B-tracks and C-tracks. At least 80 storms are simulated for the v_f effect along the A-tracks (Fig 3.9), which generally travel follow a North-Westerly (NW) direction as they approach landfall. Table 3.3 summarizes the characteristics of storms in the set modeled for the effect of v_f.

Table 3.3: Storm scenarios for v_f effect.

Storm ID	Longitude	Latitude	Vf (m/s)	cp (mb)	Rp (km)	B
1	X_{REF}	Y_{REF}	2.1	900	32.8	1.27
2	X_{REF}	Y_{REF}	5.7	900	32.8	1.27
3	X_{REF}	Y_{REF}	8.7	900	32.8	1.27
4	X_{REF}	Y_{REF}	3.1	960	32.8	1.27
5	X_{REF}	Y_{REF}	6.7	960	32.8	1.27
6	X_{REF}	Y_{REF}	10.3	960	32.8	1.27

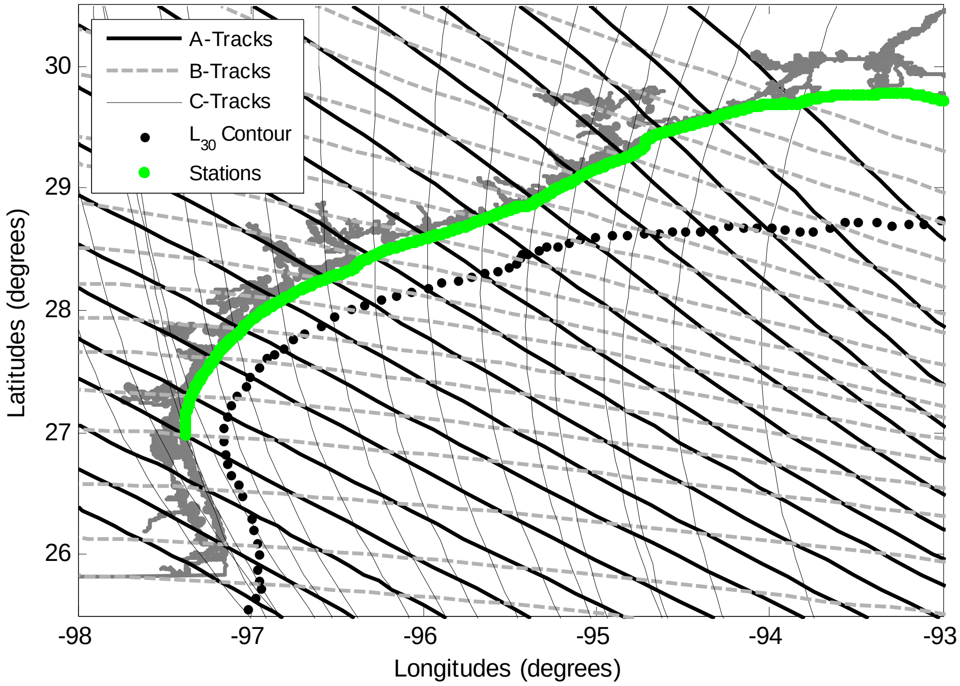

Figure 3.9: Simulation tracks of synthetic storms for open coast SRF analyses.

To include the effect of approach angle in the SRFs, three dominant track orientations are modeled per landfall location, throughout the Texas coast. Relative to compass azimuths, the first subset of storms generally follow a Northwesterly (NW) orientation as they approach landfall. Storms in this subset will hereafter be referred to as the A-Tracks. The second subset of storms generally follows a West-North-westerly (WNW) to North-westerly (NW) direction. These are hereafter referred to as the B-Tracks. Storms in the third subset range from North-North-westerly (NNW) to a North-North-easterly (NNE) orientation, and will be referred to as the C-Tracks for the remainder of this dissertation. Given that the shoreline orientation of the Texas coast is not constant throughout, the angles between the storm paths and the shore-normal direction varies with landfall location for A-, B- and C-Tracks (-15^o to 89^o). A-track ranges in magnitude from 8.43^o to 82.26^o, B-track ranges from -14.46 to 52.26^o, and C-track ranges from 44.35^o to 89.0^o.

At each landfall location (X_{LF},Y_{LF}) along the shoreline, the tracks (one from each) of the three orientations intersect, as shown in Figure 3.9. At least 54 storms are simulated for the approach angle (θ) effect (3 per landfall location).

Table 3.4: Storm scenarios for θ effect.

Storm ID	Longitude	Latitude	θ (deg)	cp (mb)	Rp (km)	B
A-Tracks	X_{LF}	Y_{LF}	NW	930	32.8	1.27
B-Tracks	X_{LF}	Y_{LF}	NWN - NW	930	32.8	1.27
C-Tracks	X_{LF}	Y_{LF}	NNW - NNE	930	32.8	1.27

Simulations to investigate the effects of sea level rise are performed along the A-tracks (Figure 3.9). The range of values modeled span the range (0.24 m – 2.10 m, estimates by year 2100) of estimates reported in Figure 2.1. Given that five scenarios are simulated per landfall location, the direction, central pressure, forward speed, and storm size are held constant to both isolate the effect of sea level rise, and minimize the number high resolution simulations to be performed. Table 3.5 shows the storm scenarios for the SLR effect. In Table 3.5, the SLR scenarios are values above current-day sea level, set to 0.24 m (based on lower limit of global mean sea level rate for the past decade – 2.4 mm/year, [Cazenave and Nerem, 2004]). A total of 90 simulations are used to investigate SLR effects on surge for SRF analyses.

In this work, the effect of SLR considered is that due global eustatic influences, as such local effects are not specially considered. The range of SLR estimates modeled here also covers estimates which would result when local land subsidence is accounted for, based on relative SRL rates in the Gulf of Mexico (Penland and Ramsey, 1990). In ADCIRC, the parameter used in effecting SLR change is the 'sea surface height above the geoid', within the nodal attributes file. All nodes of the gird are assigned the sum of the SLR value modeled, and the base water level.

Table 3.5: Storm scenarios for SLR effect.

Storm ID	Longitude	Latitude	Vf (m/s)	cp (mb)	Rp (km)	B	SLR (m)
1	X_{REF}	Y_{REF}	5.7	930	32.8	1.27	0.24
2	X_{REF}	Y_{REF}	5.7	930	32.8	1.27	0.73
3	X_{REF}	Y_{REF}	5.7	930	32.8	1.27	1.21
4	X_{REF}	Y_{REF}	5.7	930	32.8	1.27	1.69
5	X_{REF}	Y_{REF}	5.7	930	32.8	1.27	2.18

The storm sample sets shown in Tables 3.3 through 3.5 apply to SRF analyses for the open coast and bays; however, only subsets of the tracks shown in Fig 3.9 are applied for SRF analyses for the bays. Figures 3.10 and 3.11 show the tracks that apply to the bays; six landfall locations are considered for Corpus Christi Bay, and six landfall locations are considered for Matagorda Bay.

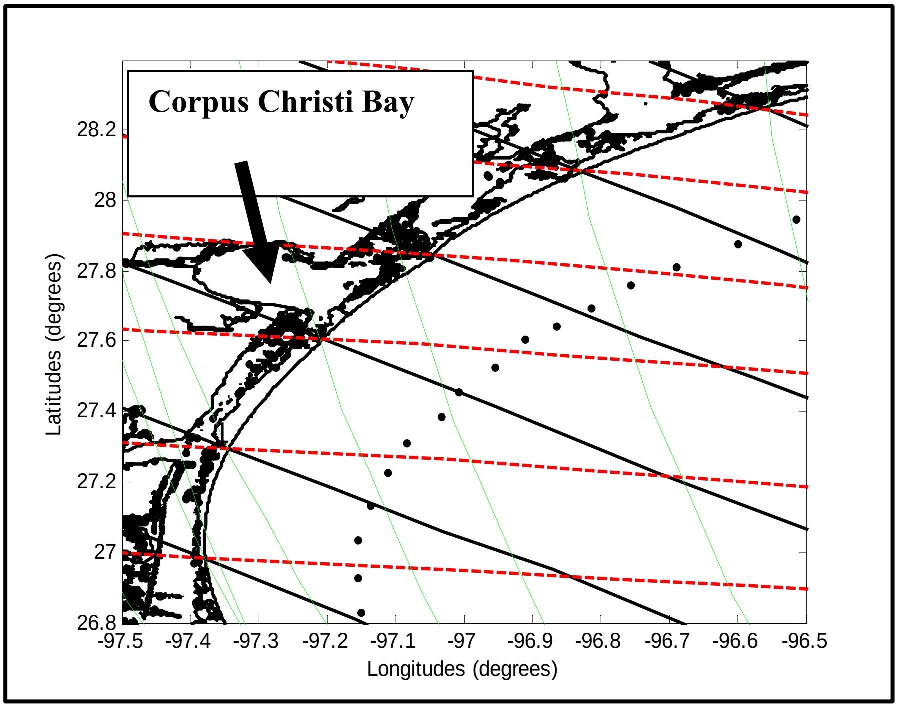

Figure 3.10: Tracks for Corpus Christi Bay analysis.

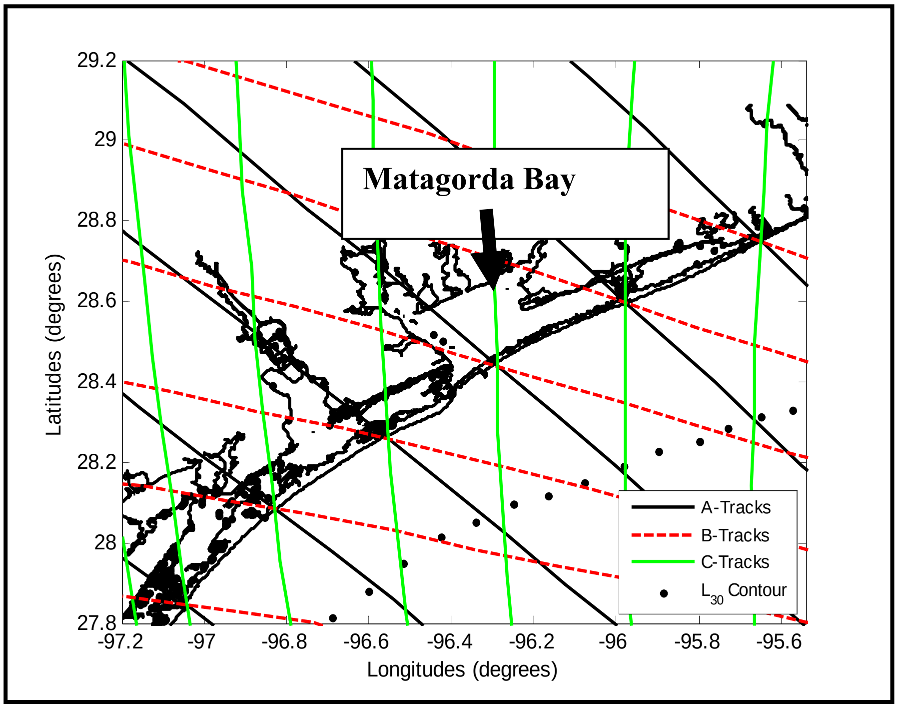

Figure 3.11: Tracks for Matagorda Bay SRF analysis.

3.7.2 Selection of Future Hurricane Intensity and Frequency Models

To account for hurricane intensity in extreme value statistics, this research assumes the model presented by Knutson and Tuleya (2004; 2008), given by Equation (3.5), which applies an 8 % mean change in central pressure deficit, for every 1^{o}C increase in sea surface temperature. Irish et al. (in press) noted that Equation (3.5) is particularly straightforward to use in evaluation of hurricane strength probabilities; they also state that Knutson and Tuleya (2004; 2008) considered thermodynamic influences and convective parameterizations in their analysis, but not wind shear; implying that the model holds only if the tropical system develops.

$$p_{\Delta SST} = p_o - \left[\left(0.08 + \varepsilon_p\right)\left(\Delta SST + \varepsilon_{\Delta SST}\right) \right] \Delta p \qquad (3.5)$$

where:

$p_{\Delta SST}$ is the projected future hurricane central pressure,

p_o is the present-day (2000s) hurricane central pressure,

ΔSST is change in sea surface temperature,

Δp is the difference between the far-field barometric pressure and the hurricane central pressure,

ε_p is the uncertainty in the fractional change in Δp with ΔSST, and

ε_p is the uncertainty in the uncertainty in the ΔSST projection.

Irish et al. (in press) presented an approximation of future projected storm rate of occurrence, which is based on climate model projections of Atlantic hurricane frequency. Their approximation, which was applied to examine the sensitivity of flood statistics to hurricane frequency parameters, considered two values of percentage change in hurricane frequency. The first value was a +19 % change corresponding to the mid-range warming scenario of the IPCC (IPCC, 2007) which is associated with a sea surface temperature of 1.72^{o}C and an average change of -33 % (Bender et al., 2010), while the second value was an estimated 23 % increase in major hurricane frequency per 1^{o}C of

SST based on Bender et al. (2010). A 3 to 6 % increase in flood elevations is seen by the 2080s, between the two values of percent frequency change, with the 23 % change giving higher values. Given the relatively small increase in flood elevations, and the conflicting evidence in the literature on decreasing versus increasing future hurricane frequencies, there is very little basis to be conservative and assume an increase in future hurricane frequencies. Thus, this research adopts the assumption of Irish et al. (in review) of 19 % (Equation 3.6), in accounting for future changes in tropical cyclone frequency within the extreme value analyses.

$$\lambda_{\Delta SST} = \lambda_o \left[1 - \left(0.19 + \varepsilon_\lambda\right)\left(\Delta SST + \varepsilon_{\Delta SST}\right)\right] \tag{3.6}$$

where:

λ_{SST} is the projected future storm rate of occurrence

λ_o is the present-day (2000s) storm rate of occurrence

3.7.3 SRF Stations for the Open Coast and Bays

The average spacing between SRF stations along the Texas coast (Fig. 3.8) is 1.2 km, and for the two bays an average spacing of 1.5 km is used. A total of 512 stations are used to investigate the performance of SRFs along the open coast. For the bays, a total of 109 and 114 stations (Figs. 3.12 and 3.13) are used in investigating the performance of the SRFs in Corpus Christi and Matagorda Bays, respectively.

Within the bays, stations are located along the edges and in areas where the shoreline is highly irregular. The variation of surge along the bays is expected to be higher at locations where boundaries are highly irregular, because such geometric boundaries affect surge re-distribution to different extents for different storms within the bays. Stations located along the coast in Figures 3.12 through 3.13 are to enable a comparison of the SRF formulations for the open coast and bays, to determine which formulations perform better at those locations.

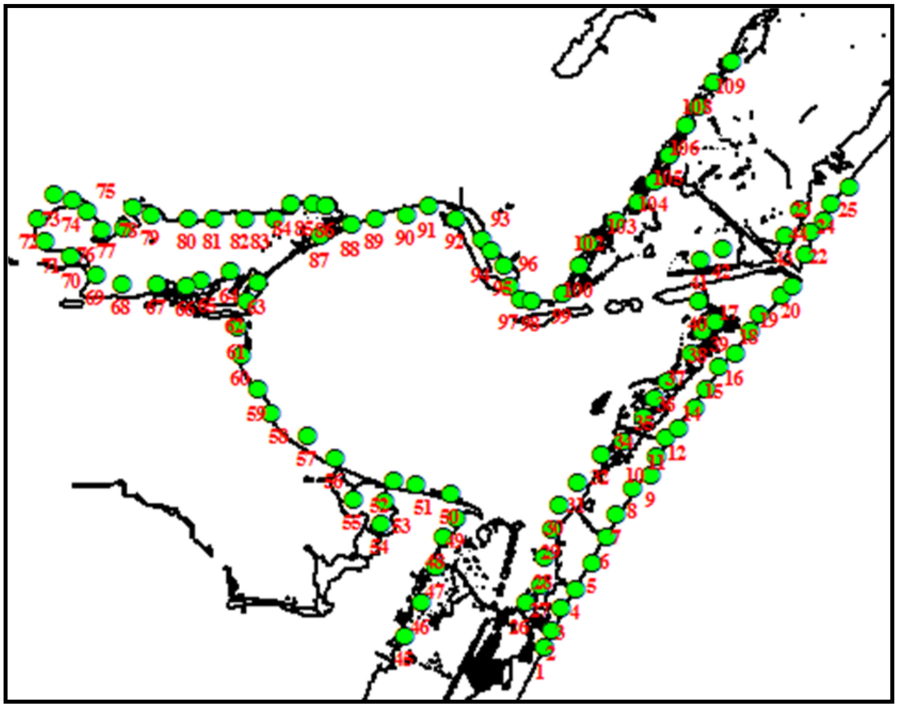

Figure 3.12: SRF stations for Corpus Christi Bay.

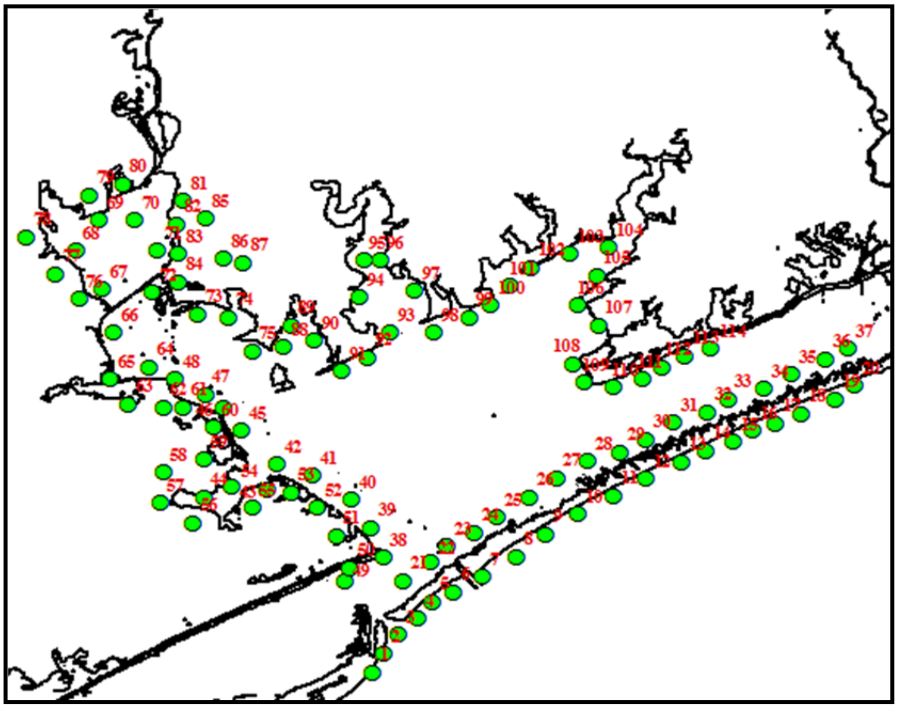

Figure 3.13: SRF stations for Matagorda Bay.

3.8 The JPM-OS Technique for Extreme Value Analysis

To obtain joint probabilities for extreme value statistics, this research adopts the flood response model presented in Irish and Resio (in press) as Equations 3.7 and 3.8:

$$z_{\max}(x) = \phi(x, p_o, R_p, v_f, \theta, x_o, MSL) + \varepsilon_z \tag{3.7}$$

$$\varepsilon_z{}^2 = \varepsilon^2{}_{tide} + \varepsilon^2{}_{surge\ \ simulation} + \varepsilon^2{}_{waves} + \varepsilon^2{}_{winds} + \ldots \tag{3.8}$$

where:

ϕ is a continuous flood response function

x is location of interest

x_o is landfall location

R_p is hurricane pressure radius near landfall (Thompson and Cardone, 1996)

θ is the hurricane approach angle with respect to the shoreline

v_f is the hurricane forward speed near landfall

MSL is the mean sea level

ε_z is the epistemic uncertainty in the flood response (Resio et al. 2009; in review)

In a similar construct for the cumulative distribution function for a storm with parameters in Equation 3.7, Resio et al. (2009) limited the number of dimensions covered to the number of parameters contained within representative PBL models, with the argument that such models provide a relatively accurate representation of the overall structure within hurricanes. The authors also argue that wind fields from PBL models have been known to provide accurate estimates of ocean response to Gulf of Mexico hurricanes. The error term in Equation (3.7) is also described as a useful way to include additional effects on water levels, such as tides.

Irish and Resio (in press) assume a Gumbel distribution to represent the conditional probability of central pressure along the coast (Equation 3.9), and a normal distribution for conditional probabilities of storm size on central pressure, forward speed on approach angle, and approach angle on landfall location (Equations 3.10 through 3.12), expressed as follows:

$$p(c_p, R_p, v_f, \theta, x) = \kappa_1 \cdot \kappa_2 \cdot \kappa_3 \cdot \kappa_4 \cdot \kappa_5$$

$$\kappa_1 = p(c_p \mid x_o) = \frac{1}{a_1(x_o)} \exp\left[-\frac{\Delta p - a_o(x_o)}{a_1(x_o)}\right] \exp\left\{-\exp\left[-\frac{\Delta p - a_o(x_o)}{a_1(x_o)}\right]\right\} \tag{3.9}$$

$$\kappa_2 = p(R_p \mid c_p) = \frac{1}{\sigma(\Delta p)\sqrt{2\pi}} \exp\left\{-\frac{\left(\overline{R}_p(\Delta p) - R_p\right)^2}{2\sigma^2(\Delta p)}\right\} \tag{3.10}$$

$$\kappa_3 = p(v_f \mid \theta) = \frac{1}{\sigma(\Delta p)\sqrt{2\pi}} \exp\left\{-\frac{\left(\overline{v}_f(\theta) - v_f\right)^2}{2\sigma^2}\right\} \tag{3.11}$$

$$\kappa_4 = p(\theta \mid x_o) = \frac{1}{\sigma(x_o)\sqrt{2\pi}} \exp\left\{-\frac{\left(\overline{\theta}(x_o) - \theta\right)^2}{2\sigma^2(x_o)}\right\} \tag{3.12}$$

$$\kappa_5 = \Phi(\lambda, x_o) \tag{3.13}$$

where:

κ_i is the probability density function for each considered parameter

a_0 and a_1 are Gumbel coefficients

σ are the standard deviations of the normal distributions

$\Phi(\lambda, x_o)$ is frequency of storms per year, per specified distance along the coast, and overbars denote normal distribution mean values.

To account for the influence of climate change in the JPM-OS implementation, the central pressures of all storms considered will be adjusted using Equation 3.5 (Knutson and Tuleya, 2004; 2008). The probability density function for central pressure (Equation 3.9) will thus include the effect of climate change. With this adjustment, the probability distribution function with all parameters is:

$$p\left(SST, c_p, R_p, v_f, \theta, x\right) = \kappa_{SST} \cdot \kappa_1 \cdot \kappa_2 \cdot \kappa_3 \cdot \kappa_4 \cdot \kappa_5 \qquad (3.14)$$

and the return period (T_r) resulting from the probabilities is given as:

$$T_r = \frac{1}{\lambda\left(1 - F\right)} \qquad (3.15)$$

where F is the cumulative distribution function of the probability density functions. Equations (3.9), (3.10), (3.13), (3.14) and (3.15) will be applied as shown in estimating inundation probabilities, in this research, whereas Equations (3.11) and (3.12) will be simplified regarding conditional dependence of the probabilities.

The discussed methodologies are applied to model storm surge for the development of SRFs and onward application to extreme value analysis in the study area.

CHAPTER IV

IMPROVED SURGE RESPONSE FUNCTIONS AND APPLICATIONS TO EXTREME VALUE ANALYSIS

4.1 Surge Trends along the Texas Coast

To develop dimensionless scaled terms for the effects of v_f , θ and sea level rise (SLR) in the surge response functions (SRFs), their surge trends need to be investigated. This is because the surge trends inform on the effects of these parameters in dimensional space, and also lead to the identification of other associated parameters/influences that may amplify or reduce the influences of v_f , θ and SLR on surge generation. Once the primary and associated parameters are identified, non-dimensional functions (or scaled terms) may be developed using dimensionless scaling.

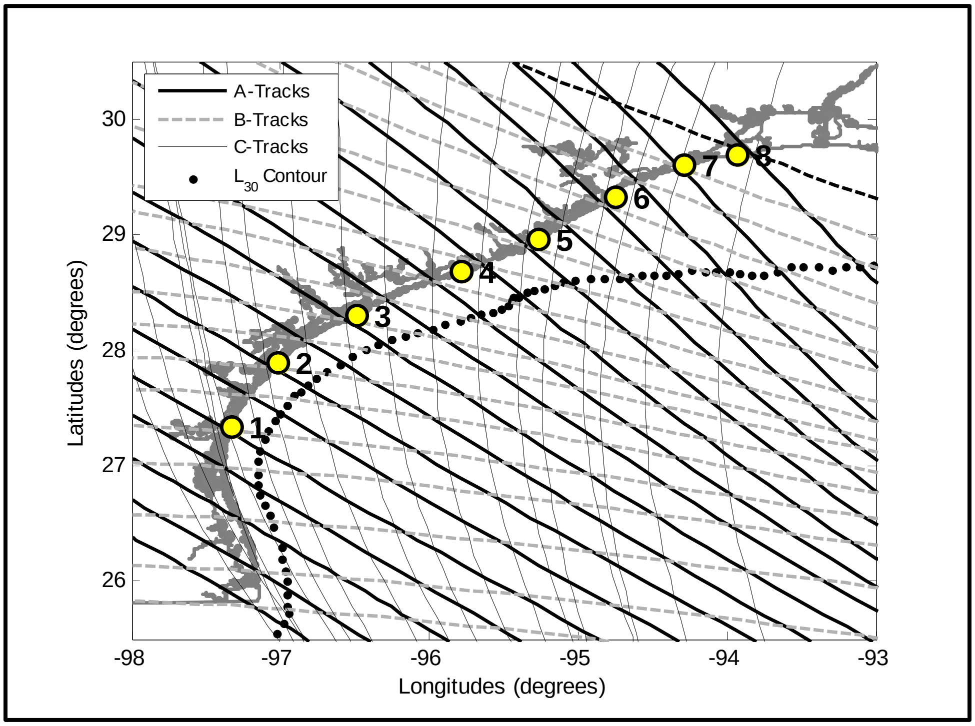

Figure 4.1: Tracks and locations for discussions on open coast results.

Of the open coast locations which span the entire Texas coast, a subset is selected for discussion of results. Figure 4.1 shows eight locations for which results will be discussed herein for the open coast. The coordinates of these locations are presented in Appendix C. For the reader’s benefit, it is re-stated here that the tracks considered for the influence of forward speed are the A-tracks in Fig. 4.1 – they are eighteen in number, and will be referred to as track 1, track 2 and so on in discussions, where track 1 is the southernmost track and track 18 is the northernmost track along the coast.

4.1.1 Open coast surge Trends as a function of Forward Speed

The variation of surge with v_f is shown in Figures 4.4 through 4.7, corresponding to locations 1, 3, 5 and 7, which have increasing values of continental shelf width. To rely on the governing physics of Equation (1.1) for explanation, it is re-written here as Equation (4.1) in terms of the width of the continental shelf measured from a 30 m depth contour, L_{30}, delineated in Fig. 4.2.

$$\zeta \propto \left(\frac{\tau_s}{gh}\right) L_{30} \tag{4.1}$$

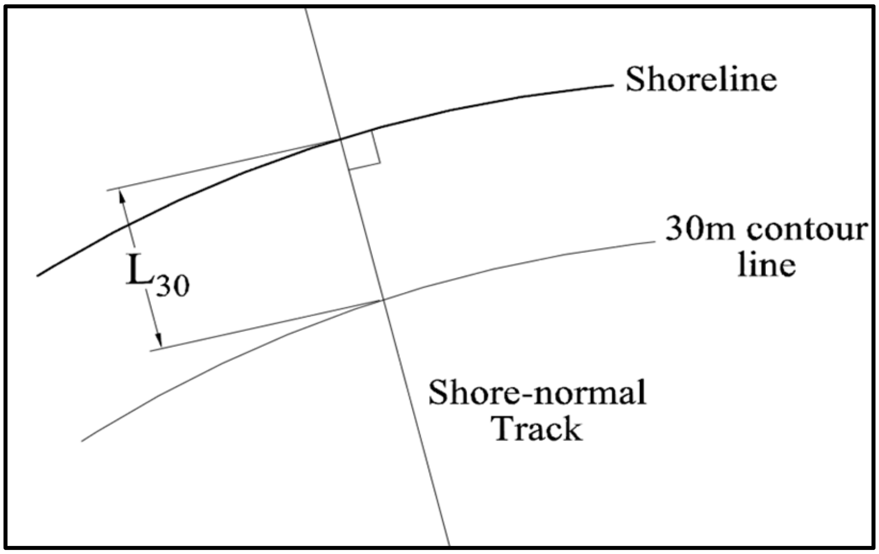

Figure 4.2: Schematic of L_{30}.

Equation (4.1) suggests that at wide shelf areas (i.e. with relatively large L_{30} values), generally, higher surge magnitudes should be expected than at narrow shelf regions, for the same storm(s). The effects of the steering winds (larger atmospheric flow) and the storm's wind speed are cumulative, resulting in higher wind stresses especially on the right side of the hurricane vortex (NOAA, 1999). The above equation also suggests therefore that locations to the right (strong side) of the storm are likely to be impacted by higher surges than the locations to the left, due to the higher wind stresses.

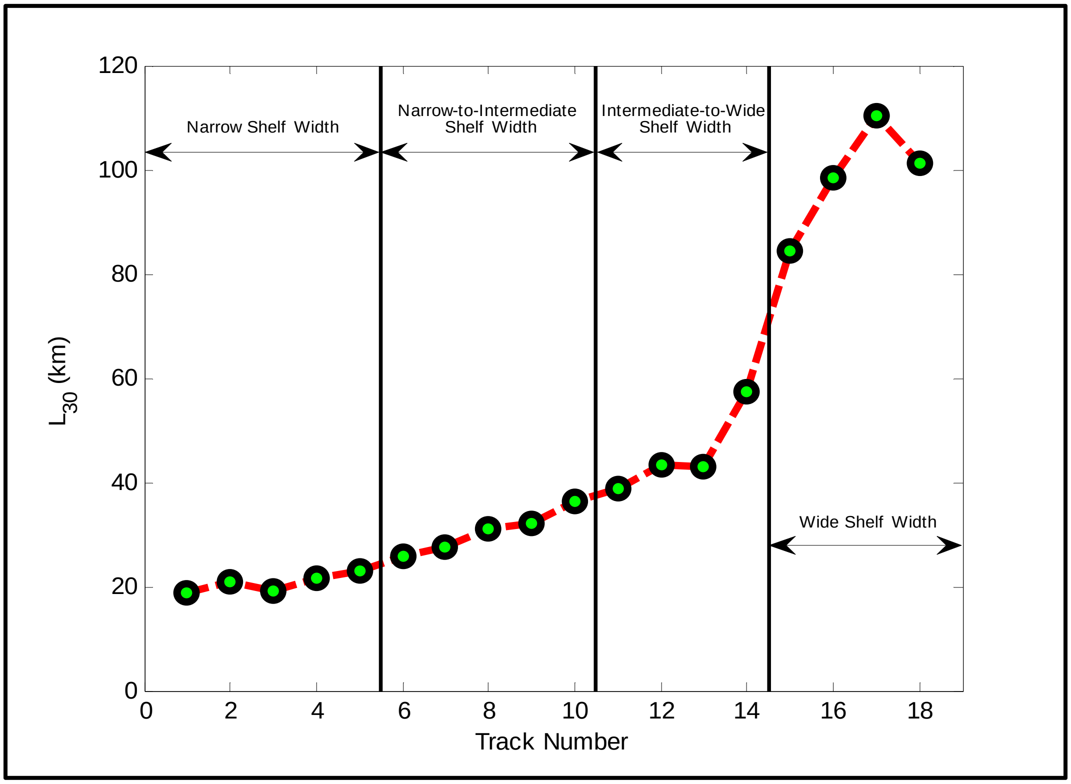

Figure 4.3: Variation of L_{30} by track.

The magnitude of L_{30} varies from low at the southern end of the Texas coast, to high values at the Northern edge of the coast (Fig. 4.3). Between tracks 13 and 17, the continental shelf widens more rapidly than between tracks 1 through 12. Following the argument relying on Equation (4.1) storms traveling across this relatively wider shelf area are expected to generate more surge than those at locations with low L_{30} values.

Figure 4.4 shows the trends at location 1 (Fig. 4.1) which is located at a narrow shelf region. At this location, the tracks producing the highest surge as a function of v_f are tracks 3 and 5, with the latter being the closest to the location considered (location 1). Tracks 7 through 18 make landfall to the right of location 1, such that the weak part of these storms impact the location, hence lower surge values. Comparing the surges of the relatively intense storms (top pane) to the weaker storms (bottom pane), it is clear that the storms with lower central pressures produce higher surges; this is expected since the pressure gradients within these storms yield stronger wind fields that generate higher surges. For storms making landfall to the left of location 1, surge increases as forward speed increases. However, for storms making landfall to the right of location 1 the differences in surge magnitudes are much smaller. This difference in surge trends for the two groups (i.e. those making landfall to the right, and left of the location of interest) demonstrates that the wind stresses primarily determine surge heights along the coast, as their intensities on the right side of the storm differ significantly from those on the left.

At locations 3, 5 and 8 for which surge trends are shown in Figs. 4.5, 4.6, and 4.7, the observations made at location 1 regarding the differences in magnitudes of surges for storms making landfall to the left and right of the location, are also clearly evident. At location 3, amongst the tracks shown, the tracks making landfall to the right of the location are tracks 10, 14, 16 and 18, and these show relatively lower surges. Similarly, relatively low surge values from storms making landfall to the right of the location of interest are identified at location 5 (tracks 14, 16 and 18) and location 8 (track 18).

A close examination of the surge trends at locations 1, 3, 5 and 8 shows that there is some influence of L_{30} on the surge magnitudes, as a function of v_f. Amongst the tracks producing the highest surges at location 1 (tracks 1, 3 and 5), the surge magnitudes increase with L_{30} – in other words, track 1 with L_{30} of 18.69 km produces lower surges than track 3 with which has L_{30} of 19.10 km, while track 5 with L_{30} of 23.05 km produces even higher surges than track 3, for all speeds considered.

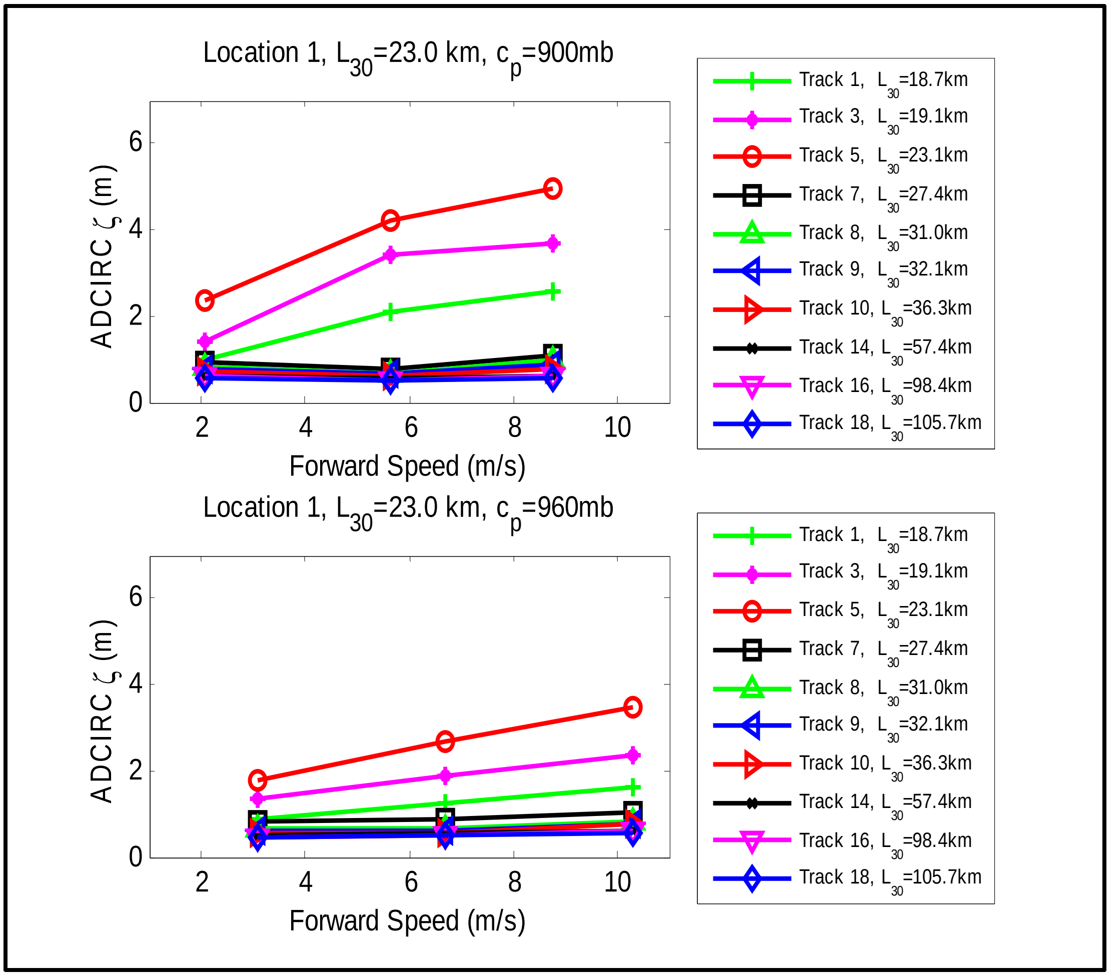

Figure 4.4: Forward speed versus surge, at narrow shelf width region. Top pane shows storms simulated with v_f = 2.1, 5.7 and 8.7 m/s with c_p = 900 mb. Bottom pane shows storms simulated with v_f = 3.1, 6.7 and 10.3 m/s with c_p = 960 mb. L_{30} at location 1 is 23.0 km.

Similar observations are made at location 3 (between tracks 5, 7 and 8), at locations 5 (between tracks 8, 9 and 10) and at location 8 (between tracks 10, 14 and 16). This increase in surge with an increase in L_{30} is consistent with the basic physics of surge generation (Equation 4.1), and is observed throughout the Texas coast.

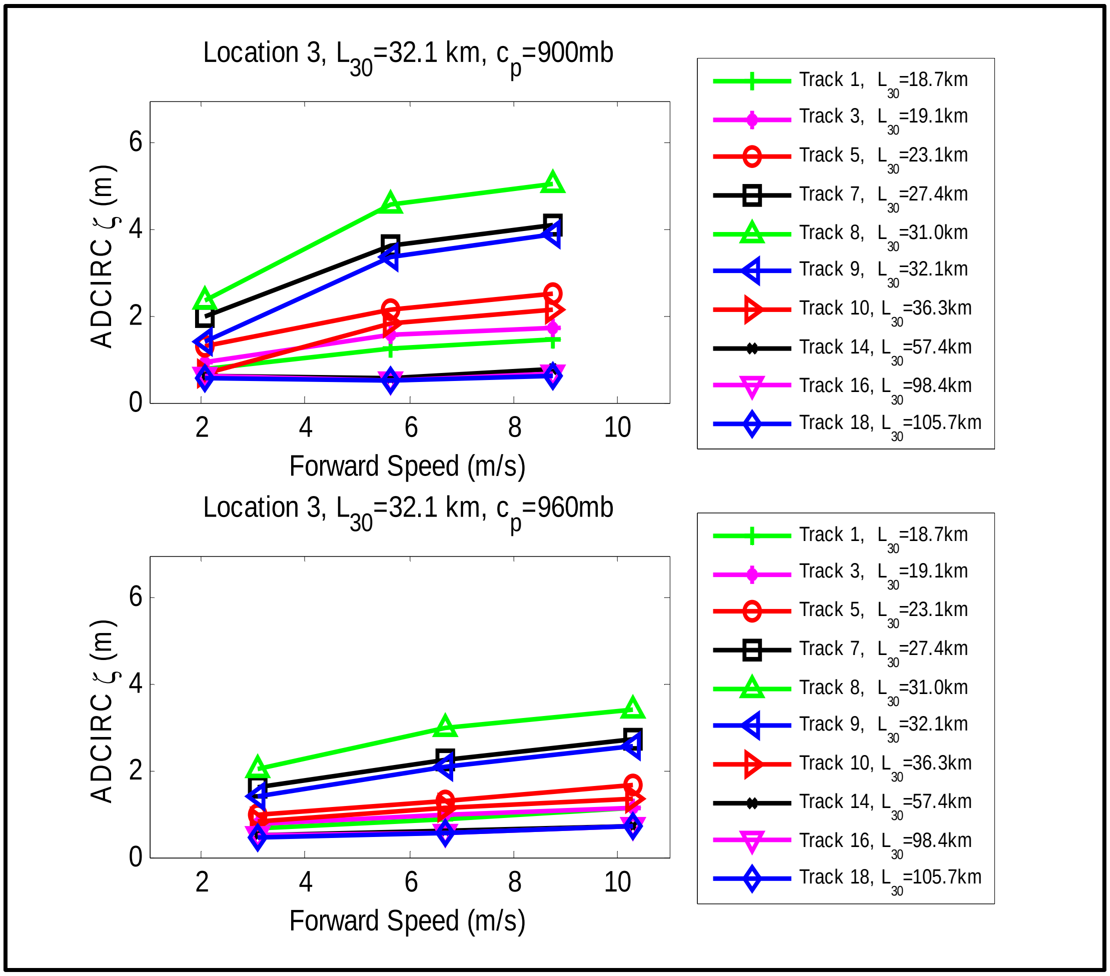

Figure 4.5: Forward speed versus surge, at narrow-to-intermediate shelf width region. Top pane shows storms simulated with v_f = 2.1, 5.7 and 8.7 m/s with c_p = 900 mb. Bottom pane shows storms simulated with v_f = 3.1, 6.7 and 10.3 m/s with c_p = 960 mb. L_{30} at location 3 is 32.1 km.

The similarity in surge values for the 5.7 m/s and 8.7 m/s storms (with c_p = 900 mb) seems to increase with L_{30}, as this observation is more conspicuous at location 8, and gradually less conspicuous at locations 5, 3 and 1. It suggests that as sustained winds continue to act, a stage may be reached where the slope of the water surface approaches equilibrium as the propagation speed increases, for a given storm size and intensity. This implies that a threshold shelf width (L_{30}) may exist, above which, as sustained winds continue to act, a stage may be reached where the slope of the water surface approaches equilibrium as the propagation speed increases, for a given storm size and intensity.

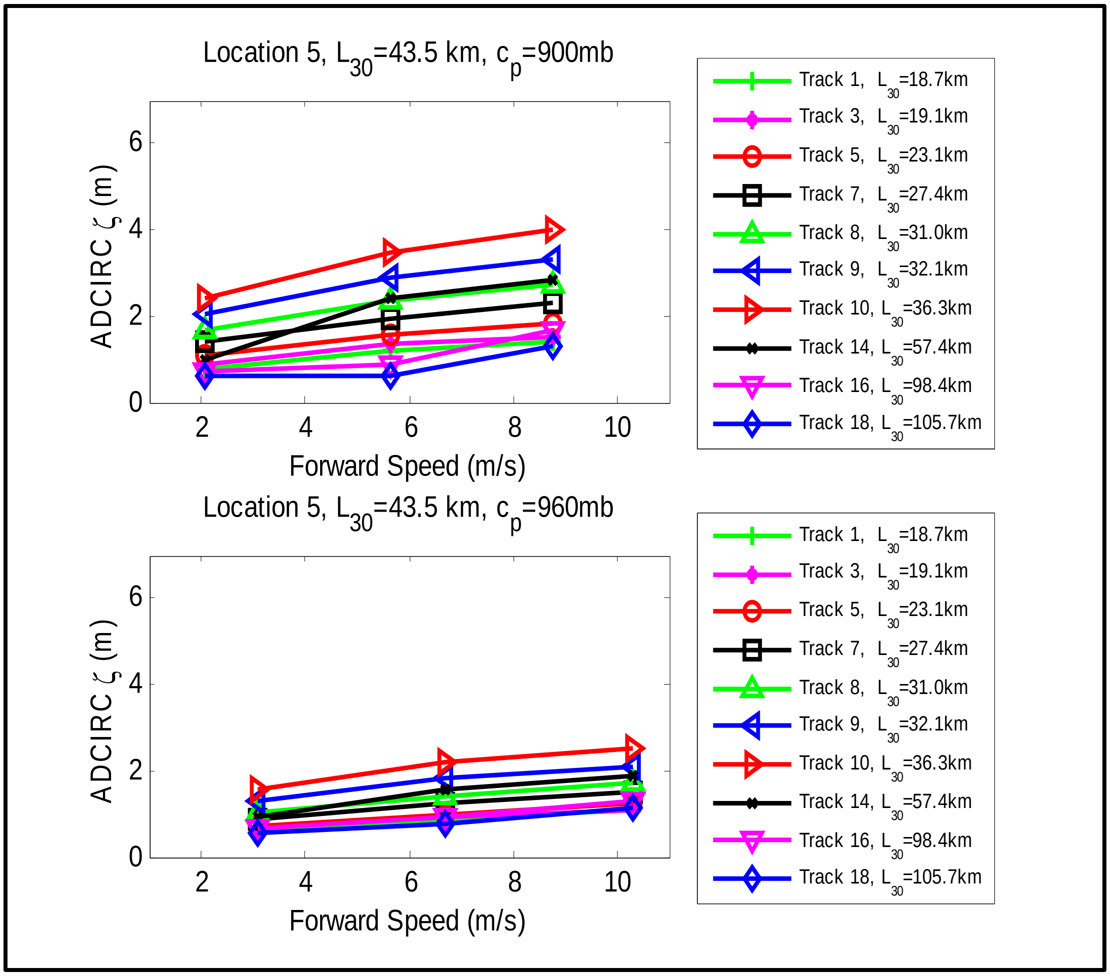

Figure 4.6: Forward speed versus surge, at intermediate-to-wide shelf width region. Top pane shows storms simulated with v_f = 2.1, 5.7 and 8.7 m/s with c_p = 900 mb. Bottom pane shows storms simulated with v_f = 3.1, 6.7 and 10.3 m/s with c_p = 960 mb. L_{30} at location 5 is 43.5 km.

The existence of a threshold shelf width would in turn suggest that storms traveling across relatively narrower continental shelves would have less time for surge generation (other parameters held the same).

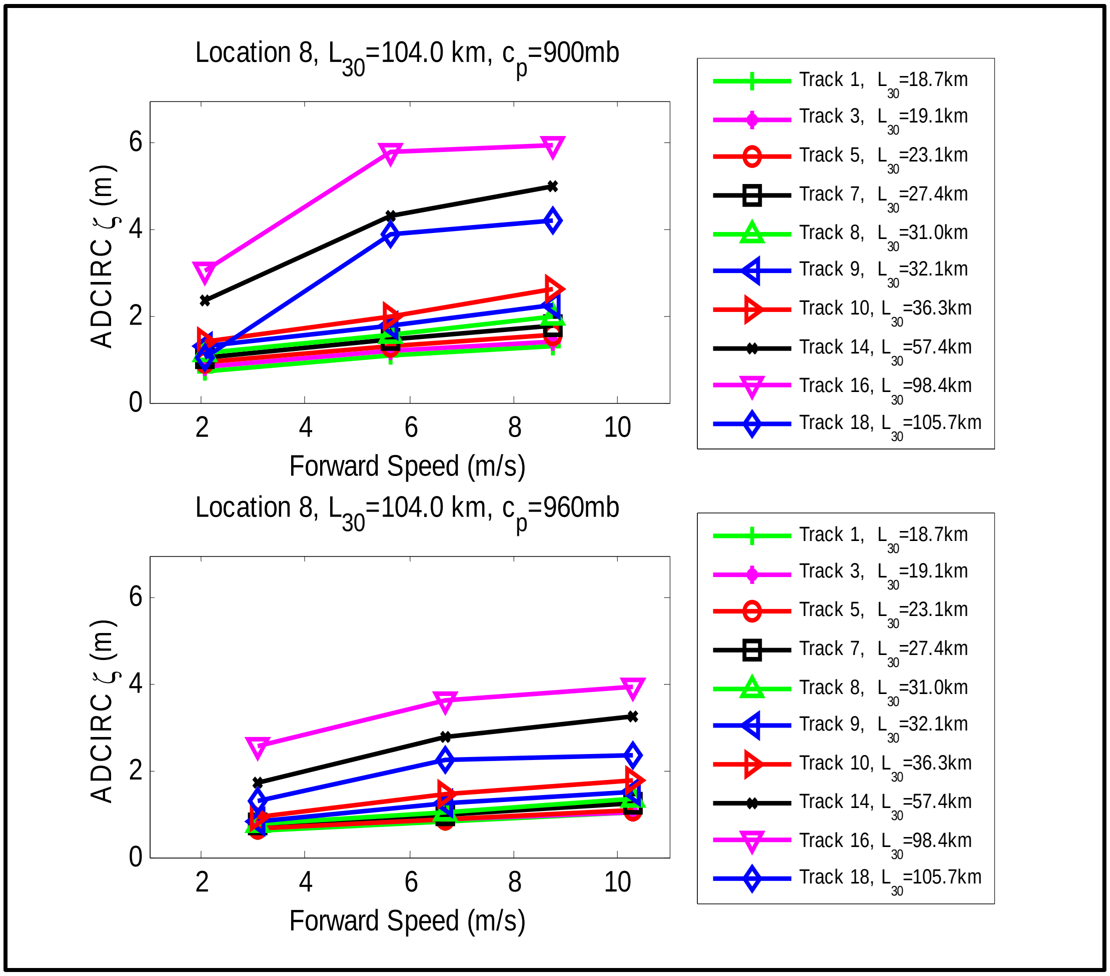

Figure 4.7: Forward speed versus surge, at wide shelf width region. Top pane shows storms simulated with v_f = 2.1, 5.7 and 8.7 m/s with c_p = 900 mb. Bottom pane shows storms simulated with v_f = 3.1, 6.7 and 10.3 m/s with c_p = 960 mb. L_{30} at location 8 is 104.00 km.

Based on the above-discussed surge trends for v_f, the major findings can be summarized as follows:

- For a given forward speed, the width of the continental shelf which the storm crosses as it approaches landfall significantly influences the actual time available for surge generation on the coast, hence influences surge magnitudes.
- At all locations discussed, there is a corresponding increase in surge on the coast with an increase in forward speed; however, this seems to be true only for storms making landfall to the left of the locations of interest. Although Rego and Li

(2009) stated that hurricane forward speeds have a positive effect on surge, the authors did not report on how the location of landfall may affect these positive trends.

- At sufficiently wide shelf regions, there is a tendency for storms to produce similar surges, as v_f increases – all other parameters remaining the same. This agrees with Jelesnianski's (1972) finding that "for a given storm size, there is a critical storm speed that generates an upper maximum surge". However, Jelesnianski (1972) implied that this finding may be an artifact of the dynamic model used in their work. To find the same behavior in this case where a different and widely accepted model is used, suggests that this phenomenon is practical, and not an artifact of a model.

The hypothesis here is that to adequately represent the influence of forward speed in the SRFs, the required dimensionless formulation needs to account for the dependence on shelf width, to capture the time taken for a storm of given forward speed to generate surge over the shelf. For such formulation, conditional weighting may be required to control the influence of L_{30} contribution to surge generation at different locations along the coast.

4.1.2 Surge Trends as a Function of Approach Angle, at the Coast

Variations in storm approach angles impact surge trends, mainly based on the characteristics of the shelf area which the storms cross, and the distance to the location of interest relative to the track and landfall location. For the open coast, surge trends as a function of the three approach angle groups are investigated (Figs. 4.9 through 4.12) at the same four locations (1, 3, 5 and 8) discussed in section 4.1.1 on forward speed trends. On these plots, 'LF-loc' abbreviates 'landfall location', and will be used in discussions here.

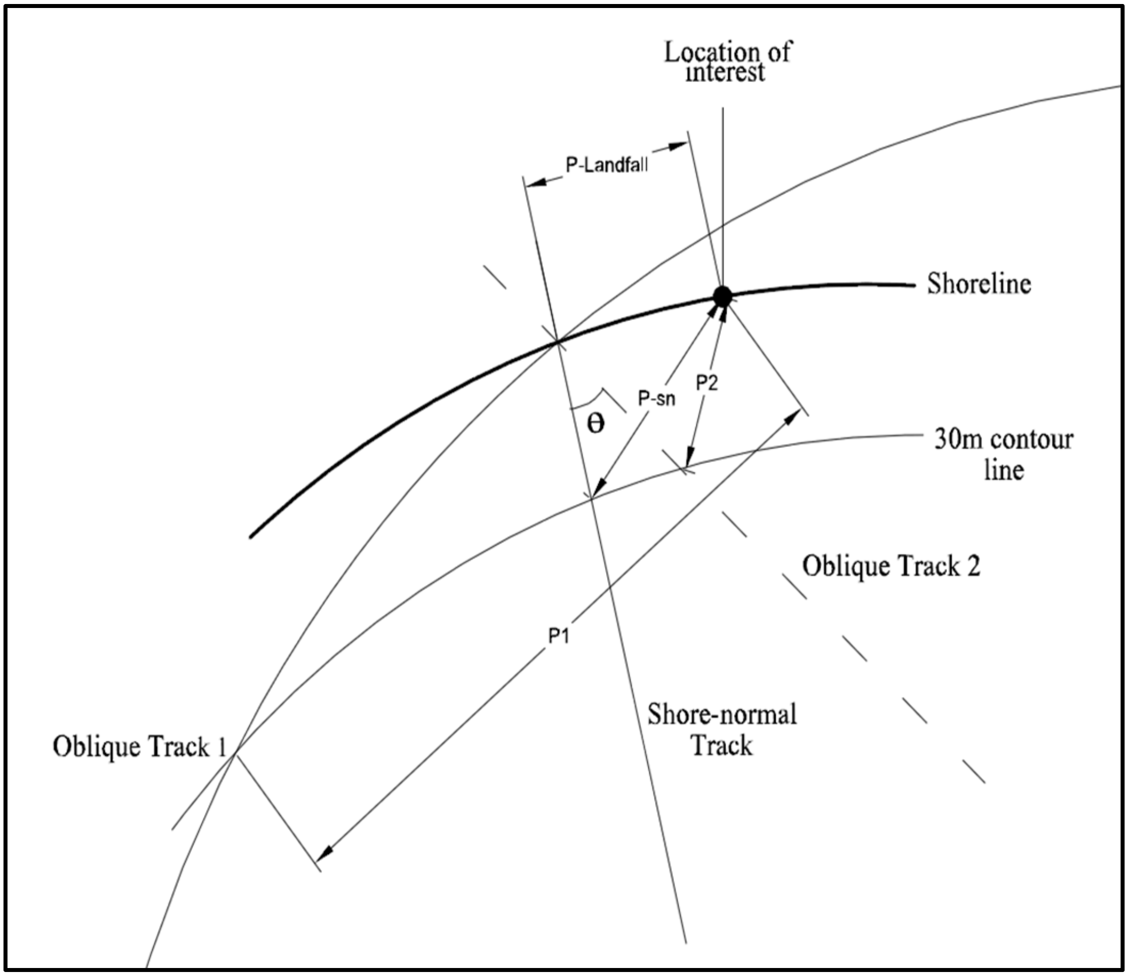

Figure 4.8: Descriptive sketch of proximities of track and landfall to location of interest.

At each landfall location, three tracks with different orientations intersect. There are eighteen landfall locations considered for the influence of approach angle, and these will be referred to as LF-loc 1, LF-loc 2 etc., with LF-loc 1 representing ‘landfall location 1’ and LF-loc 2 representing ‘landfall location 2’, and so on. Figure 4.8 illustrates the parameters ‘proximity of landfall to location of interest’ (P-Landfall) and ‘proximity of track to location of interest’ (P1, P2 and P-sn for oblique tracks 1 and 2, and shore-normal track). These two measures will also be used in discussions, and are illustrated here for clarity. For further clarity, high proximity implies nearness (of track or landfall) to the location of interest, and low or small proximity implies the distance between the two considered points is large.

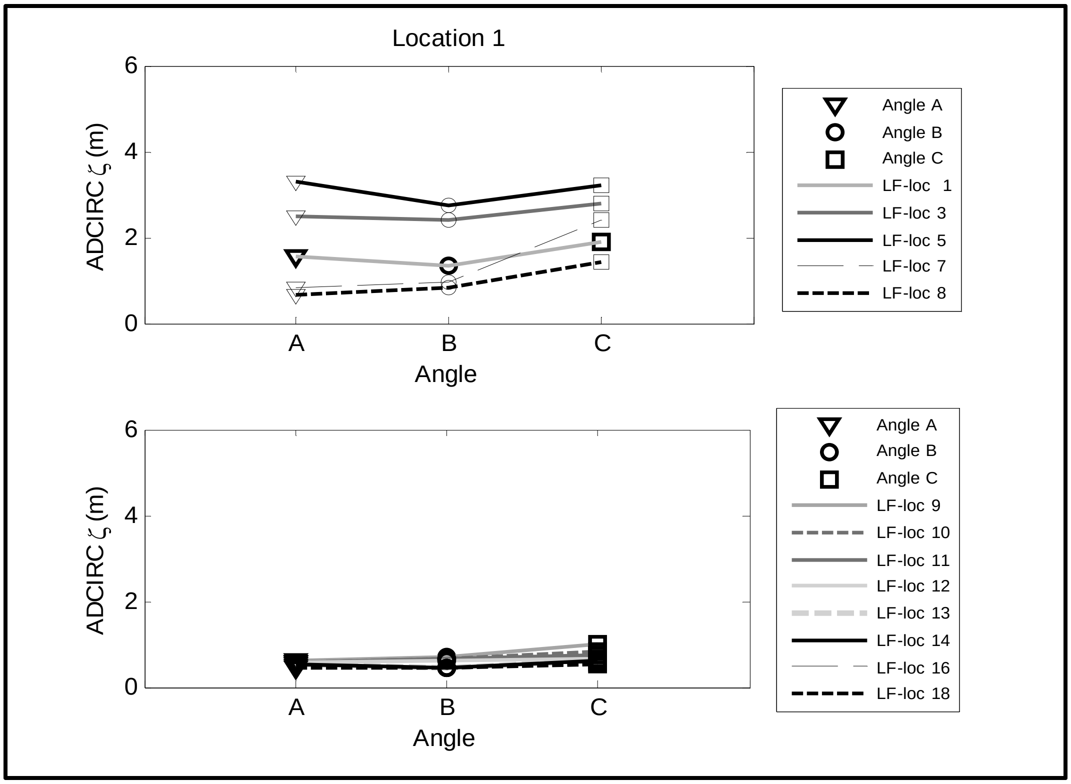

Figure 4.9: Approach angle versus surge, at narrow shelf width region. Top pane shows surge trends from tracks making landfall at LF-locs 1, 3, 5, 7 and 8. Bottom pane shows surge trends for storms making landfall at LF-locs 9, 10, 11, 12, 13, 14, 16 and 18.

Similar to the forward speed trends, tracks making landfall to the left of, and close to, each considered location produce the highest surges because their more intense winds (on their right side) produce higher wind stresses leading to higher surges. Three main effects seem to impact the surge magnitudes as a function of approach angle, measured at an open coast location:

- first, whether or not the orientation of the storm is such that the strongest portion of winds pushes surge toward the location;
- second, the stretch of shelf length actually traversed by the storm (-relatively long distances enhance surge generation, other factors remaining the same);
- and third, the proximity of the storm’s path to the location of interest as it approaches the shoreline. As shown in Fig. 4.8, this measure is different from the distance of landfall point to the location of interest – the latter is a

quantity measured alongshore (and is one of the major factors that influence surge heights on the coast), while the former is measured over the continental shelf.

These effects have varying dominating potentials against each other along the Texas coast, and this is evident in the surge trends.

In the narrow shelf area (location 1, Fig. 4.9), surges from tracks making landfall to the right of the location show no significant dependence on approach angle – this is because their landfall locations are sufficiently far from location 1, that surge generated at their regions of landfall barely translate to an increase in water level at location 30. Angle C storms produce highest surges on landfall locations 9 and 10, because their paths have the highest proximity to location 30, relative to angles A and B tracks.

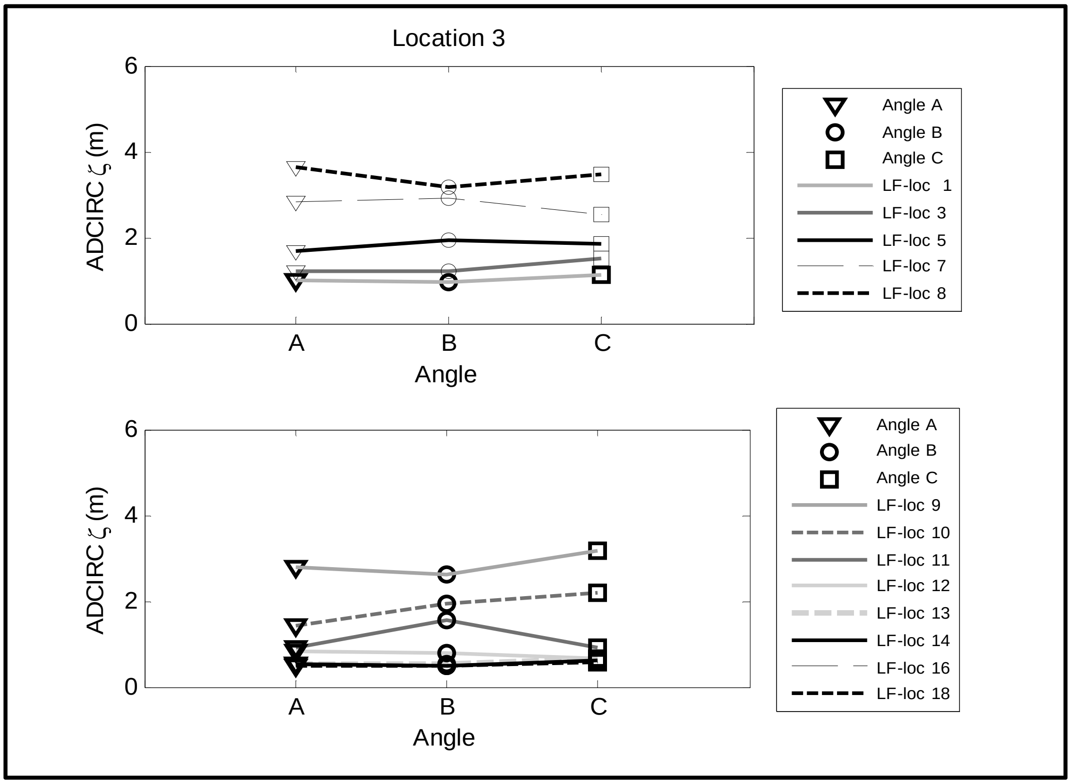

Figure 4.10: Approach angle versus surge, at narrow-to-intermediate shelf width region. Top pane shows surge trends from tracks making landfall at LF-locs 1, 3, 5, 7 and 8. Bottom pane shows surge trends for storms making landfall at LF-locs 9, 10, 11, 12, 13, 14, 16 and 18.

However, significant surge is generated at location 1 from storms tracking on the left of the location. Angle C storms mostly generate higher surges (LF-loc 1, 3, 8 and 7, Fig. 4.6) because they are oriented such that the strong winds push surge right up to the location. Additionally, the actual length traversed by angle C storms on the continental shelf is greater than those of angles B and C. However, at LF-loc 5 which is right at location 1, angle A produces a slightly higher surge value than angle C (and angle B) storms – here angle A is closer to shore-normal than angles B and C, and the effect of the onshore directed winds pushing surge onto the coast seems to dominate in this case because LF-loc 5 is very close to location 1.

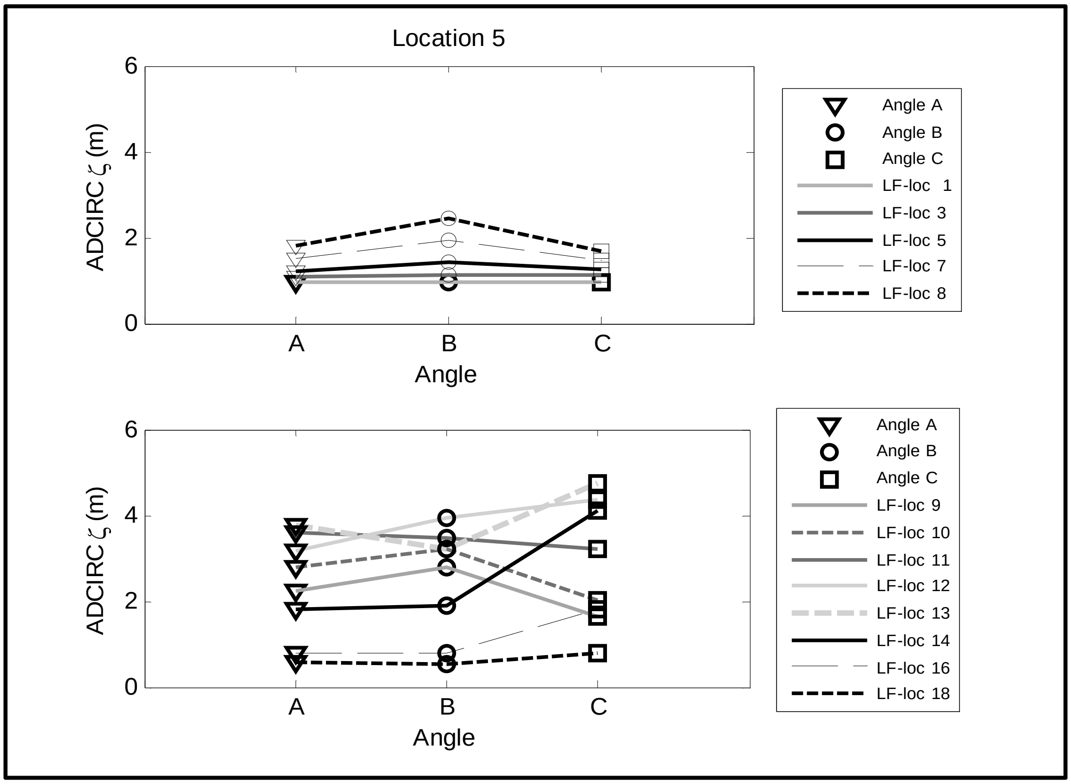

Figure 4.11: Approach angle versus surge, at intermediate-to-wide shelf width region. Top pane shows surge trends from tracks making landfall at LF-locs 1, 3, 5, 7 and 8. Bottom pane shows surge trends for storms making landfall at LF-locs 9, 10, 11, 12, 13, 14, 16 and 18.

At location 3 (narrow-to-intermediate shelf width region), the storms on LF-loc 12, 13, 14, 16 and 18 (Fig. 4.10) have very small differences in surge as a function of approach angle, and this is because they are sufficiently distant from the location under consideration. On LF-locs 1 and 3, angle C produces higher surges than angles A and B, because its orientation favors the translation of surge toward the location relative to the other two angles; in other words as they approach landfall, angle C storm paths are more directed toward location 3 than angles A and B paths. At LF-locs 9 (closest to location 3) and 10, angle C dominates B and C because it has the closest orientation to shore-normal, implying that the effects of onshore-directed winds pushing surge toward the location dominate. The effect of the stretch of shelf width crossed by a storm while generating surge is seen at LF-loc 11; here Angle B which has a storm path that traverses a longer stretch of the continental shelf width produces the highest surge relative to the other two orientation groups. This is not surprising, as longer fetch lengths allow more surge generation leading to higher surge values.

Considering location 5 (Fig. 4.11), LF-locs 1 and 3 are sufficiently distant that the variations in approach angle produce no significant changes in surge. On LF-locs 5, 7, 8, 9 and 10, the points of landfall are also distant from location 5, but angle B tracks have the highest proximity to the location, hence higher surge values from this orientation relative to angles A and C. Proximity to location 5, combined with longer distance traveled across the continental shelf, allows angle C storms to generate higher surges on LF-locs 14, 16 and 18 relative to the two other angle groups, and this dominance over angles A and B diminishes as the tracks are located farther away to the right (smallest dominance on LF-loc 18), indicating that the proximity of the tracks to the location has the relatively stronger influence in this case. On LF-locs 12 and 13, angle C generates higher surge than angle B, primarily due to the fact that its orientation or path is directed toward location 5, allowing more surge to build towards the location. Between angles A and B storms, on LF-loc 12 angle B has a closer proximity to the location, and crosses a longer stretch of the shelf, whereas on LF-loc 13 angle B is oriented such that the impact of the storm’s intense portion in driving surge up to the location is less than that of angle A.

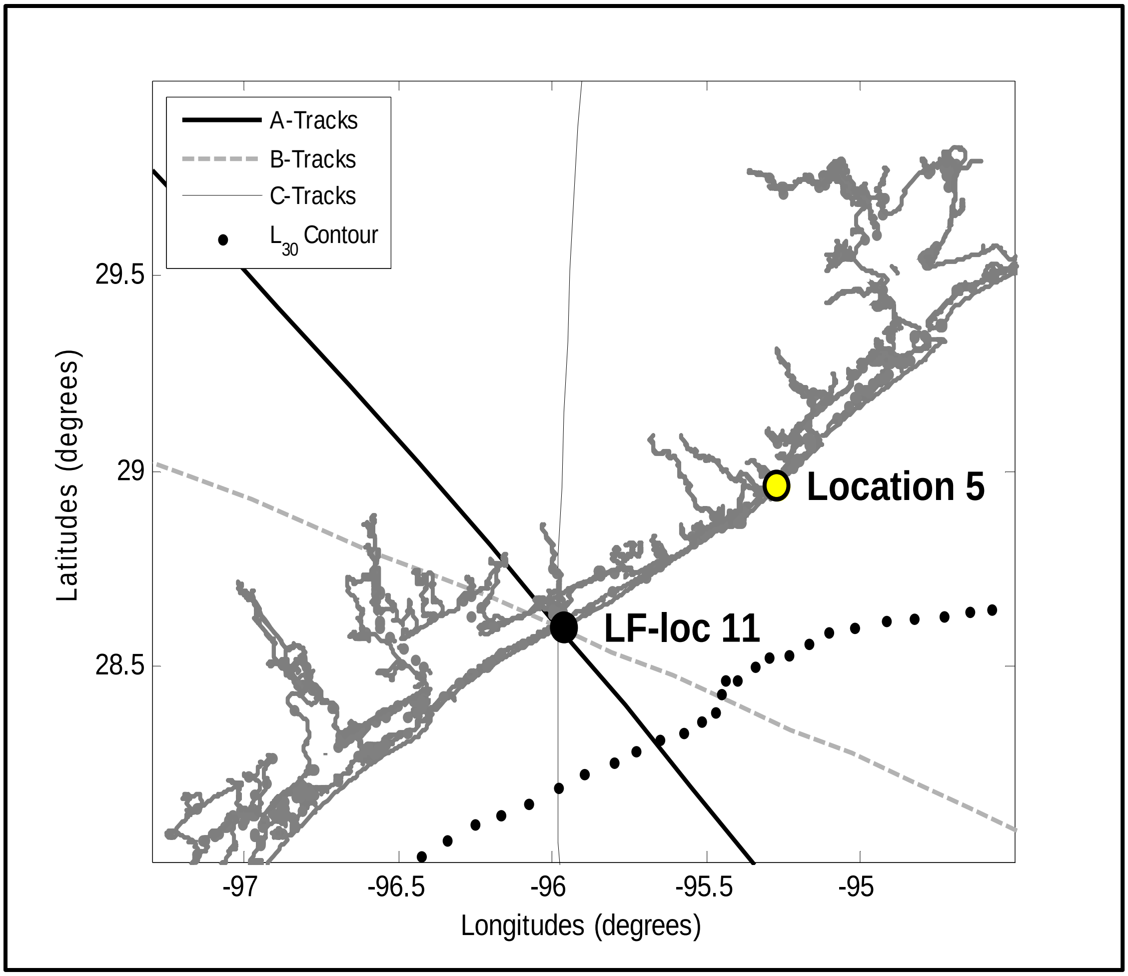

Figure 4.12: Tracks at LF-loc 11 (intermediate-to-wide shelf width region).

The surge trend for LF-loc 11 is somewhat unexpected, given that the proximity of angle B track to the location is higher than that of angle A, and that angle B dominates on LF-loc 10 where the relative characteristics of the three angles are similar to those at LF-loc 11. LF-loc 11 is located in the intermediate-to-wide shelf region (Fig. 4.3 and Fig. 4.12) between Matagorda and Galveston. The dominance of surge from angle A over angles B and C may be due an additional effect, such as alongshore winds with dominant direction coinciding with that of angle A storm. This would produce a cumulative effect on the surge magnitude generated, and would be consistent with the hypothesis of Song et al. (2012) on the anomaly of surge behavior within this region of the Texas coast, where the track orientations considered by the authors are the same as angle A tracks.

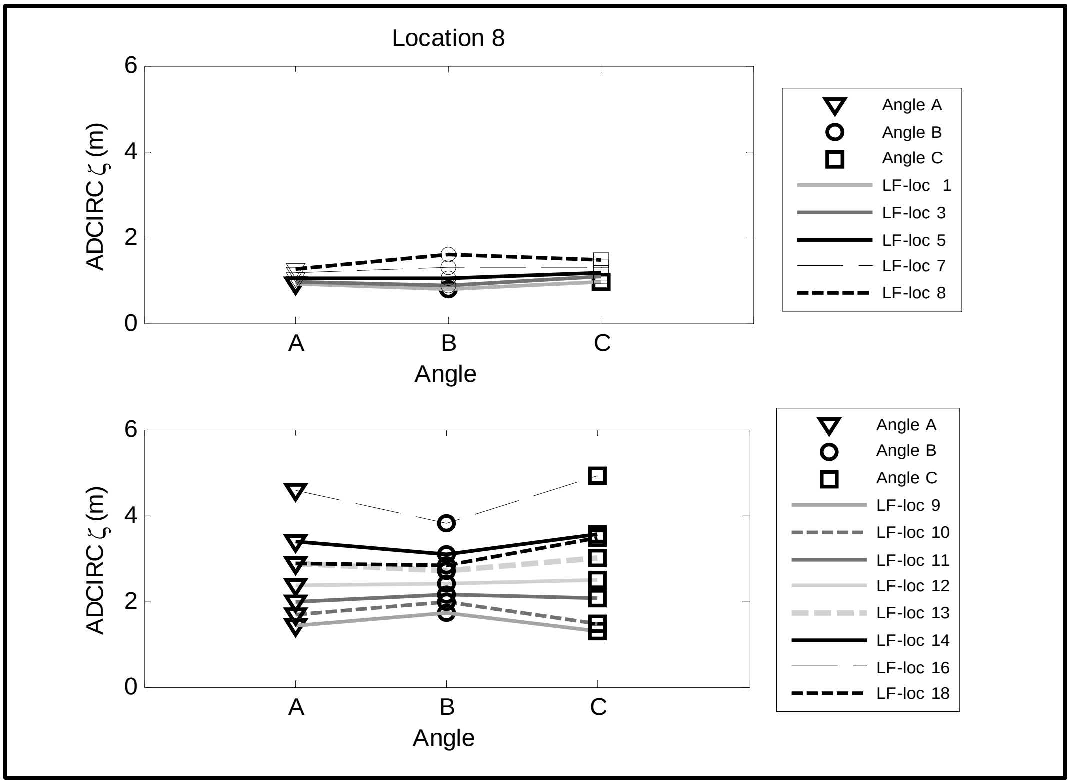

Figure 4.13: Approach angle versus surge, at wide shelf width region. Top pane shows surge trends from tracks making landfall at LF-locs 1, 3, 5, 7 and 8. Bottom pane shows surge trends for storms making landfall at LF-locs 9, 10, 11, 12, 13, 14, 16 and 18.

At location 8 (Fig. 4.13), LF-locs 1, 3, and 5 have minor differences in surge as a function of approach angle, and angle C slightly dominates angles A and B in surge values, mainly due to its orientation being able to drive more surge on the coast toward the north. The effect of proximity of track to location gradually takes over on LF-locs 7, 8, 9, 10, 11 and 12, where angle B slightly dominates A and C. On LF-locs 13, 14, 16 and 18 the combined effects of onshore-directed winds (especially when orientation is close to shore-normal) and length traversed by the storm across the shelf makes angle C storms produce higher surges (though only slightly less than angle A surges).

On studying the surge trends for the effect of approach angle, some findings have been made which have not been explicitly discussed in literature, along with others which have been previously reported. The influence of onshore-directed winds on surge being greater for storms approaching the coast at angles close to shore-normal was reported by

Irish and Resio (2010) – here, this phenomenon is seen to hold true for the range of track orientations investigated in this research. On the other hand, the role of varying fetch lengths (i.e. actual length traversed by a storm over the shelf as it approaches landfall) associated with different angles of approach on a coast with varying shoreline orientation has not been explicitly discussed. Through the examination of the θ trends, it has also been deduced that closeness of a storm's track (as it crosses the continental shelf) to a location of interest, is an important factor that may have been overlooked in surge analysis – this quantity may be used (if needed) in analysis as the minimum distance to the location of interest, as the storm crosses the continental shelf. More importantly, this research finds that for a region with varying shoreline orientations (such as the Texas coast), these different effects discussed have varying dominance potentials over each other on surge generation.

The primary findings from the surge trends as a function of approach angle indicate that the formulation to account for the effect of this parameter should at a minimum include a measure of the length over which the storm traverses across the continental shelf, and the storm angle relative to the shore-normal direction. The proximity of the storm to the location of interest is already accounted for in the existing form of the surge response functions (Equation 2.9).

4.1.3 Surge Trends as a Function of Sea Level Rise, at the Coast

Surge trends for SLR are presented in Figures 4.14 through 4.17 for the four open coast locations under discussion. The top pane of each of these figures shows actual surge $(\eta_s - SLR)$, plotted against the water level without sea level rise, ζ_0. Here the quantity η_s is the total level after the storm (with SRL included). The bottom pane shows the plots of actual surge ($\eta_s - SLR$) against SLR. At locations 1, 3 and 5, for all tracks along the Texas coast, a linear trend is found in the plots of actual surge versus no-SLR water levels, as the plotted points fall on an exact-match line (top panes of Figs. 4.14 through 4.16). The maximum difference in surge between storms on each track is approximately

0.2 m. This implied direct relationship observed between the two quantities suggests that the influence of SLR on surge generation on the coast is very small. At location 8, however, as the track locations move northward (tracks, 11, 13, 14, 16 and 17), surge magnitudes gradually deviate from the exact-match line, delineating the effect of SLR on surge. As SLR increases, the increase in water depth at alongshore locations causes a reduction in the extent to which the wind stress-induced currents interact with bottom friction; this inhibits surge generation at the coast. At location 8 (Fig. 4.17, top pane), the slight deviation of surge from the exact-match line suggests that if surge generation is limited over a longer distance, then surge magnitudes reduce correspondingly. Equation (4.2) expresses this mathematically, and suggests that with SLR considered, the difference in surges at two locations with varying shelf widths is a function of the wind speed, the water depth and the difference in L_{30} between the two locations.

$$\Delta\zeta(L_{30}) = f\left(U, h, L_{30}(x_1), L_{30}(x_2)\right) \tag{4.2}$$

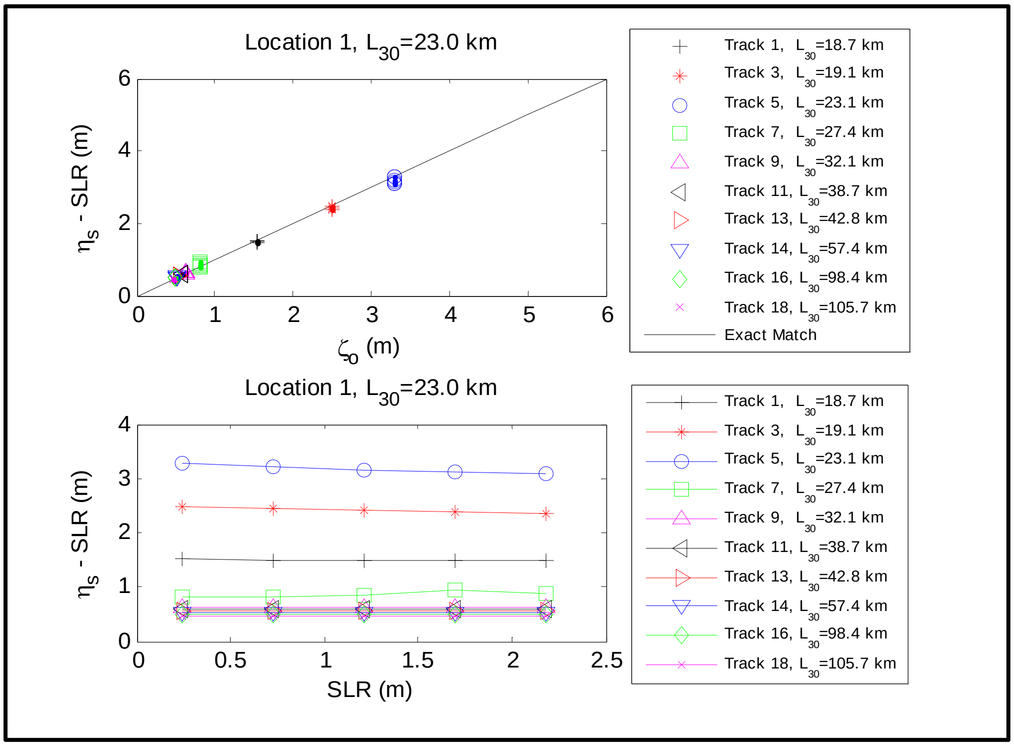

Figure 4.14: Sea level rise trends at narrow shelf width region. Top pane shows water level less SLR versus base (i.e. no SLR) surge. Bottom pane shows water level less SLR, versus SLR.

Surge trends as a function of SLR (bottom panes of Figs. 4.14 through 4.17) at locations 1, 3, 5 and 8 show that with an increase in SLR, surge magnitudes reduce for storms making landfall to the left of the location of interest. This is based on the just-described effect of increased water depth and reduced influence of wind stresses. For storms making landfall to the right of the location of interest, surge magnitudes either slightly increase or remain unchanged at open coast locations. This implies that the relatively weaker winds on the left side of the storm either have a positive or negligible influence on surge generation.

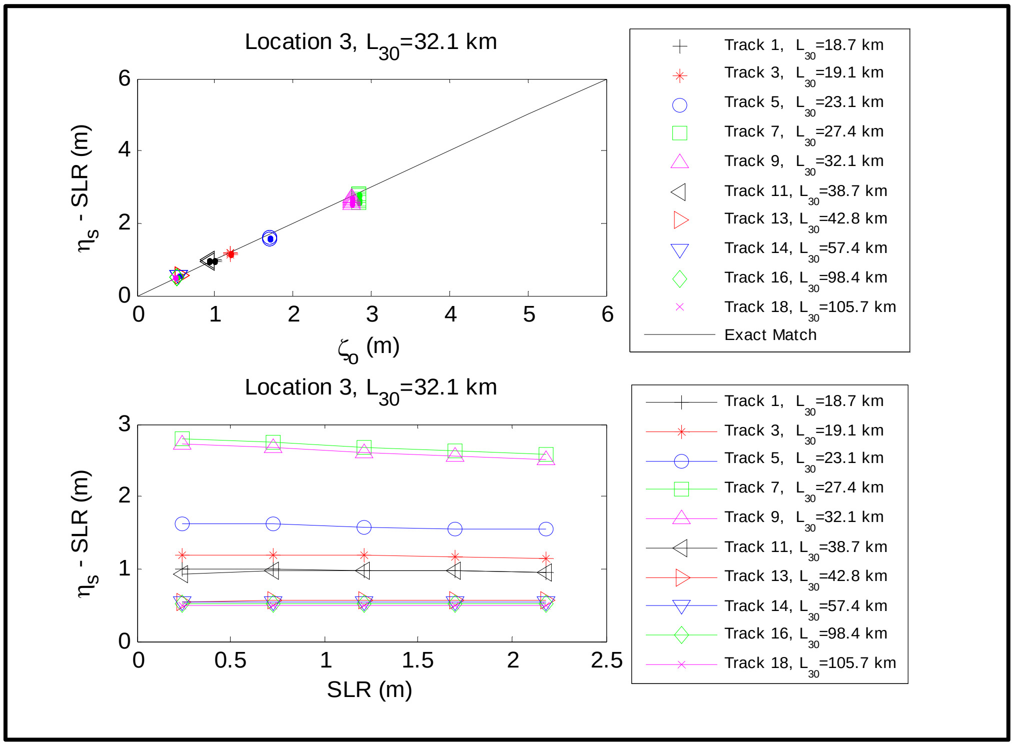

Figure 4.15: Sea level rise trends at narrow-to-intermediate shelf width region. Top pane shows water level less SLR versus base (i.e. no SLR) surge. Bottom pane shows water level less SLR, versus SLR.

The slopes of these trends vary, with the highest (i.e. in absolute value) slopes produced by tracks generating the highest surges, and the smallest slopes by those producing the smallest surges. It follows therefore, that the variation of surge with SLR at a location of interest increases with proximity to landfall location, for storms making landfall to the left of the location. Based on a linear fit, the ranges of slopes are – 0.09 to 0.05 at location 1, – 0.12 to 0.01 at location 3, – 0.09 to 0.00 at location 5 and – 0.29 to – 0.01 at location 8.

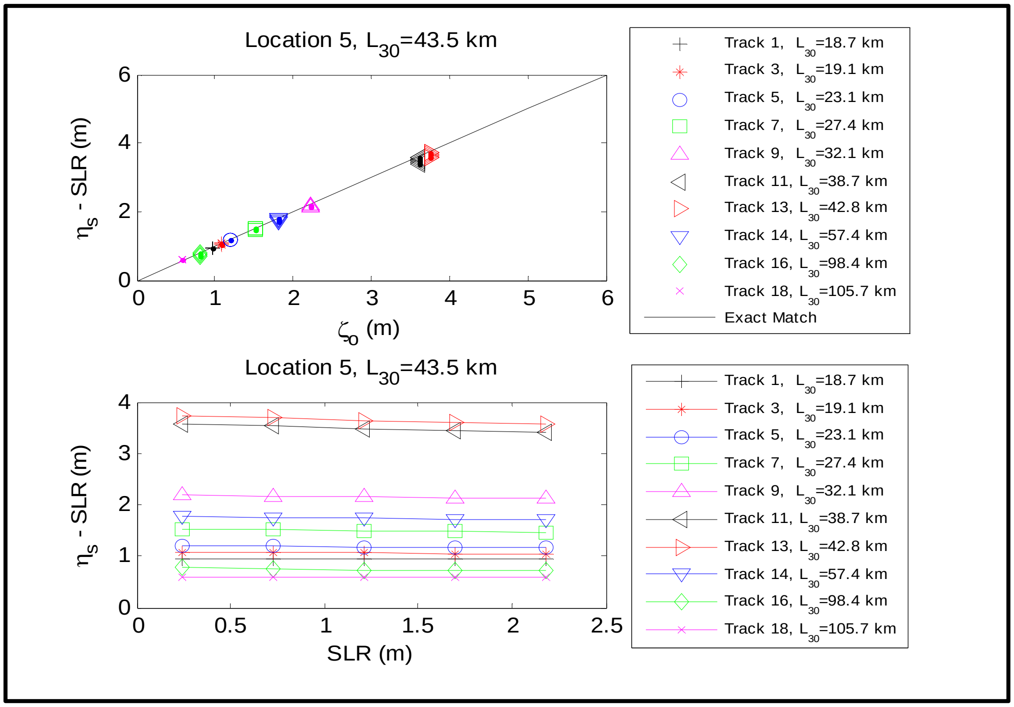

Figure 4.16: Sea level rise trends at intermediate-to-wide shelf width region. Top pane shows water level less SLR versus base (i.e. no SLR) surge. Bottom pane shows water level less SLR, versus SLR.

Observations discussed here for the effects of SLR on surge at open coast locations have not been reported with this level of detail in the literature. The primary findings here are that:

- surge will decrease with increase in SLR for storms making landfall to the left of the location of interest, but will either slightly increase or remain unchanged for storms making landfall to the right of the considered location. This is due to the differing effects of sustained winds on the left and right side of the storm on surge generation as SLR increases.
- as the continental shelf width increases, the behavior of surge trends (with the effect of SLR) gradually transition from being close to an exact match between

$\eta_s - SLR$ and ζ_O, to a slight reduction in $\eta_s - SLR$, as ζ_O increases. This is associated with a reduction of the water surface slope.

- the variation of surge as function of SLR increases with proximity to landfall location for storms making landfall to the left of the location of interest.

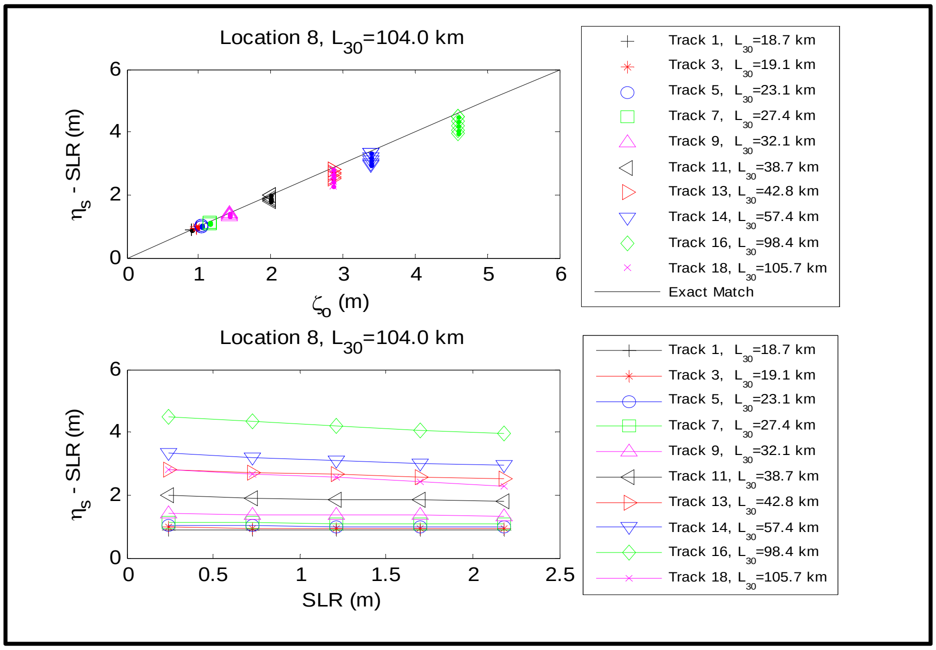

Figure 4.17: Sea Level Rise trends at wide shelf width region. Top pane shows water level less SLR versus base (i.e. no SLR) surge. Bottom pane shows water level less SLR, versus SLR.

The surge trends as function of SLR suggest that it is unnecessary to explicitly incorporate the simulations for the SLR effect in the response function analyses. With trends ranging from linear to weakly non-linear, the hypothesis here is that it is possible to account for the contribution of SLR through a simplified correction in dimensional space. At every location of interest, the best simple model (e.g. first order polynomial) could be used to incorporate the effect of SLR in the dimensional SRF surge.

4.2 Surge Trends in Coastal Bays

For coastal bays, the behavior of surge as a function of forward speed, approach angle and sea level rise is somewhat different from those at open coast locations. The physical features (such as barrier islands and irregular shorelines within the bay) interfere with the movement of water mass, changing its course. Additionally, because bays are semi-confined basins, redistribution of surge makes surge trends more irregular compared to the open coast. Investigating these trends aids the understanding of the most useful parameters to apply in representing the influences of v_f, θ and SLR.

4.2.1 Surge Trends as a Function of Forward Speed in the Bays

For discussions here, tracks will be referred to as 'track 1', 'track 2' etc., with track 1 being the first track at the lower left corner (Fig. 4.18 for Corpus Christi Bay tracks, and Fig. 4.19 for Matagorda Bay tracks), and track 2 is the next track to the right of track 1, and so on. For easy access, SRF stations for Corpus Christi and Matagorda Bays are re-shown in Figs. 4.20 and 4.21.

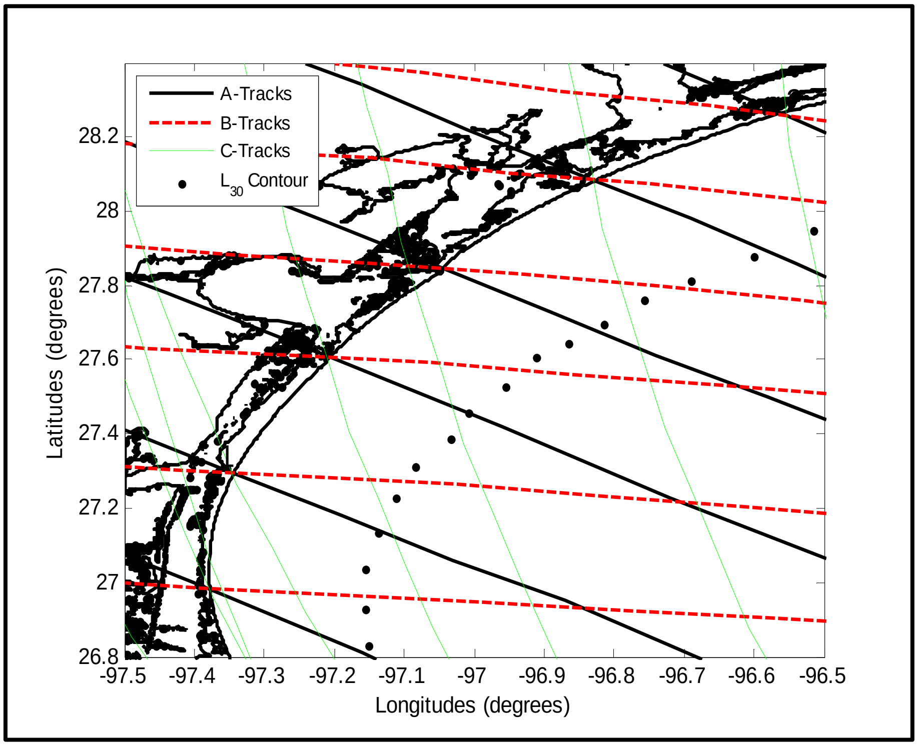

Figure 4.18: Tracks for Corpus Christi Bay SRF analysis. For each orientation group, track 1 is the track making landfall at the lower left corner of the region; track 2 is next to track 1, track 3 is after track 2, etc.

Using the group of tracks defined (Figs. 4.18) for SRF development in Corpus Christi Bay, surge trends as a function of forward speed are developed and shown in Figures 4.22, 4.23, and 4.25 through 4.28. A total of six tracks are used to assess the variation of surge as a function of v_f, with the six scenarios discussed in Chapter III (Table 3.3). Assessing the trends for the first track (Fig. 4.22), which is to the left of the bay, the intense (900mb, top pane) group of storms show an increase in surge as forward speed increases. Surge heights of the 5.7 m/s and 8.7 m/s storms are much greater than those of the 2.1 m/s storm everywhere along the bay. However, for the weaker (960 mb, bottom pane) group of storms the variation in forward speed produces no significant differences in surge heights behind the barrier island and inside the bay. For both groups of storms (900 mb and 960 mb), surge heights increase with forward speed at the open coast stations (as seen in Figs. 4.4 through 4.7 of the open coast surge trends discussions).

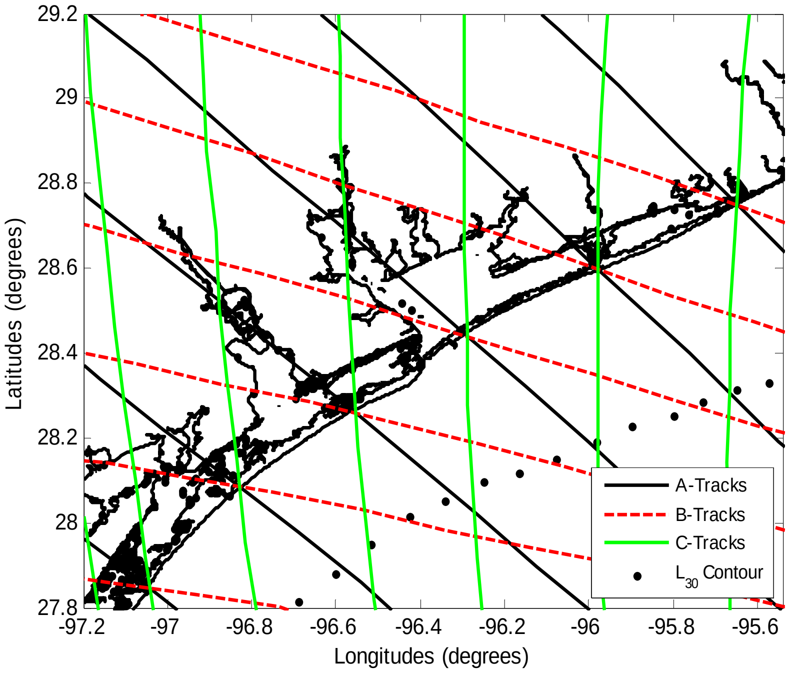

Figure 4.19: Tracks for Matagorda Bay SRF analysis. For each orientation group, track 1 is the track making landfall at the lower left corner of the region; track 2 is next to track 1, track 3 is after track 2, etc.

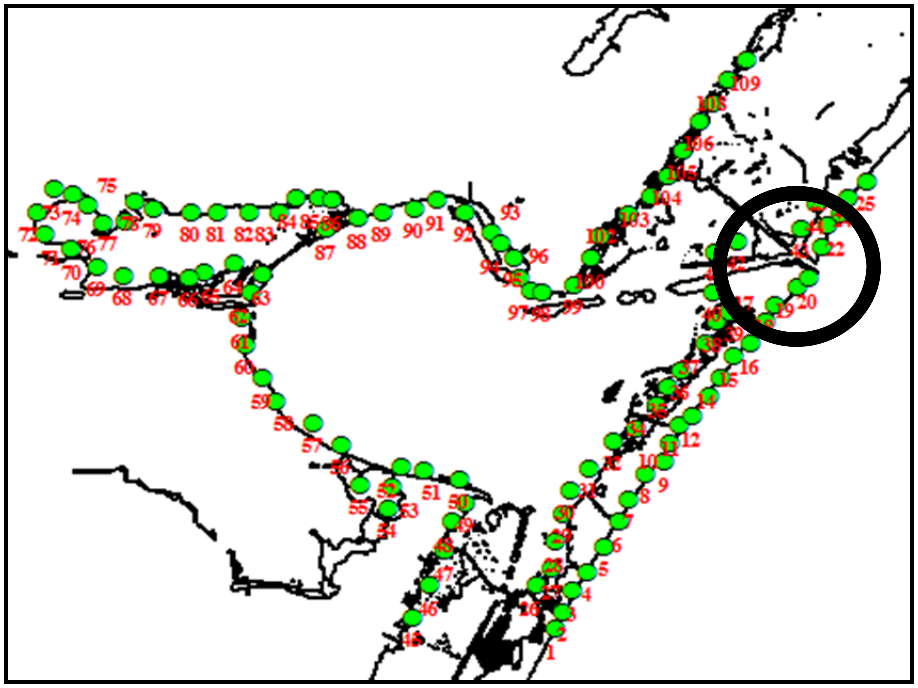

Figure 4.20: SRF stations for Corpus Christi Bay. Circled area is channel entrance into the bay, around Port Aransas, TX – highlighted here for discussions in this section. Small dots are stations used in SRF analysis – a total of 109 points.

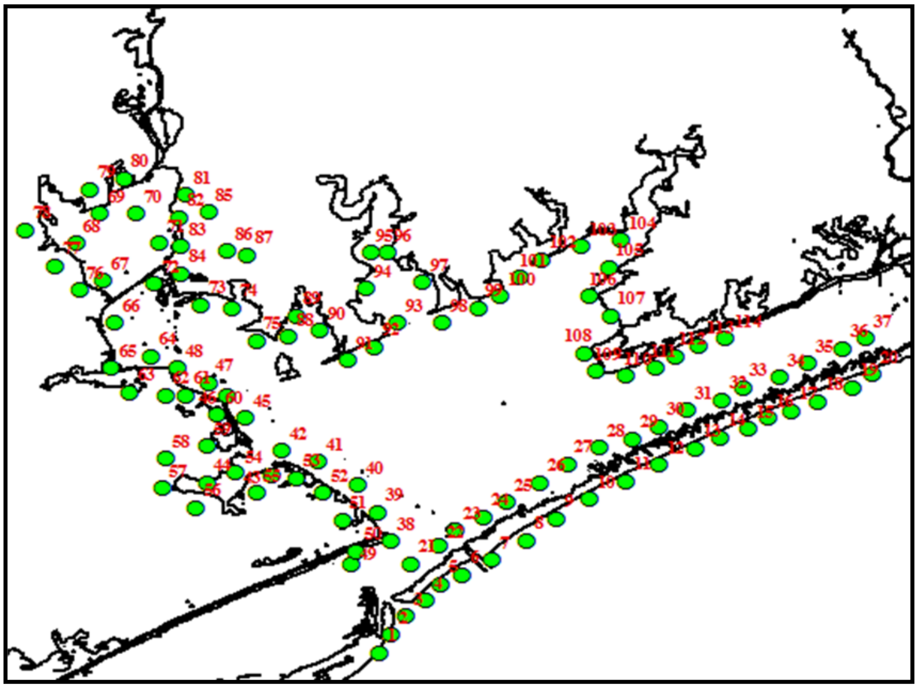

Figure 4.21: SRF stations for Matagorda Bay. Small dots are stations used in SRF analysis. A total of 114 stations are used.

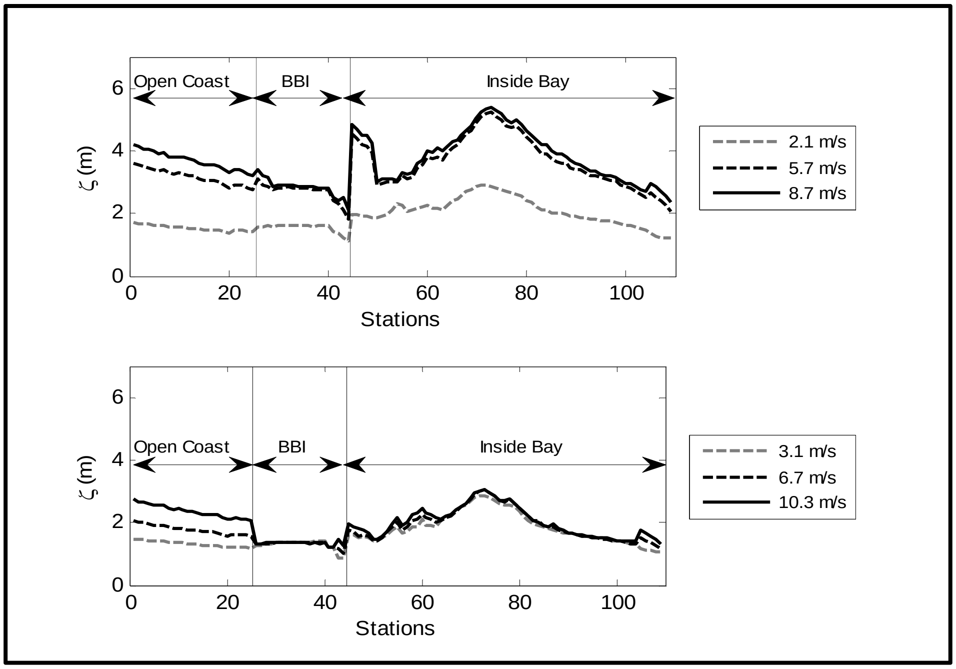

Figure 4.22: Surge trends for v_f scenarios, on track 1 for Corpus Christi Bay. Top pane shows storms simulated at c_p = 900 mb, while bottom pane shows storms simulated at c_p = 960 mb.

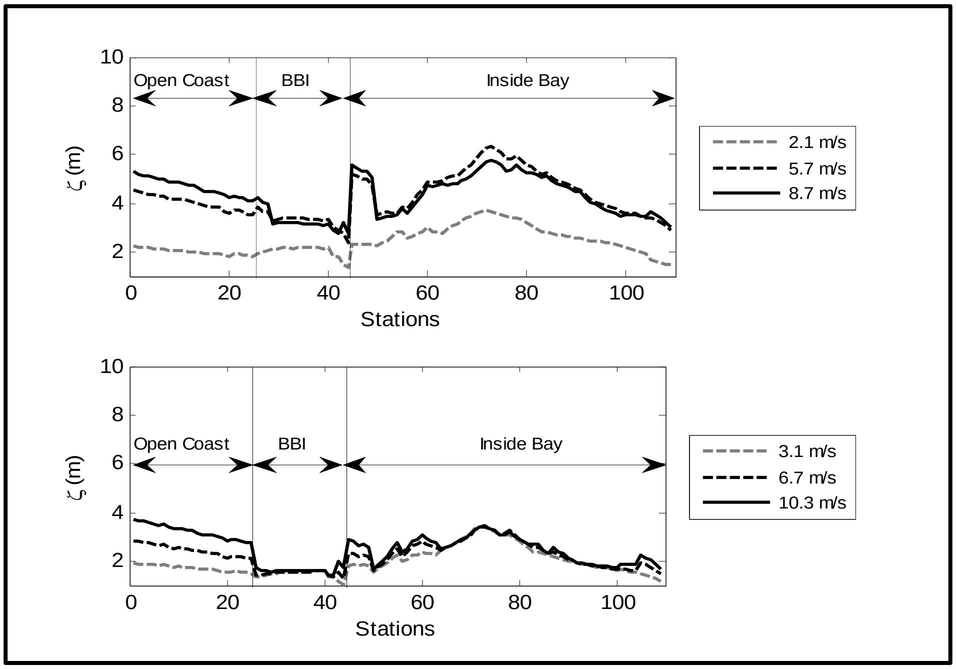

Figure 4.23: Surge trends for v_f scenarios, on track 2 for Corpus Christi Bay. Top pane shows storms simulated at c_p = 900 mb, while bottom pane shows storms simulated at c_p = 960 mb.

The location of the track 2 for Corpus Christi bay is such that a good portion of the winds from this storm blow over the bay. As such, surge heights from this track (Fig. 4.18) are higher than those from track 1. In both tracks 1 and 2, it is observed that the highest surge values within the bay are recorded in the interior/northern edge of the bay. This is reasonable, not only because this section of the bay is relatively flat, but also because surge builds up in the bay as the water mass penetrates farther in due to the fact the bay is a semi-closed system. The abrupt jump in the surge trends between stations 42 to 44 is due to surge entering the bay through the channels surrounding Port Aransas (circled region in Fig. 4.20), in addition to surge entering the bay through the eastern edge, western edge and over the barrier island.

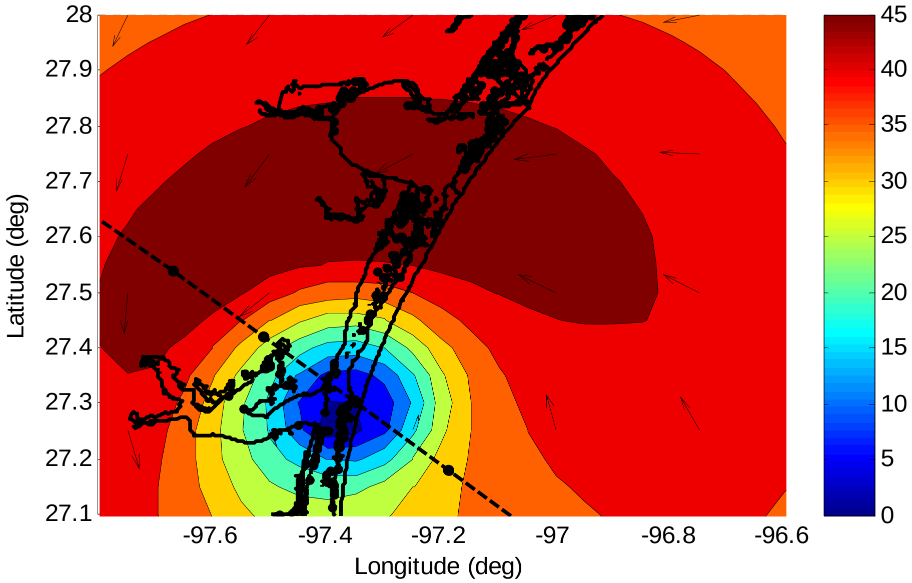

Figure 4.24: Illustration of intense winds on bay.

It is also interesting to note that for track 2, at the northern-edge locations of the bay (Nueces Bay, stations 65 to 80, Fig. 4.20) surge generated by the 5.7 m/s storm is higher than that generated by the 8.7 m/s storm. This behavior is also observed in Matagorda

Bay (Figs. 4.29, 4.30 and 4.31). It suggests that if a storm is sufficiently intense, and traveling on a path with size such that its winds impact the bay significantly (illustrated in Fig. 4.24), a stage is reached when the interior portions of the bay no longer experience an increase in surge heights, as forward speed increases. This is similar to Jelesnianski's (1972) findings for surge over representative shelves, relating to the existence of 'critical speeds' beyond which surge does not increase. Additionally, this finding also agrees with Weisberg and Zheng (2006), who reported that storms with slower speeds produce higher surges in Tampa Bay, FL, than fast storms, especially at interior locations of the bay.

Track 3 for Corpus Christi Bay is located such that not much of the storms' intense winds act over the bay. As a result, surge heights from this track are generally lower (especially at stations at the northern edge of the bay) than those from tracks 1 and 2. The disparity between the trends for the intense storms and those of the relatively weaker storms are similar to those of tracks 1 and 2. Similar surge trends are observed for tracks 4, 5 and 6 (Figs. 4.26 through 4.28) of Corpus Christ Bay, except that the surge magnitudes progressively decrease as the tracks move further away from the bay to the right – such that the weak part of the storms impact the bay, hence producing relatively smaller surge magnitudes.

In general the surge trends relative to v_f for Matagorda Bay (Figs. 4.29 through 4.34) are similar to those of Corpus Christi Bay. Since the distribution of mass throughout the bay is dependent on the storm speed, we hypothesize that a dimensionless time scale comprised of the time it takes for surge to build up and be re-distributed in the bay, and a representative characteristic time associated with the bay geometry (or an effective length parameter), will be important in accounting for the contribution of forward speed in the surge response functions.

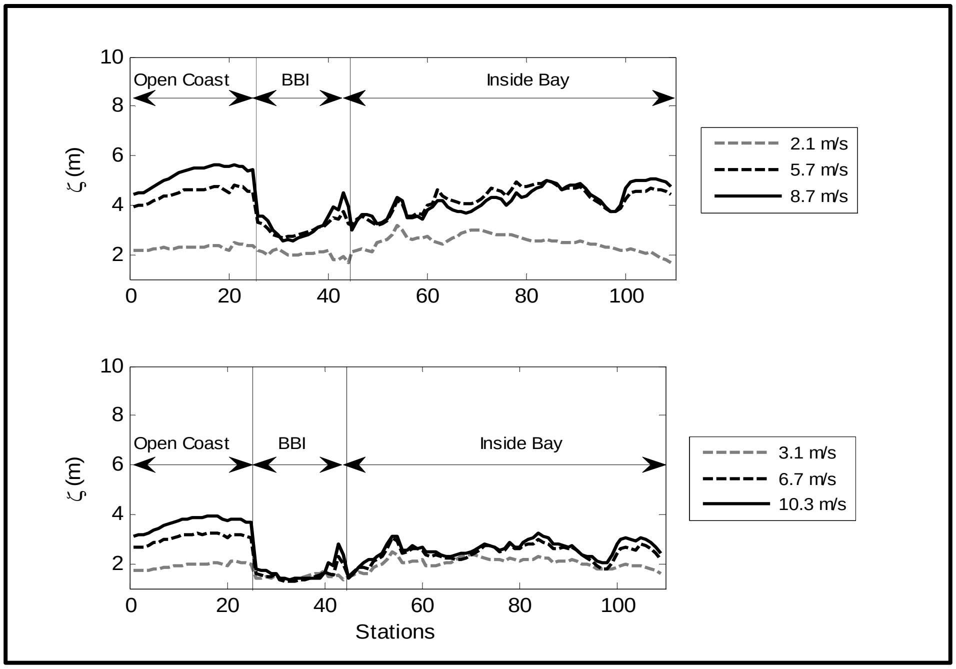

Figure 4.25: Surge trends for v_f scenarios, on track 3 for Corpus Christi Bay. Top pane shows storms simulated at c_p = 900 mb, while bottom pane shows storms simulated at c_p = 960 mb.

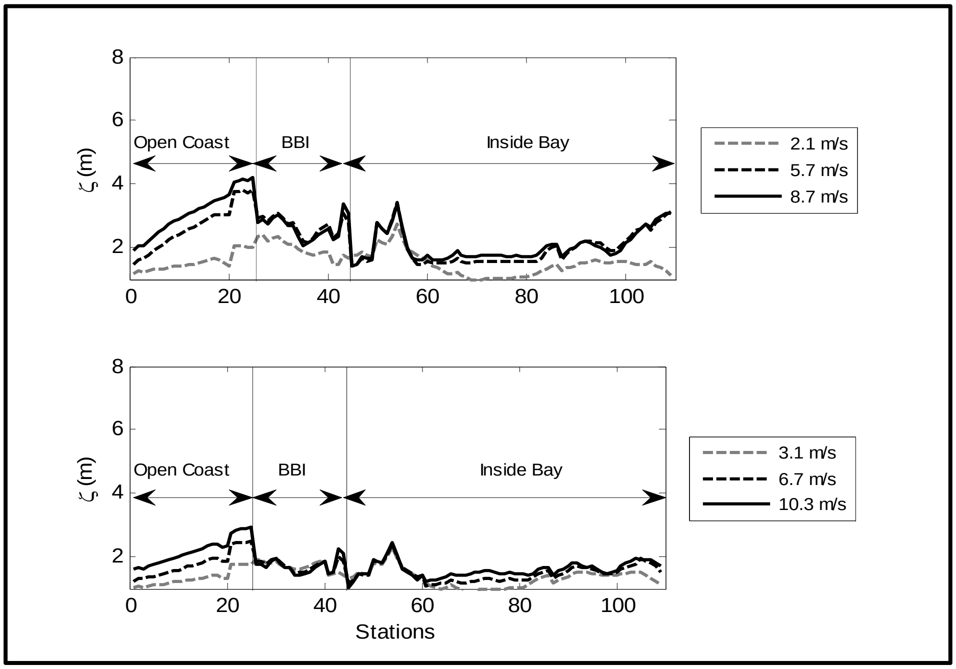

Figure 4.26: Surge trends for v_f scenarios, on track 4 for Corpus Christi Bay. Top pane shows storms simulated at c_p = 900 mb, while bottom pane shows storms simulated at c_p = 960 mb.

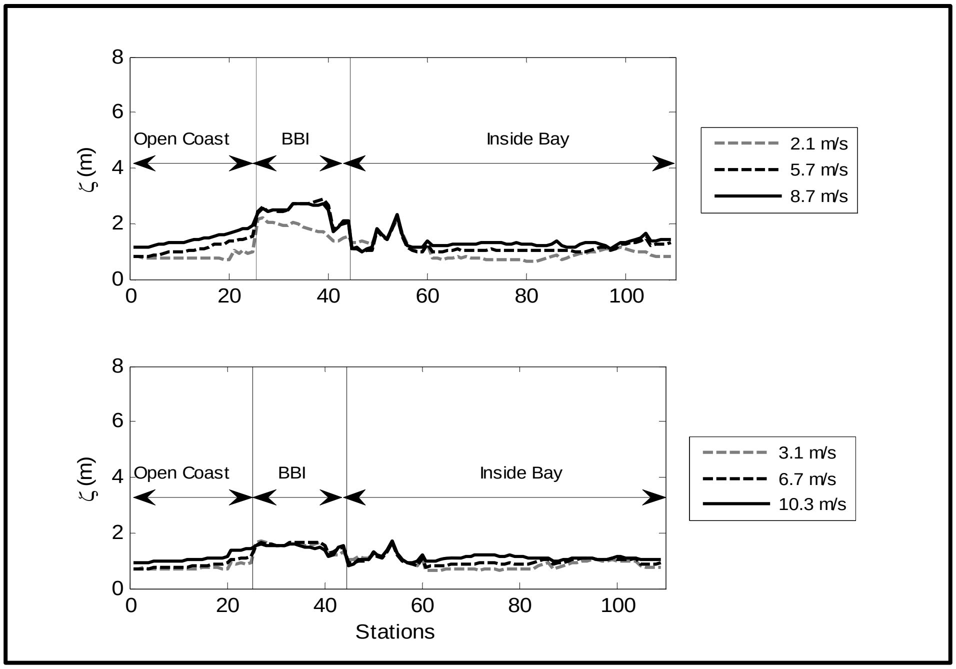

Figure 4.27: Surge trends for v_f scenarios, on track 5 for Corpus Christi Bay. Top pane shows storms simulated at c_p = 900 mb, while bottom pane shows storms simulated at c_p = 960 mb.

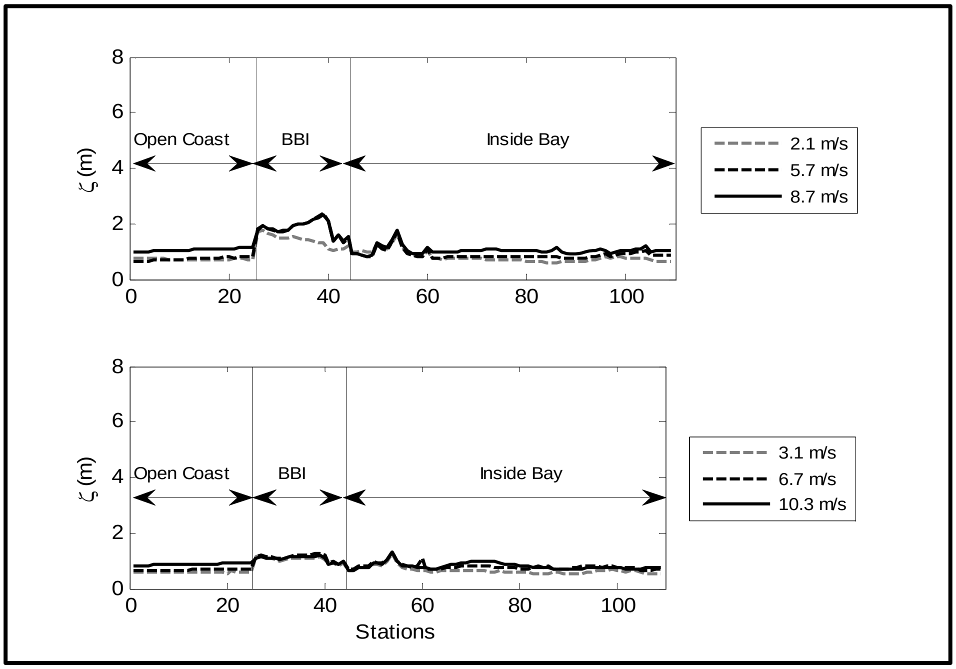

Figure 4.28: Surge trends for v_f scenarios, on track 6 for Corpus Christi Bay. Top pane shows storms simulated at c_p = 900 mb, while bottom pane shows storms simulated at c_p = 960 mb.

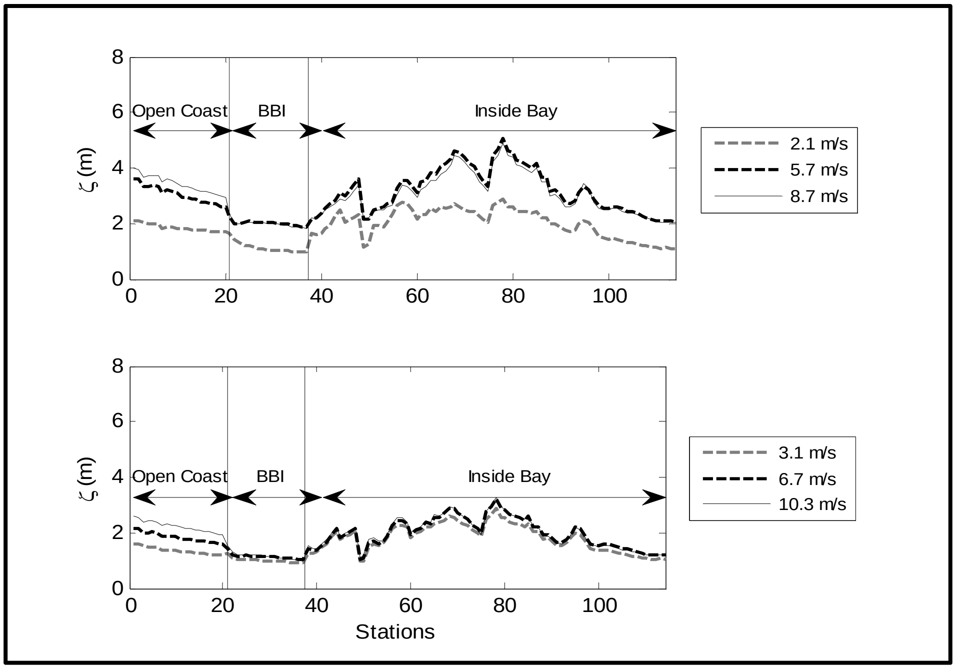

Figure 4.29: Surge trends for v_f scenarios, on track 1 for Matagorda Bay. Top pane shows storms simulated at c_p = 900 mb, while bottom pane shows storms simulated at c_p = 960 mb.

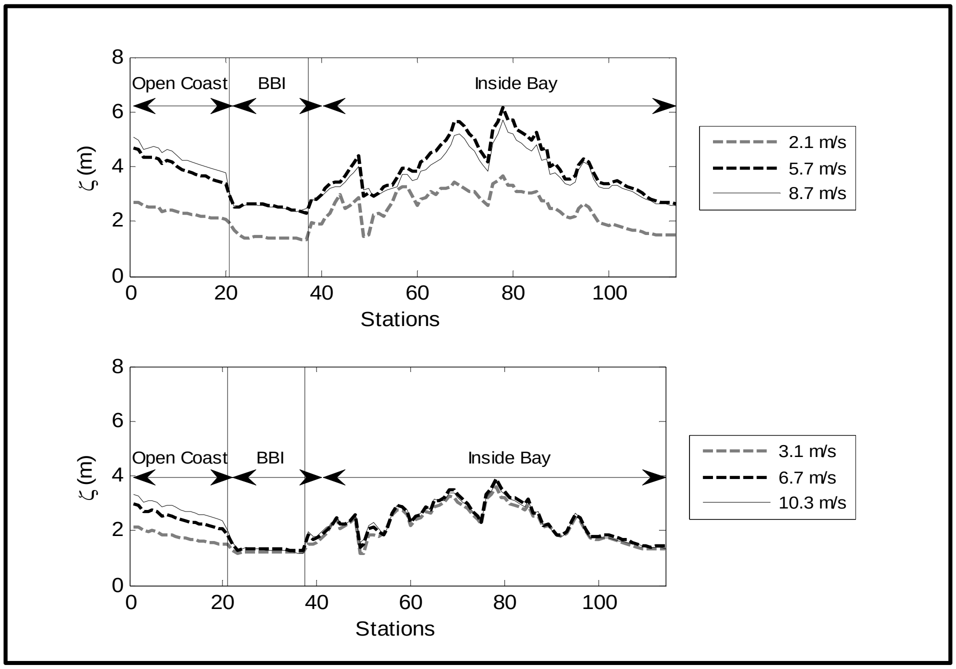

Figure 4.30: Surge trends for v_f scenarios, on track 2 for Matagorda Bay. Top pane shows storms simulated at c_p = 900 mb, while bottom pane shows storms simulated at c_p = 960 mb.

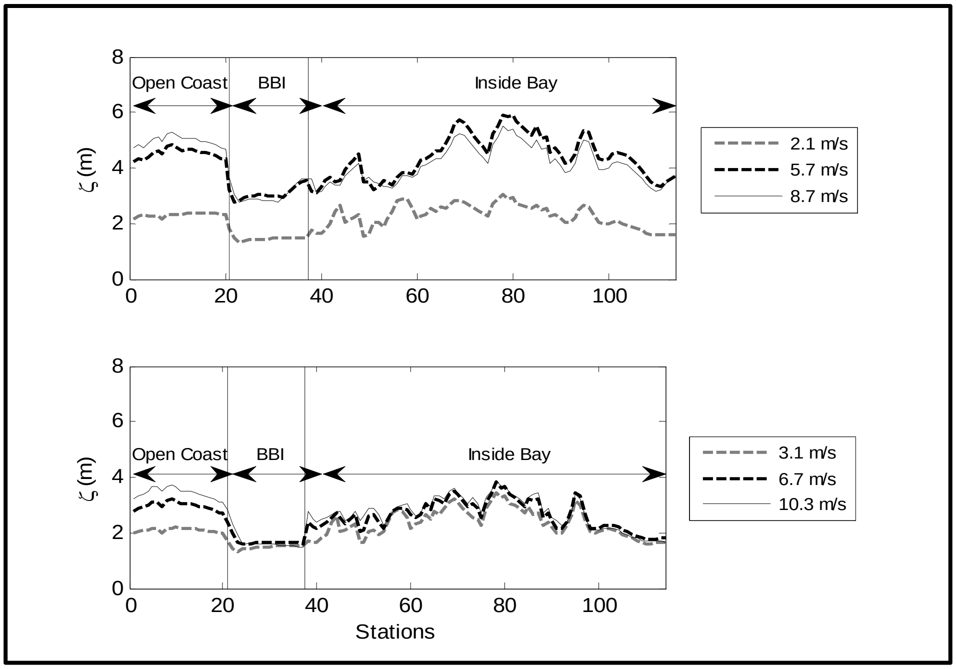

Figure 4.31: Surge trends for v_f scenarios, on track 3 for Matagorda Bay. Top pane shows storms simulated at c_p = 900 mb, while bottom pane shows storms simulated at c_p = 960 mb.

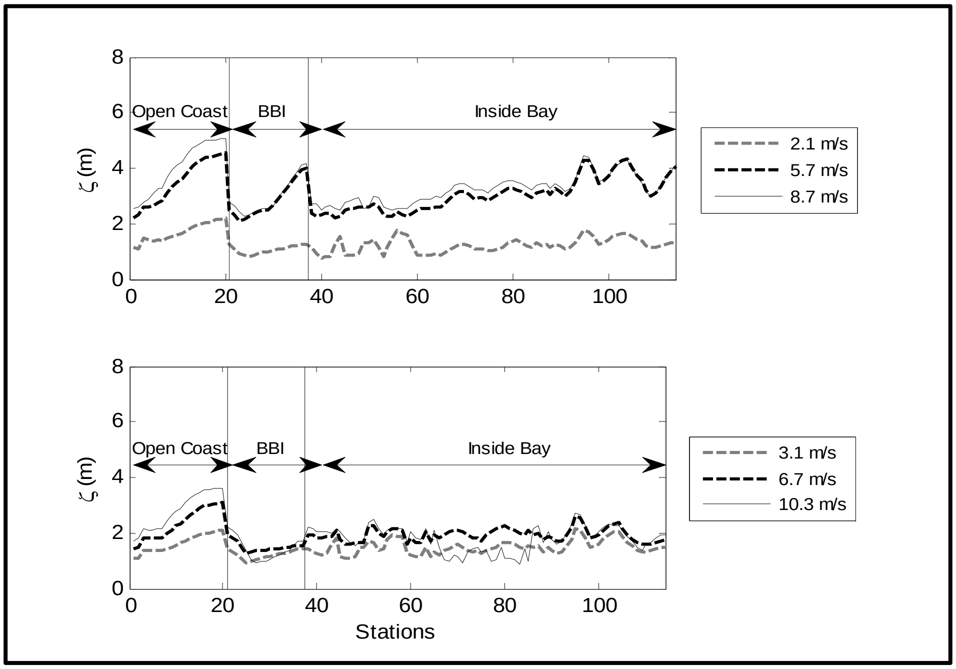

Figure 4.32: Surge trends for v_f scenarios, on track 4 for Matagorda Bay. Top pane shows storms simulated at c_p = 900 mb, while bottom pane shows storms simulated at c_p = 960 mb.

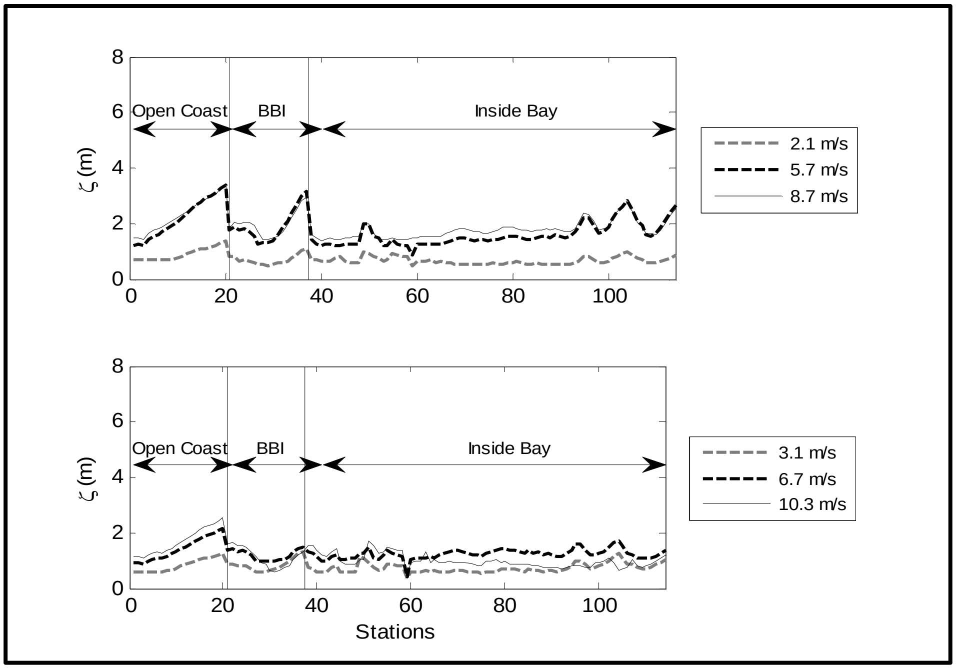

Figure 4.33: Surge trends for v_f scenarios, on track 5 for Matagorda Bay. Top pane shows storms simulated at c_p = 900 mb, while bottom pane shows storms simulated at c_p = 960 mb.

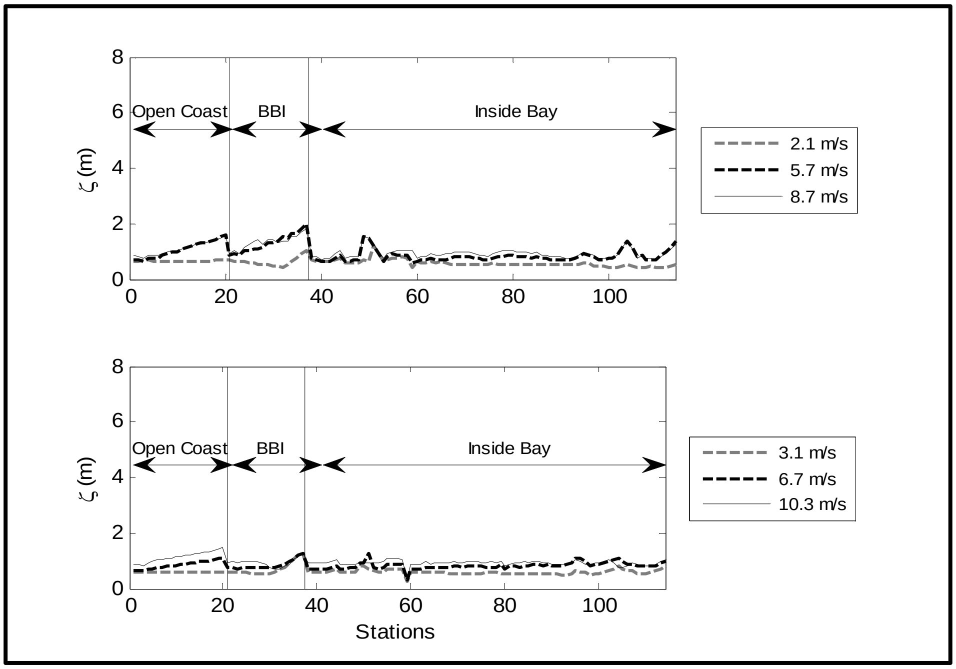

Figure 4.34: Surge trends for v_f scenarios, on track 6 for Matagorda Bay. Top pane shows storms simulated at c_p = 900 mb, while bottom pane shows storms simulated at c_p = 960 mb.

4.2.2 Surge Trends as a Function of Approach Angle in the Bays

Regarding the influence of approach angle on surge in bays, two major measures seem to drive surge magnitudes; these are;

- the proximity of the storm track to the entrance of the bay as the storm travels towards or across the coast, and,
- the distance of the storm track to the station(s) of interest inside the bay, as the storm traverses inland beyond the bay.

For storms oriented such that sustained winds drive surge easily through the entrance of the bay (over the barrier islands and through the channels), higher surge magnitudes are expected – as opposed to otherwise oriented storms. An illustration of this effect is shown in Fig. 4.35 with three tracks (A-track, B-track and C-track), of which A-track and B-track are oriented with the tendency to produce higher surges in the bay as mentioned earlier. As storms travel inland, their paths may get closer to some interior stations of the bay. With such close proximity, such stations are bound to experience relative higher surges compared to others not close to the track (e.g. on the opposite side of the bay).

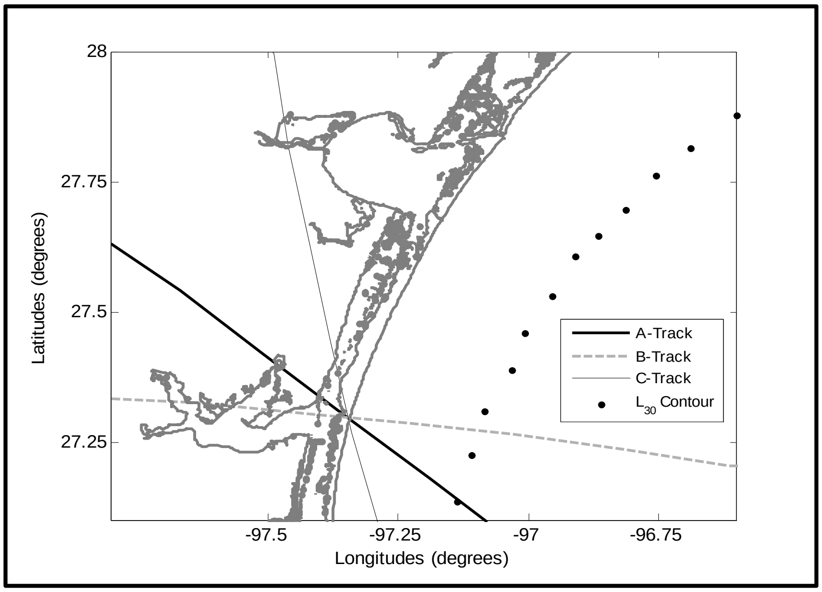

Figure 4.35: Illustration of storm orientations relative to bay.

Similar to the open coast discussions, landfall locations (i.e. intersection of storms with different orientations at the shoreline, as shown in Fig. 4.35) considered for the influence of approach angle will be referred to as LF-loc 1, LF-loc 2 etc., with LF-loc 1 representing ‘landfall location 1’ and LF-loc 2 representing ‘landfall location 2’, and so on.

Figures 4.36 through 4.41 show the surge trends as a function of approach angle for Corpus Christ Bay. The just-mentioned effects of track proximity to the entrance of the bay and interior stations are seen to manifest in the trends. At LF-loc 1 for Corpus Christi Bay, the C-track has the highest proximity to the interior stations as the storm travels inland. Interestingly, A-track generates higher surge at the stations on the northern edge (stations 70 to 78, Fig. 4.20). This is likely due to the fact that the storm’s orientation is almost parallel to the long axis of Corpus Christi Bay, and the onshore directed winds drive surge farther into the bay than the other two track orientations.

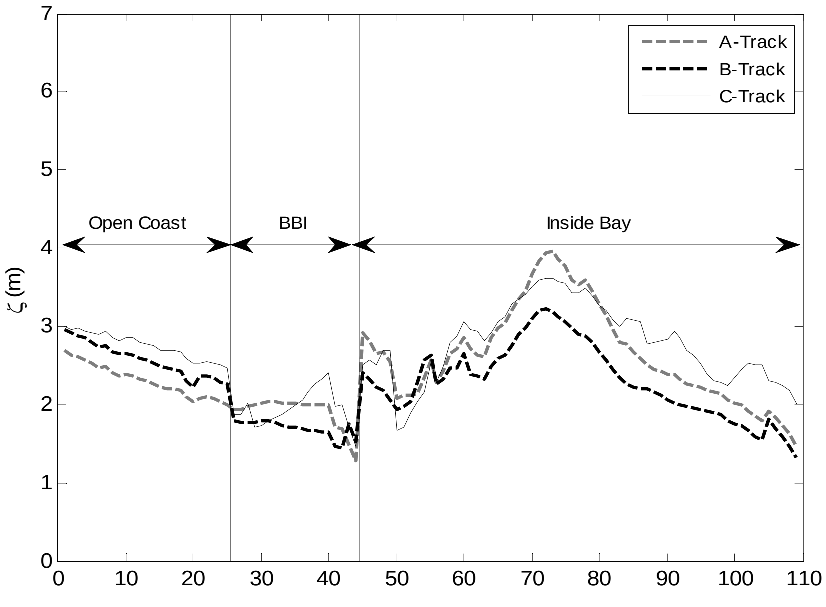

Figure 4.36: Surge trends for θ scenarios, on landfall location 1 for Corpus Christi Bay. BBI denotes ‘Behind Barrier Island’.

This dominance of C-track over A-track and B-track at locations on the northern edge of the bay (stations 70 to 78, Fig. 4.20) is also observed in trends for tracks making landfall on LF-loc 2.

At LF-loc 2 which is also on the left hand side of the bay, but closer to the bay, A-track and B-track have a stronger potential to drive surge through the entrance of the bay than C-track, thus they produce higher surges in the bay. For landfall locations much closer to the bay there is no clear trend or dominance of one track orientation over others (Figs. 4.38 and 4.39). The effects of track proximity can hardly be isolated for these cases, possibly because the re-distribution patterns of surges from the different tracks is different when the landfall locations are right at the entrance of the bay. As the landfall locations move away from the entrance of the bay to the right (LF-loc 4, LF-loc 5 and LF-loc 6), the influence of proximity of the storm paths to the entrance of the bay, on surge generation, seems to increase. For these cases (Figs. 4.40 and 4.41), C-tracks produce higher surges, followed by A-tracks.

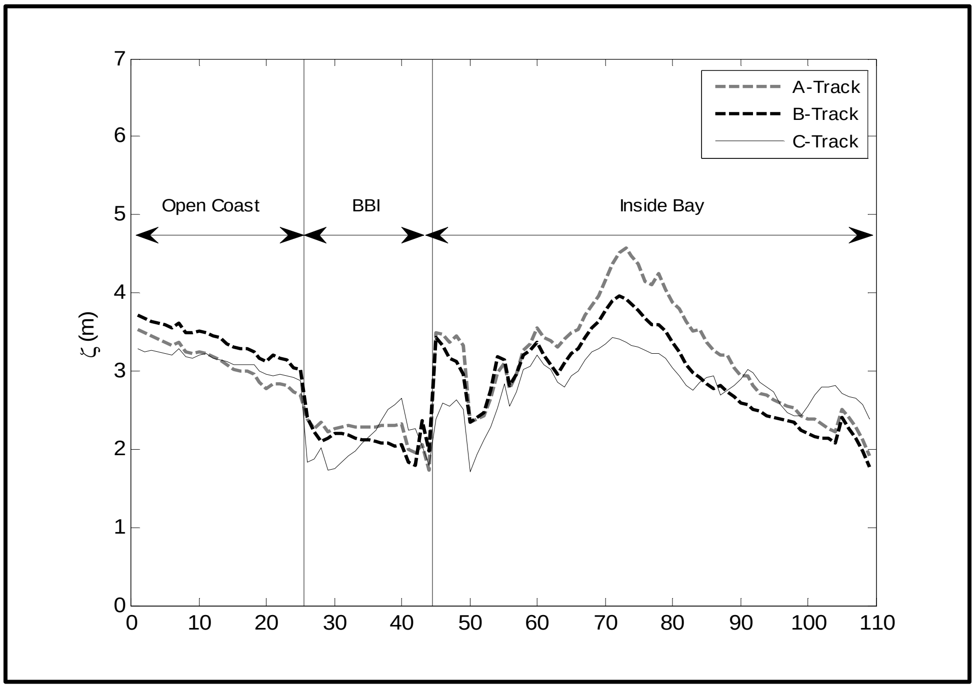

Figure 4.37: Surge trends for θ scenarios, on landfall location 2 for Corpus Christi Bay. BBI denotes 'Behind Barrier Island'.

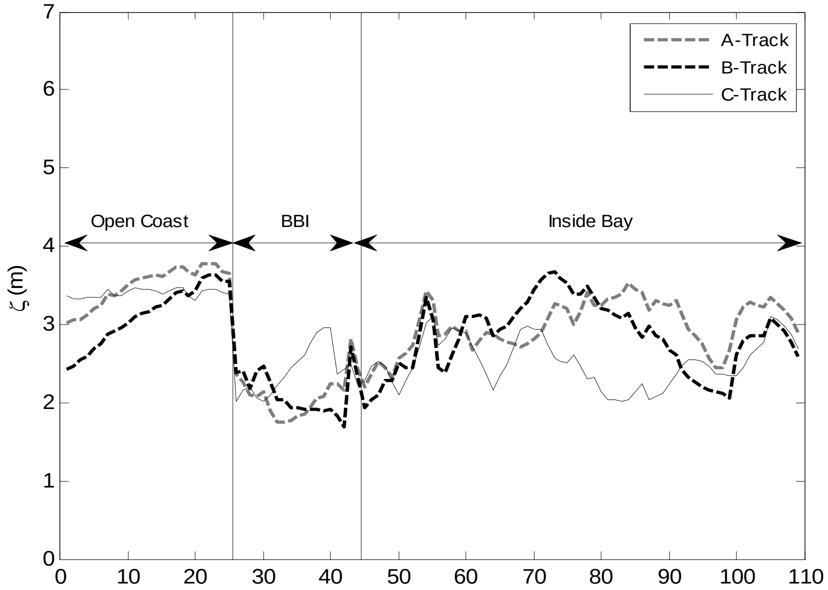

Figure 4.38: Surge trends for θ scenarios, on landfall location 3 for Corpus Christi Bay. BBI denotes 'Behind Barrier Island'.

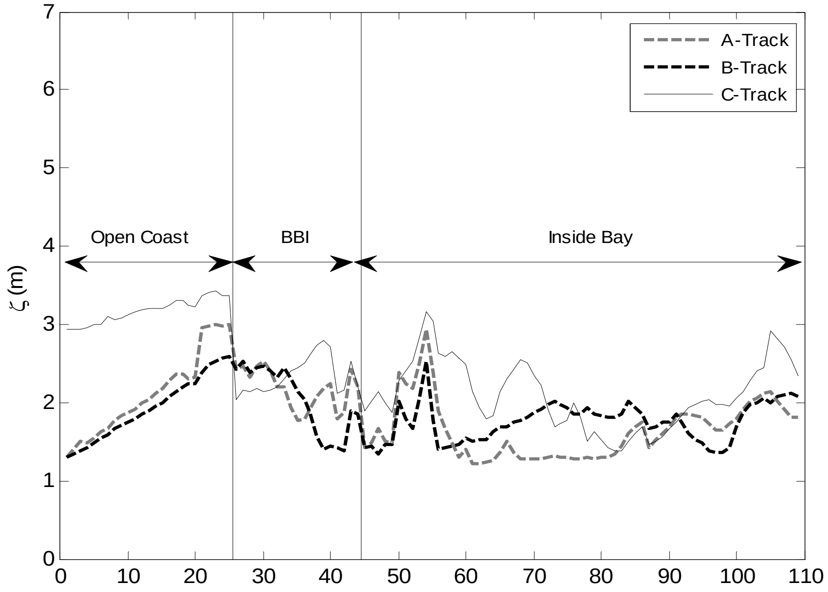

Figure 4.39: Surge trends for θ scenarios, on landfall location 4 for Corpus Christi Bay. BBI denotes 'Behind Barrier Island'.

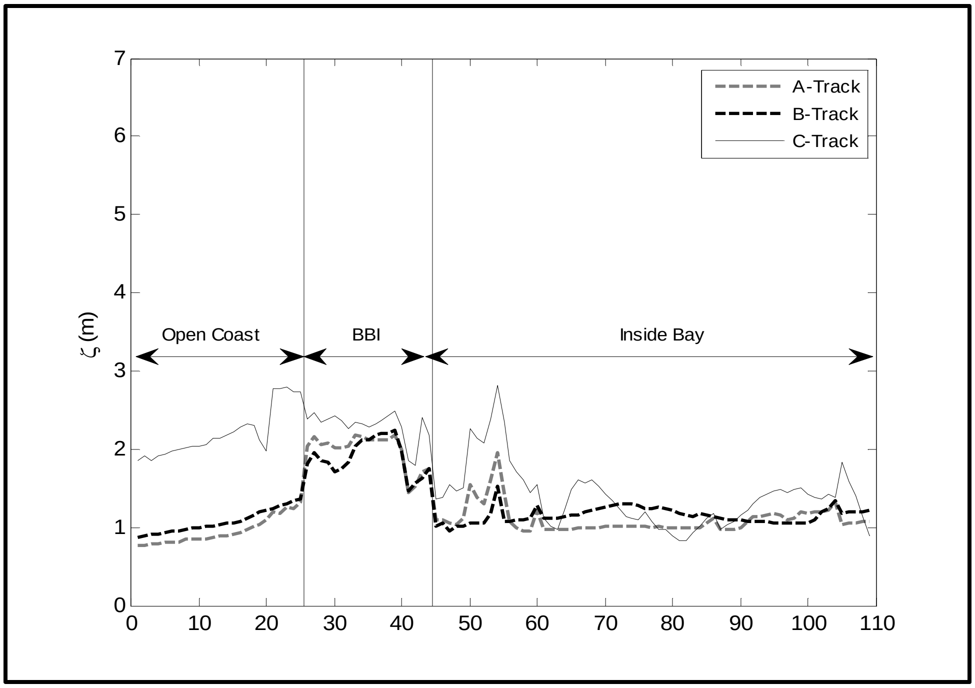

Figure 4.40: Surge trends for θ scenarios, on landfall location 5 for Corpus Christi Bay. BBI denotes 'Behind Barrier Island'.

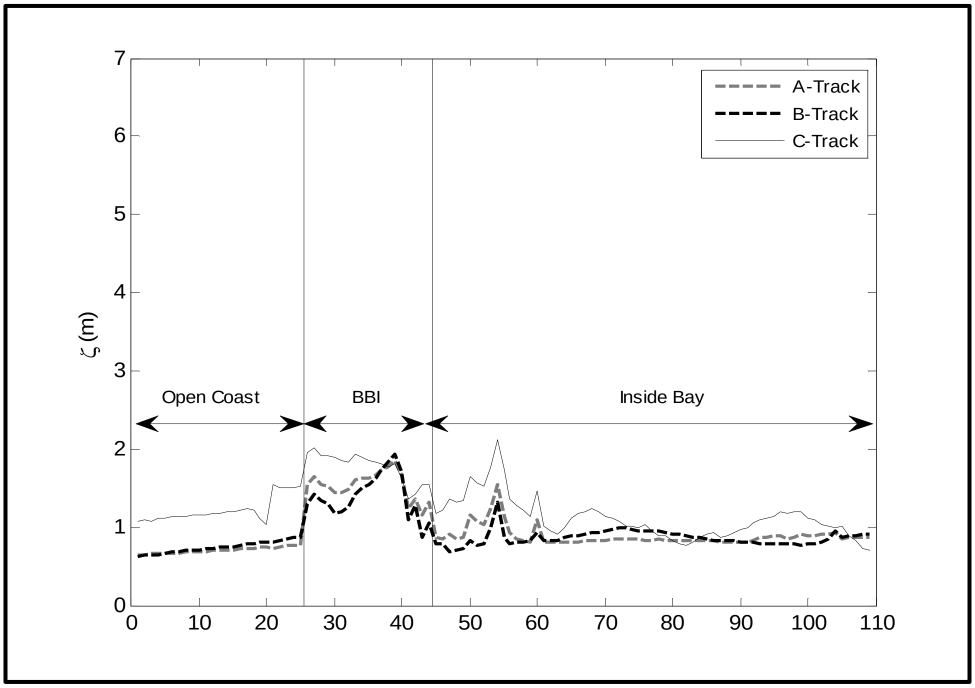

Figure 4.41: Surge trends for θ scenarios, on landfall location 6 for Corpus Christi Bay. BBI denotes 'Behind Barrier Island'.

Similar influences of the two major measures (proximity of the storm track to the entrance of the bay, and distance of the storm track to the station of interest inside the bay) discussed here in regards to the approach angle of storms have been observed in surge trends for Matagorda Bay (Figs. 4.42 through 4.47). The extents to which these two effects may introduce differences in surge magnitudes between one track orientation and another in the bays may be influenced by factors on the open coast (such as the length traveled by each storm across the continental shelf), and the shape and orientation of the bay itself. For instance, for LF-loc 4 of Matagorda Bay (Fig. 4.45), which is close to the edge of the barrier island, the extent to which the surge trends are dissimilar is less than those of the corresponding locations for Corpus Christi Bay (Figs. 4.38 and 4.39), and B-track shows dominance in surge heights almost everywhere inside the bay – this suggests that the re-distribution of surge in the bay (which would be influenced by the shape of the bay/basin) is less variable than in Corpus Christi Bay. As such, while the proximity of storm track to the bay entrance (as the storm crosses the coast) and interior stations (as the storm travels inland) need to be considered in developing formulations to account for the influence of approach angle in the response functions, the possibility that the actual formulations may vary from bay to bay is acknowledged – owing to other possible influences mentioned (e.g. L_{30} in the vicinity of the bay, and the shape of the bay).

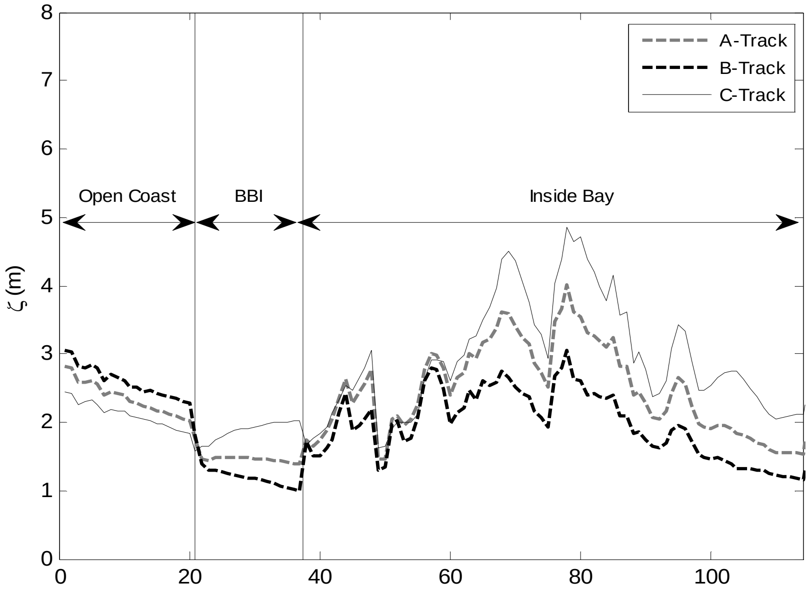

Figure 4.42: Surge trends for θ scenarios, on landfall location 1 for Matagorda Bay. BBI denotes ‘Behind Barrier Island’.

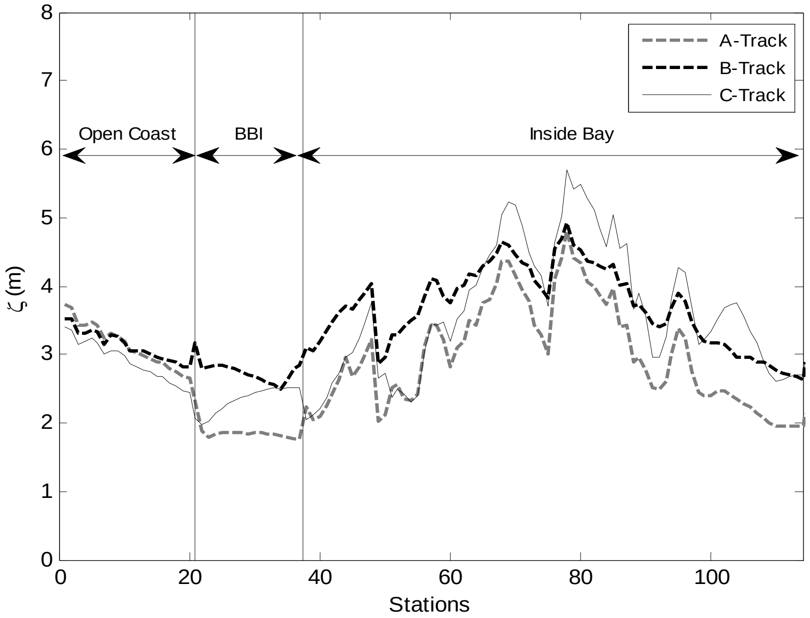

Figure 4.43: Surge trends for θ scenarios, on landfall location 2 for Matagorda Bay. BBI denotes ‘Behind Barrier Island’.

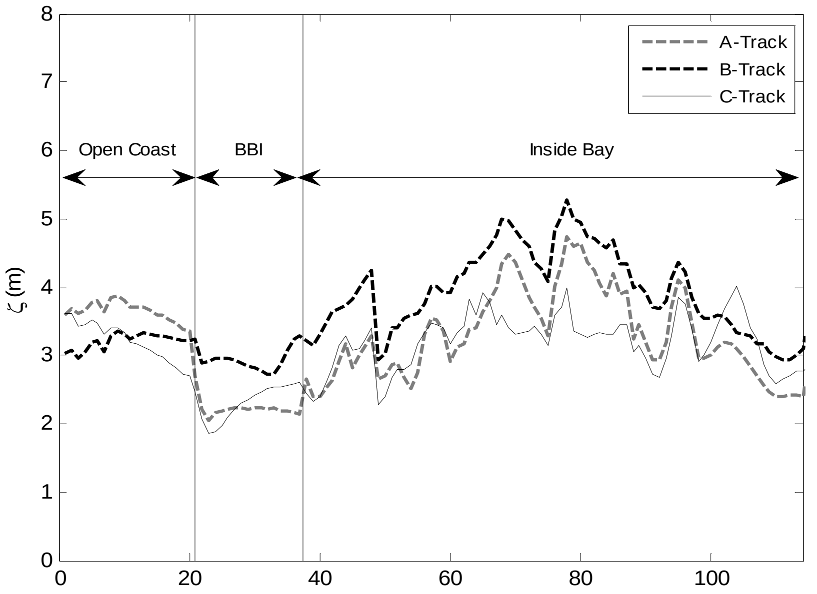

Figure 4.44: Surge trends for θ scenarios, on landfall location 3 for Matagorda Bay. BBI denotes 'Behind Barrier Island'.

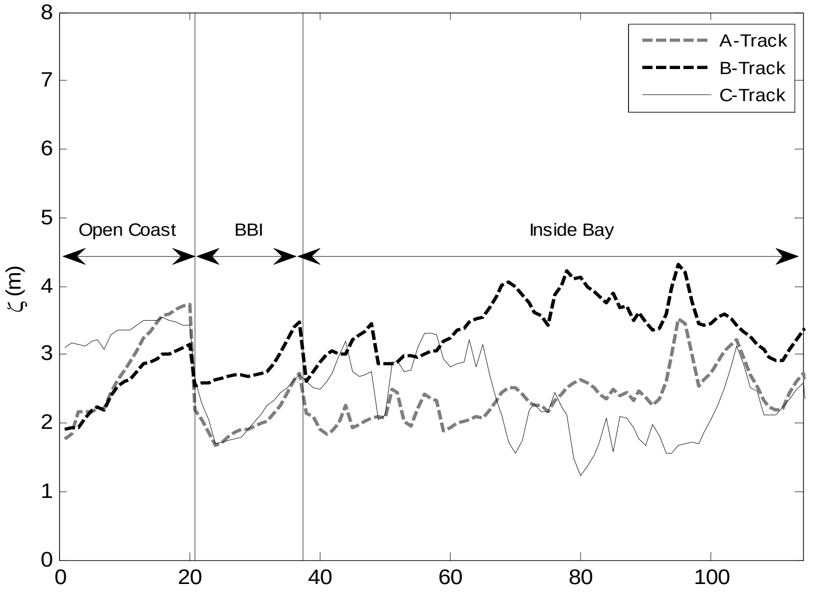

Figure 4.45: Surge trends for θ scenarios, on landfall location 4 for Matagorda Bay. BBI denotes 'Behind Barrier Island'.

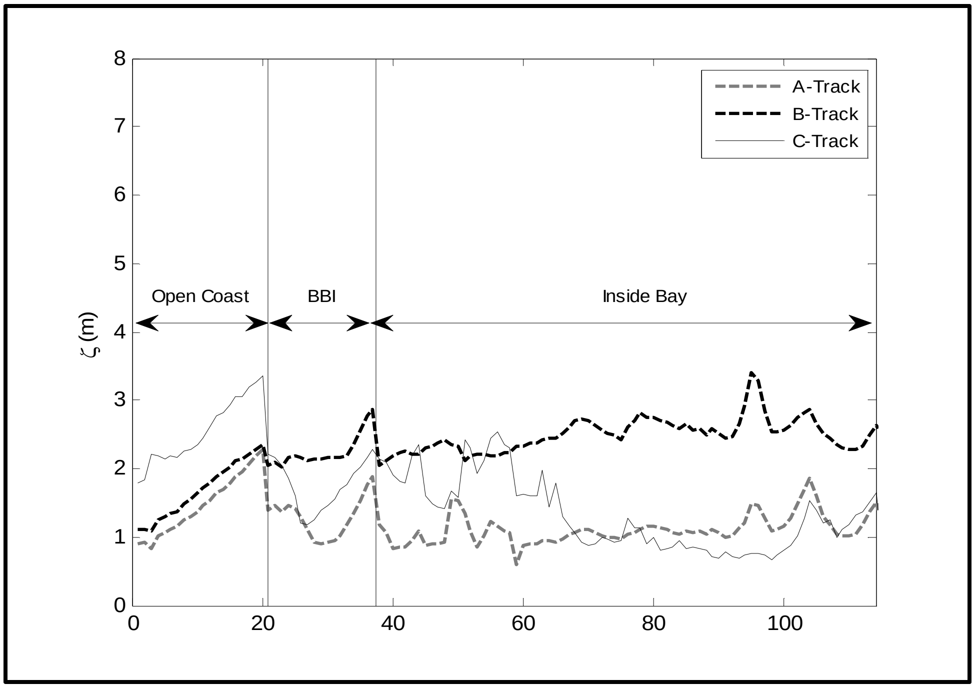

Figure 4.46: Surge trends for θ scenarios, on landfall location 5 for Matagorda Bay. BBI denotes 'Behind Barrier Island'.

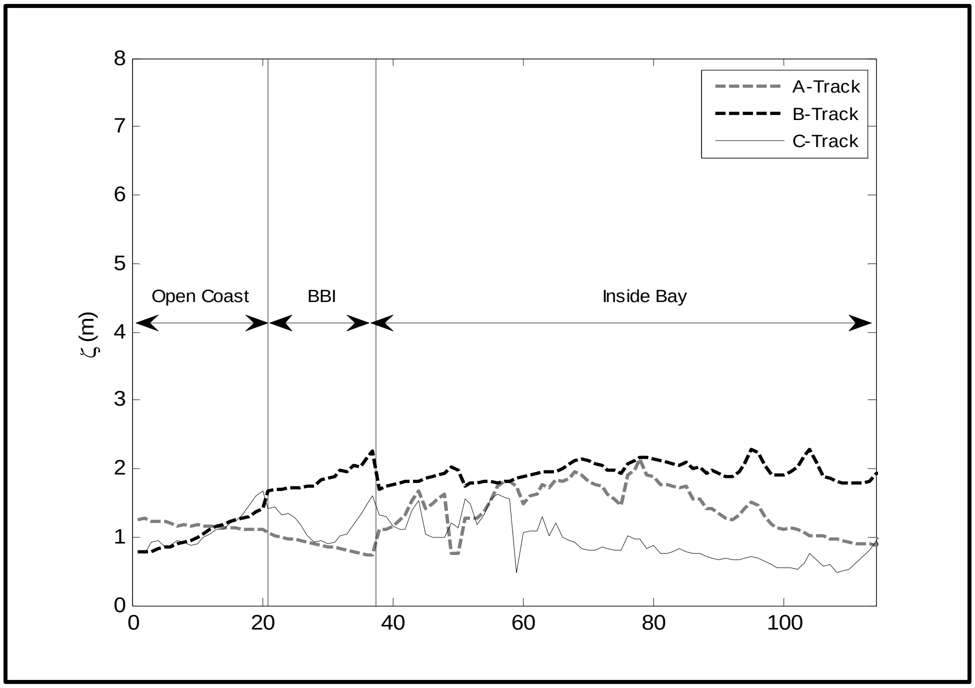

Figure 4.47: Surge trends for θ scenarios, on landfall location 6 for Matagorda Bay. BBI denotes 'Behind Barrier Island'.

4.2.3 Surge Trends as a Function of Sea Level Rise in the Bays

For discussions on the surge trends as a function of SLR in bays, four stations within each bay are selected. These stations are selected from the western, northern, eastern, and southern edges of each bay. Stations 56, 72, 95 and 32 are selected from the western, northern, eastern and southern edges of Corpus Christi Bay (Fig. 4.20), while Stations 48, 80, 108 and 26 are selected from the western, northern, eastern, and southern edges of Matagorda Bay, respectively (Fig. 4.21). Figures 4.48 through 4.51 show the water level trends with respect to SLR for Corpus Christi Bay, while Figs. 4.52 through 4.55 show water level trends for Matagorda Bay.

First, plots of surge ($\eta_s - SLR$) versus no-SLR water levels for Corpus Christi Bay (Top panes of Figs. 4.36 through 4.39) show that change in SLR yields a corresponding change in surge. At the lowest value of SLR, 0.24 m, the change in surge is very small, as the surge versus no-SLR data points for this condition fall on the exact-match line, at all four corners of the bay.

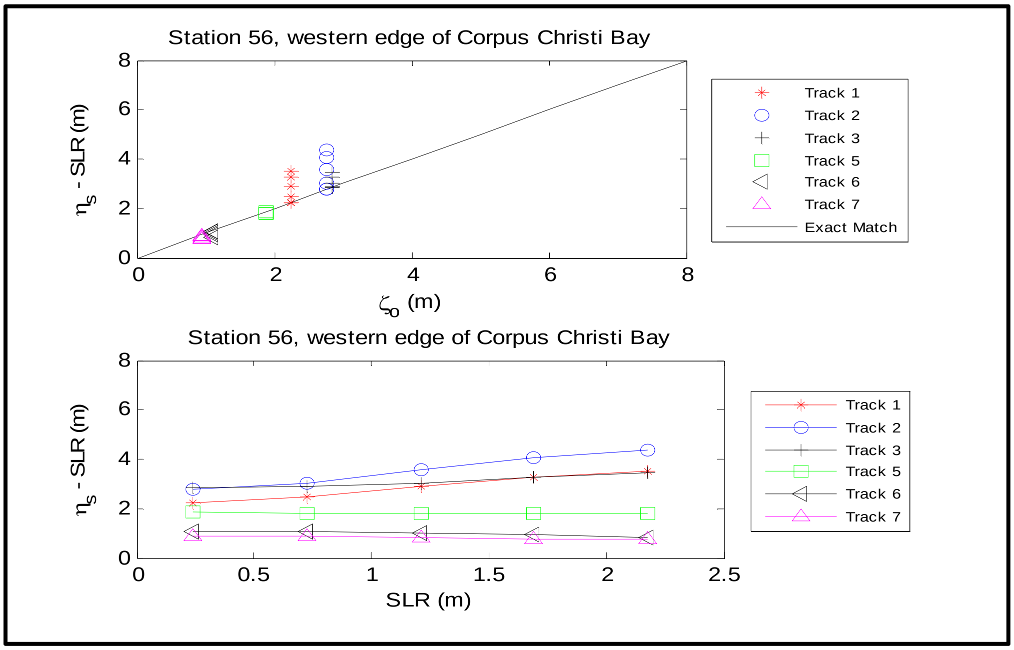

Figure 4.48: Surge trends for SLR at station 56 of Corpus Christi Bay. Top pane shows water level less SLR versus base (i.e. no SLR) surge. Bottom pane shows water level less SLR, versus SLR.

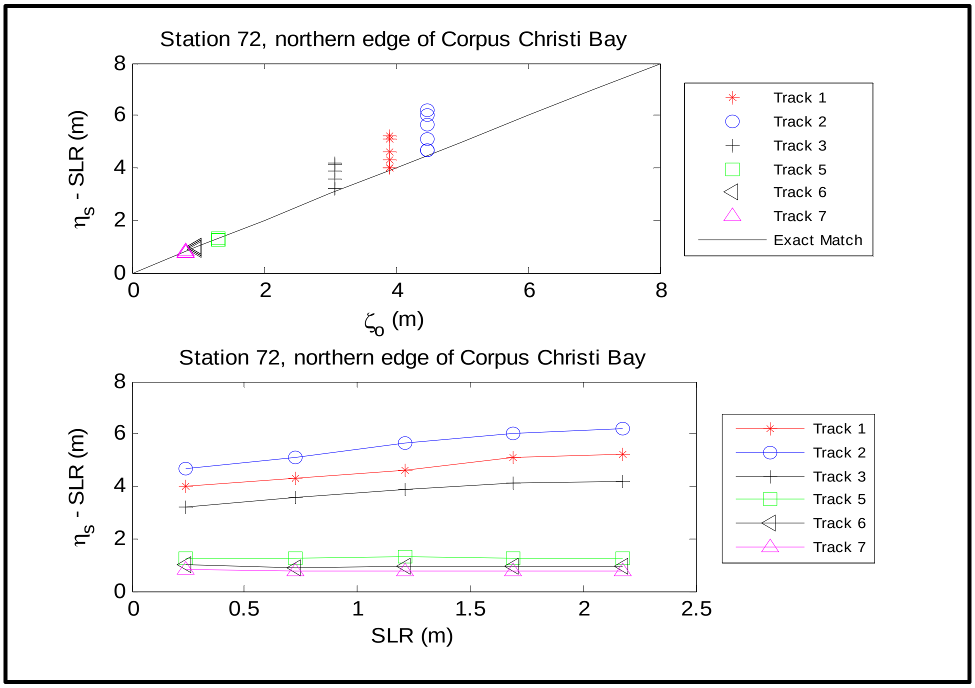

Figure 4.49: Surge trends for SLR at station 72 of Corpus Christi Bay. Top pane shows water level less SLR versus base (i.e. no SLR) surge. Bottom pane shows water level less SLR, versus SLR.

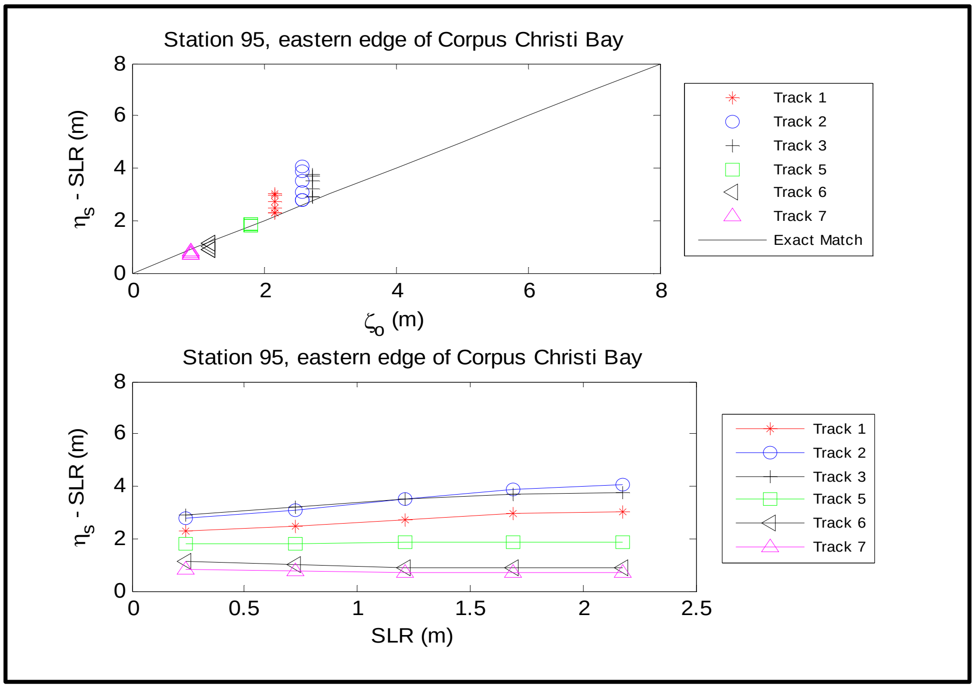

Figure 4.50: Surge trends for SLR at station 95 of Corpus Christi Bay. Top pane shows water level less SLR versus base (i.e. no SLR) surge. Bottom pane shows water level less SLR, versus SLR.

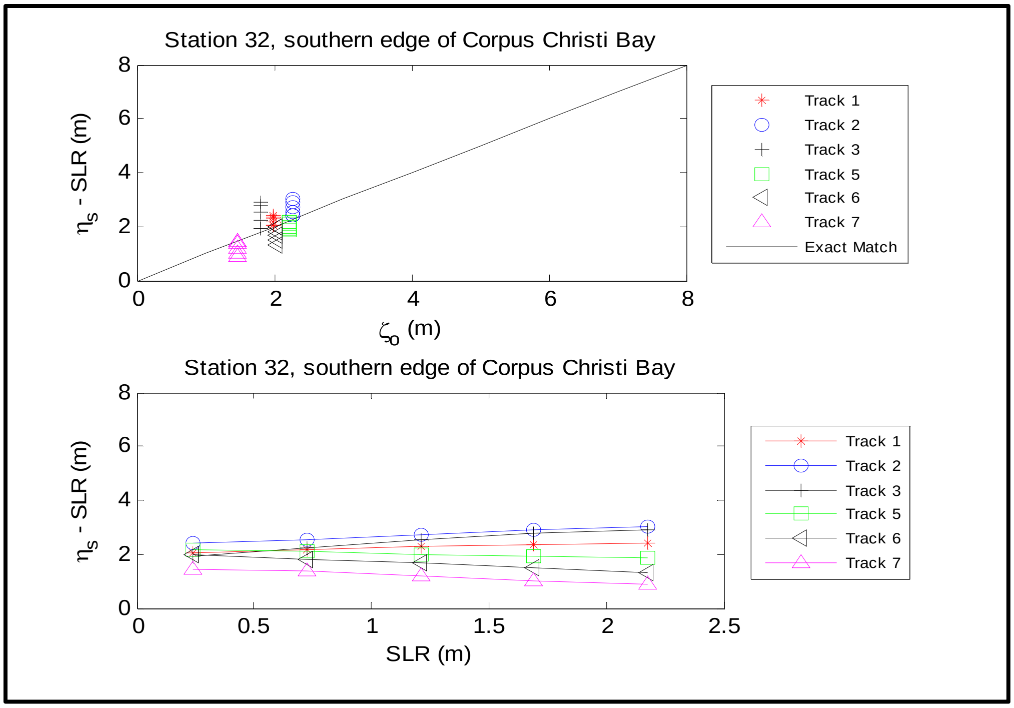

Figure 4.51: Surge trends for SLR at station 32 of Corpus Christi Bay. Top pane shows water level less SLR versus base (i.e. no SLR) surge. Bottom pane shows water level less SLR, versus SLR.

In the top panes of Figs. 4.48 through 4.51, the deviation of surge from an exact-match line can be seen for storms on different tracks. The bottom panes of these figures delineate that tracks making landfall to the left of the bays show an increase in surge as SLR increases; this is attributed to sustained winds driving surge sufficiently to cause an overtopping of the barrier islands (which are less than 1 meter at many of their sections, in both Corpus Christi and Matagorda Bays). Given that the bay is semi-confined, sustained wind action on the increasing water mass results in a build-up of surge as the boundaries support surge generation. Figures 4.56 and 4.57 show the inundation of the barrier islands for the cases when SLR=0.24 m and 0.73 m, for Corpus Christi Bay, and Fig. 4.58 shows inundation of the barrier island at Matagorda Bay when SLR=0.24 m. The inundation plots are generated with tracks making landfall at LF-loc 2 and LF-loc 3 for Corpus Christi and Matagorda Bays respectively; they show that barrier islands are almost completely inundated by surge in Corpus Christi when SLR=0.24 m (un-overtopped sections are barely noticeable – circled portion of Fig. 4.40), and completely inundated when SLR is 0.73 m. At Matagorda Bay, the barrier island is completely inundated when SLR=0.24 m. It should be noted here that storms simulated for the SLR effect are fairly intense (c_p=930 mb), and that the extent of inundation may be less for weaker storms. Again, the deviation of surges from the exact-match line for storms making landfall to the left of the bay is also seen in Matagorda Bay trends (Figs. 4.52 through 4.55).

Further observations of surge with respect to SLR only (bottom pane of Figs. 4.48 through 4.51) clearly show that surge may decrease with SLR, for tracks making landfall on the right side of the bay. This is seen at the four stations (56, 72, 95 and 32) selected for discussion in Corpus Christi Bay. At Matagorda Bay, this observation is made at station 26 (Fig. 4.55). This may be due to the weak side of the storm not driving much surge to these locations of the bay.

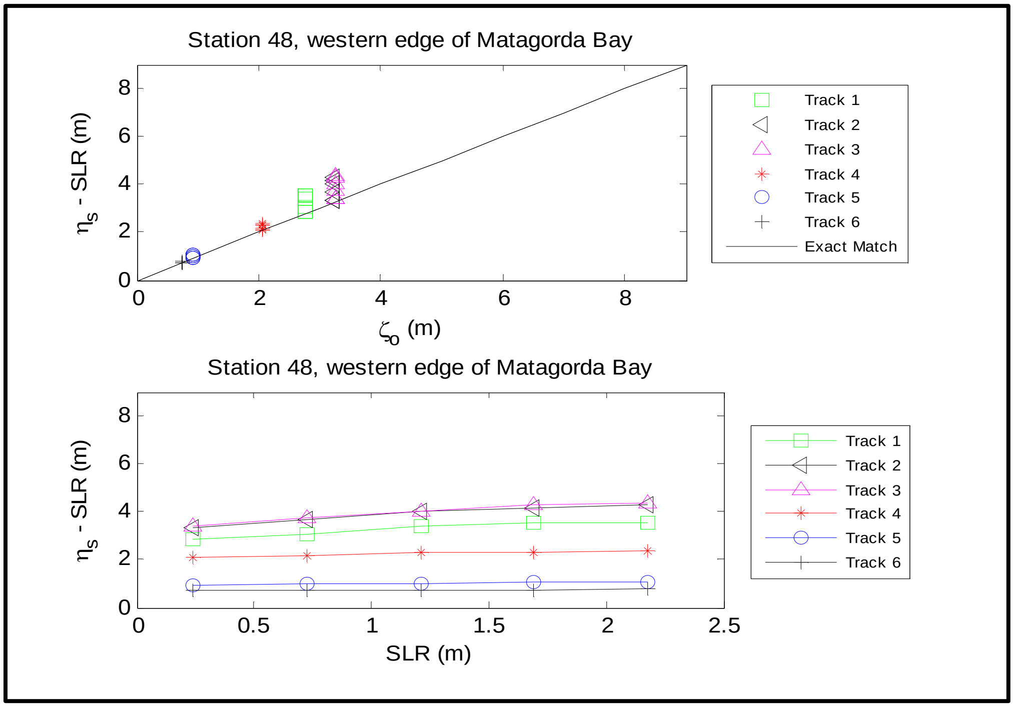

Figure 4.52: Surge trends for SLR at station 48 of Matagorda Bay. Top pane shows water level less SLR versus base (i.e. no SLR) surge. Bottom pane shows water level less SLR, versus SLR.

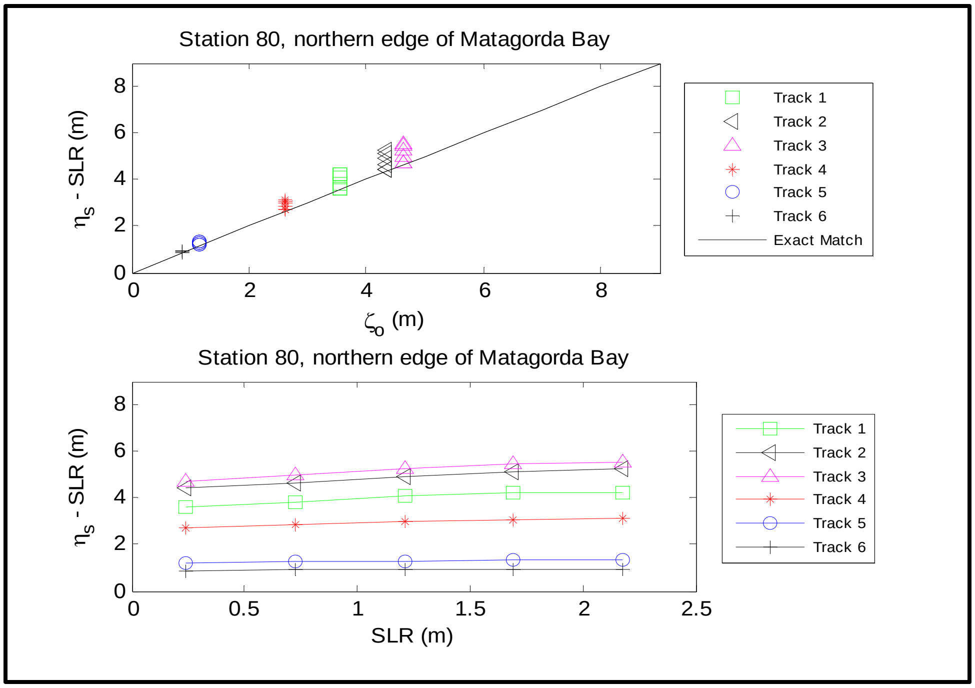

Figure 4.53: Surge trends for SLR at station 80 of Matagorda Bay. Top pane shows water level less SLR versus base (i.e. no SLR) surge. Bottom pane shows water level less SLR, versus SLR.

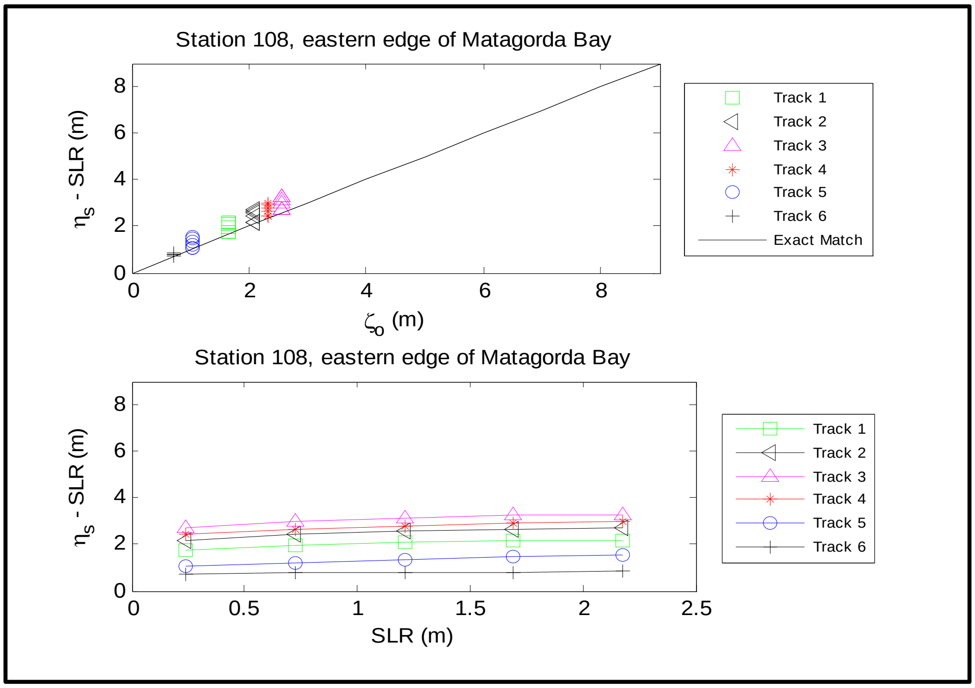

Figure 4.54: Surge trends for SLR at station 108 of Matagorda Bay. Top pane shows water level less SLR versus base (i.e. no SLR) surge. Bottom pane shows water level less SLR, versus SLR.

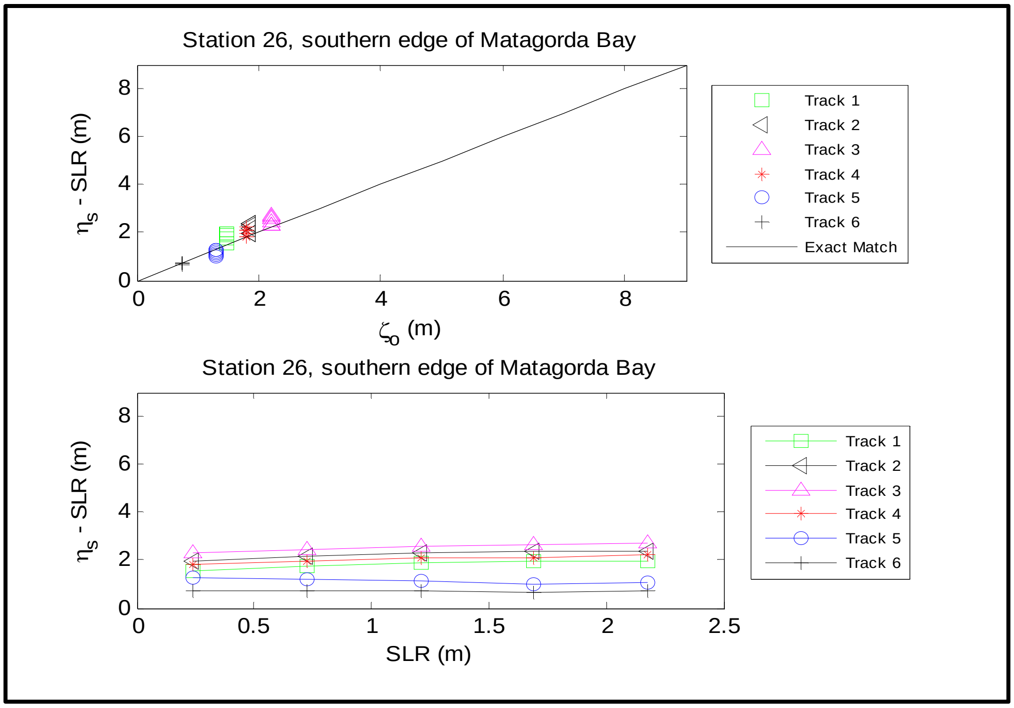

Figure 4.55: Surge trends for SLR at station 26 of Matagorda Bay. Top pane shows water level less SLR versus base (i.e. no SLR) surge. Bottom pane shows water level less SLR, versus SLR.

A summary of the range of slopes for the surge versus SLR trends is presented in Table 4.1 – these are obtained using a linear fit to data for each track, at each of the discussed stations. The range of slopes for both Corpus Christi and Matagorda Bays suggest that the trends may be classified as linear to weakly non-linear, which agrees with the findings of Smith et al. (2010) on the trends observed at southeast Louisiana, USA. The differing impacts of the left and right storm winds on the bay when SLR is considered have not been explicitly discussed in literature.

Table 4.1: Slopes of surge trends with respect to SLR.

Bay	Station	Description	Minimum Slope	Maximum Slope
Corpus Christi	56	western edge of bay	-0.11	0.88
	72	northern edge of bay	-0.04	0.84
	95	eastern edge of bay	-0.13	0.68
	32	southern edge of bay	-0.34	0.51
Matagorda	48	western edge of bay	0.01	0.51
	80	northern edge of bay	0.03	0.43
	108	eastern edge of bay	0.06	0.29
	26	southern edge of bay	-0.12	0.22

While this observation may seem very basic or expected, it is still worth being established and supported with data, as has been done in this research. Specifically, by investigating these trends it has been shown that linearity or non-linearity of surge trends as a function of SLR can be associated to the landfall locations of the storms considered for a given bay. It is interesting that the reduction in surge as SLR increases, for storms making landfall to the right of the bay, is observed at all four stations discussed for Corpus Christi Bay, while in Matagorda Bay only station 26 shows this observation. Tracks which make landfall to the right of Corpus Christi Bay pass through the same region (Fig. 4.59, bordered area) as tracks making landfall to the left of Matagorda Bay. In this region, other estuaries (Copano Bay, Aransas Bay, and San Antonio Bay) exist; one possible explanation to this observation is that tracks making landfall in this region push water mass into these estuaries, as well as Matagorda Bay, more than into Corpus Christi Bay. On the other hand, surge from storms making landfall to the right side of Matagorda Bay will probably make it into the bay – more significantly than in the case of Corpus Christi. Given the relatively linear nature of the surge trends as a function of SLR, we hypothesize that the influence of SLR can be incorporated into the surge response functions for bays through a straightforward polynomial correction in dimensional surge space.

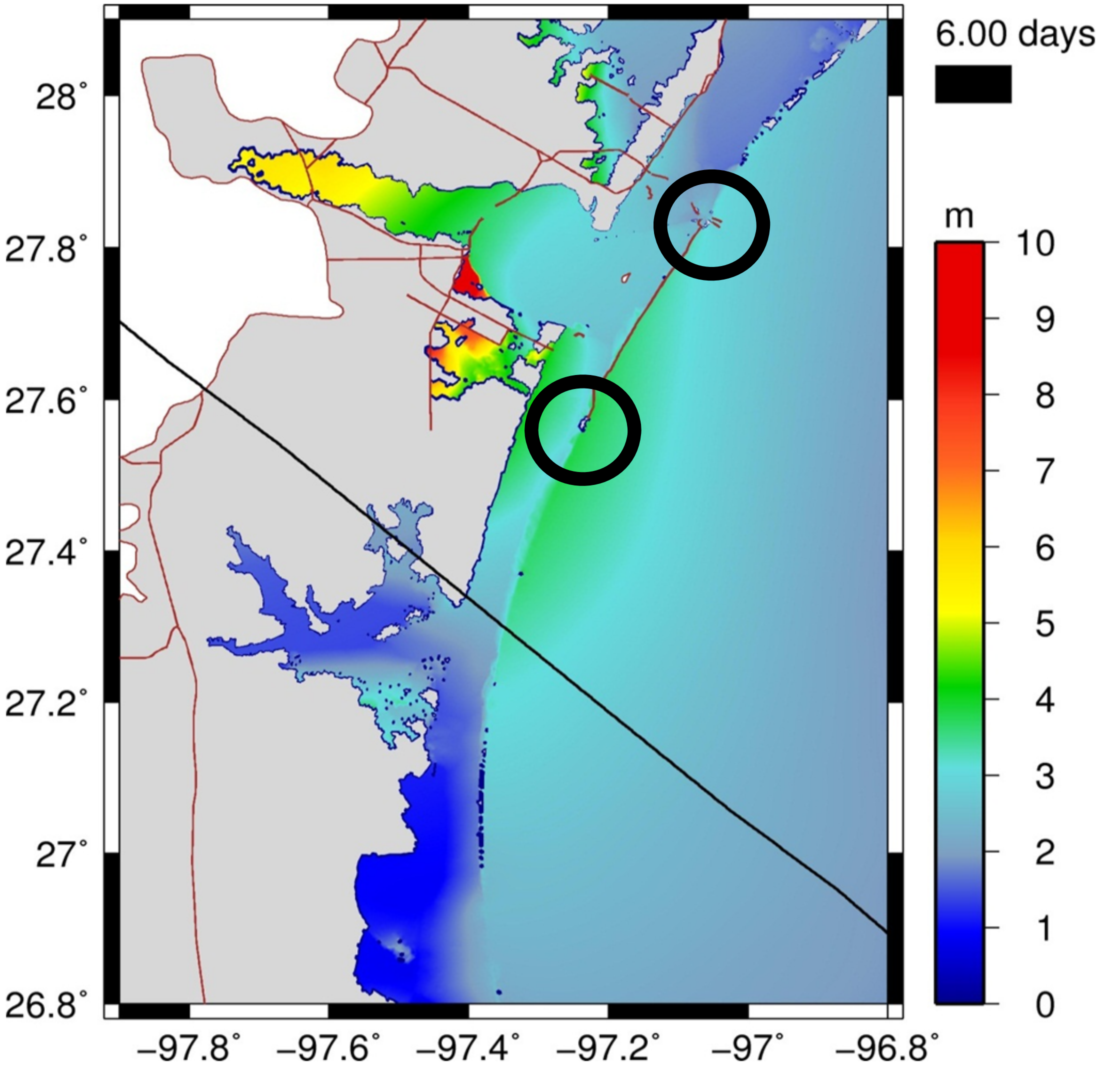

Figure 4.56: Barrier island inundation at Corpus Christi Bay, when SLR=0.24 m. Black line is storm track. Circled portions are sections of the barrier island that are not overtopped.

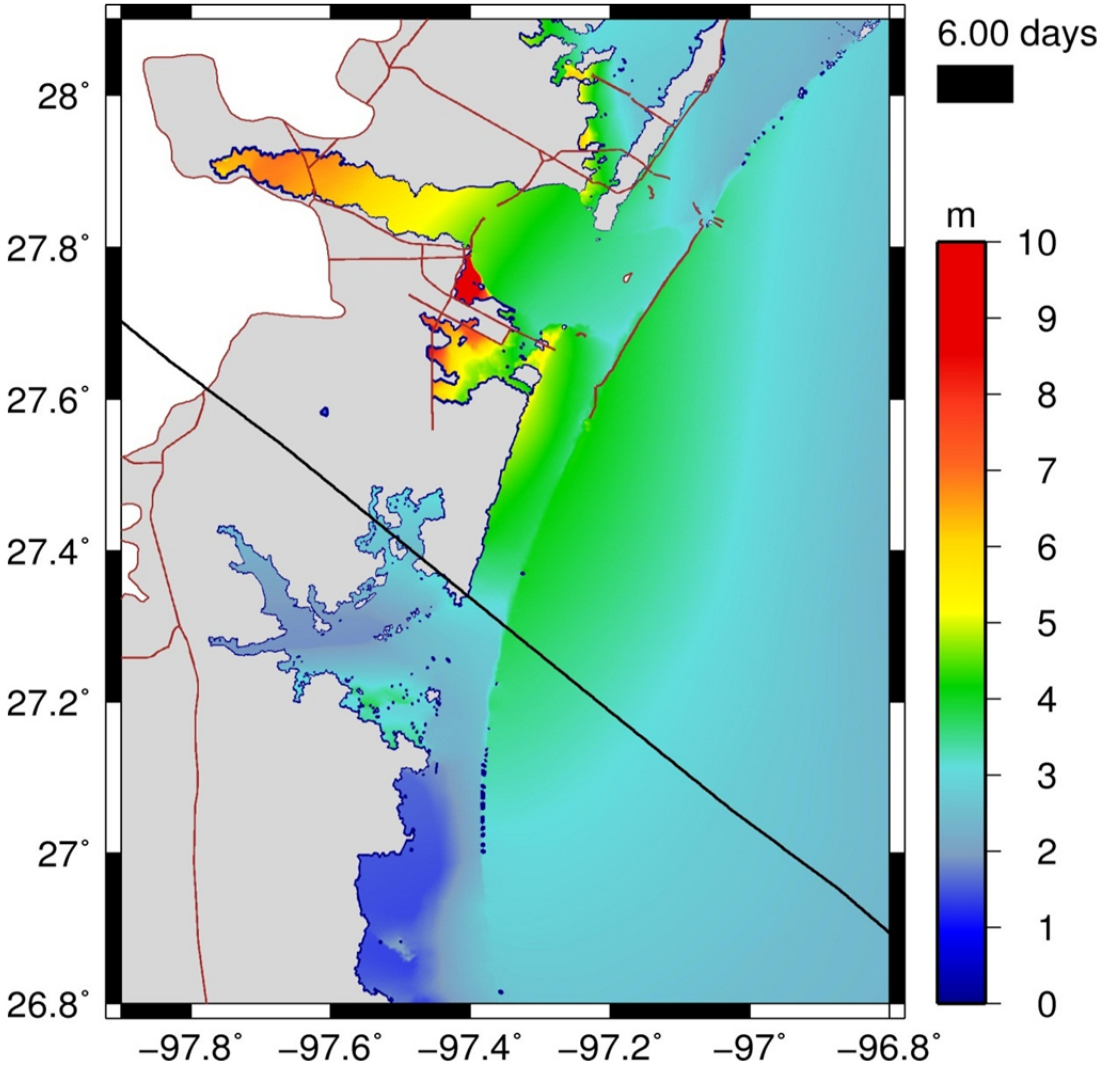

Figure 4.57: Barrier island inundation at Corpus Christi Bay, when SLR=0.73 m. Black line is storm track.

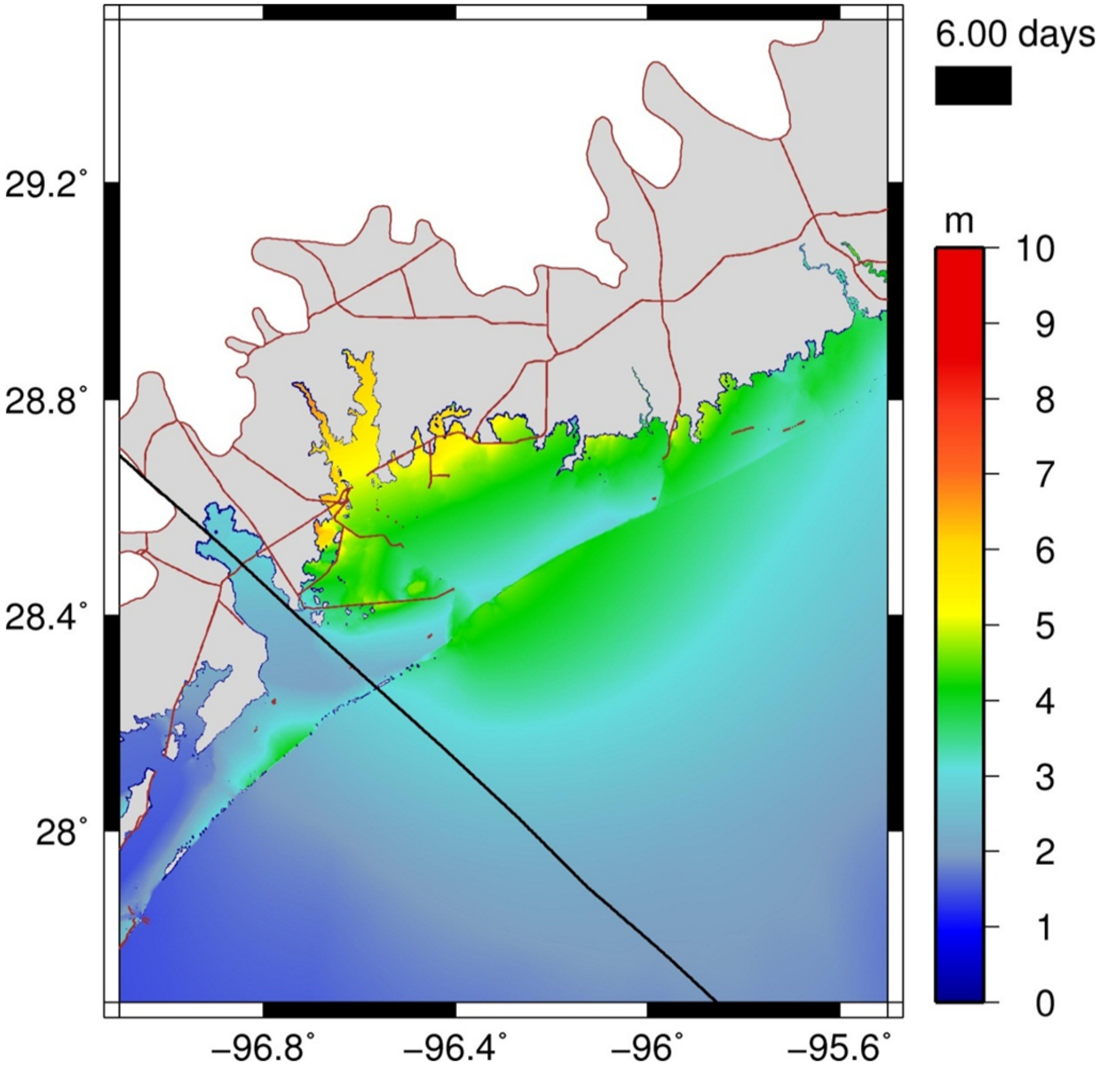

Figure 4.58: Barrier island inundation at Matagorda Bay, when SLR=0.24 m. Black line is storm track.

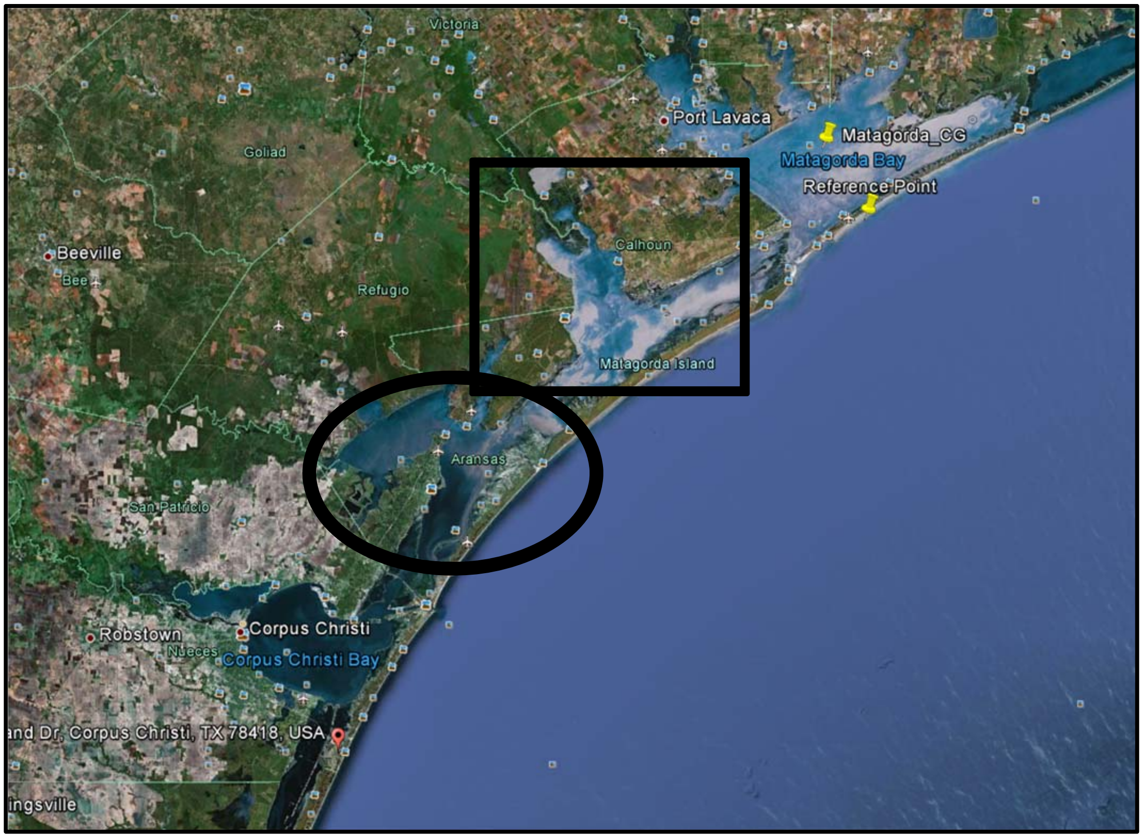

Figure 4.59: Region of Copano, Aransas and San Antonio Bays. Oval area encloses Copano Bay, and boxed area encloses San Antonio Bay.

4.3 Surge Response Functions with v_f, θ and SLR for Open Coast Locations

On including the simulated data for forward speed and approach angle into the SRF analysis, the performance of the SRF form of Song et al. (2012) (which hereafter will be referred to as the previous version of the open coast SRFs) is tested on the data. Figures 4.60 through 4.63 show the performance of the previous version of the open coast SRFs at locations 1, 3, 5 and 7 defined in Fig. 4.1; the performance at locations 2, 4, 6 and 8 are shown in Appendix A (Figs. A4.1 through A4.4).

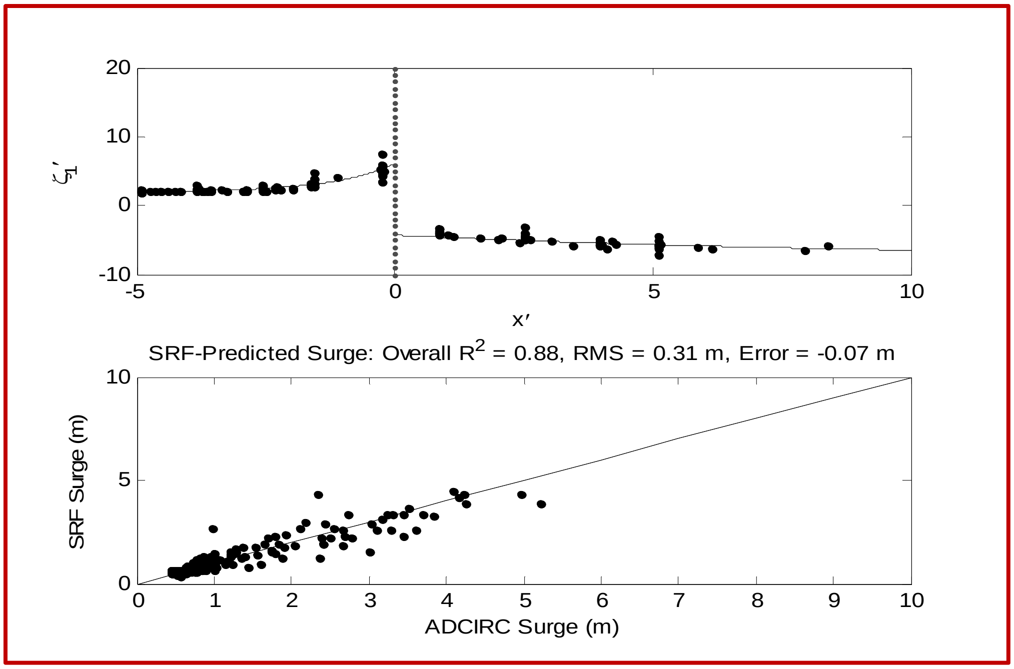

Figure 4.60: Performance of previous SRFs at Location 1 of Fig. 4.1. Top pane shows the plot of the dimensionless data using Equations 2.8 and 2.9. Bottom pane shows the back-prediction of surge using the dimensional SRFs.

On inspecting the SRF plots (Figs. 4.60 through 4.63), some scatter can be seen in the dimensionless data, especially at location 3 (Fig. 4.61) and location 5 (Fig. 4.62). The uncertainty in the prediction of surges ranges from 0.31 m at location 1 to 0.37 m at location 7. Prior to the inclusion of v_f and θ data into the SRF analysis, the uncertainties at locations 1, 3, 5 and 7 ranged from 0.11 m to 0.22 m (Song et. al. 2012). While the errors observed after the addition of v_f and θ data are not too large, the hypothesis here is that accounting for the influences of forward speed and approach angle can reduce the uncertainties associated with the SRFs.

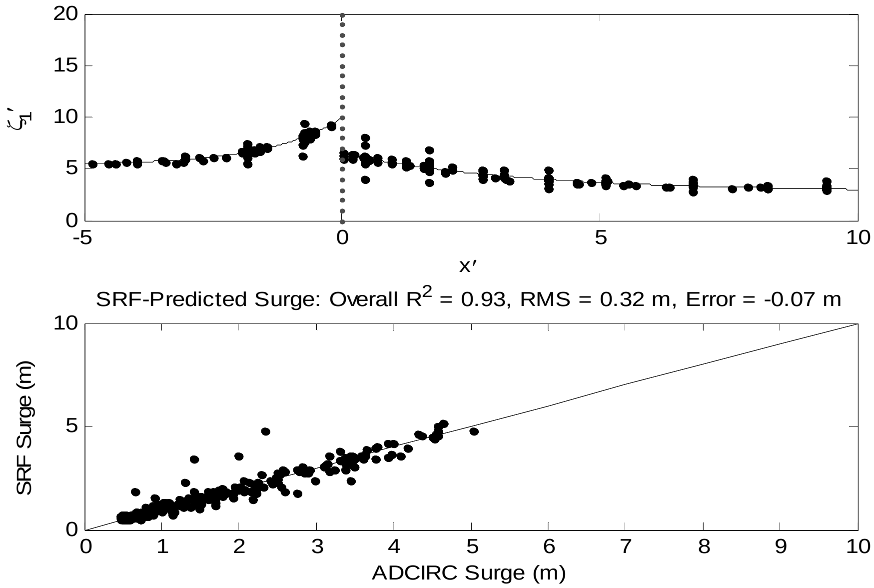

Figure 4.61: Performance of previous SRFs at Location 3 of Fig. 4.1. Top pane shows the plot of the dimensionless data using Equations 2.8 and 2.9. Bottom pane shows the back-prediction of surge using the dimensional SRFs.

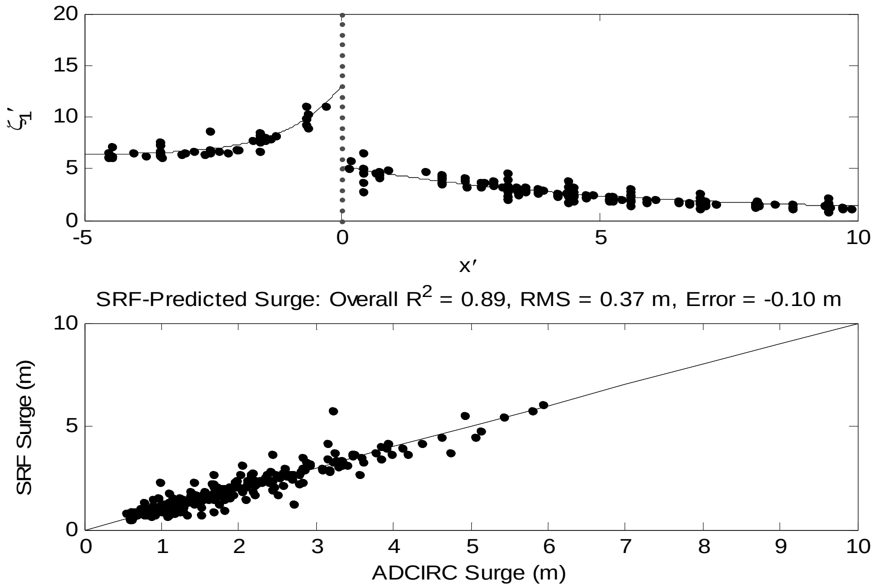

Figure 4.62: Performance of previous SRFs at Location 5 of Fig. 4.1. Top pane shows the plot of the dimensionless data using Equations 2.8 and 2.9. Bottom pane shows the back-prediction of surge using the dimensional SRFs.

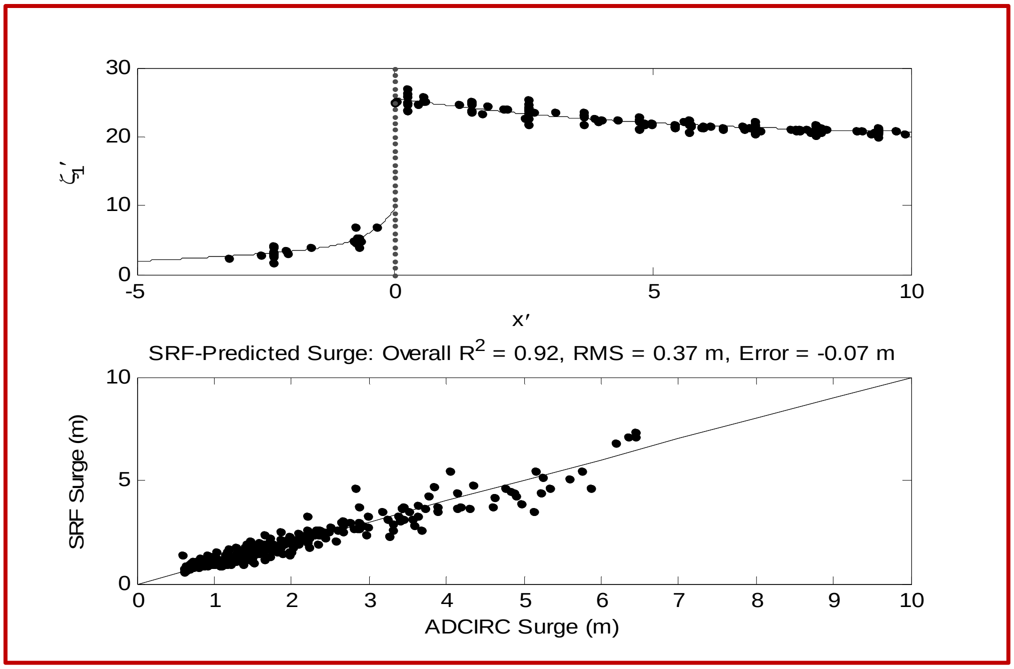

Figure 4.63: Performance of previous SRFs at Location 7 of Fig. 4.1. Top pane shows the plot of the dimensionless data using Equations 2.8 and 2.9. Bottom pane shows the back-prediction of surge using the dimensional SRFs.

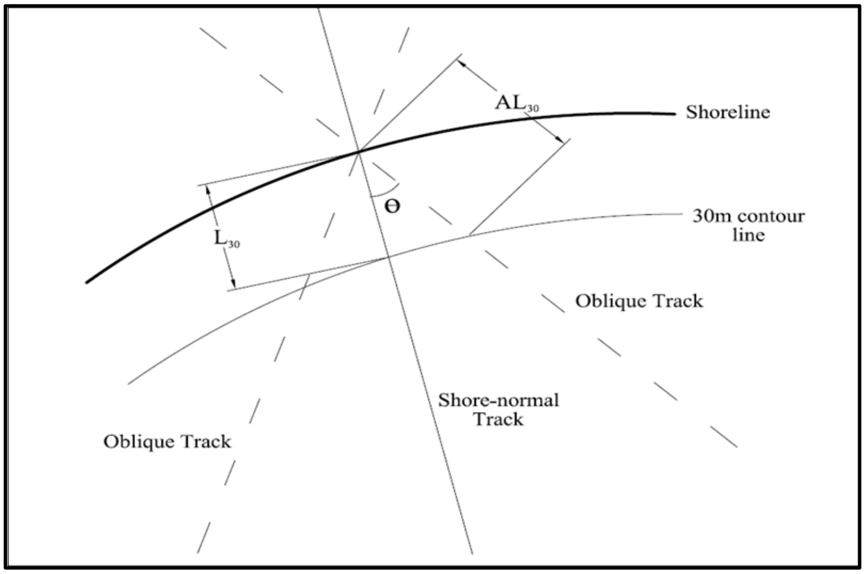

Figure 4.64: Schematic of shelf distances for shore-normal and oblique storm tracks.

To incorporate forward speed, approach angle and sea level rise in the response functions, dimensionless scaled terms have been developed to represent their contributions to surge response. For hurricane forward speed, the hypothesis here is that storms traveling at speeds much higher than a threshold speed allow less time over the shelf for surge generation, while storms traveling at speeds much lower than such threshold speed do not produce sufficient wind stress to generate high surges. While the degree to which this hypothesis holds may be dependent on establishing the appropriate threshold speeds for every section (narrow, intermediate, and wide) of the continental shelf, its performance is tested here using one defined threshold speed for the entire coast.

The formulation developed to account for forward speed in the SRFs is therefore:

$$\Psi_{vf} = F_{L_{30}}\left(\frac{L_{30}}{L_{30-ref}}\right)\frac{v_f}{v_{ref}} \tag{4.3}$$

where:

$$F_{L_{30}}\left(\frac{L_{30}}{L_{30-ref}}\right) = \begin{cases} \dfrac{L_{30}}{L_{30-ref}} & when \quad L_{30} < L_{30-ref} \\ 1 & when \quad L_{30} \geq L_{30-ref} \end{cases} \tag{4.4}$$

Here v_{ref} is the mean value of hurricane forward speed in the Gulf of Mexico, and is established as the threshold forward speed value (5.7 m/s). Physically, Equation (4.3) relates the time available for surge generation for a storm of given speed, to a characteristic time defined as the time it would take for a storm propagating at 5.7 m/s to generate surge over/across a continental shelf section with given width. This dimensionless time (which is implicitly represented by the ratio of velocities) is weighted by the function $F_{L_{30}}$ given in Equation (4.4). Considering that the impact of the shelf width plays a role on the effect of forward speed on surge (as shown in section 4.1; i.e. Figs. 4.4 through 4.7), Equation 4.4 compensates for the differences in surge response trends between narrow shelf regions (here, defined by regions with

$L_{30} < L_{30-ref}$) and wide shelf regions. The linear, relatively steeper surge trends on the narrow shelf region of the coast suggest that because the shelf is not sufficiently wide for surge generation to approach equilibrium, the effect of the varying speeds is more pronounced. In other words, the width of the shelf has a limited impact on surge generation compared to the propagating speed of the storm. Conversely, for sufficiently wide shelf widths, the variation of surge with forward speed seems to decrease (i.e. observed as less steep trends), and tends to approach some asymptote for the very intense storms at very wide shelf regions (Fig 4.7). The magnitude of $F_{L_{30}}$ is therefore always between 0 and 1. The value of L_{30-ref} is 40 km for the Texas coast (Song et al. 2012).

The formulation to account for hurricane approach angle at open coast is based on considering the shelf length covered by a storm approaching the coast at a shore-normal direction L_{30}, in comparison to the actual shelf length covered by a storm approaching the coast at a non-zero angle relative to the shore-normal direction, AL_{30}. Figure 4.64 illustrates the above-described lengths, and shows that for storms rotated away for the shore-normal axis, the actual length across the shelf from the 30 m contour line to the shoreline is:

$$AL_{30} = \frac{L_{30}}{\cos(\theta)} \tag{4.5}$$

The influence of rotating the hurricane wind field by θ may be isolated by normalizing the shore-normal shelf length (L_{30}) by the non-zero orientation shelf length (AL_{30}) to obtain a non-dimensional contribution of the approach angle to surge generation as:

$$\Psi_{\theta} = \frac{L_{30}}{L_{30}/\cos(\theta)} = \cos(\theta) \tag{4.6}$$

No modifications are made to the dimensionless alongshore axis of the current open coast SRFs; however, by incorporating Equations (4.3) and (4.6) in the dimensionless surge axis of the SRFs (Equation 2.8), the modified surge axis of the SRFs is given by Equation (4.7), while the alongshore axis of the SRFs (Equation 4.8) is the same as Equation (2.9).

$$\zeta_2' = \frac{\zeta\gamma}{\Delta p} + m_2(x,x')\left(\frac{P_{far} - c_p}{P_{far} - c_{p-\max}}\right)^{\alpha(x,x')}\left(\frac{R_p / L_{30}(x_O)}{\left[R_p / L_{30}\right]_{ref}}\right)^{\beta(x,x')} + F_{L_{30}}\left(\frac{L_{30}}{L_{30-ref}}\right)\frac{v_f}{v_{ref}} - \cos(\theta) \tag{4.7}$$

$$x' = \frac{(x - x_o)}{R_p} - \lambda(x_o) + a_2 H\left(\frac{(x - x_o)}{R_p} - \lambda(x_o)\right)\left(\frac{R_p}{L_{30}}\right) - F(1 - R')H(1 - R') \tag{4.8}$$

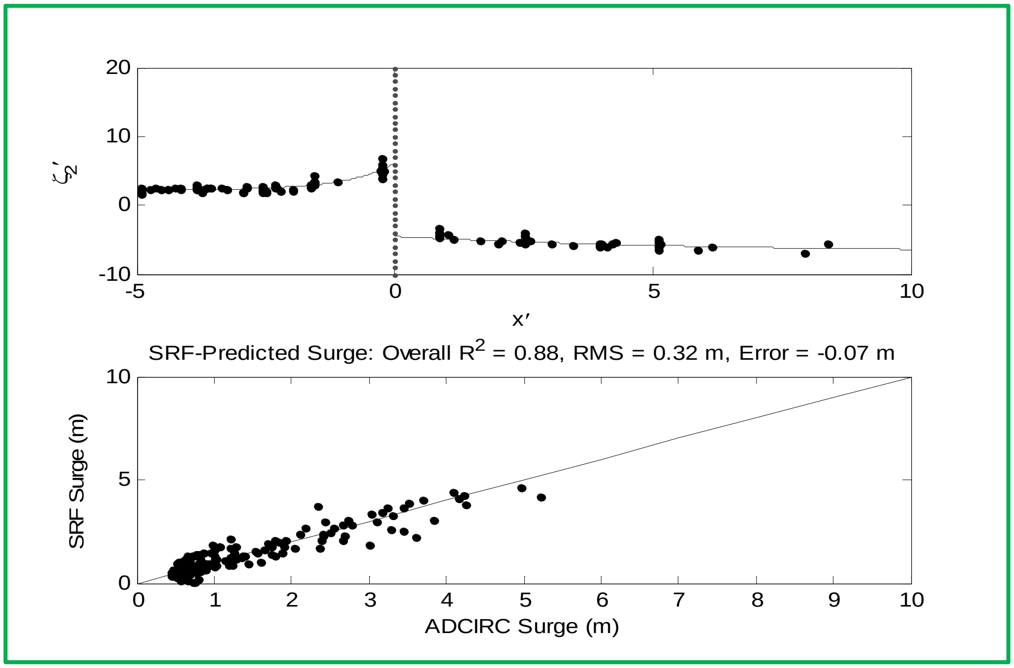

Figure 4.65: Performance of revised SRF at Location 1 of Fig. 4.1. Top pane shows the plot of the dimensionless data using Equations 4.7 and 4.8. Bottom pane shows the back-prediction of surge using the dimensional SRFs.

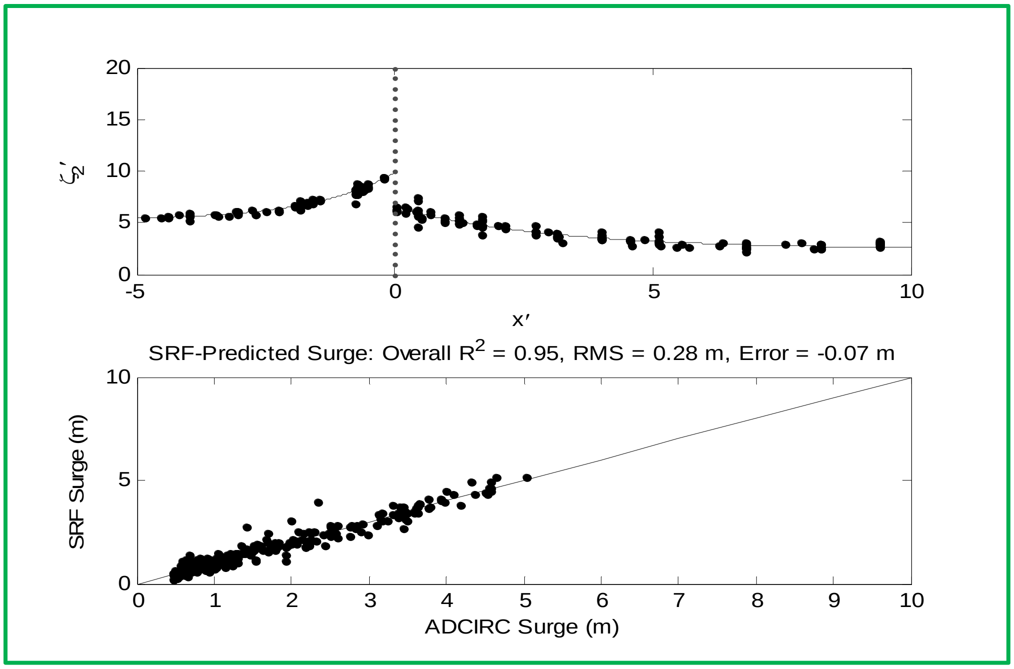

Figure 4.66: Performance of revised SRF at Location 3 of Fig. 4.1. Top pane shows the plot of the dimensionless data using Equations 4.7 and 4.8. Bottom pane shows the back-prediction of surge using the dimensional SRFs.

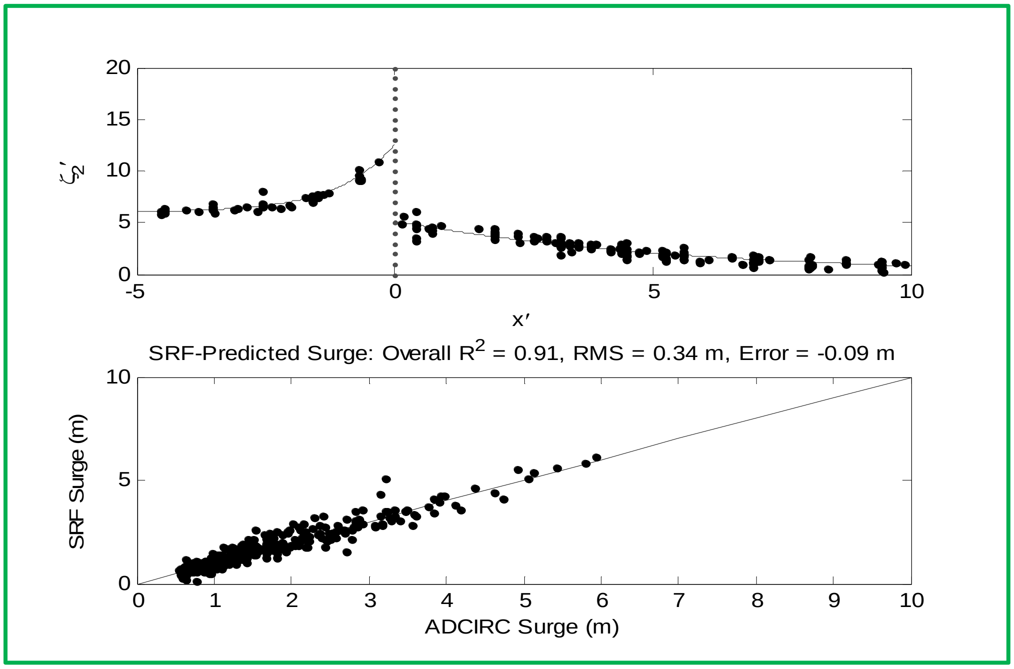

Figure 4.67: Performance of revised SRF at Location 5 of Fig. 4.1. Top pane shows the plot of the dimensionless data using Equations 4.7 and 4.8. Bottom pane shows the back-prediction of surge using the dimensional SRFs.

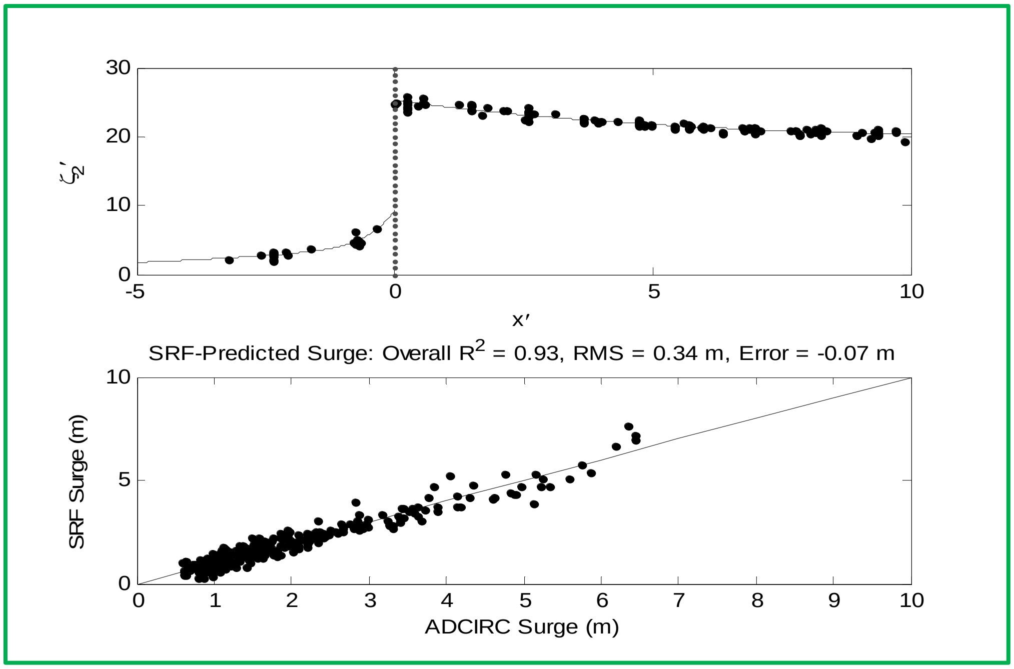

Figure 4.68 Performance of revised SRF at Location 7 of Fig. 4.1. Top pane shows the plot of the dimensionless data using Equations 4.7 and 4.8. Bottom pane shows the back-prediction of surge using the dimensional SRFs.

By splitting up the dimensionless surge distributions into $\zeta_2'(x < 0)$ and $\zeta_2'(x \geq 0)$, the behavior of surge response in the two categories is better represented, and the surge data in these two categories are easily represented by separate model fits.

The plots of surge data using the revised SRFs (Equations 4.7 and 4.8) is shown at eight open coast locations; Figures 4.65 through 4.68 show these results at alternate locations (1, 3, 5 and 7 of Fig. 4.1), whereas the results at locations 2, 4, 6, and 8 are shown in Appendix A (Figs A4.5, A4.6, A4.7 and A4.8, respectively). The upper panes of Figures (4.65) through (4.68) show the collapse of the simulated surge data, while the performance (or back-prediction of surge using the SRFs) of the SRFs is demonstrated in the lower panes, for the respective locations. In order to develop a model for the response functions, the exponential function presented in Equation (4.9) is applied.

$$\Phi' = \begin{cases} u_1 \exp(u_2 x') + u_3 \exp(u_4 x') & when \quad x' < 0 \\ v_1 \exp(v_2 x') + v_3 \exp(v_4 x') & when \quad x' \geq 0 \end{cases} \tag{4.9}$$

At all eight locations, Equation (4.9) is used to fit the dimensionless data and obtain a model for the SRFs. The model coefficients are given in Table 4.2, while the dimensionless scaling coefficients are given in Table 4.3.

Table 4.2: Dimensionless model coefficients for Equation (4.9).

Station	R^2(u/v)	u_1	u_2	u_3	u_4	v_1	v_2	v_3	v_4
1	0.85/0.83	2.335	0.010	3.725	1.123	-7.144	-0.002	2.602	-0.151
2	0.94/0.86	8.297	0.003	3.551	0.608	-3.566	0.008	3.744	-0.522
3	0.96/0.92	5.310	0.002	4.510	0.641	3.930	-0.347	2.602	-0.006
4	0.95/0.91	3.842	-0.008	5.502	0.745	3.826	-0.328	1.179	-0.050
5	0.95/0.88	5.854	-0.006	6.671	0.898	1.030E+04	-0.153	-1.029E+04	-0.153
6	0.93/0.94	1.024	-0.040	6.278	0.748	5.448	-0.186	16.380	0.000
7	0.91/0.93	4.228	0.178	5.158	2.100	5.965	-0.178	19.330	0.000
8	0.81/0.93	8.018	0.446	0.000	0.000	5.856	-0.173	18.650	0.000

Table 4.3: Dimensionless scaling coefficients for Equations (4.4) and (4.5).

Station	a_1	a_2	b_1	b_2	x' range	α	β	m_2
1	0.000	0.000	0.000	-0.898	$x<0$	0.500	0.100	-1.827
					$x \geq 0$	0.100	0.050	8.475
2	0.717	0.004	0.000	0.000	$x<0$	0.100	0.050	-8.559
					$x \geq 0$	0.150	0.050	5.524
3	1.555	-0.244	0.000	0.000	$x<0$	0.100	0.050	-5.469
					$x \geq 0$	0.150	0.050	-2.128
4	0.000	0.341	0.000	0.000	$x<0$	0.200	0.000	-4.079
					$x \geq 0$	0.000	1.000	-0.577
5	0.000	0.000	0.000	0.000	$x<0$	0.200	0.000	-6.054
					$x \geq 0$	0.000	1.000	0.294
6	0.000	0.000	0.000	-2.148	$x<0$	1.000	0.100	-1.185
					$x \geq 0$	0.005	0.000	-16.468
7	0.000	0.000	0.000	-0.342	$x<0$	1.000	0.100	-1.842
					$x \geq 0$	0.005	0.000	-19.479
8	0.000	0.000	0.000	0.000	$x<0$	1.000	0.100	-2.617
					$x \geq 0$	0.005	0.000	-18.828

The dimensionless surge plots show that with the revised version of the SRFs, the dimensionless surges collapse better than with the previous SRF version; the scatter due to outliers is reduced at most locations, allowing the same model form (Equation 4.9) used to fit the original data in Song et al. (2012) to be used here. The back-prediction of surges also shows that the revised SRFs have the potential to estimate surge with a decent amount of accuracy. Root mean square errors at the eight locations range from a minimum of 0.28 m to a maximum of 0.34 m. In addition to the fact that the inclusion of forward speed and approach angle to the SRFs allows the evaluation of additional scenarios (regarding extreme value statistics), more accuracy has been achieved at all but one location – location 1. The performances of the SRFs from Song et al. (2012) and the revised SRFs discussed here are compared at locations 1 through 8 of Fig. 4.1, as shown in Table 4.4. Comparisons are based on 98.5% of all data considered – outliers constituting about 1.5% of all data are excluded from comparisons and from all open coast SRF plots shown.

A 3.23% reduction in accuracy is seen at location 1 using the revised SRFs. This finding indicates that at least one of the formulations applied to improve the SRFs is not needed. On further investigation it was found that ignoring the approach angle term ($\cos(\theta)$) in the SRFs yields an improvement in error (root-mean-square) from 0.32 m to 0.29 m at this location. This improvement suggests (in reference to the formulation for approach angle) that at open coast locations with shelf widths as small as that at location 1 (23 km), the correction applied for approach angle is excessive compared to the surge variation with approach angle at this location. Figure 4.69 shows the SRF performance at location 1, with the approach angle term ignored. To account for this observation at location 1 regarding the approach angle formulation, the $\cos(\theta)$ term needs to be appropriately scaled with a coefficient that perhaps will depend on characteristics of the continental shelf along the coast – this task is part of ongoing research, and is not presented here.

Table 4.4: Comparison of SRF errors.

Station	Root-mean-square error (m)		Mean Error (m)		Overall R^2	
	Song et al. (2012)	Revised SRF	Song et al. (2012)	Revised SRF	Song et al. (2012)	Revised SRF
1	0.31	0.32	-0.07	-0.07	0.88	0.88
2	0.33	0.31	-0.08	-0.08	0.89	0.91
3	0.32	0.28	-0.07	-0.07	0.93	0.95
4	0.34	0.32	-0.08	-0.08	0.92	0.93
5	0.37	0.34	-0.10	-0.09	0.89	0.91
6	0.31	0.29	-0.07	-0.07	0.93	0.94
7	0.37	0.34	-0.07	-0.07	0.92	0.93
8	0.34	0.33	-0.06	-0.06	0.92	0.93

Table 4.5: SRF Improvement due to inclusion of v_f and θ.

Station	Difference in root-mean-square errors (m) Previous - Revised	% Improvement
1	-0.01	-3.2
2	0.02	6.1
3	0.04	12.5
4	0.02	5.9
5	0.03	8.1
6	0.02	6.5
7	0.03	8.1
8	0.01	2.9

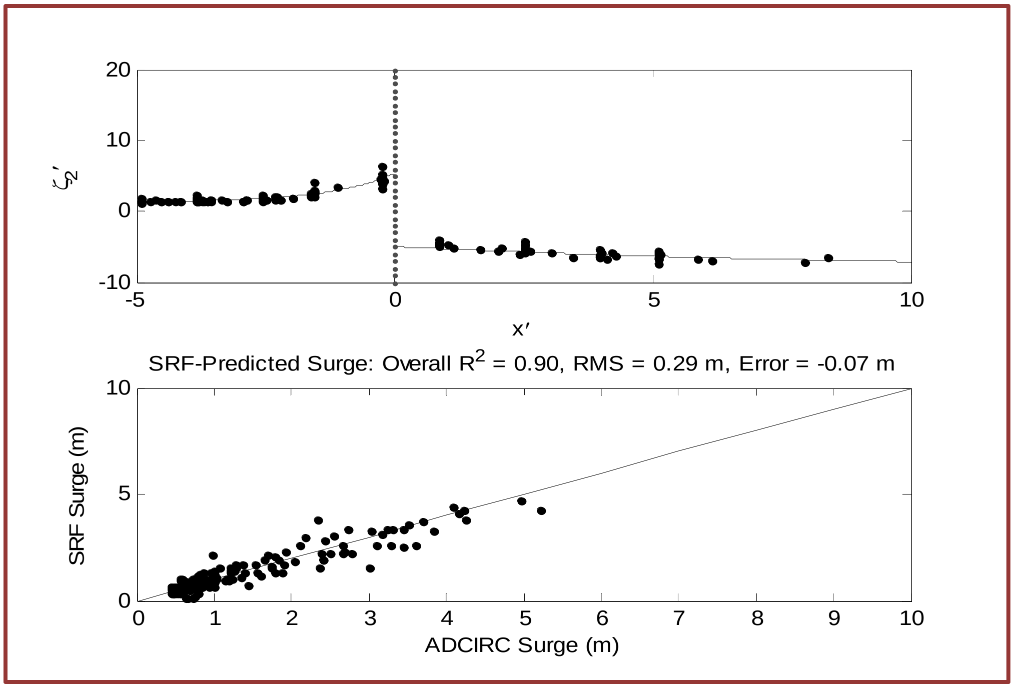

SRF-Predicted Surge: Overall R^2 = 0.90, RMS = 0.29 m, Error = -0.07 m

Figure 4.69: Performance of revised SRFs at Location of 1 of Fig. 4.1, with approach angle term of Equation 4.7 ignored. Top pane shows the plot of the dimensionless data using Equation 4.7 less $\cos(\theta)$, and 4.8. Bottom pane shows the back-prediction of surge using the dimensional SRFs.

The percentage improvements presented in Table 4.5 reflect the overall performance of the formulations for forward speed and approach angle (Equations 4.3 through 4.6). A maximum overall percentage improvement of 12.5% is obtained at location 3. On close observation, some additional scatter is seen in the revised SRF surge prediction plots (bottom panes of Figs. 4.65 through 4.68) especially for low values of ADCIRC surge. This warranted further investigation into the errors associated with different ranges of estimated surge values. Figures 4.70 through 4.77 show the comparison between the revised SRF form and that of Song et al. (2012) for different ranges of surge – these results show that at locations 2, 3, 7 and 8 corresponding to narrow-to-intermediate (i.e. locations 2 and 3) and wide (locations 7 and 8) shelf width regions, the revised form of the SRFs performs better than the Song et al. (2012) version in predicting very high (5 m or greater) surge events. At location 1 (narrow shelf width region), the previous version of the SRFs clearly performs better than the revised SRFs, predicting surges with smaller errors over nearly all ranges of surge values in the data. At locations 4 and 5, the revised

SRFs mostly performs worse than the previous formulation. At location 6, for surges between 2 to 6 m, the revised SRF estimates surge with smaller errors than the previous version; however, for the highest surge values (6 to 7m), the previous version of the SRFs has a better performance in surge estimation at this location. This seemingly inconsistent dominance of the revised SRFs over the previous version (by location) led to further investigation into the range of surge values over which the revised model performs better.

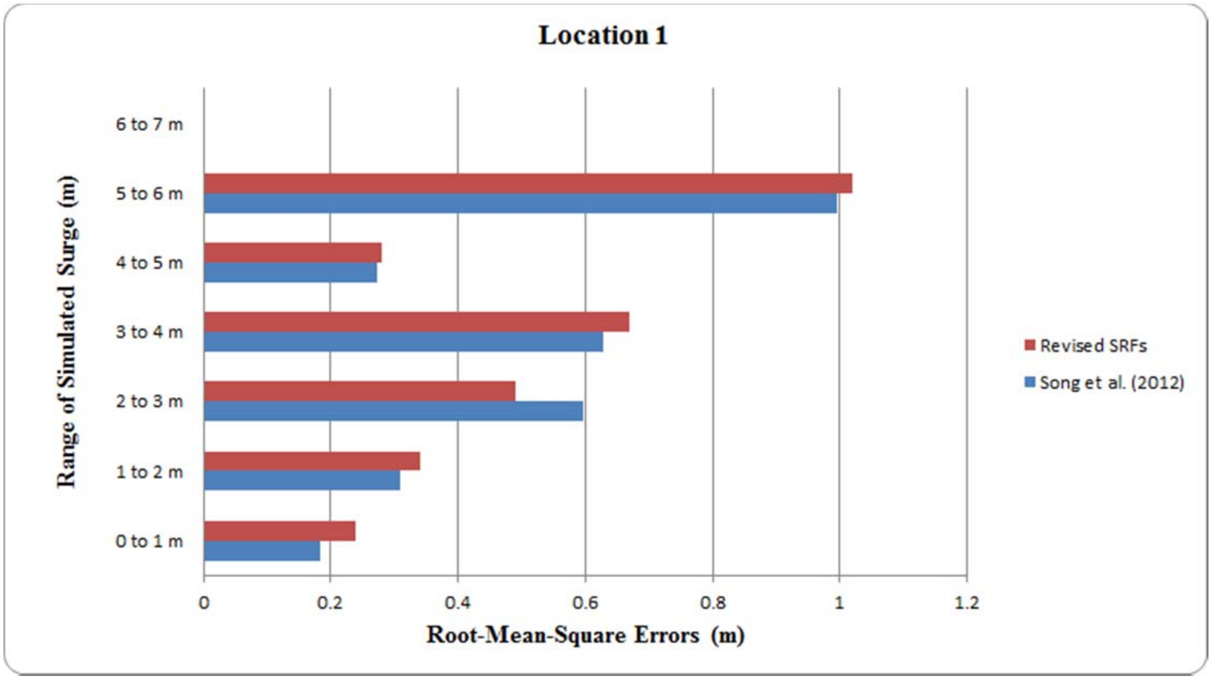

Figure 4.70: Comparison of root-mean-square errors for different ranges of surge estimates at location 1.

To identify the range of surge values over which SRF improvement is significant, six thresholds are defined. These are:

- surge values greater than or equal to 2 m,
- surge values greater than or equal to 3 m,
- surge values greater than or equal to 4 m,
- surge values greater than or equal to 5 m, and
- surge values greater than or equal to 6 m.

For each case of defined surge threshold (ζ_{thresh}), the number of bins (at increments of 1 m as shown in Figs. 4.70 through 4.77) with surge equal to or above the threshold value is determined. Among the bins with surge equal to or above the threshold value, the bins where the root mean square errors of the revised SRF form are less than those of Song et al. (2012) are counted. A simple ratio of the number of bins in which the revised SRF form shows dominance (i.e. has smaller errors), to the total number of bins satisfying the threshold value of surge, is calculated. The results of this assessment are presented in Table 4.6.

Table 4.6: Comparison of SRF performance by surge bins.

ζ_{thresh} (m)	Total number of bins with $\zeta \geq \zeta_{thresh}$	Number of bins with $RMS_{\mathrm{Re}vised} < RMS_{\mathrm{Pr}evious}$	% Dominance = 100*(column 3 / column 2)
2.0	35	23	65%
3.0	27	18	66%
4.0	19	13	68%
5.0	11	7	63%
6.0	3	2	66%

Without excluding any data based on thresholds of surge, the total number of surge bins over the 1 m to 7 m range is 51. The total number of bins with surge above 2 m is 35 – this represents 68% of the surge magnitudes in the data set. Table 4.6 shows that the revised SRF model generally estimates surge with higher accuracy than the previous form for storms that generate up to, and above 2 m of surge. For extreme value analysis, the extreme events are the most important. This result therefore shows that accounting for the influences of v_f and θ has made the SRFs for the open coasts more robust in surge estimation, for application to extreme value analysis.

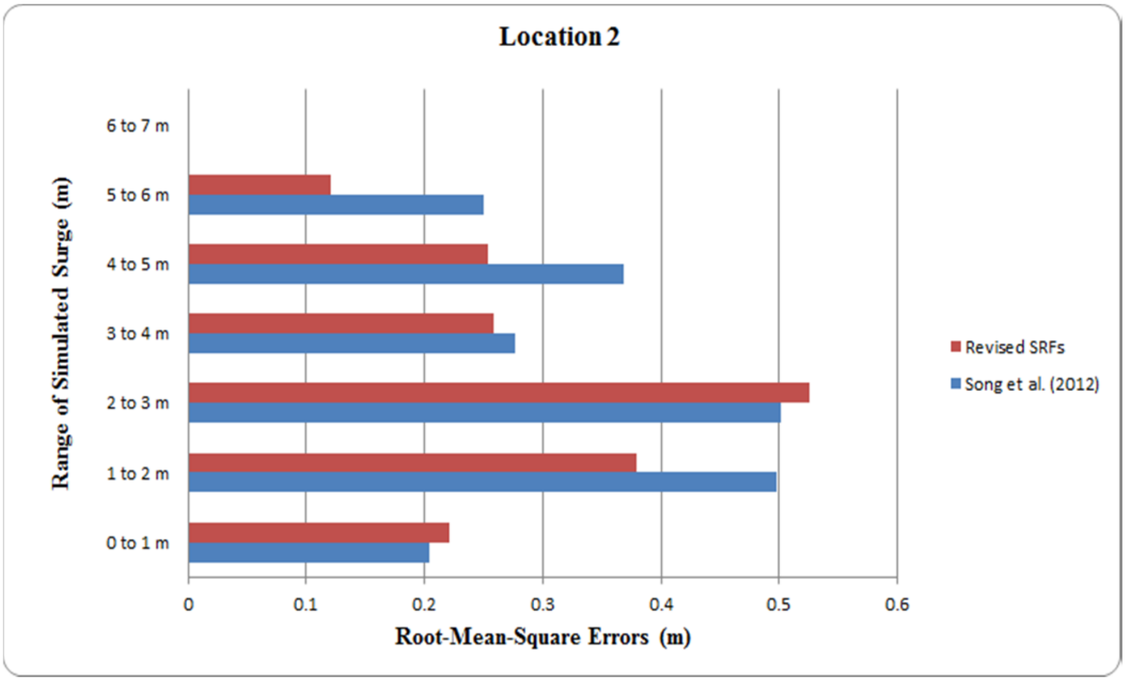

Figure 4.71: Comparison of root-mean-square errors for different ranges of surge estimates at location 2.

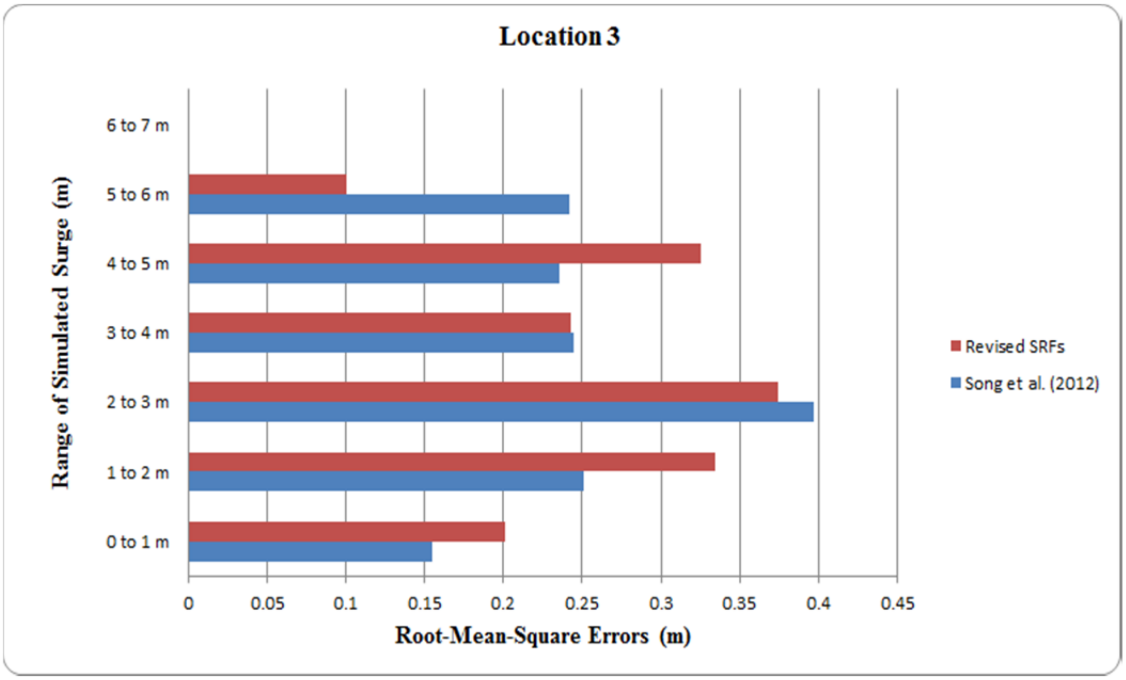

Figure 4.72: Comparison of root-mean-square errors for different ranges of surge estimates at location 3.

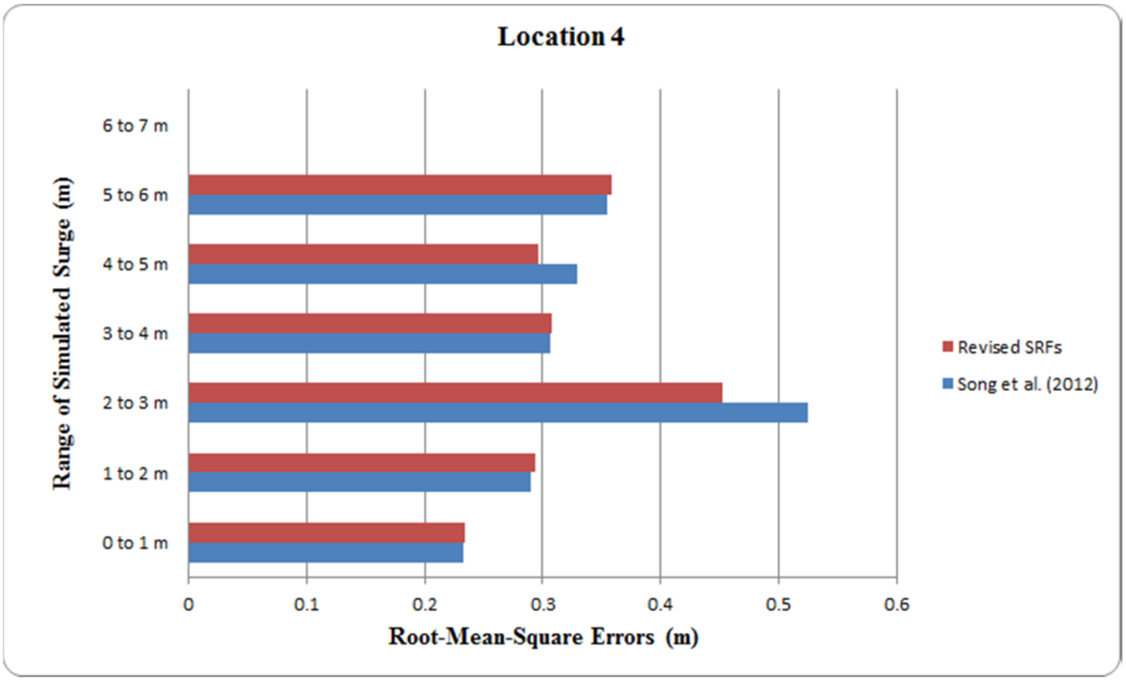

Figure 4.73: Comparison of root-mean-square errors for different ranges of surge estimates at location 4.

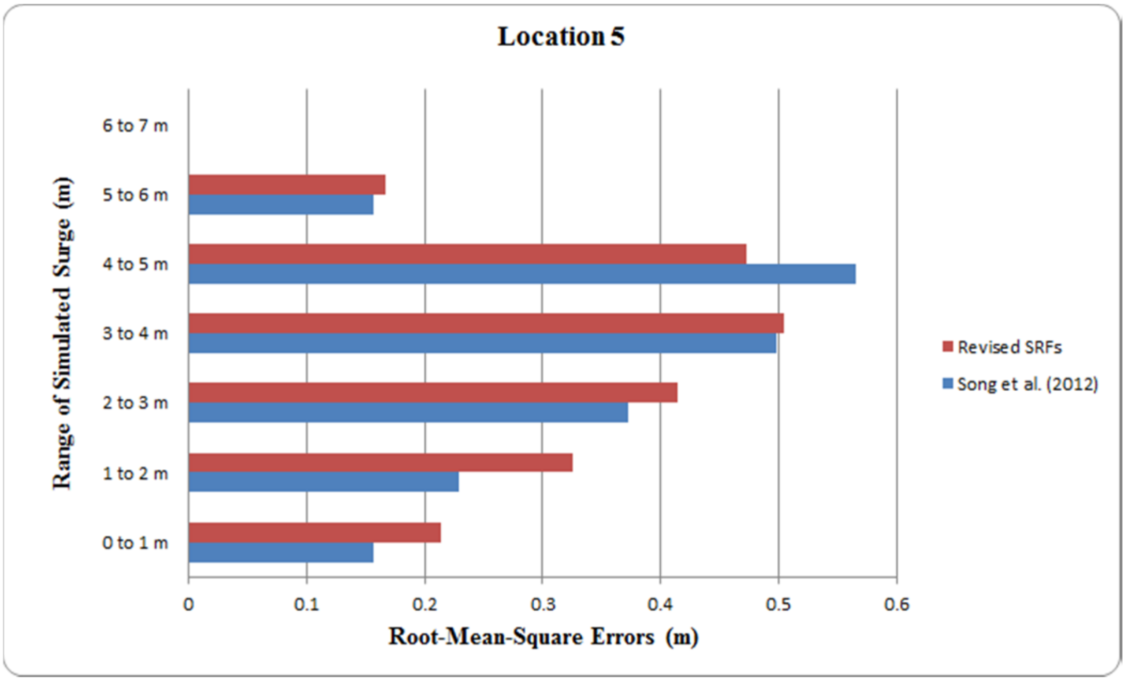

Figure 4.74: Comparison of root-mean-square errors for different ranges of surge estimates at location 5.

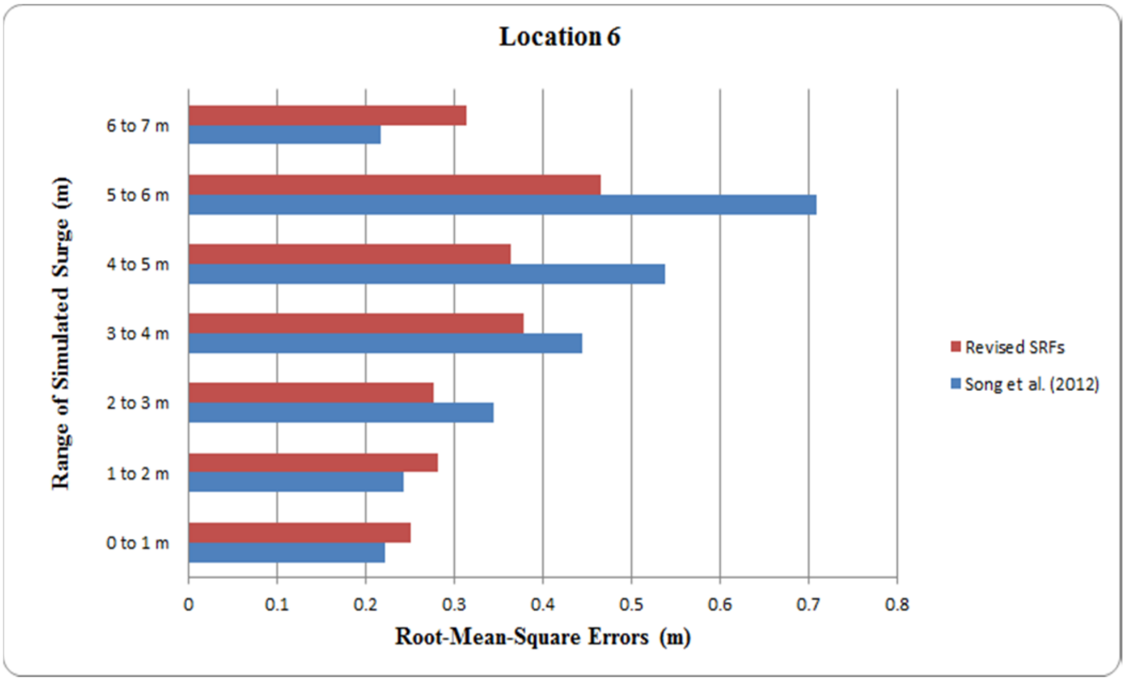

Figure 4.75: Comparison of root-mean-square errors for different ranges of surge estimates at location 6.

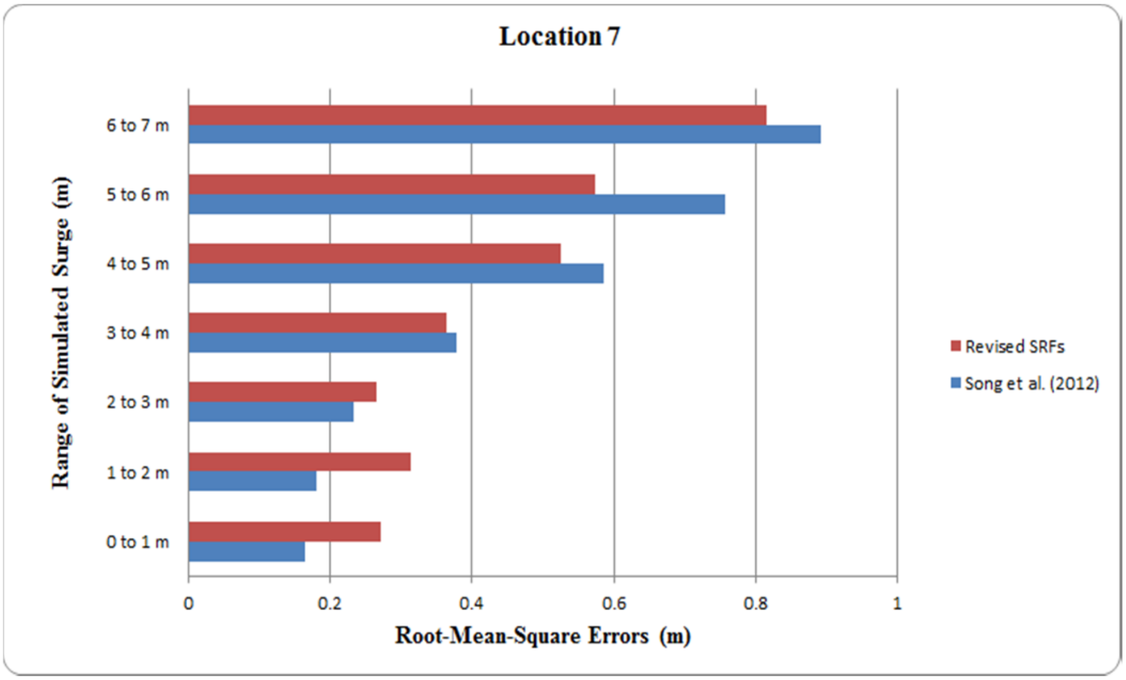

Figure 4.76: Comparison of root-mean-square errors for different ranges of surge estimates at location 7.

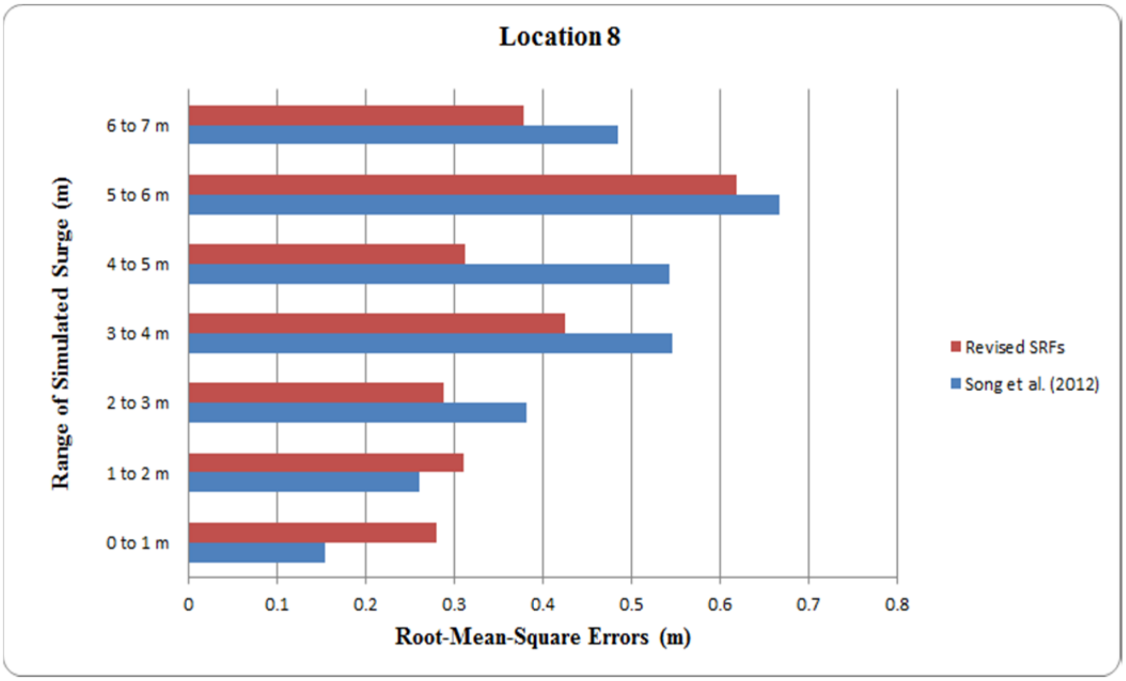

Figure 4.77: Comparison of root-mean-square errors for different ranges of surge estimates at location 8.

To incorporate sea level rise (SLR) in the response functions, a dimensional correction is applied. Having observed strong linear trends of surge with respect to SLR at open coast locations, the correction applied is a straight line equation at every location of interest. The linear relationship between surge and SLR (as deduced from the trends) is:

$$\eta_s - SLR = k\zeta_o + l \tag{4.10}$$

where:

$\eta_s - SLR = \zeta$ (i.e. actual surge with SLR considered),

k is the slope of the linear fit to the $(\eta_s - SLR)$ versus ζ_o data at a location of interest, and:

l is the intercept of the linear fit to the $(\eta_s - SLR)$ versus ζ_o data at the same location of interest.

The dimensional surge obtained from Equation 4.7 is:

$$\zeta = \zeta_o = \frac{\Delta p}{\gamma}\left(\Phi' - \left[m_2(x,x')\left(\frac{P_{far} - c_p}{P_{far} - c_{p-\max}} \right)^{\alpha(x,x')} \left(\frac{R_p \big/ L_{30}(x_O)}{\left[R_p \big/ L_{30} \right]_{ref}} \right)^{\beta(x,x')} \right] - H\left(\frac{L_{30}}{L_{30-ref}} \right) \frac{v_f}{v_{ref}} + \cos(\theta) \right) \tag{4.11}$$

Equation (4.11) shows that the dimensional SRF surge is the equivalent of ζ_o, as it contains no effect of SLR. The final water level, with SRL correction is given as:

$$\eta_s = k\zeta_o + l + SLR \tag{4.12}$$

For a perfectly linear trend of surge versus SLR, k =1, and l =0, so that Equation (4.12) becomes:

$$\eta_s(k = 1, l = 0) = \zeta_o + SLR \tag{4.13}$$

and if $SLR = 0$, then:

$$\eta_s(k = 1, l = 0, SLR = 0) = \zeta_o \tag{4.14}$$

This linear formulation will be applied to adjust dimensional surge for the influence of SLR, while generating surge scenarios for extreme value analysis. By using this simplified form of adjustment for the effect of SLR in the SRFs, unnecessary analysis of data is avoided in the developing the SRFs, and excessive computational burden is avoided in generating SLR scenarios for extreme value analysis.

4.4 Surge Response Functions with v_f, θ and SLR for Bays

4.4.1 SRF Formulation for Bays

To incorporate the effects of v_f, θ and SLR in the SRFs for bays, Katyal's (2009) formulation is modified. Dimensionless terms are developed to account for the influences of these parameters, based on findings in the surge trends. The dimensionless surge axis is discussed first, followed by the dimensionless spatial axis. For the influence of forward speed, the formulation is based on the premise that depending on the speed of the storm, surge may or may not be fully developed in the bay. In other words, relatively fast storms may not allow sufficient time for surge to build-up in the bays, as would rather slower storms. The extent to which this holds may depend on the actual time it takes for surge to fully develop inside a given bay. Weisberg and Zheng (2006) presented an expression (Equation 4.15) for the time required for mass distribution to be effected to steady state within a rectangular bay, when acted on by steady axially directed wind stress, as:

$$T_b = \frac{{L_b}^2 \beta}{\pi g h_o} \tag{4.15}$$

where:

L_b = length of the bay along its major axis,

β = turbulent resistance coefficient (given as$1.5 \times 10^{-3} s^{-1}$),

g = acceleration due to gravity (9.81m/s), and

h_o = the average still water depth in the bay

From Equation (4.15), a characteristic velocity is deduced (Equation 4.16) as:

$$v_b = \frac{L_b}{T_b} \tag{4.16}$$

Equation (4.16) assumes that the bay is rectangular, and that the winds are blowing steadily along an axis parallel to the major axis of the bay; it suggests that for a given bay, a storm traveling at a speed of v_b and oriented such that its wind stresses act axially on the bay is expected to cause full mass distribution inside a rectangular bay. Comparatively, Matagorda Bay is closer in shape to a rectangular bay than Corpus Christi Bay. While the shapes of Corpus Christi and Matagorda bays may not be considered rectangles, this principle is assumed to hold for the two bays, and is applied in accounting for the influence of forward speed in the SRFs. The dimensionless scaling term for forward speed is:

$$\Psi_{v_f} = \left(\frac{v_b}{v_f}\right) \qquad (4.17)$$

Equation (4.17) thus gives the relative effect of a storm's speed on mass distribution inside the bay.

The influence of approach angle is incorporated in the bay SRFs in a similar way to that of the open coast SRFs (i.e. as a function of *AL₃₀* – Fig. 4.78):

$$\Psi_\theta = \frac{L_{30}}{L_{30} \big/ \cos(\theta)} = \cos(\theta) \qquad (4.18)$$

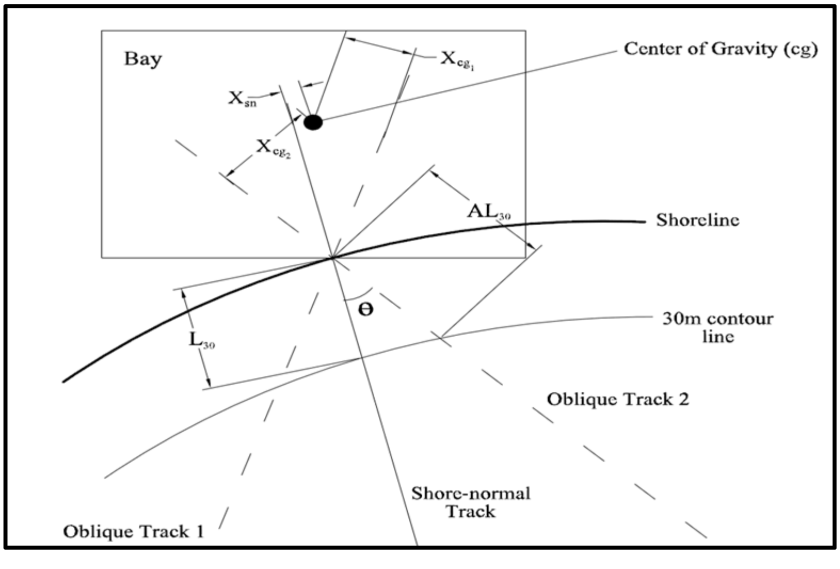

Figure 4.78: Schematic showing X_{cg} for tracks of different orientations.

Katyal (2009) considered a term for the influence of storm size, that was applied conditionally (Equation 2.13, repeated here as Equation 4.19 for quick reference). The revised form of the SRFs uses a different term (Equation 4.20) in the dimensionless surge axis to account for the influence of storm size, which gives a better distribution of the surge data of varying R_p.

$$F_{\zeta'}\left(\Delta p, R_p, \zeta, S_b\right) = \begin{cases} \zeta c R_p & for \quad \dfrac{\Delta p}{\gamma} < 0.9m \,\&\, R_p > S_b \\ 1 & Otherwise \end{cases} \tag{4.19}$$

$$\Psi_{R_p} = \left(\frac{R_p}{D_{cg-\max}}\right) \tag{4.20}$$

where:

$D_{cg-\max}$ is the maximum distance from the center of gravity of the bay, to the shoreline of the bay; it is a characteristic measure of the farthest distance through which water mass will move inside the bay. The dimensionless surge axis of the SRFs for bays is:

$$\zeta' = \left(\frac{\zeta\gamma}{\Delta p}\left[\cos(\theta)\right]^{\mu(x')} - m_x \frac{\Delta p}{\gamma}\right)\left(\kappa_b \frac{R_p}{D_{cg-\max}}\right) + \left(c\frac{v_b}{v_f}\right) + \kappa(x') \tag{4.21}$$

where:

$\mu(x')$ is a dimensionless constant varying by x' (defined in Table 4.7),

m_x is a location dependent fit coefficient,

κ_b is a shape factor (defined in Table 4.7),

$\kappa(x')$ is a shift parameter (defined in Table 4.7),

S_b is the characteristic size of each bay, measured at the shoreline as half the width of the bay,

X_O is the distance from a reference point (Fig. 4.79) sited in front of each bay, to the landfall location of each storm,

c is a dimensionless constant, defined as $\frac{v_{f_{\min-ref}}}{v_{f_{\max-ref}}}$, with $v_{f_{\min-ref}}$ being a representative low forward speed (2.25 m/s) and $v_{f_{\max-ref}}$ being a representative high forward speed (11.8 m/s), for the region. Here c is calculated as 0.19 for both bays.

The reference point for X_O is the point of intersection between the shoreline and a shore-normal axis passing through the center of gravity of the bay (Fig. 4.79). For Corpus Christi Bay and Matagorda Bay the coordinates of the respective reference points are:

- Corpus Christ Bay: Longitude = -97.14 ^{o}, Latitude = 27.71^o
- Matagorda Bay: Longitude = -96.25 ^{o}, Latitude = 28.45^o

The values of $\mu(x')$, $\kappa(x')$, κ_b and L_b are summarized in Table 4.7.

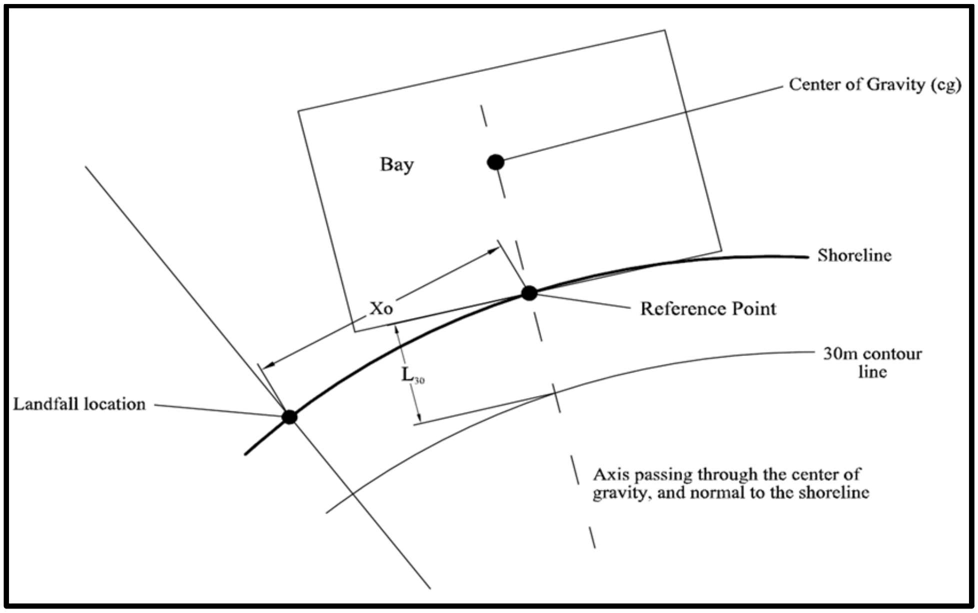

Figure 4.79: Schematic showing X_o.

Table 4.7: Values of ζ' coefficients for Corpus Christi and Matagorda Bays.

Parameter	Bay			
	Corpus Christi	Corpus Christi	Matagorda	Matagorda
	$x' < 0$	$x' \geq 0$	$x' < 0$	$x' \geq 0$
$\mu(x')$	0.0	1.0	1.0	1.0
$\kappa(x')$	$\left(\frac{S_b}{X_O}\right)^{\omega}$	0.0	0.0	$\left(\frac{S_b}{X_O}\right)^{\omega}$
ω	1.0	0.0	0.0	2.0
κ_b	1.0	1.0	B/L_b	B/L_b
c	0.19	0.19	0.19	0.19
L_b	40 km		50 km	
h_0	3.0 m		2.5 m	

In Table 4.7, the value of $\mu(x' < 0)$ for Corpus Christi Bay differs from $\mu(x' \geq 0)$ and the values for Matagorda Bay. The value of this term being equal to zero means that the approach angle correction was not applied for this group of storms - it was observed that by turning off the influence of the $\cos(\theta)$ term, better results (more than 10% improvement at several stations) were obtained. Storms in this group make landfall on the right side of Corpus Christi Bay, and are predominantly characterized by θ less than 45^{o}, as opposed to storms in the $x' < 0$ group which are predominantly characterized by θ much greater than 45^{o}. Obtaining better results when the value of $\mu(x' < 0)$ is set equal to zero for this class of storms in Corpus Christi Bay, implies that the formulation for approach angle (Equation 4.18) does not effectively describe the impact of approach angle on the bay, for this class of storms. Perhaps for this region, surge variation with approach angle in the bay is more dependent on the minimum distance from the storm track to the center of gravity of the bay, than it is on the actual length the storm traverses as it crosses the continental shelf. This hypothesis was not explored sufficiently to be confirmed and presented in this dissertation – it is part of ongoing research.

Another observation to make in comparing the parameters in Table 4.7 for the two bays, is that the $\left(\frac{S_b}{X_O}\right)^{\omega}$ term is applied in reverse pattern (applied to $x' < 0$ for Corpus Christi Bay, and to $x' \geq 0$ for Matagorda Bay). This dimensionless shift parameter was necessitated by an observed separation in the data from the same tracks (Figs. 4.80) in Corpus Christi and Matagorda Bays which made it otherwise difficult to obtain a good model fit for the SRF data, hence inducing significant errors in the SRF surge back-predictions. Figures 4.81 and 4.82 show the separation of dimensionless surge distributions for these tracks (tracks 4, 5 and 6 for Corpus Christi Bay, - same as tracks 1, 2 and 3 for Matagorda Bay).

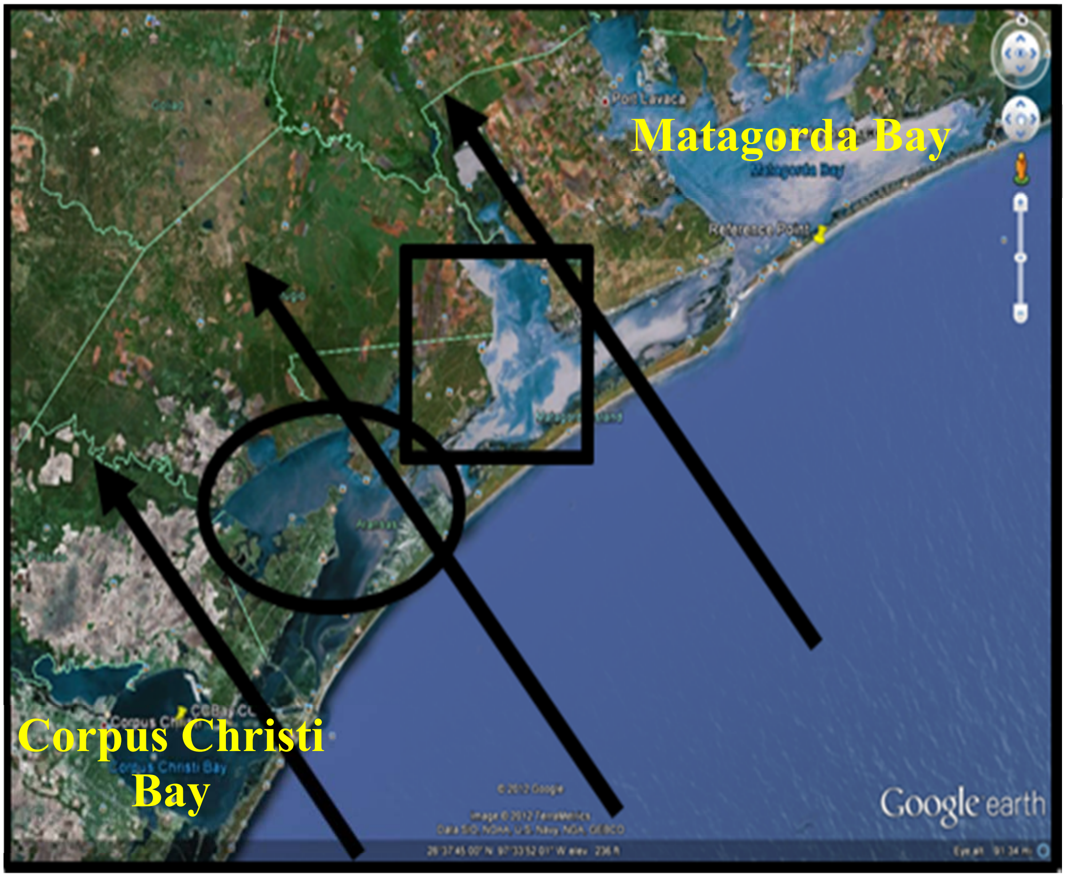

Figure 4.80: Copano Bay (oval area) and San Antonio Bay (boxed area) in-between Corpus Christi and Matagorda Bays. From the southwest corner of the figure, the first track is track 4 for Corpus Christi Bay, followed by tracks 5 and 6. The same three tracks are tracks 1 (first from southwest corner of figure), 2 and 3 for Matagorda Bay analysis. Picture is captured from Google earth.

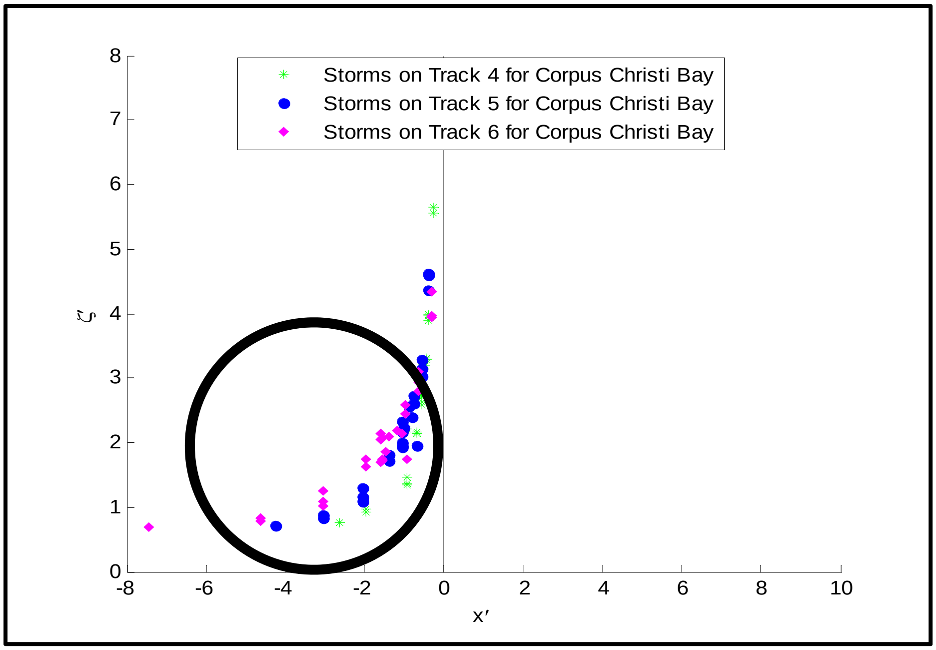

Figure 4.81: Plot of dimensionless SRFs using Equation 4.21 without the $\kappa(x')$ term, and Equation 4.22. Storms are on Tracks 4, 5 and 6 of Corpus Christi Bay (Fig. 4.18). Circled portion of plot shows scatter incurred when $\kappa(x')$ is excluded in Equation 4.21.

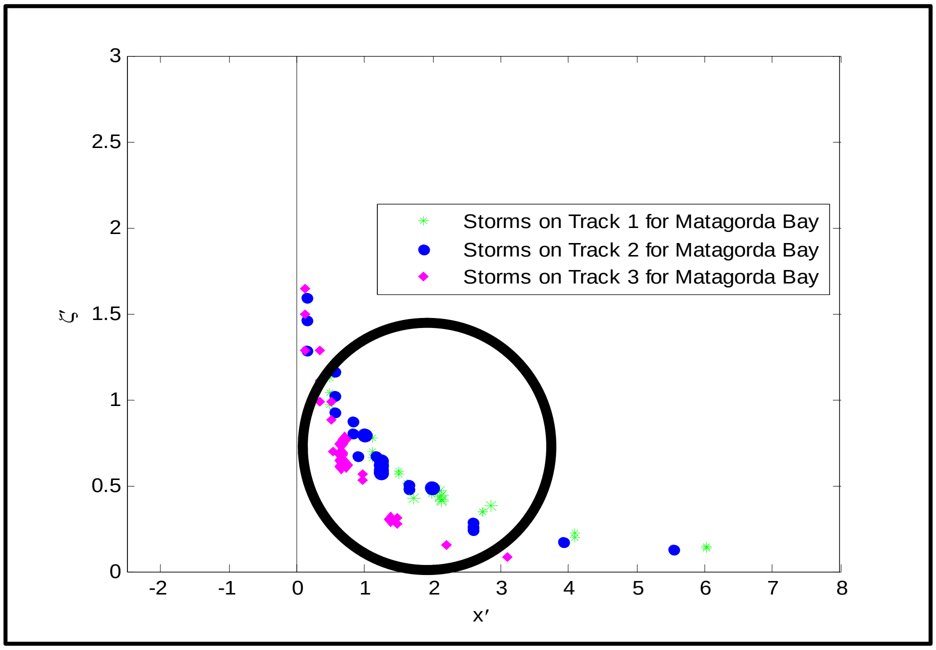

Figure 4.82: Plot of dimensionless SRFs using Equation 4.21 without the $\kappa(x')$ term, and Equation 4.22. Storms are on Tracks 1, 2 and 3 of Matagorda Bay (Fig. 4.19). Circled portion of plot shows scatter incurred when $\kappa(x')$ is excluded in Equation 4.21.

Tracks 4, 5 and 6 for Corpus Christi Bay are the same as tracks 1, 2 and 3 for Matagorda Bay - they make landfall between the two bays, in the region of Copano Bay and San Antonio Bay (Fig. 4.80). It was suspected that the presence of Copano and San Antonio Bays in this region impacted the amount of surge generated by storms on these tracks. On investigation, water level maps (Figs. 4.83 through 4.85) of typical storms on these tracks show a significant amount of surge in Copano and San Antonio Bays. The presence of a significant amount of surge in Copano and San Antonio Bays, and the pattern of data separation in Figs. 4.81 and 4.82 suggested that the separation in surge data is a function of proximity of landfall location to the entrance of the bay. Informed by this observation, the shift parameter is developed to account for the relative closeness of the storm to the entrance of the bay. The term is scaled by the coefficient ω, which is determined by inspection. Strong winds for storms on these tracks are directed toward Matagorda Bay, while the weaker portions of their wind fields are toward Corpus Christi Bay. It is not surprising then that the magnitude of ω needed to correct for this effect adequately is different for Corpus Christi and Matagorda Bays. In the current formulation, the shift term is only applied to storms in the domain described for the two bays.

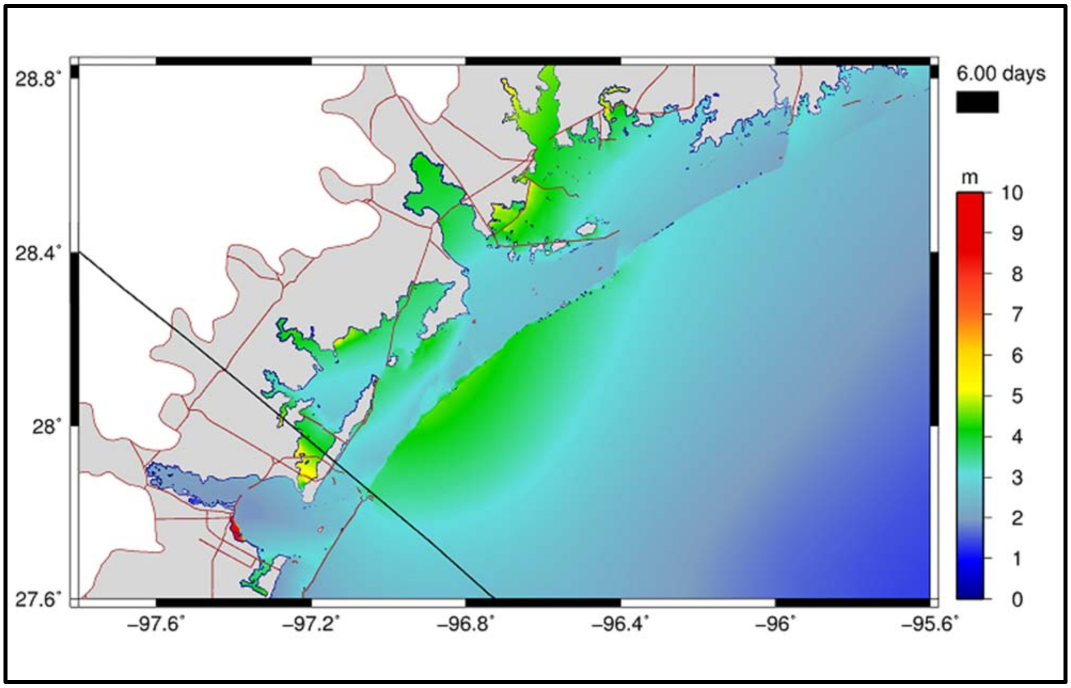

Figure 4.83: Surge map for storm on track 4 of Corpus Christi Bay. Black line indicates storm track. Track 4 of Corpus Christi Bay is the same as track 1 for Matagorda Bay.

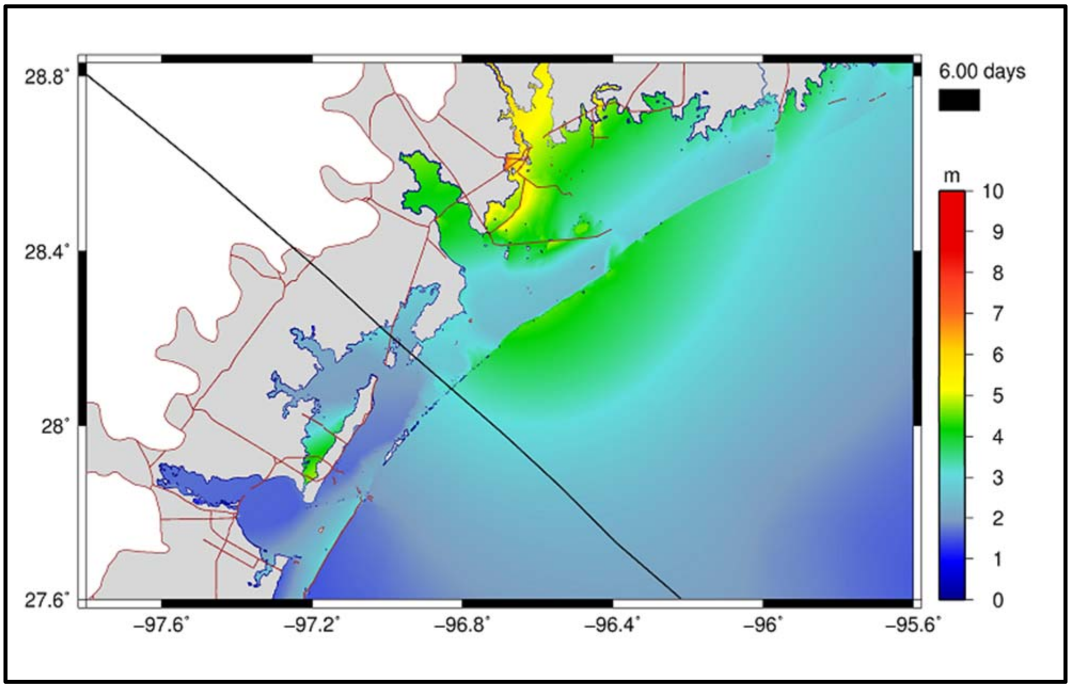

Figure 4.84: Surge map for storm on track 5 of Corpus Christi Bay. Black line indicates storm track. Track 5 of Corpus Christi Bay is the same as track 2 for Matagorda Bay.

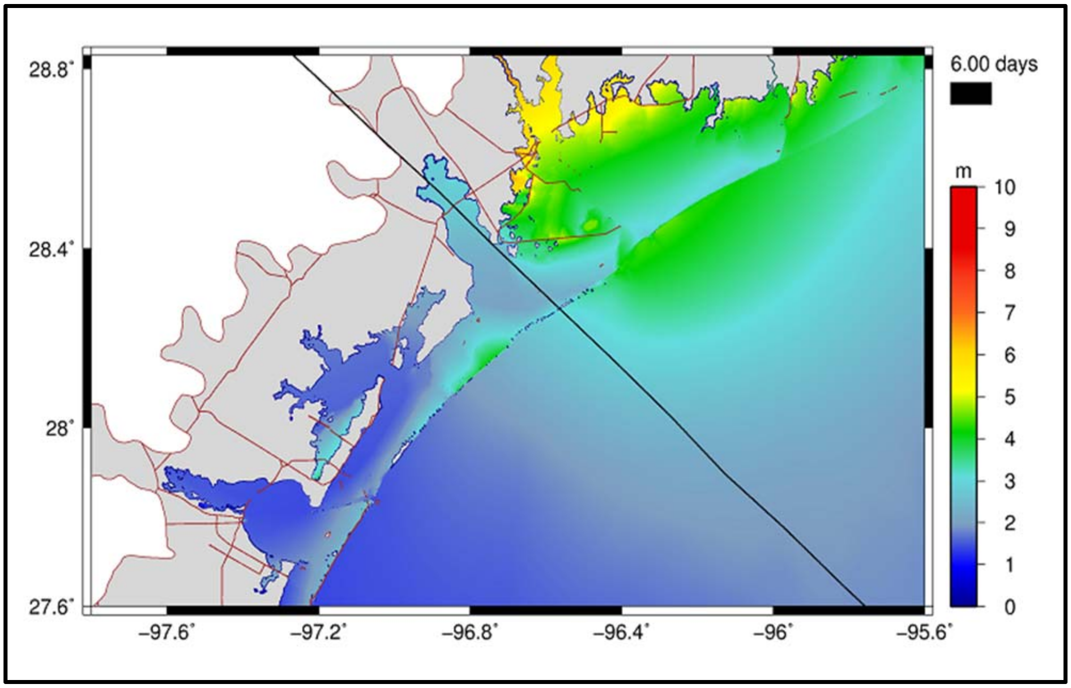

Figure 4.85: Surge map for storm on track 6 of Corpus Christi Bay. Black line indicates storm track. Track 6 of Corpus Christi Bay is the same as track 3 for Matagorda Bay.

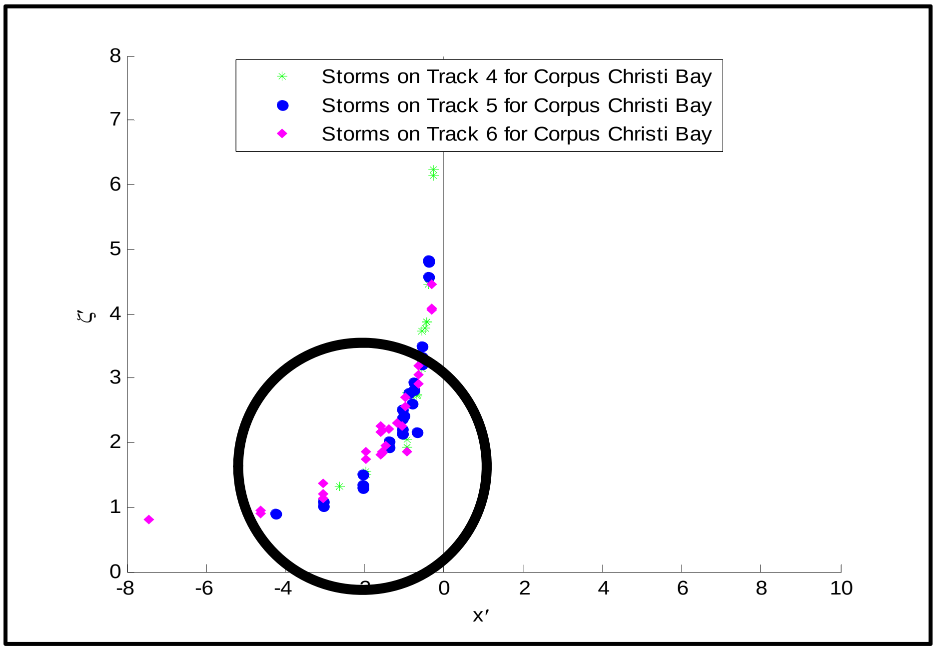

Figure 4.86: Plot of dimensionless SRFs using Equation 4.21 with the $\kappa(x')$ term, and Equation 4.22. Storms are on Tracks 4, 5 and 6 of Corpus Christi Bay (Fig. 4.18). Circled portion of plot shows scatter incurred when $\kappa(x')$ is included in Equation 4.21.

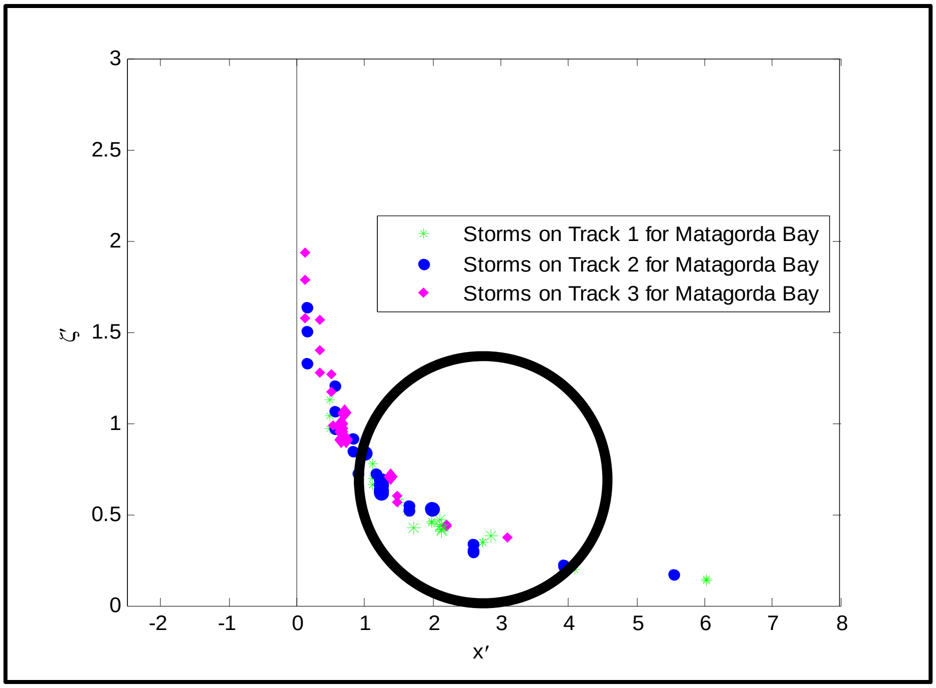

Figure 4.87: Plot of dimensionless SRFs using Equation 4.21 with the $\kappa(x')$ term, and Equation 4.22. Storms are on Tracks 1, 2 and 3 of Matagorda Bay (Fig. 4.19). Circled portion of plot shows scatter incurred when $\kappa(x')$ is included in Equation 4.21.

On squaring the shift term in Matagorda Bay ($\omega = 2$), better results were obtained; suggesting that only a relatively small contribution of this effect is required to correct for the separation in surge distributions of the different tracks, at majority of the stations within the bay. Figures 4.86 and 4.87 show the reduction in scatter achieved in the dimensionless SRF data for Corpus Christi and Matagorda Bays respectively by applying the shift parameter; the SRF results improved by up to 30% in some locations within Matagorda and Corpus Christi Bays.

The shape factor is applied to account for the influence of the bay's shape on mass distribution. Mass distribution patterns in a narrow, long bay are not expected to be the same as in a wide, long bay. The expectation for such difference to exist due to the bay's shape is because the accumulation of mass occurs as water under the action of wind stress encounters a rigid boundary (Weisberg and Zheng, 2006). To account for the influence of the closeness of the bay's boundary to the center of mass on surge re-distribution, the length of the bay and the shortest width to the center of the bay are considered. In Table 4.7, B is the shortest width to the bay boundary, from an axis passing through the center of gravity of the bay, and L_b is the length of the bay along its major axis (i.e. perpendicular to the coast); for Matagorda Bay, these values are 9.5 km and 50 km respectively. On applying the ${B}/{L_b}$ ratio to the SRFs for Corpus Christi Bay, the results were worse than when this term is ignored. This indicated that this ratio does not appropriately represent the influence of the bay's shape on surge generation in Corpus Christi Bay. While the shape of Matagorda Bay may be approximated to a rectangular bay, the shape of Corpus Christi Bay tends more towards a combination of a rectangular water way attached to a triangular bay. The influence of such a composite bay shape on surge is not clear at this point, and needs to be further investigated. For lack of a better shape factor for Corpus Christi Bay, the current SRF formulation assumes a value of 1.0, implying that the shape of the bay is not explicitly accounted for in surge generation.

The non-dimensional spatial axis of the response functions for the bays is:

$$x' = \frac{X_{cg}}{R_p} + \frac{S_b}{X_{cg}} + F'_{x'} + \left(F'_{R_p} + F'_{c_p v_f} + F'_{\theta}\right) \tag{4.22}$$

where:

$F'_{x'}$ is a spatial dimensionless coefficient determined iteratively, and shown to correlate with ${X_o}/{L_{30}}$ for both Corpus Christi (R^2=0.92) and Matagorda (R^2=0.87) Bays (Figs. 4.88 and 4.89). The additional terms, F'_{R_p}, $F'_{c_p v_f}$ and F'_{θ} are dimensionless metrics developed to adjust specific classes of storms (less than 6% of the data) with characteristics below or above some identified threshold value of storm size, central pressure, forward speed, and approach angle, respectively. The definitions of these classes of storms and their adjustment metrics are summarized in Tables 4.8 and 4.9 for Corpus Christi and Matagorda Bays respectively.

Table 4.8: Dimensionless spatial coefficients for Corpus Christi Bay SRFs.

Term	F'_{R_p}		$F'_{c_p v_f}$		F'_θ	
Class	$x' < 0$	$x' \geq 0$	$x' < 0$	$x' \geq 0$	$x' < 0$	$x' \geq 0$
Conditions	$R_p \geq 65$ km or: $R_p \leq 15$ km (for $X_o \leq$ 50km) or: $R_p < 15$ km (for $X_o >$ 50km)	$R_p \geq 65$ km	-	$\frac{\Delta p}{\gamma} \leq 0.55$ m and $v_f \leq v_{f_{threah}}$	-	$\theta \geq \theta_{thresh}$
Metric	$F'_{R_p} = -\frac{S_b}{R_p}$	$F'_{R_p} = \frac{S_b}{R_p}$	-	$F'_{c_p v_f} = \frac{v_{f_{thresh}}}{v_f}$	-	$F'_\theta =$ $\cos(\theta - \theta_{thresh})$

Table 4.9: Dimensionless spatial coefficients for Matagorda Bay SRFs.

Term	F'_{R_p}		$F'_{c_p v_f}$		F'_θ	
Class	$x' < 0$	$x' \geq 0$	$x' < 0$	$x' \geq 0$	$x' < 0$	$x' \geq 0$
Conditions	$R_p \leq S_b$ and $X_O < 0$	-	-	$v_f \leq v_{f_{threah}}$	$\theta < 0$ and X_O	-
Metric	$F'_{R_p} = -\frac{S_b}{R_p}$	-	-	$F'_{c_p v_f} = \frac{v_{f_{thresh}}}{v_f}$	$1 - \frac{X_{cg}}{R_p}$, if $X_{cg} \geq 0$ and $\sin(\theta_{thresh})\frac{R_p}{X_O}$, if $X_{cg} < 0$	-

In Tables 4.8 and 4.9, $v_{f_{thresh}}$ is a characteristic velocity, given by:

$$v_{f_{thresh}} = \upsilon \frac{L_b}{T_{ch}} \qquad (4.23)$$

where υ is a coefficient determined by inspection of the dimensionless data, and has values of 0.50 and 0.67 for Corpus Christi and Matagorda Bays, respectively.

As seen in Tables 4.8 and 4.9, there are differences in the coefficients and metrics of the SRFs for Corpus Christi and Matagorda Bay. These differences arise from the disparities in the way certain storms (defined by the conditions in Tables 4.8 and 4.9) impact both bays, and the fact that the two bays have different shapes and sizes. Furthermore, the shoreline orientation and continental shelf width around Corpus Christi differs from Matagorda Bay area. Around Corpus Christi Bay, the shoreline orientation (relative to true north) within the area covered by the considered tracks ranges from -2.9 ^{o} to 63.8 ^{o}, and L_{30} ranges from 21.7 km to 32.0 km. In the Matagorda Bay area, the shoreline orientation ranges from 28.3 ^{o} to 66.7 ^{o}, while L_{30} varies from 27.38 km to 43.44 km. The characteristic sizes (half the width of the bay, measured at the shoreline) of the bays are 10 km for Corpus Christi and 15 km for Matagorda Bay.

Regarding storm size (F'_{R_p}), storms smaller than or much larger than the minimum distance from their path to the center of the bay, are not adequately represented in dimensionless space by the first term of Equation 4.22 – because the magnitudes resulting from the ratio (X_{cg} / R_p) is either too high or too low. Depending on their landfall locations relative to the bays, and their sizes relative to the size of the bays, surge generated by these storms could be high or low within the bays. The adjustment metrics are developed to account for this limitation in the first term of Equation 4.22. For Corpus Christi and Matagorda Bays, the disparity in the conditions and metrics for F'_{R_p} are due to the variation in the ratio (X_{cg} / R_p) of these storms at the two bays.

The need for $F'_{c_p v_f}$ arises for storms with low speeds, which consequently generate relatively small surge values. In dimensionless space these storms fall away from majority of the data. In order to capture their contribution in the SRFs, the metric shown in Tables 4.8 and 4.9 are developed to adjust their location. The developed metric showed to be more effective when scaled by a coefficient (Equation 4.23). In Corpus Christi Bay, only storms that are both slow and weak (i.e. c_p = 960 mb) fall in this group, as opposed to Matagorda Bay where even the more intense storms (i.e. c_p = 900 mb) require this adjustment. This observation suggests that the coefficients may have some dependency on the storm intensity (or more generally, ζ'). While these coefficients are different for Matagorda and Corpus Christi Bays, the difference in the values for both bays is not enormous. Further investigation is needed to systematically derive this coefficient (υ) for each bay.

Applying F'_θ to adjust storms in the dimensionless spatial axis of the SRFs also stems from the limitations of the first term of Equation 4.22. Storms traveling past the bay at angles below or above some identified threshold, have X_{cg} values too large or too small to be well represented in the dimensionless spatial axis. The metrics developed were guided by the identification of parameters most sensitive to the surge variations due to varying angles of approach, for this class of storms. The shoreline orientation varies (over a range of -2.9 to 66.7^o) between Corpus Christi and Matagorda Bays; as such, the threshold for storms which need adjustment (F'_θ) are different for the two bays. In Corpus Christi Bay, these storms have θ values greater than 70^o, and in Matagorda storms requiring adjustment have θ values less than 0^o, with some being close to -15^o, hence the assumption of θ_{thresh} as 70^o for Corpus Christi Bay, and -15^o for Matagorda Bay. For bays located along a shoreline with varying orientations, it is challenging to systematically define one threshold metric for the adjustment of storms within this group. However, more simulations over the region, and over more approach angles could lead to a better approach in determining such a metric.

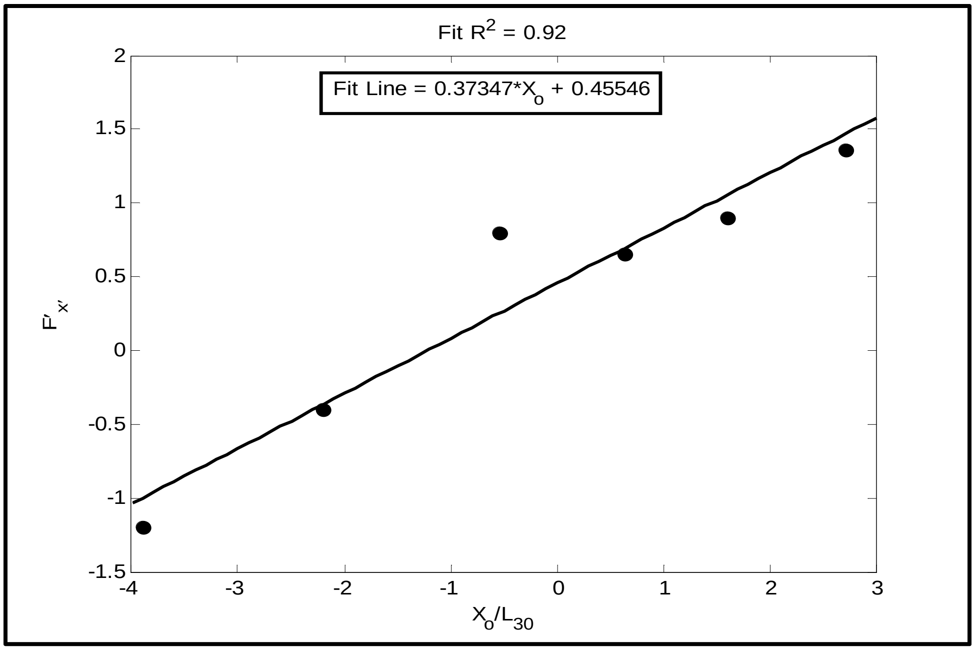

Figure 4.88: Relationship between $F'_{x'}$ and X_O/L_{30} for Corpus Christi Bay.

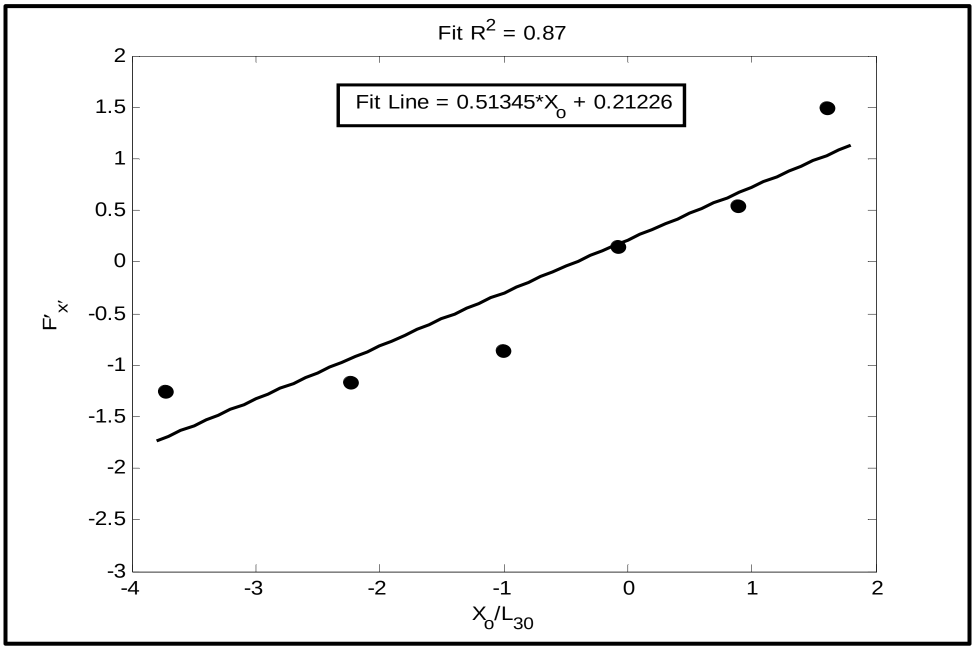

Figure 4.89: Relationship between $F'_{x'}$ and X_O/L_{30} for Matagorda Bay.

4.4.2 Limitations of the Current Form of the Bay SRFs

The SRFs for the bays have more dependency on site-specific parameters than desired. Ultimately, a form of the SRFs which can be applied to any bay with the least amount of site-specific information is required, and would be more useful to the coastal community. In comparing the conditions, metrics and coefficients of the current form of the bay SRFs, its limitations are clearly highlighted, with emphasis on the aspects that require further investigation. Additionally, the steps that may lead to the reduction of these limitations are also provided. They are:

- The SRFs for Matagorda Bay includes the effect of a shape factor, while that of Corpus Christi Bay assumes a value of 1.0. To obtain a better understanding of the influence of this term, simplified idealized grids for bays of different geometries need to be created for sensitivity analysis. The geometry of a bay must have some impact on surge generation; the degree to which this affects surge magnitudes can be better understood by simulating the same storms around bays of different shapes, and studying the surge trends at different locations within the bays. This could lead to a better metric to account for the influence of the bay shapes on surge generation.
- A shift term is used to correct for the influence of surge variations for storms making landfall in a region where other bays are located (to one side of the bays studied in this research). The current form does not show whether or not this term would be important if the adjacent bays were much smaller or much bigger than the bays of interest. A more general condition could be developed by studying surge trends with and without the presence of adjacent bays, to guide the application of this term in the SRFs.
- For storms with θ less than 45^{o} making landfall to the right side of Corpus Christi Bay, the approach angle correction was turned off. A different parameterization to account for the influence of varying approach angles on

surge needs to be developed. A modification of the current form to include some dependence on X_{cg} is recommended.

- There are variations in the conditions and metrics for F'_{R_p}, $F'_{c_p v_f}$ and F'_{θ}. More universal metrics can be developed through sensitivity tests using idealized grids over the range of storm parameters discussed in this research. Such sensitivity tests should cover variations in bay shapes, sizes, the orientation of the shoreline, and the width of the continental shelf around the bays.

While the highlighted limitations may not be completely eliminated by applying the above recommended steps, the suggested steps would lead to a better understanding of the influence of the mentioned parameters on surge generation in the bays. A better understanding of the influence of these factors would lead to a reduction in site-specific terms/coefficients.

4.4.2 Performance of the Revised Form of the Bay SRFs

For discussions here, subsets of the stations used in SRF development in Corpus Christi and Matagorda Bays are selected. A total of 24 locations are selected for Corpus Christi Bay, and 22 locations are selected for Matagorda Bay. These locations are shown in Figs. 4.90 and 4.91, and their coordinates are given in Appendix C. To create appropriate context here, first, results obtained by applying Katyal’s (2009) formulation to the data set including simulations for v_f and θ are presented. The dimensionless surge data and back-prediction of surge at selected locations in Corpus Christi and Matagorda Bay are shown in Figs. 4.92 through 4.101. Values of 2.2x10^{-5} m^{-2} (in Corpus Christi Bay), and 2.5x10^{-5} m^{-2} (in Matagorda Bay) for the coefficient c in Equation 2.13, perform better than Katyal’s recommended values in surge estimation (by over 50%), and are applied to his SRF model. Two types of models were fit to the dimensionless data – the first being a continuous exponential-type function (Equation 2.15) across the entire spatial axis of the SRFs, and the second being Equation 4.24. The SRF performance with the model that fit the data with the least amount of errors is shown here – Equation 4.24 gave a better fit to the data.

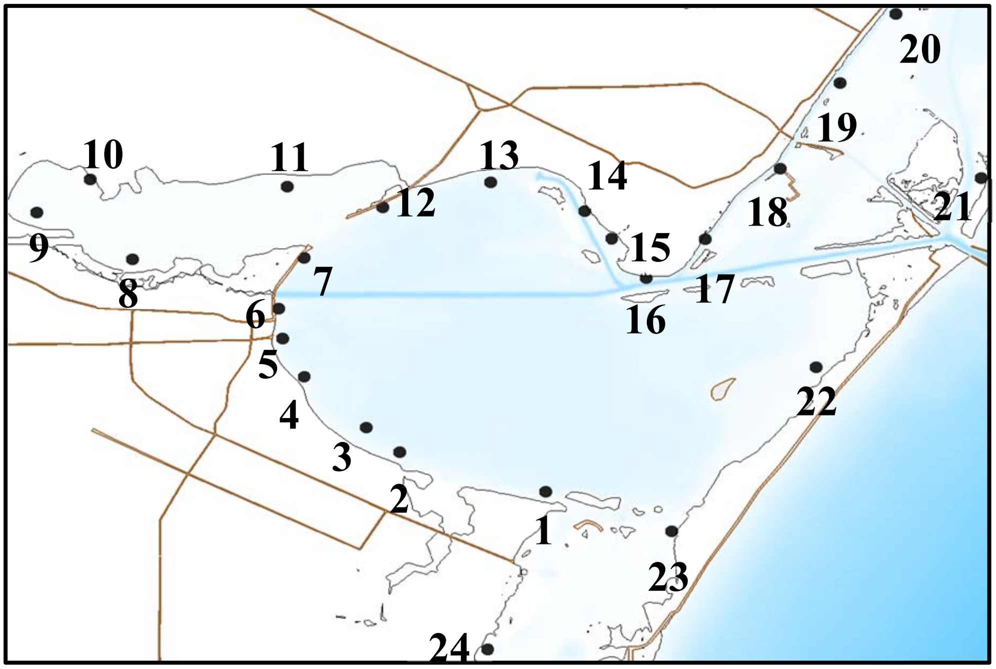

Figure 4.90: SRF locations for Corpus Christi Bay.

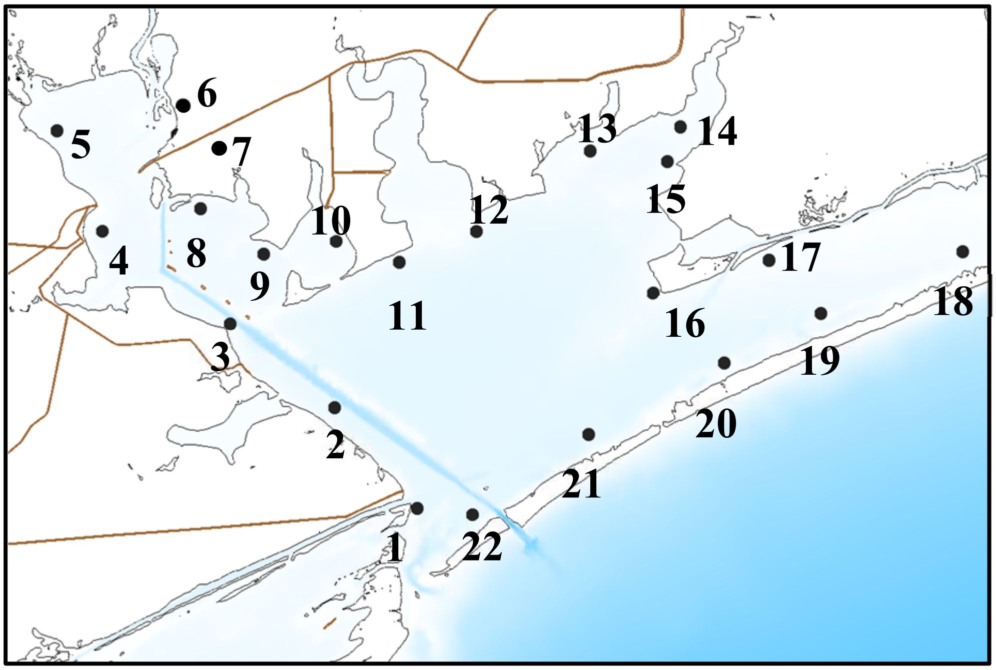

Figure 4.91: SRF locations for Matagorda Bay.

$$\Phi' = \begin{cases} u_1 \exp(u_2 x') + u_3 \exp(u_4 x') & when \quad x' < 0 \\ v_1 \exp(v_2 x') + v_3 \exp(v_4 x') & when \quad x' \geq 0 \end{cases} \tag{4.24}$$

Figures 4.92 through 4.101 show the performance of the Katyal (2009) SRFs in Corpus Christi Bay (i.e. Figs. 4.92 through 4.96) and Matagorda Bay (i.e. Figs. 4.97 through 4.101) for selected locations. The top panes of these figures show the non-dimensional SRF data with the fit, while the bottom panes show the back-prediction of surge by the SRFs. A lot of scatter can be seen on these plots, and the root-mean-square errors associated with the back-prediction of surges are at least 0.50 m at all locations investigated. The scatter in the data is caused by the added v_f and θ data, clearly indicating that the variation of surge due to v_f and θ in the bays is significant and requires adequate scaling laws to account for the influence of these two parameters in the response functions.

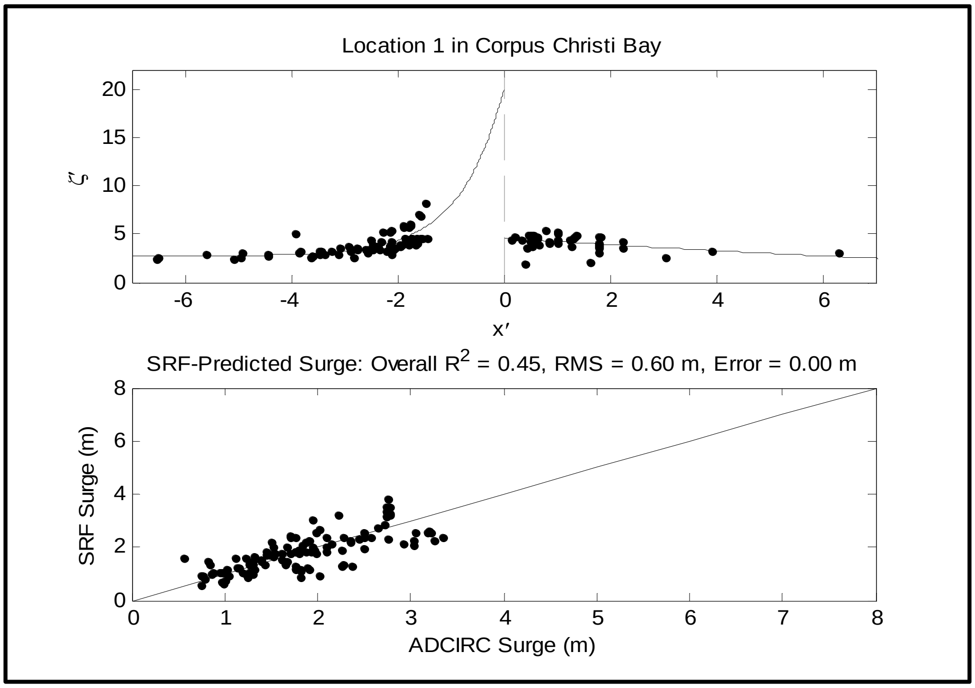

Figure 4.92: Performance of Katyal (2009) formulation at Location 1 of Corpus Christi Bay, without v_f and θ correction. Top pane shows the plot of the dimensionless data using Equations 2.11 and 2.12. Bottom pane shows the back-prediction of surge using the dimensional SRFs.

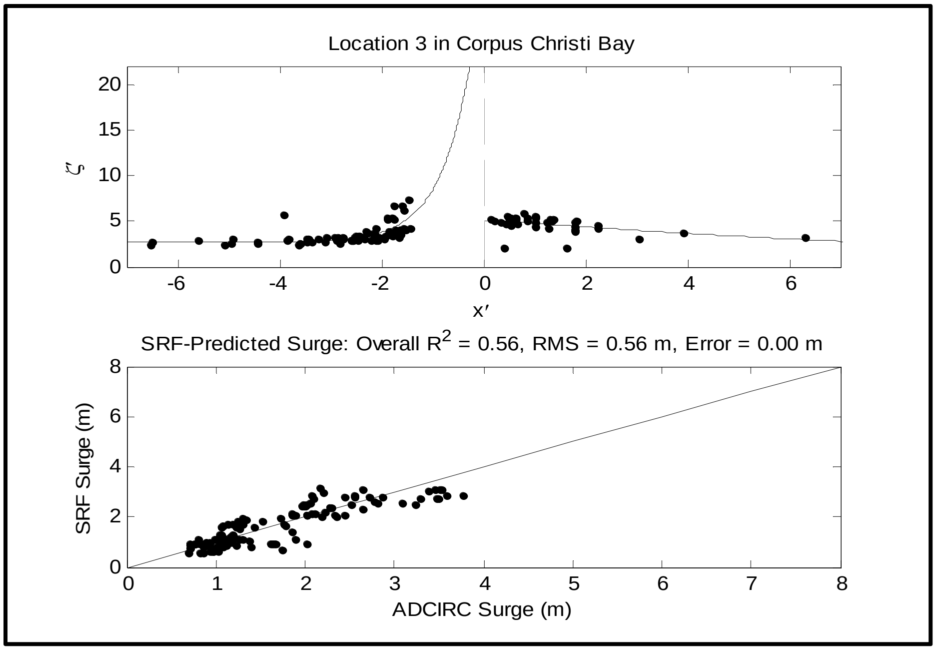

Figure 4.93 Performance of Katyal (2009) formulation at Location 3 of Corpus Christi Bay, without v_f and θ correction. Top pane shows the plot of the dimensionless data using Equations 2.11 and 2.12. Bottom pane shows the back-prediction of surge using the dimensional SRFs.

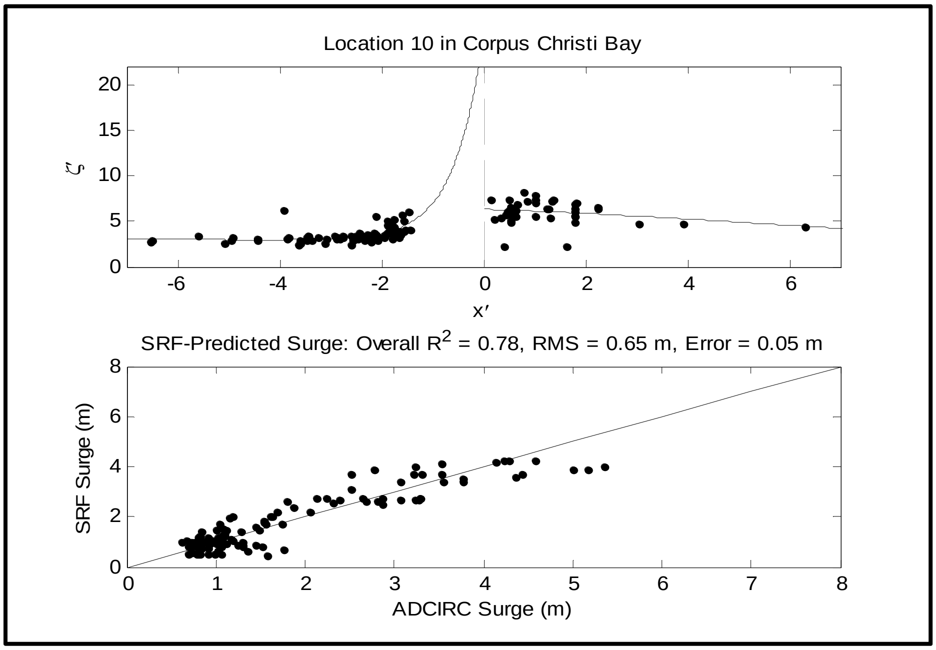

Figure 4.94: Performance of Katyal (2009) formulation at Location 10 of Corpus Christi Bay, without v_f and θ correction. Top pane shows the plot of the dimensionless data using Equations 2.11 and 2.12. Bottom pane shows the back-prediction of surge using the dimensional SRFs.

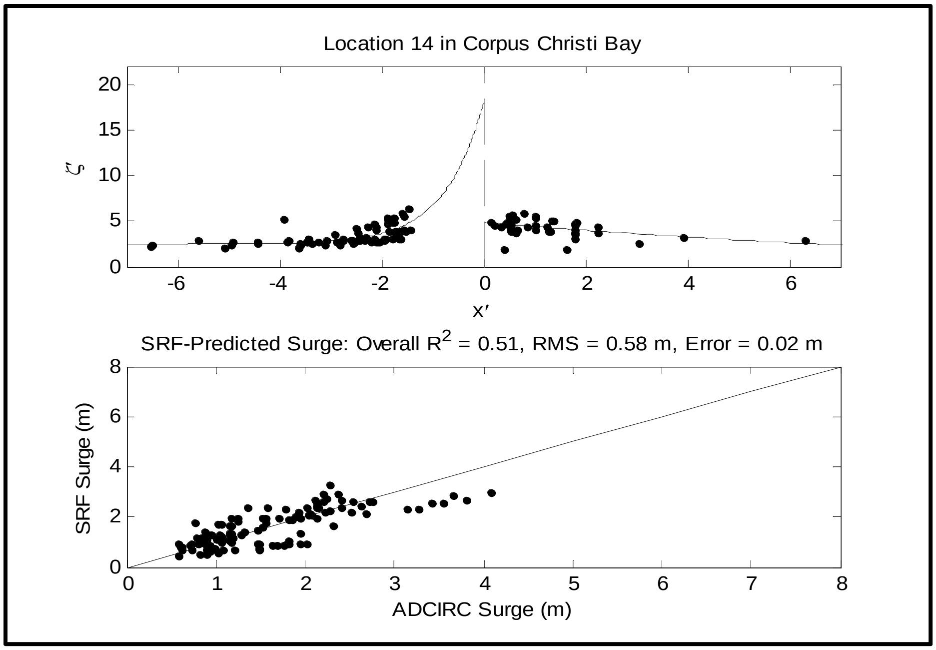

Figure 4.95: Performance of Katyal (2009) formulation at Location 14 of Corpus Christi Bay, without v_f and θ correction. Top pane shows the plot of the dimensionless data using Equations 2.11 and 2.12. Bottom pane shows the back-prediction of surge using the dimensional SRFs.

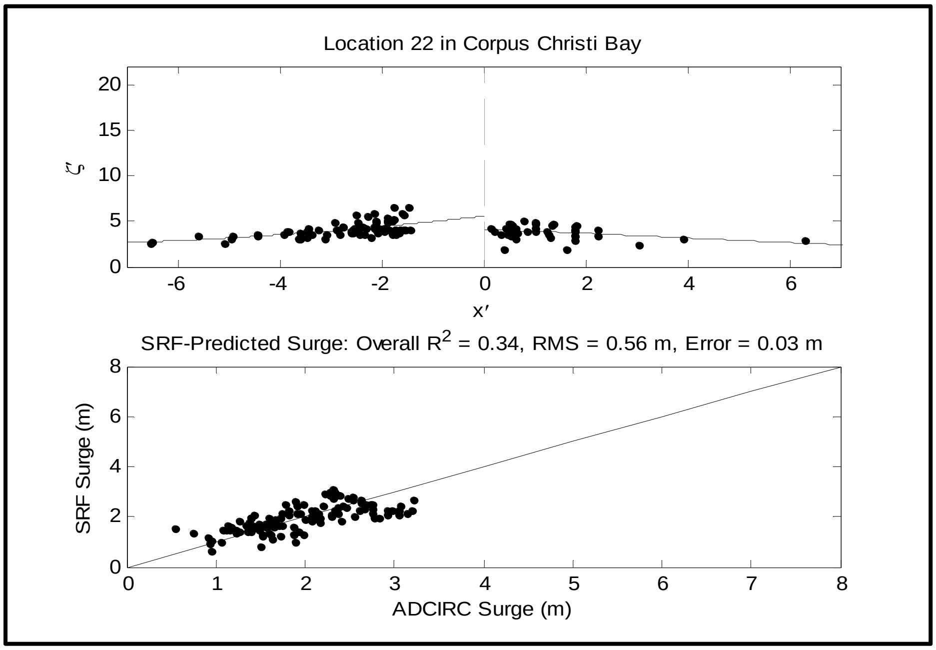

Figure 4.96: Performance of Katyal (2009) formulation at Location 22 of Corpus Christi Bay, without v_f and θ correction. Top pane shows the plot of the dimensionless data using Equations 2.11 and 2.12. Bottom pane shows the back-prediction of surge using the dimensional SRFs.

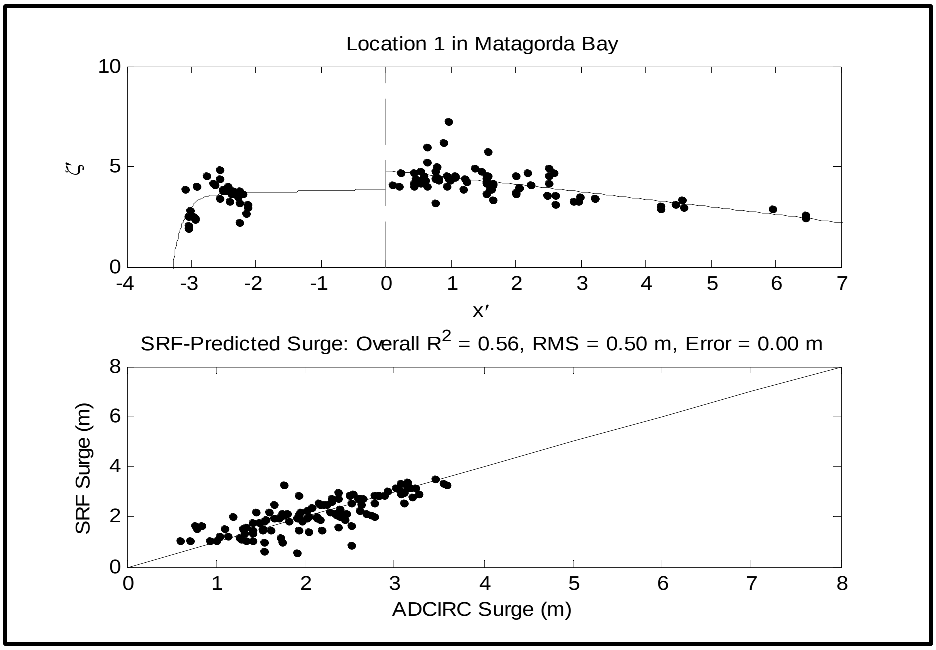

Figure 4.97: Performance of Katyal (2009) formulation at Location 1 of Matagorda Bay, without v_f and θ correction. Top pane shows the plot of the dimensionless data using Equations 2.11 and 2.12. Bottom pane shows the back-prediction of surge using the dimensional SRFs.

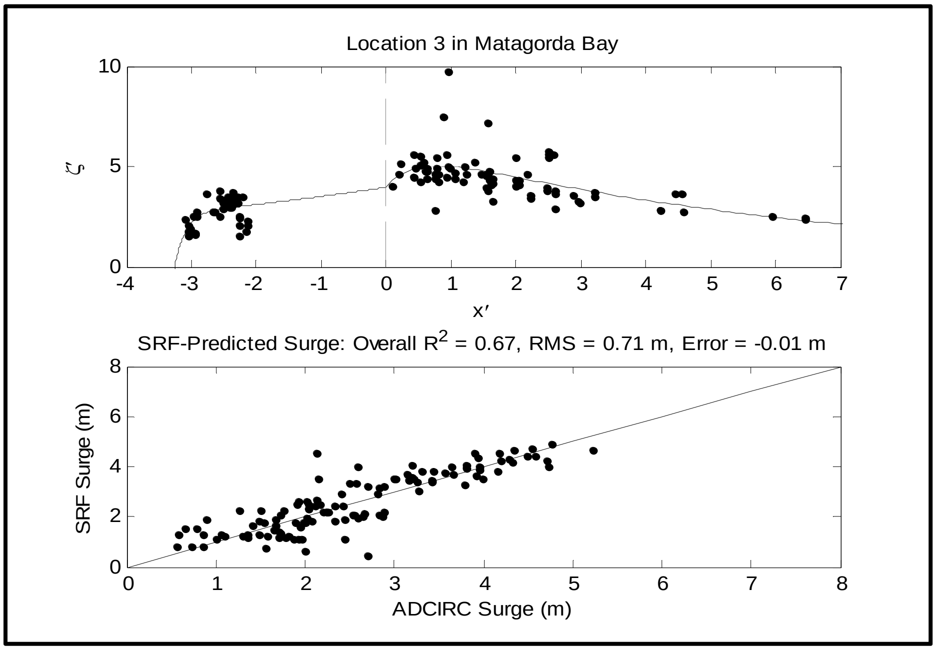

Figure 4.98: Performance of Katyal (2009) formulation at Location 3 of Matagorda Bay, without v_f and θ correction. Top pane shows the plot of the dimensionless data using Equations 2.11 and 2.12. Bottom pane shows the back-prediction of surge using the dimensional SRFs.

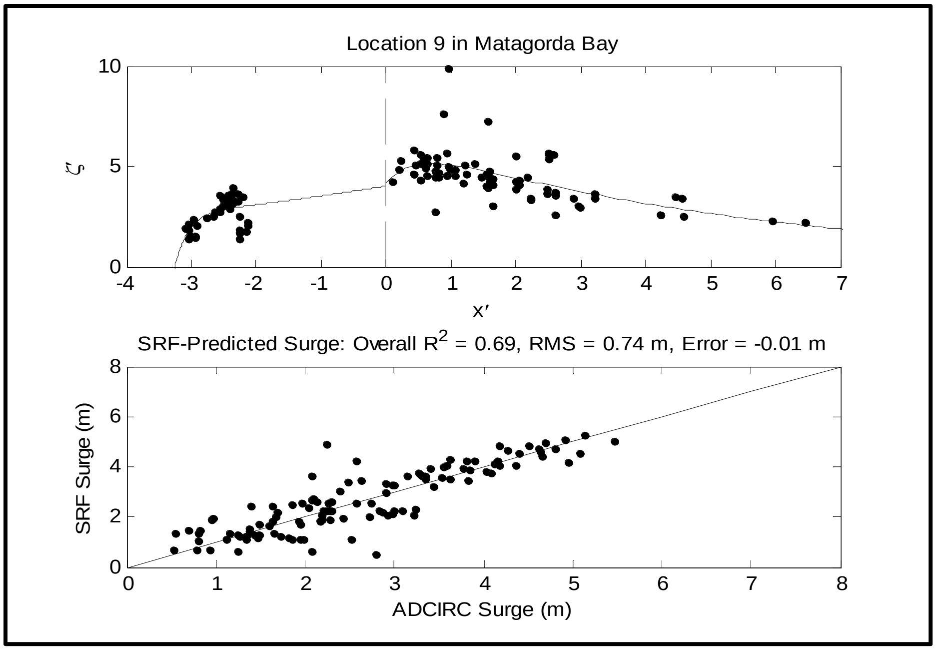

Figure 4.99: Performance of Katyal (2009) formulation at Location 9 of Matagorda Bay, without v_f and θ correction. Top pane shows the plot of the dimensionless data using Equations 2.11 and 2.12. Bottom pane shows the back-prediction of surge using the dimensional SRFs.

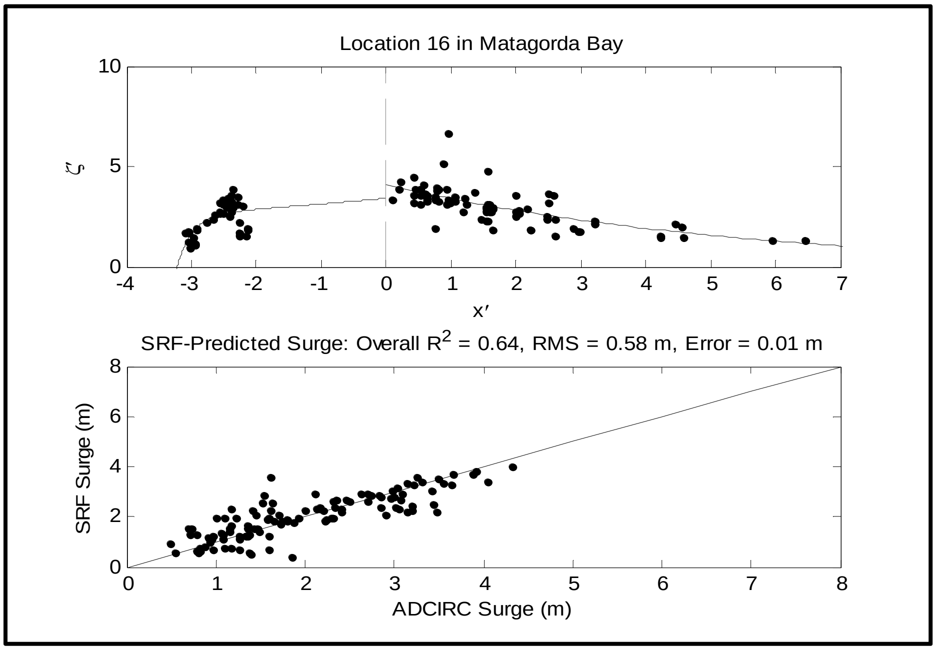

Figure 4.100: Performance of Katyal (2009) formulation at Location 16 of Matagorda Bay, without v_f and θ correction. Top pane shows the plot of the dimensionless data using Equations 2.11 and 2.12. Bottom pane shows the back-prediction of surge using the dimensional SRFs.

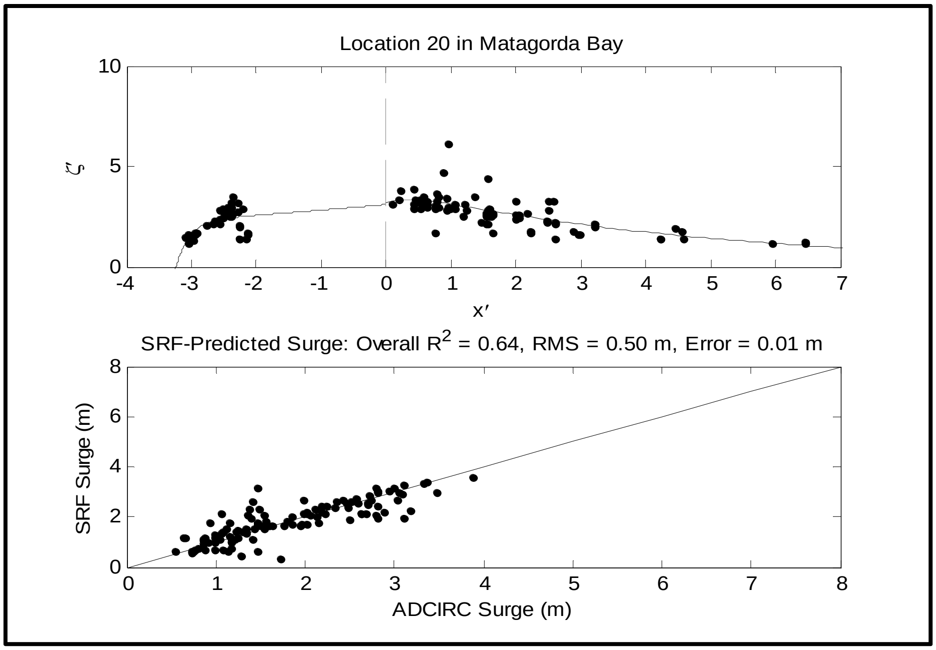

Figure 4.101: Performance of Katyal (2009) formulation at Location 20 of Matagorda Bay, without v_f and θ correction. Top pane shows the plot of the dimensionless data using Equations 2.11 and 2.12. Bottom pane shows the back-prediction of surge using the dimensional SRFs.

The non-dimensional SRF data obtained using Equations (4.21) and (4.22) are fitted with Equation (4.24), to obtain a model for the SRFs. Similar to the open coast SRFs, splitting the data into $x' < 0$ and $x' \geq 0$ domains allows for a better representation of surge distributions in dimensionless space. Figures 4.102 through 4.109 show the performance of the revised SRFs at selected locations in Corpus Christi Bay, while Figs. 4.110 through 4.117 show the performance of the revised SRFs at selected locations in Matagorda Bay. The top panes of these figures show the non-dimensional SRF data with the fit, while the bottom panes show the back-prediction of surge by the SRFs. Errors associated with surge estimation in Corpus Christi Bay using the revised response functions are summarized in Table 4.10; similar results are presented in Table 4.11 for Matagorda Bay. For Corpus Christi Bay, the root mean square errors range from 0.34 m to a maximum of 0.56 m. In Corpus Christi Bay, locations with errors higher than 0.40 m are those close to adjacent water bodies like Nueces Bay (e.g. locations 6 through 13 in Fig. 4.90) and more complex regions, e.g. Aransas Pass, Texas (e.g. locations 17 through 20 in Fig. 4.90).

Table 4.10: SRF errors in Corpus Christi Bay at selected locations.

Location	Root-Mean-Square Error (m)	Mean Error (m)	Overall R^2
1	0.38	0.00	0.72
3	0.38	-0.01	0.78
6	0.44	0.00	0.83
10	0.52	0.02	0.84
12	0.43	-0.01	0.83
14	0.36	0.00	0.81
21	0.34	-0.02	0.70
22	0.43	-0.01	0.54

In these regions, the relatively higher errors suggest that there are other factors or variables that influence surge generation, which are not adequately captured by the revised SRF formulation. A major difference between the locations where the SRFs are predicting surge with small errors and those where the errors are relatively higher is the water depth. While the mean water depth within the middle part of Corpus Christi Bay is around 3 m, locations in Nueces Bay and those around Aransas pass have water depths of about 0.5 m or less. In addition, the region around location 24 and locations 17 through 20 are more complex than the interior part of the bay. In Matagorda Bay, locations with the highest back-prediction errors are also those with very shallow (much less than 0.5 m) water depths, around complex boundaries (e.g. locations 4 through 9). Around the middle sections of Corpus Christi and Matagorda Bays, the accuracy of the SRFs is much higher, demonstrating that the process of surge generation within this region is relatively well described by the SRFs. Overall, the performance of the revised SRFs in Matagorda Bay is better than in Corpus Christi Bay, as majority of locations investigated have root mean square errors of less than 0.4 m; the errors range from 0.31 m to 0.49 m; Corpus Christi Bay has more complex regions (relatively flat areas with highly irregular boundaries). The physics of surge generation and re-distribution in these highly complex, relatively shallow-depth regions seems not to be well captured by the current SRF formulation. For these regions, additional influences such as low water depth and complexity of the location need to be explicitly accounted for in the SRFs.

Table 4.11: SRF errors in Matagorda Bay at selected locations.

Location	Root-Mean-Square Error (m)	Mean Error (m)	Overall R^2
1	0.33	0.07	0.78
3	0.35	0.06	0.90
5	0.49	0.07	0.90
9	0.34	0.07	0.93
13	0.43	0.09	0.88
16	0.34	0.07	0.88
18	0.47	0.08	0.81
20	0.31	0.06	0.85

To delineate the performance of the revised SRFs, prediction errors at select locations around the bays are presented in Tables 4.10 and 4.11 for Corpus Christi and Matagorda Bays, respectively. Table 4.12 summarizes the differences between Katyal (2009) and the revised SRFs for the bays; the percent improvement in surge estimation using the revised SRFs is also presented for the two bays. The comparisons show that the developed formulations for forward speed, and approach angle are needed to adequately represent the influence of v_f and θ in the SRFs. Using the revised SRF formulation, the scatter in the dimensionless surge data is significantly reduced in both bays. The application of the revised SRFs with v_f and θ formulations improves the accuracy in surge estimations (by as much as 54% in Matagorda Bay). Appendix B (Figs. B4.1 through B4.27) shows SRF results using the revised formulation for other locations in Corpus Christi and Matagorda Bays that are not shown in this section. Comparisons are based on 93% of all data considered for each bay – outliers constituting about 7% of all data are excluded from comparisons and from all bay SRF plots shown.

Table 4.12: Comparison of SRF performance (Revised versus Katyal [2009]).

Bay	Location	Root-Mean-Square Error (m)		Mean Error (m)		Overall R^2		% Impr--ovement in RMS Error
		Katyal (2009)	Revised SRFs	Katyal (2009)	Revised SRFs	Katyal (2009)	Revised SRFs	
Corpus Christi Bay	1	0.60	0.38	0.00	0.00	0.45	0.72	36.7
	3	0.56	0.38	0.00	-0.01	0.56	0.78	32.1
	10	0.65	0.52	0.05	0.02	0.78	0.84	20.0
	14	0.58	0.36	0.02	0.00	0.51	0.81	37.9
	22	0.56	0.43	0.03	-0.01	0.34	0.54	23.2
Matagorda Bay	1	0.50	0.33	0.00	0.07	0.56	0.78	34.0
	3	0.71	0.35	-0.01	0.06	0.67	0.90	50.7
	9	0.74	0.34	-0.01	0.07	0.69	0.93	54.1
	16	0.58	0.34	0.01	0.07	0.64	0.88	41.4
	20	0.50	0.31	0.01	0.06	0.64	0.85	38.0

Similar to the open coast formulations, to incorporate sea level rise (SLR) in the response functions for the bays, a dimensional correction is applied. The surge trends observed in the bays as a function of SLR are not perfectly linear (Fig. 4.48 through 4.55), but have weak curvatures at all locations discussed. As such, the correction proposed for the incorporation of SLR in the bay SRFs is a first order polynomial equation, at every location of interest. This relationship between surge and SLR (as deduced from the trends) is:

$$\eta_s - SLR = k\zeta_o + l \tag{4.25}$$

where:

$\eta_s - SLR = \zeta$ (i.e. actual surge with SLR considered)

k is the slope of the linear fit to the $(\eta_s - SLR)$ versus ζ_o data at a location of interest, and:

l is the intercept of the linear fit to the $(\eta_s - SLR)$ versus ζ_o data at the same location of interest.

The dimensional surge obtained from Equation (4.21) is:

$$\zeta = \zeta_o = \frac{\Delta p}{\gamma} \frac{1}{[\cos(\theta)]^{\mu(x')}} \left(\frac{\Phi' - \kappa(x') - \left(c \frac{v_b}{v_f} \right)}{\left(\kappa_b \frac{R_p}{D_{cg-\max}} \right)} + m_x \frac{\Delta p}{\gamma} \right) \tag{4.26}$$

Equation (4.26) shows that the dimensional SRF surge is the equivalent of ζ_o, as it contains no effect of SLR. The final water level, with SRL correction is given as:

$$\eta_s = k\zeta_o + l + SLR \tag{4.27}$$

For a perfectly linear trend of surge versus SLR, k =1, and l =0, so that Equation (4.27) becomes:

$$\eta_s(k = 1, l = 0) = \zeta_o + SLR \tag{4.28}$$

and if $SLR = 0$, then:

$$\eta_s(k = 1, l = 0, SLR = 0) = \zeta_o \tag{4.29}$$

The application of this linear formulation to generate surge scenarios for extreme value analysis obviates computational burdens and saves time, without compromising the accuracy of the surge estimates. Although it was found in the investigation of surge trends with SLR that the linearity of surge trends has some dependence on landfall location, that effect is not explicitly accounted for in the correction for SLR. Since the linear fit adopted here applies to all the data at each location of interest, the influence of landfall location is implicitly accounted for. A non-linear model for the SLR correction is not justifiable, given the limited number of data points used in analysis.

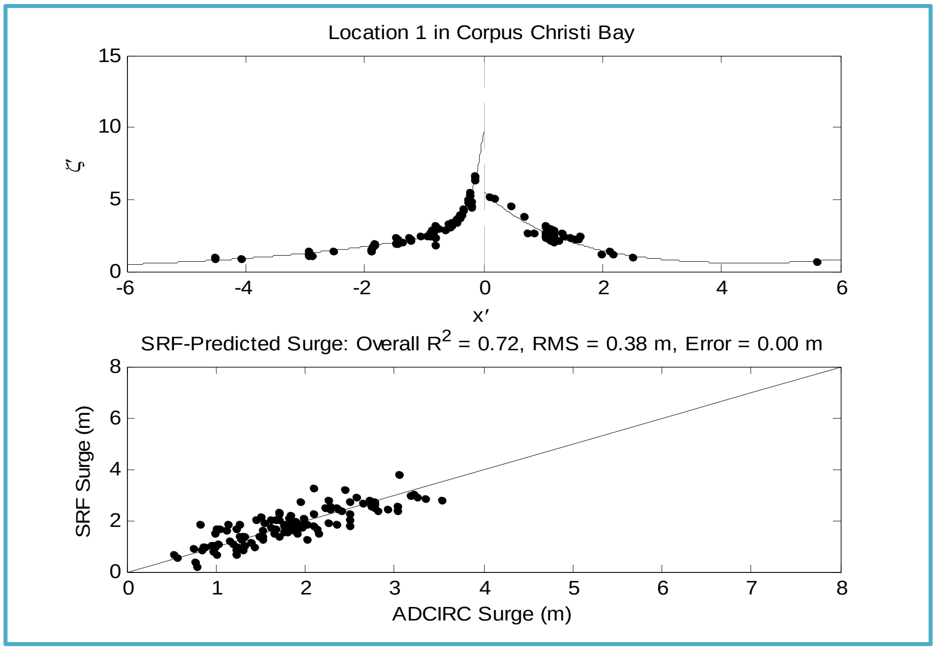

Figure 4.102: Performance of revised SRF formulation at Location 1 of Corpus Christi Bay, with v_f and θ correction. Top pane shows the plot of the dimensionless data using Equations 4.21 and 4.22. Bottom pane shows the back-prediction of surge using the dimensional SRFs.

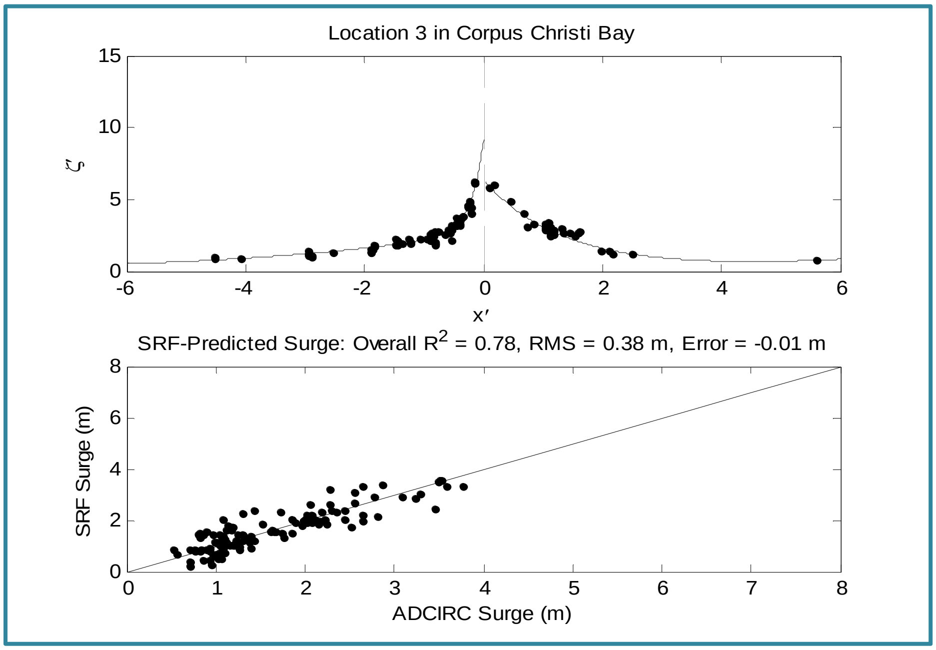

Figure 4.103: Performance of revised SRF formulation at Location 3 of Corpus Christi Bay, with v_f and θ correction. Top pane shows the plot of the dimensionless data using Equations 4.21 and 4.22. Bottom pane shows the back-prediction of surge using the dimensional SRFs.

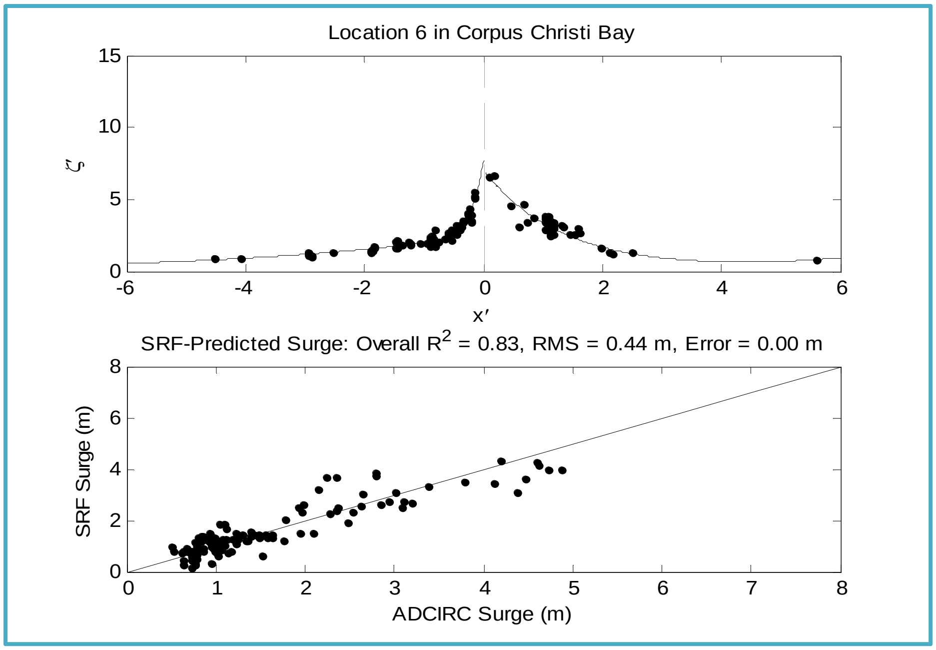

Location 6 in Corpus Christi Bay

SRF-Predicted Surge: Overall R^2 = 0.83, RMS = 0.44 m, Error = 0.00 m

Figure 4.104: Performance of revised SRF formulation at Location 6 of Corpus Christi Bay, with v_f and θ correction. Top pane shows the plot of the dimensionless data using Equations 4.21 and 4.22. Bottom pane shows the back-prediction of surge using the dimensional SRFs.

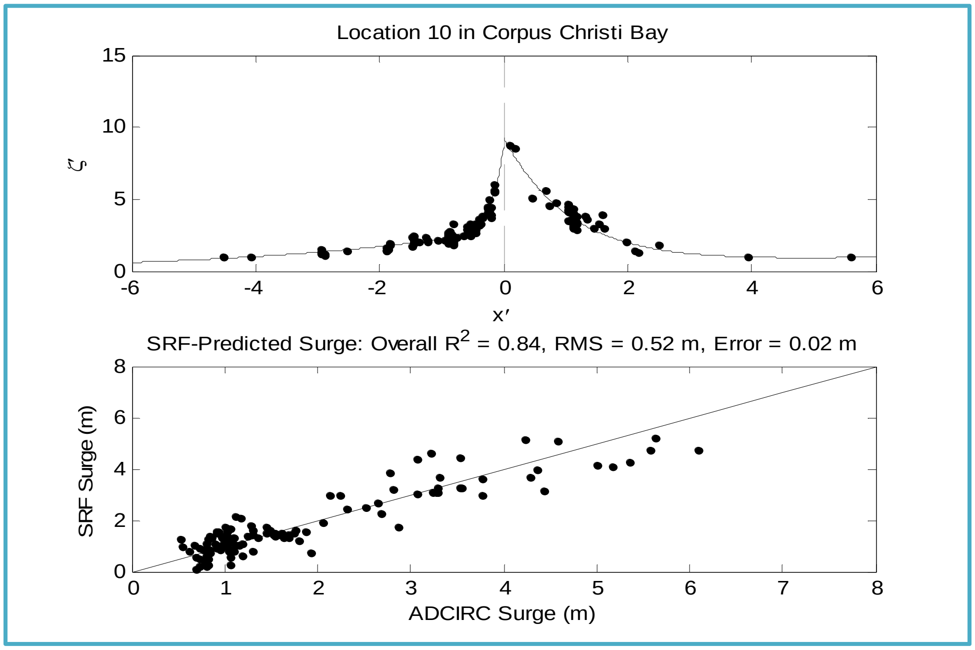

Location 10 in Corpus Christi Bay

SRF-Predicted Surge: Overall R^2 = 0.84, RMS = 0.52 m, Error = 0.02 m

Figure 4.105: Performance of revised SRF formulation at Location 10 of Corpus Christi Bay, with v_f and θ correction. Top pane shows the plot of the dimensionless data using Equations 4.21 and 4.22. Bottom pane shows the back-prediction of surge using the dimensional SRFs.

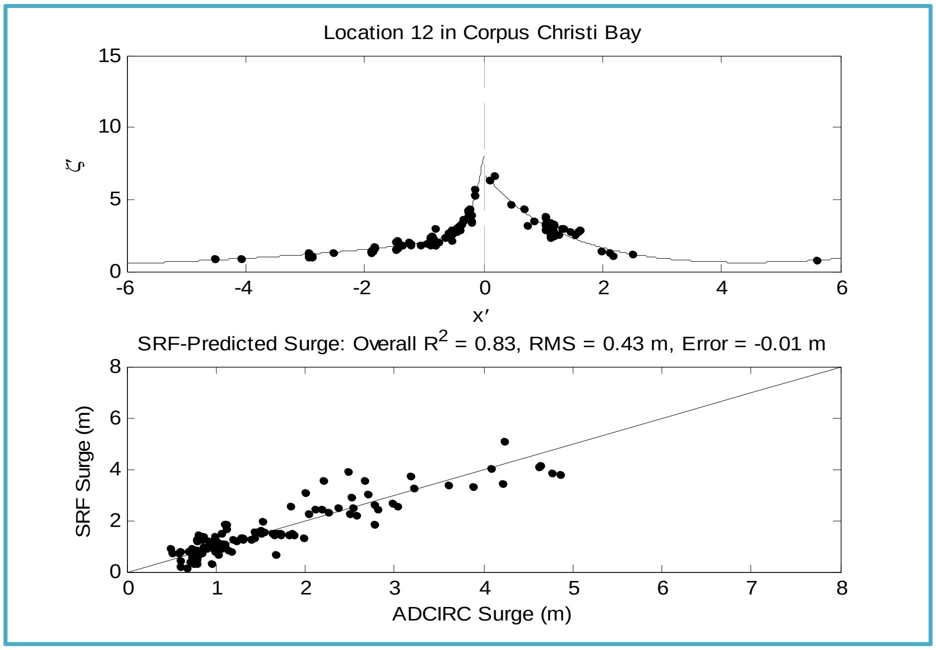

Figure 4.106: Performance of revised SRF formulation at Location 12 of Corpus Christi Bay, with v_f and θ correction. Top pane shows the plot of the dimensionless data using Equations 4.21 and 4.22. Bottom pane shows the back-prediction of surge using the dimensional SRFs.

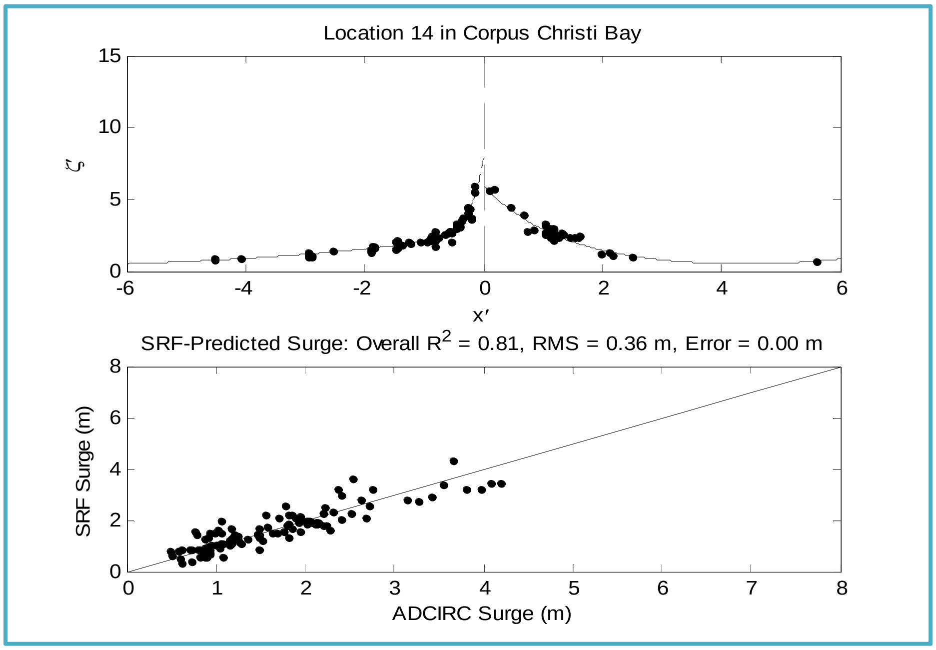

Figure 4.107: Performance of revised SRF formulation at Location 14 of Corpus Christi Bay, with v_f and θ correction. Top pane shows the plot of the dimensionless data using Equations 4.21 and 4.22. Bottom pane shows the back-prediction of surge using the dimensional SRFs.

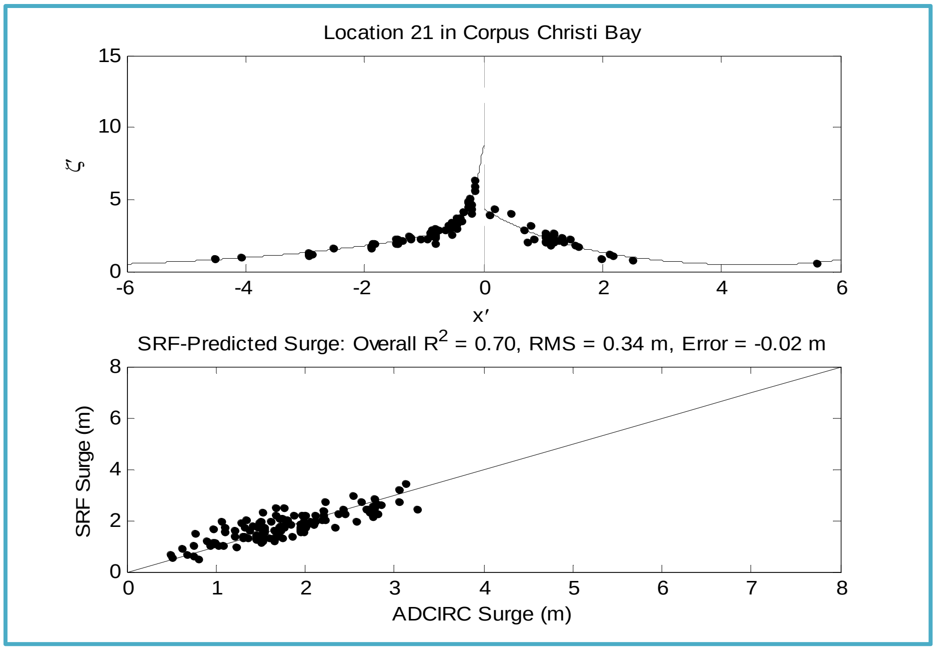

Figure 4.108: Performance of revised SRF formulation at Location 21 of Corpus Christi Bay, with v_f and θ correction. Top pane shows the plot of the dimensionless data using Equations 4.21 and 4.22. Bottom pane shows the back-prediction of surge using the dimensional SRFs.

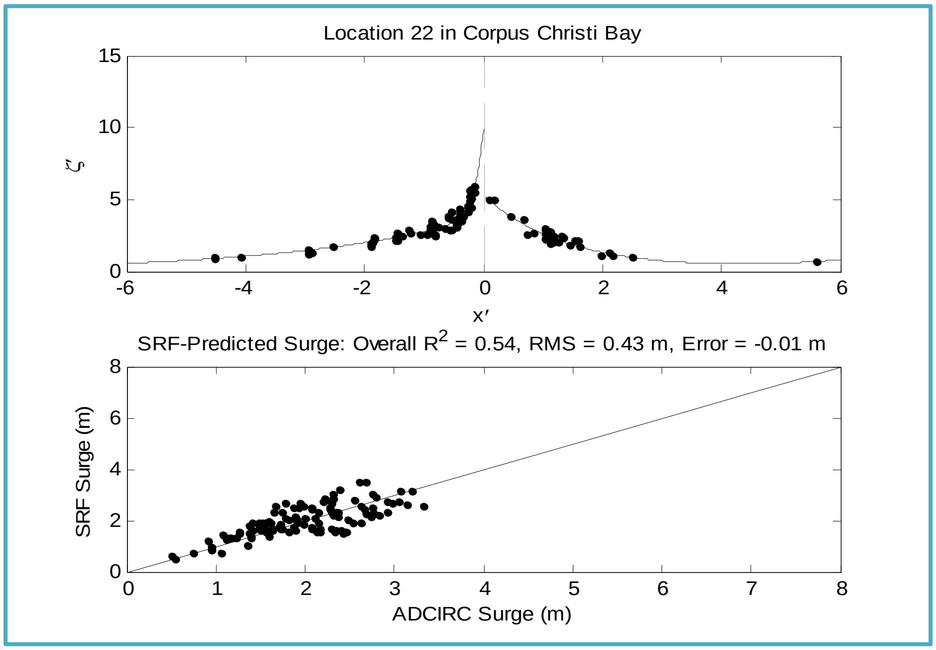

Figure 4.109: Performance of revised SRF formulation at Location 22 of Corpus Christi Bay, with v_f and θ correction. Top pane shows the plot of the dimensionless data using Equations 4.21 and 4.22. Bottom pane shows the back-prediction of surge using the dimensional SRFs.

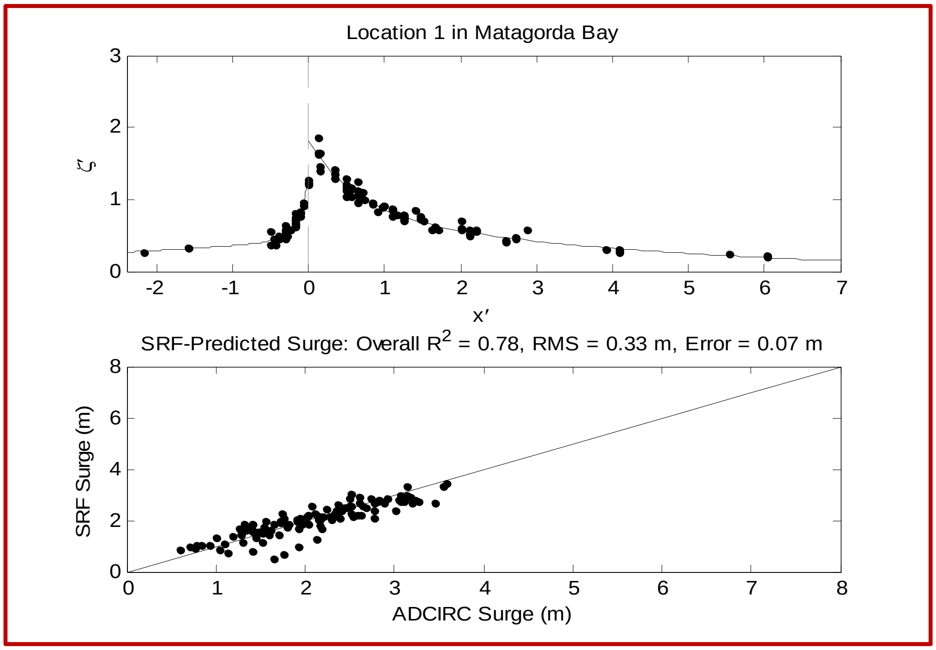

Figure 4.110: Performance of revised SRF formulation at Location 1 of Matagorda Bay, with v_f and θ correction. Top pane shows the plot of the dimensionless data using Equations 4.21 and 4.22. Bottom pane shows the back-prediction of surge using the dimensional SRFs.

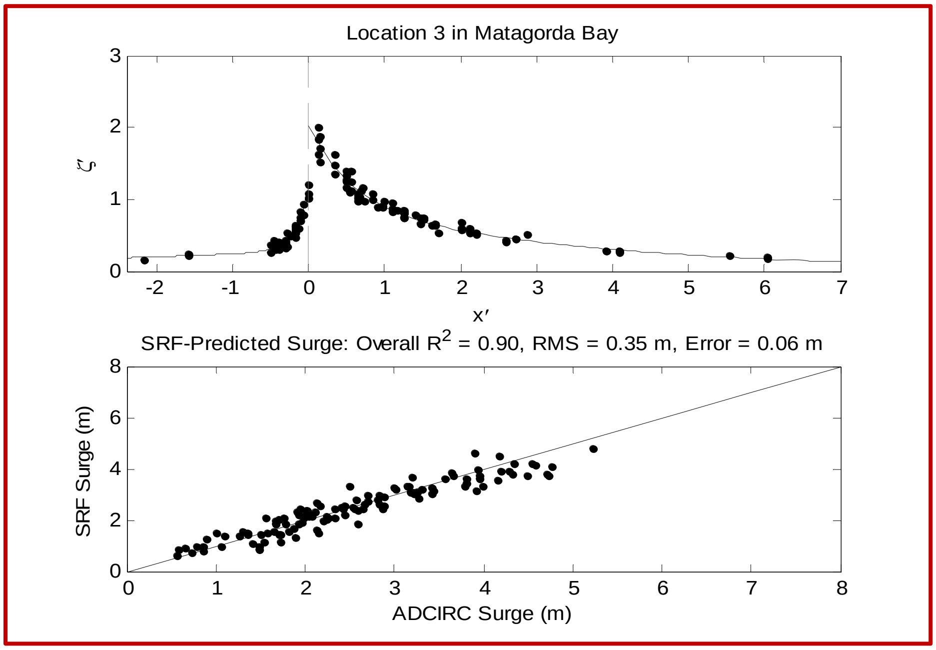

Figure 4.111: Performance of revised SRF formulation at Location 3 of Matagorda Bay, with v_f and θ correction. Top pane shows the plot of the dimensionless data using Equations 4.21 and 4.22. Bottom pane shows the back-prediction of surge using the dimensional SRFs.

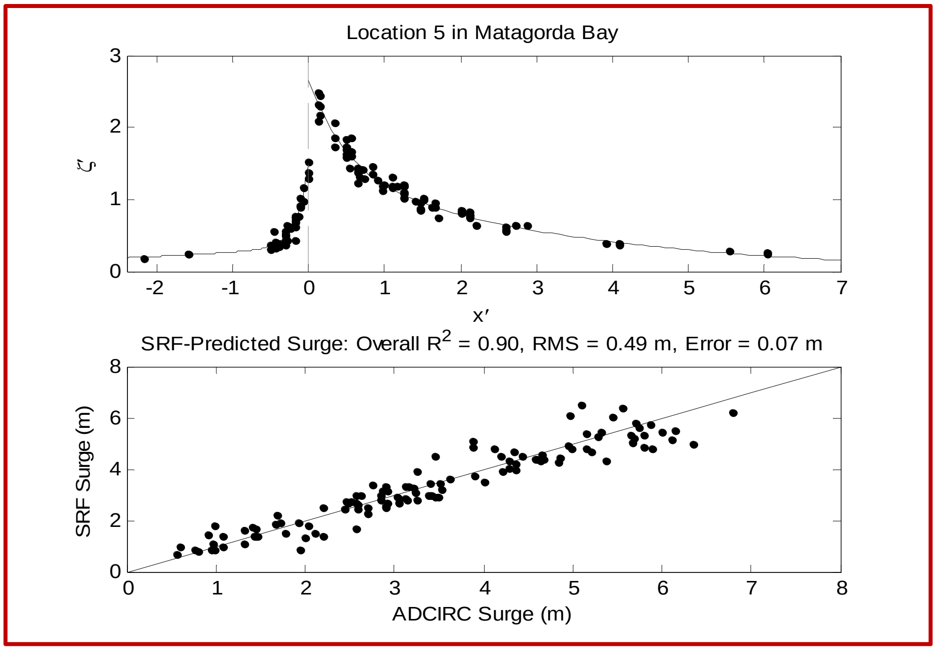

Figure 4.112: Performance of revised SRF formulation at Location 5 of Matagorda Bay, with v_f and θ correction. Top pane shows the plot of the dimensionless data using Equations 4.21 and 4.22. Bottom pane shows the back-prediction of surge using the dimensional SRFs.

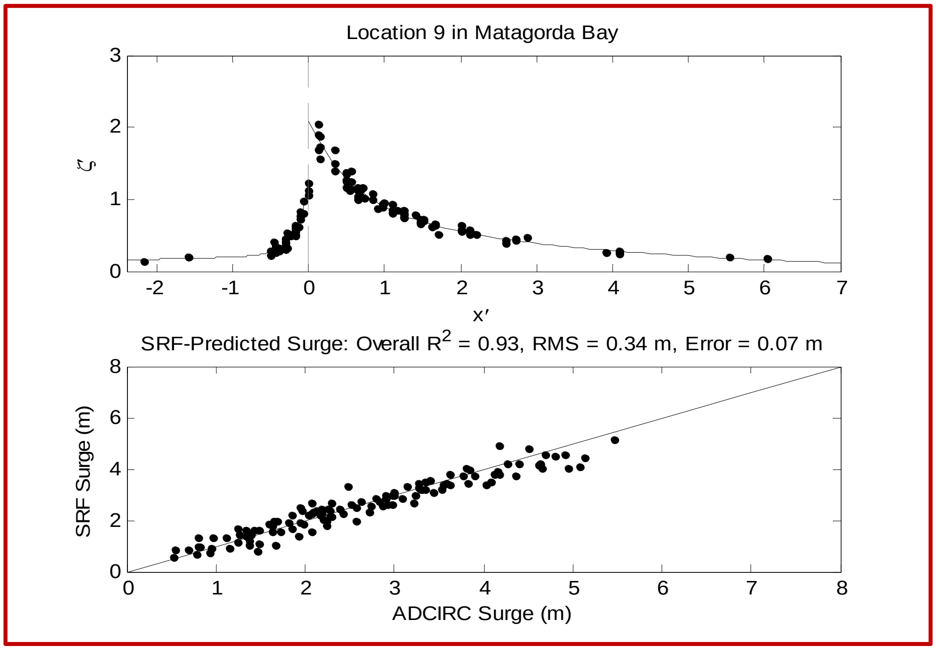

Figure 4.113: Performance of revised SRF formulation at Location 9 of Matagorda Bay, with v_f and θ correction. Top pane shows the plot of the dimensionless data using Equations 4.21 and 4.22. Bottom pane shows the back-prediction of surge using the dimensional SRFs.

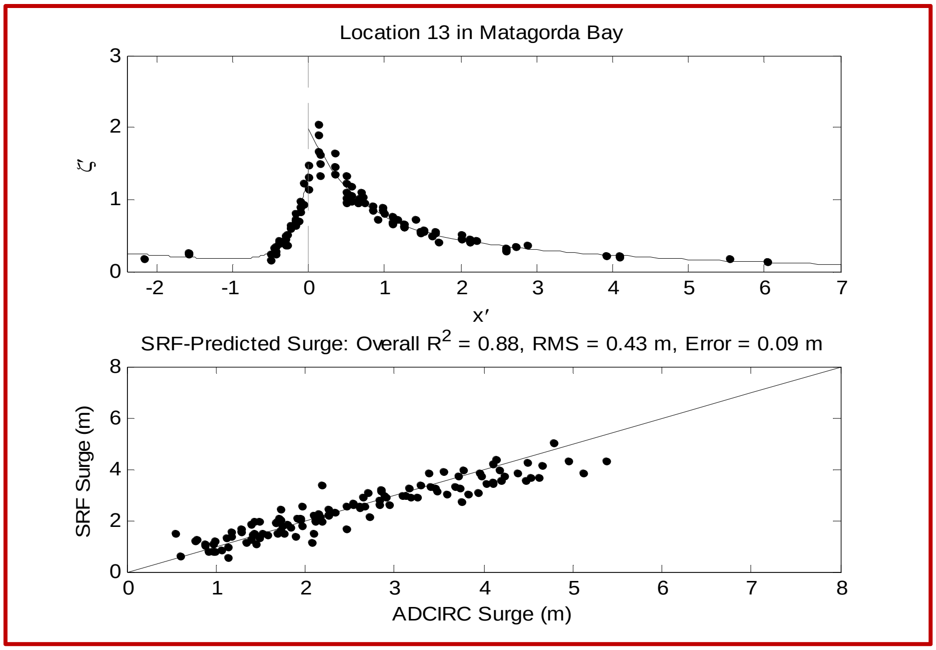
Location 13 in Matagorda Bay

SRF-Predicted Surge: Overall R^2 = 0.88, RMS = 0.43 m, Error = 0.09 m

Figure 4.114: Performance of revised SRF formulation at Location 13 of Matagorda Bay, with v_f and θ correction. Top pane shows the plot of the dimensionless data using Equations 4.21 and 4.22. Bottom pane shows the back-prediction of surge using the dimensional SRFs.

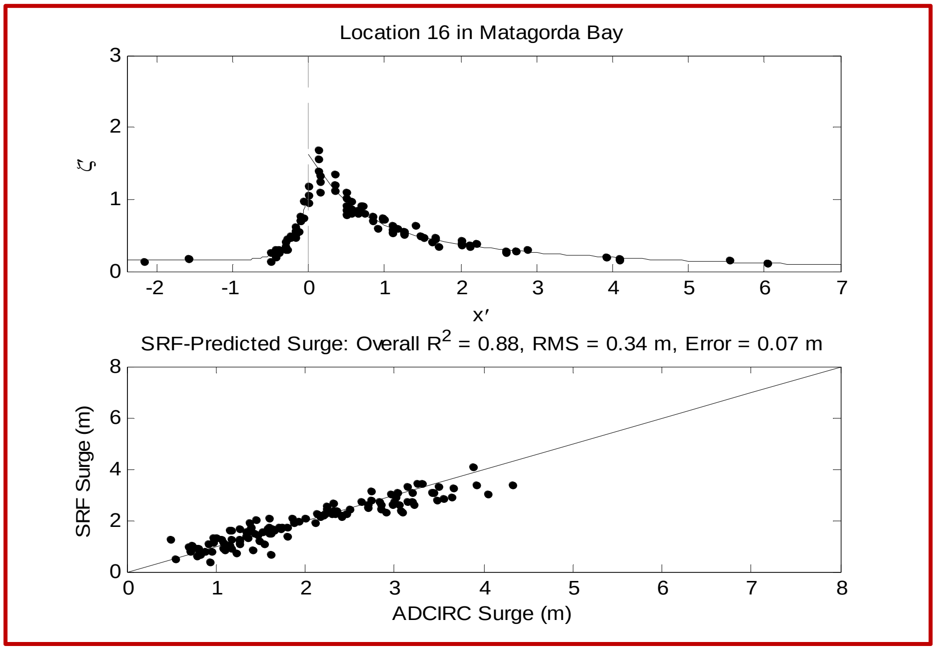
Location 16 in Matagorda Bay

SRF-Predicted Surge: Overall R^2 = 0.88, RMS = 0.34 m, Error = 0.07 m

Figure 4.115: Performance of revised SRF formulation at Location 16 of Matagorda Bay, with v_f and θ correction. Top pane shows the plot of the dimensionless data using Equations 4.21 and 4.22. Bottom pane shows the back-prediction of surge using the dimensional SRFs.

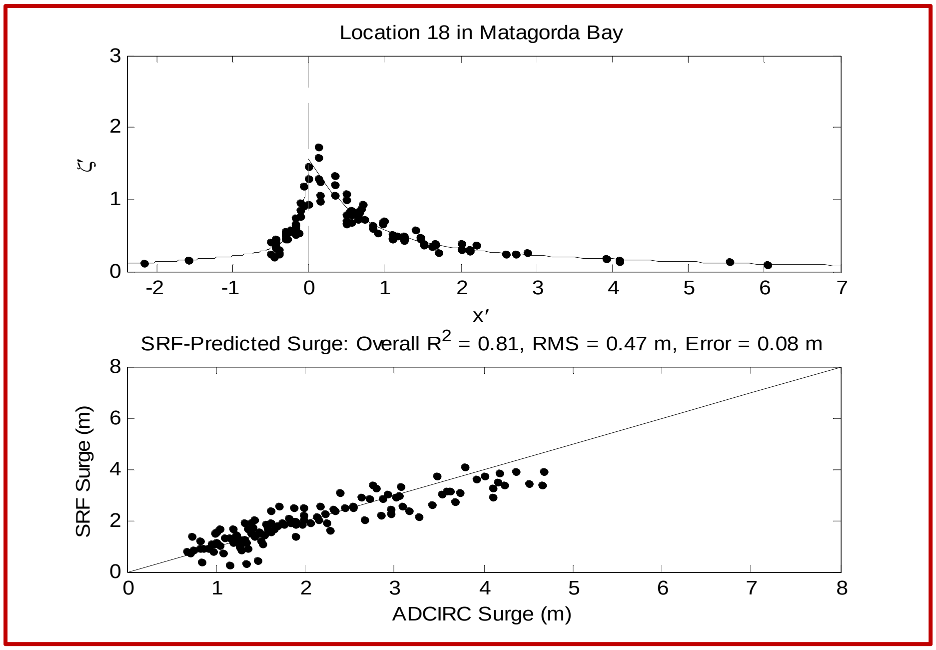

Figure 4.116: Performance of revised SRF formulation at Location 18 of Matagorda Bay, with v_f and θ correction. Top pane shows the plot of the dimensionless data using Equations 4.21 and 4.22. Bottom pane shows the back-prediction of surge using the dimensional SRFs.

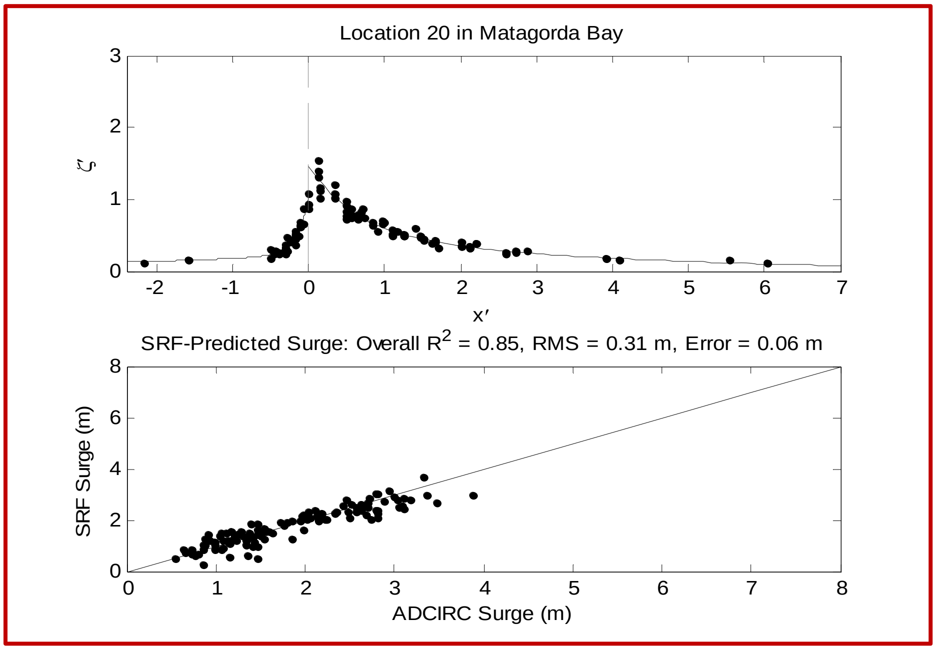

Figure 4.117: Performance of revised SRF formulation at Location 20 of Matagorda Bay, with v_f and θ correction. Top pane shows the plot of the dimensionless data using Equations 4.21 and 4.22. Bottom pane shows the back-prediction of surge using the dimensional SRFs.

4.5 Extreme Value Analysis using the JPM-OS

The Joint Probability Method with Optimal Sampling (JPM-OS) analysis is demonstrated in this section using the revised SRFs for the open coast locations. The hypothesis here is that if different scenarios of v_f, θ, and SLR are considered in developing the n-dimensional matrix (where n is the number of parameters considered) applied in the estimating the probabilities, then the return periods associated with the surge values of interest will be different than if these additional scenarios were not considered. To test this hypothesis, surge matrices with, and without consideration of v_f and θ are developed and the JPM-OS analysis is performed. To evaluate the conditional probabilities, Equations 4.30 through 4.34 are used. Equations 4.30, 4.31, and 4.34 are same as used in Irish and Resio (in press), while Equations 4.32 and 4.33 assume (for simplicity) that the probability of v_f is independent of θ, and the probability of θ is independent of landfall location (x_o), respectively.

$$\kappa_1 = p\left(c_p \mid x_o\right) = \frac{1}{a_1(x_o)} \exp\left[-\frac{\Delta p - a_o(x_o)}{a_1(x_o)}\right] \exp\left\{-\exp\left[-\frac{\Delta p - a_o(x_o)}{a_1(x_o)}\right]\right\} \tag{4.30}$$

$$\kappa_2 = p\left(R_p \mid c_p\right) = \frac{1}{\sigma(\Delta p)\sqrt{2\pi}} \exp\left\{-\frac{\left(\bar{R}_p(\Delta p) - R_p\right)^2}{2\sigma^2(\Delta p)}\right\} \tag{4.31}$$

$$\kappa_3 = p\left(v_f\right) = \frac{1}{\sigma\sqrt{2\pi}} \exp\left\{-\frac{\left(\bar{v}_f - v_f\right)^2}{2\sigma^2}\right\} \tag{4.32}$$

$$\kappa_4 = p(\theta) = \frac{1}{\sigma(x_o)\sqrt{2\pi}} \exp\left\{-\frac{\left(\bar{\theta} - \theta\right)^2}{2\sigma^2}\right\} \tag{4.33}$$

$$\kappa_5 = \Phi\left(\lambda, x_o\right) \tag{4.34}$$

Table 4.13 summarizes the range of values covered for each parameter in the surge matrix for the JPM-OS analysis. For assessing the influence of v_f and θ on surge versus return period curves, no climate change adjustment is made to the central pressures. To assess the impact of climate change on the surge versus return period curves, all central pressure values are adjusted for climate change based on the model presented by Knutson and Tuleya (2004; 2008):

$$p_{\Delta SST} = p_o - \lfloor (0.08 + \varepsilon_p)(\Delta SST + \varepsilon_{\Delta SST}) \rfloor \Delta p \tag{4.35}$$

where:

ε_p, the uncertainty in the fractional change in Δp with ΔSST is assumed = 0;

and:

$\varepsilon_{\Delta SST}$, the uncertainty in the ΔSST projection is also assumed = 0.

4.5.1 Effect of v_f and θ on Surge versus Return Period Curves

To isolate the influence of v_f and θ surge scenarios on the extreme value probabilities, the return period (T_r) versus ζ curves in Figs. 4.64 through 4.67 are calculated considering:

- surge values and probabilities for only c_p and R_p scenarios (i.e. the c_pR_p curve)
- surge values and probabilities for c_p, R_p and θ scenarios (i.e. the $c_pR_p\theta$ curve), using values in Equation 4.39 for the parameters in the normal distribution (Equation 4.33).
- surge values and probabilities for c_p, R_p and v_f scenarios (i.e. the $c_pR_pv_f$ curve), using values in Equation 4.40 for the parameters in the normal distribution (Equation 4.32).

Table 4.13: Range of values for parameters.

Parameter	Minimum Value	Maximum Value	Interval (Surge and Probability Matrices)
c_p (mb)	770	970	5
R_p (km)	8	120	4
v_f (m/s)	1.54	10.80	4.37
θ (°)	-80	80	10
SLR (m)	0.5	2.0	0.5
x_o (km)	-135	500	5

For the conditional probability of R_p on c_p (Equation 4.31), Irish et al. (2011) present Equations 4.36 and 4.37 for the mean and standard deviation, respectively.

$$\overline{R_p}(\Delta p) = a * \left(\left[c_{p-\max} - c_p\right] - 900\right) + b\,, \tag{4.36}$$

$$\sigma_{(R_p|c_p)} = c\overline{R_p}(\Delta p) \tag{4.37}$$

where a, b and c are constants given as:

a = 0.6 km/mb

b = 26 km

c = 0.4

For the probabilities $p(v_f)$ and $p(\theta)$, the mean and standard deviations are assumed as summarized in Equations 4.39 and 4.40. For practical purposes, these values should be obtained through analyses of observational data from reliable databases, such as HURDAT (NOAA); however, for the purpose of illustrating the JPM-OS in this work, assumed values are applied. The return periods associated with the surge probabilities are calculated as:

$$T_r = \frac{1}{\lambda(1-F)} \tag{4.38}$$

where F is the cumulative distribution function of the probability density functions.

$$for \qquad p(v_f): \quad \begin{cases} \overline{v_f} = 5.7\, m/s \\ \sigma_{v_f} = 3.75\, m/s \end{cases} \tag{4.39}$$

$$for \qquad p(\theta): \quad \begin{cases} \overline{\theta} = 0^o \\ \sigma_\theta = 40^o \end{cases} \tag{4.40}$$

For comparison of error statistics in the T_r versus ζ curves for different scenarios and across the selected locations, return periods of 50, 100, 500 and 1000 years are selected as focus. This range of return periods are typically considered for coastal engineering projects. The impact of including v_f and θ scenarios in the surge matrix for the JPM-OS is delineated in Figures 4.118 through 4.121, which show trends of T_r versus ζ at locations 1, 3, 5 and 7 of the open coast discussions. At locations 1 and 3, some increment in surge is seen over the range of return periods chosen. Locations 5 and 7 however show hardy noticeable changes in the curves.

A summary of the statistics for the curves in Figs. 4.118 through 4.121 is presented in Table 4.14 – differences are calculated using the case when only c_p and R_p scenarios are included in the surge matrix as base case. For the case when θ is accounted for, over all four locations the maximum percentage difference is 5.2 % - observed at location 1 for the 100-yr return period. At locations 1, 3 and 5 the maximum percentage differences are 3.9 %, 1.7 % and 2.8 % respectively. The return periods associated with the maximum percentage differences in surge vary from location to location.

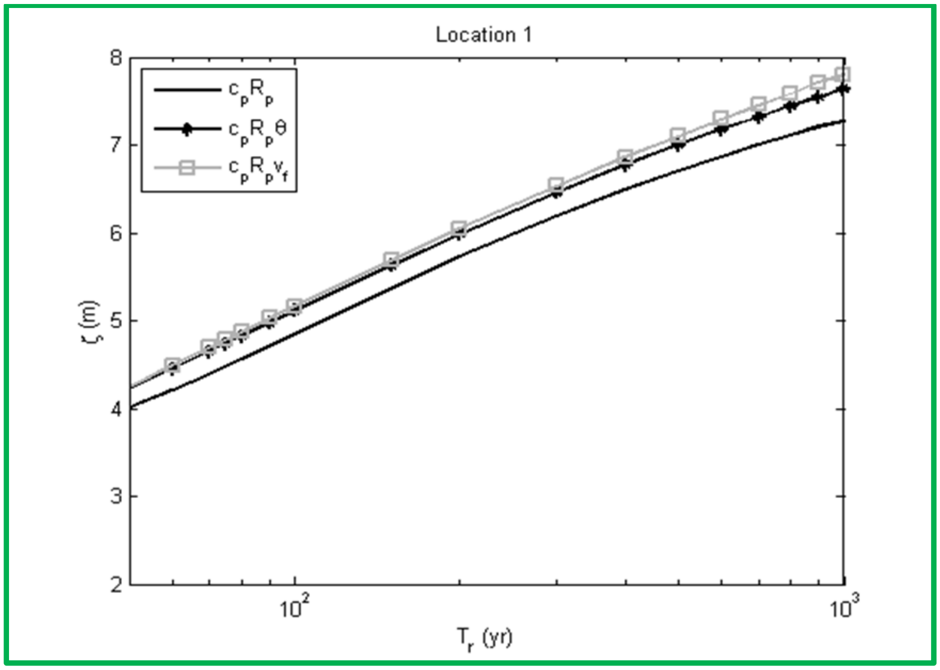

Figure 4.118: Effect of v_f and θ on ζ versus T_r trends at Location 1.

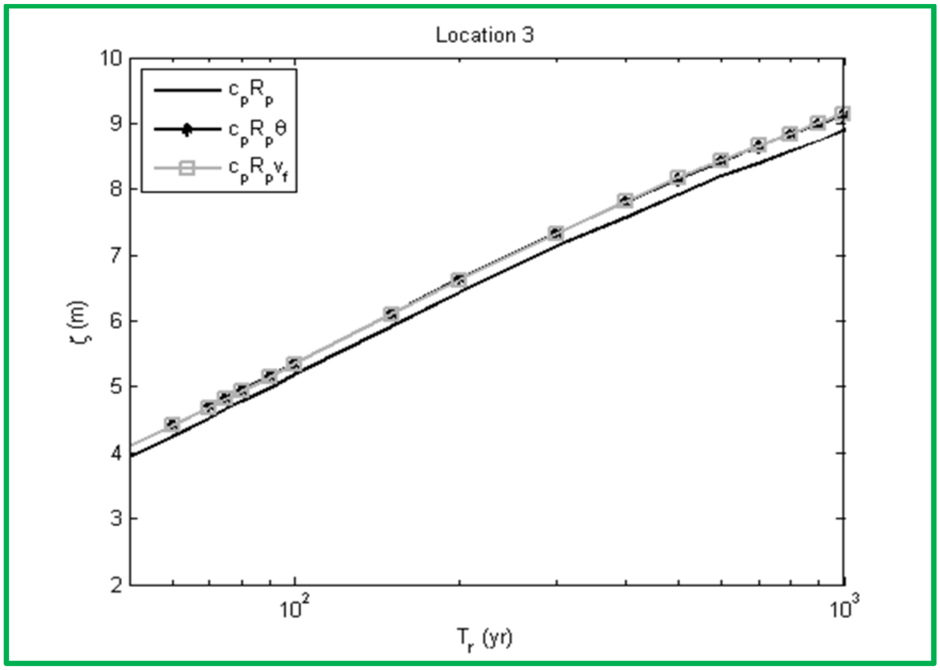

Figure 4.119: Effect of v_f and θ on ζ versus T_r trends at Location 3.

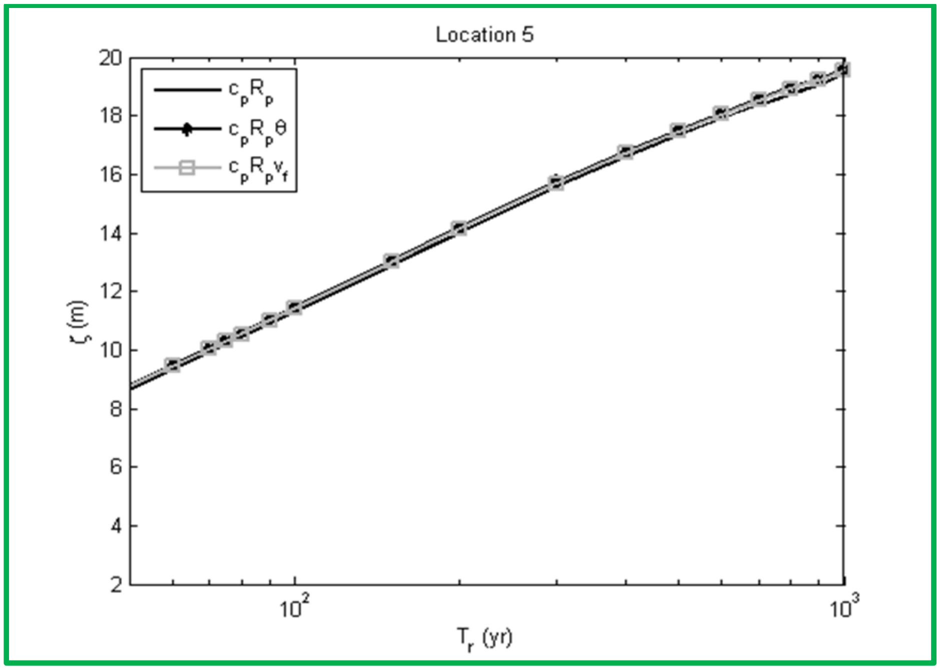

Figure 4.120: Effect of v_f and θ on ζ versus T_r trends at Location 5.

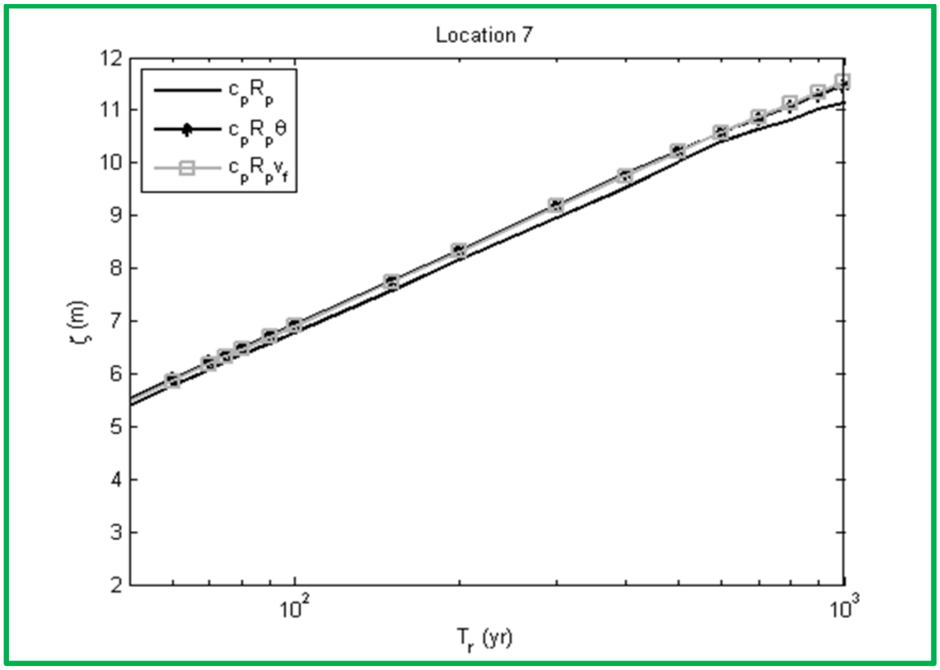

Figure 4.121: Effect of v_f and θ on ζ versus T_r trends at Location 7.

Similarly, for the case when v_f is accounted for in the surge matrix for the JPM-OS, only a small increment in surge is seen over the range of return periods (50 – 1000 years). The maximum percentage difference is 6.7 % at location 1. At locations 3, 5, and 7 the maximum percentage differences are 4.3 %, 1.2 % and 3.5 %. The magnitudes of these percentage differences in surge suggest that the impact of including v_f and θ scenarios on return periods is very small.

Table 4.14: Summary of differences in surge for JPM analysis with and without v_f and θ for specified return periods.

Location	Return Period (yr)	$\zeta_{c_pR_p\theta} - \zeta_{c_pR_p}$ (m)	$\zeta_{c_pR_pv_f} - \zeta_{c_pR_p}$ (m)	% Difference for $\zeta_{c_pR_p\theta}$	% Difference for $\zeta_{c_pR_pv_f}$
1	50	0.22	0.24	**5.1**	**5.7**
	100	0.26	0.31	**5.2**	**6.0**
	500	0.30	0.40	**4.3**	**5.6**
	1000	0.37	0.53	**4.8**	**6.7**
3	50	0.16	0.18	**3.9**	**4.3**
	100	0.18	0.17	**3.4**	**3.2**
	500	0.23	0.25	**2.8**	**3.0**
	1000	0.22	0.25	**2.4**	**2.7**
5	50	0.15	0.11	**1.7**	**1.2**
	100	0.19	0.13	**1.7**	**1.1**
	500	0.17	0.13	**1.0**	**0.7**
	1000	0.15	0.10	**0.7**	**0.5**
7	50	0.13	0.10	**2.4**	**1.8**
	100	0.17	0.14	**2.5**	**2.1**
	500	0.21	0.19	**2.1**	**1.8**
	1000	0.32	0.40	**2.8**	**3.5**

4.5.2 Sensitivity Tests on $p(v_f)$ and $p(\theta)$

In addition to the scenarios aimed at delineating the effects of v_f, θ and SLR in the JPM-OS analysis, sensitivity tests were also performed to see the response of the extreme value probabilities to the assumed mean and standard deviation values in Equations 4.39 and 4.40. These tests allow the results of the extreme value analyses to be interpreted with the correct perspective. Table 4.25 summarizes the mean and standard deviations for v_f and θ used in the sensitivity tests.

Table 4.15: Values used in sensitivity analysis

Test case $p(v_f)$	$\overline{v_f}$ (m/s)	σ_{v_f} (m/s)	Test case $p(\theta)$	$\overline{\theta}$ (deg)	σ_θ (deg)
case 1	4.7	3.75	case 1	-7.5	40.0
case 2	3.7	3.75	case 2	-15.0	40.0
case 3	2.7	3.75	case 3	-22.5	40.0
case 4	1.7	3.75	case 4	-30.0	40.0
case 5	5.7	5.75	case 5	0.0	10.0
case 6	5.7	4.75	case 6	0.0	20.0
case 7	5.7	2.75	case 7	0.0	30.0
case 8	5.7	1.75	case 8	0.0	50.0
case 9	5.7	3.75	case 9	0.0	40.0

Results of the sensitivity analyses for the influence of assumed mean and standard deviation of approach angle are presented in Figs. 4.122 through 4.129. The sensitivity tests show that varying the mean of the probability distribution for approach angle has practically no impact on the surge probabilities. Table 4.16 shows the statistics for the sensitivity tests – the maximum percentage difference in surge when the mean of the probability distribution varies from -30 ^{o} to 0 ^{o} is 1.6 %, and this difference is associated with a return period of 50 years. The fact that there is barely an increase in surge over all return periods for this case suggests that surge magnitudes from storms with varying approach angles are evenly distributed about the mean surge value.

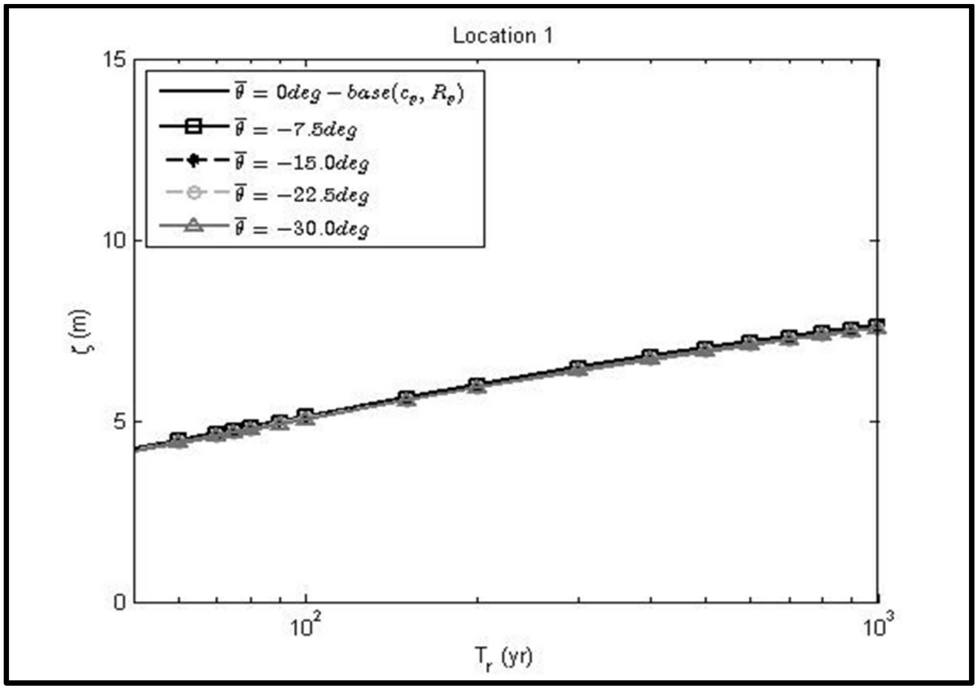

Figure 4.122: Sensitivity of $\overline{\theta}$ to ζ versus T_r trends at Location 1.

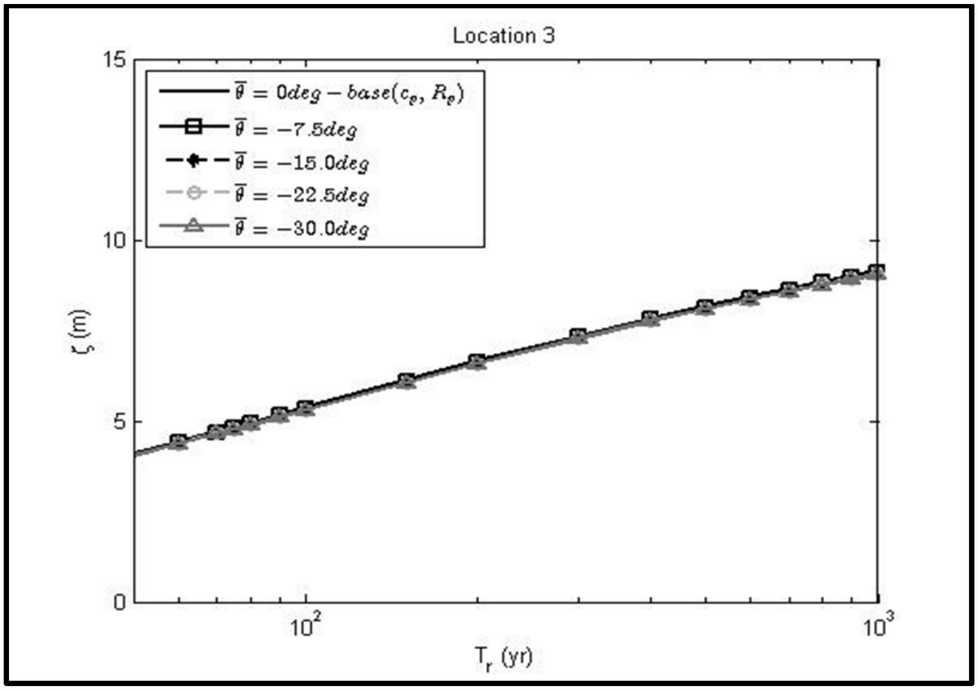

Figure 4.123: Sensitivity of $\overline{\theta}$ to ζ versus T_r trends at Location 3.

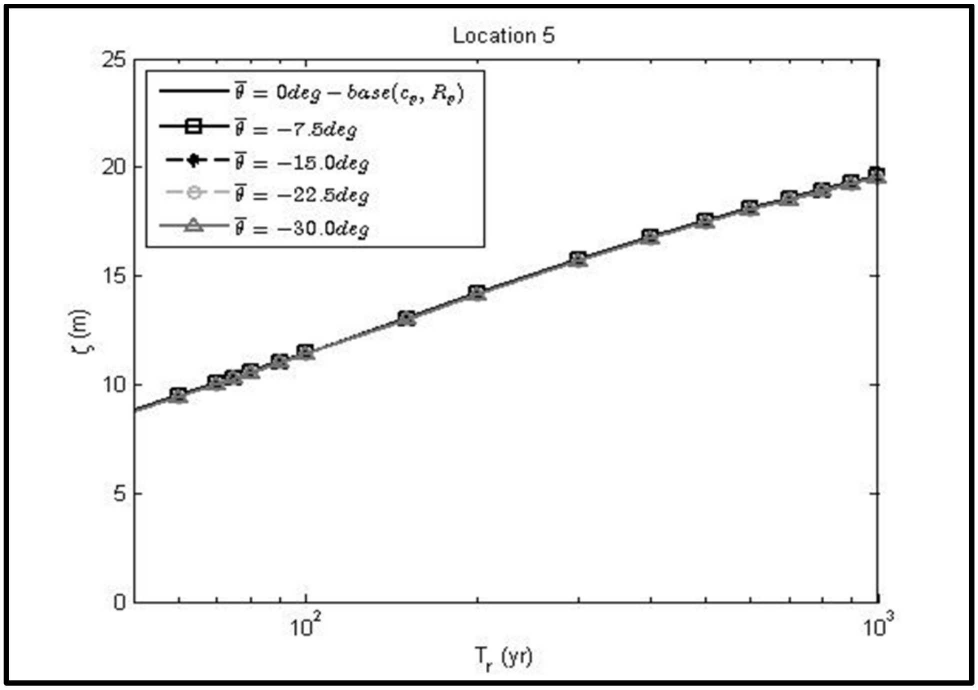

Figure 4.124: Sensitivity of $\overline{\theta}$ to ζ versus T_r trends at Location 5.

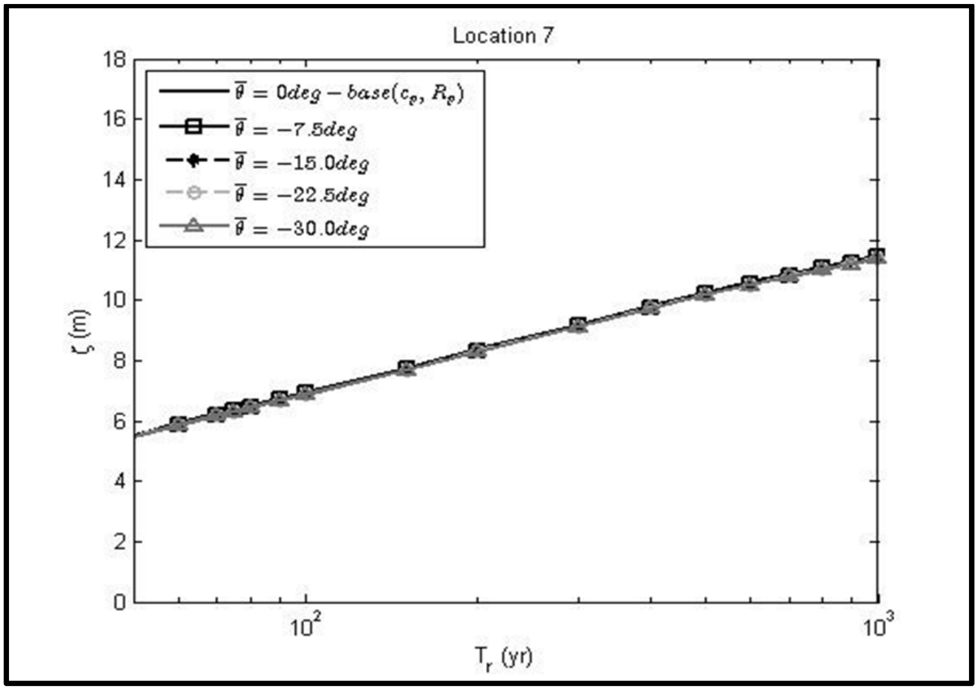

Figure 4.125: Sensitivity of $\overline{\theta}$ to ζ versus T_r trends at Location 7.

With this low sensitivity of the T_r values to surge, it implies that if the assumed mean value in Equation 4.40 deviated from the true mean value by up to 30 ^{o}, the uncertainty associated with the obtained T_r versus ζ curves in Figs. 4.118 through 4.121 could only increase by at most 1.6 %. The assumed standard deviation (σ_θ) in Equation 4.40 on the other hand is seen to have a greater impact on the probability curves over the range of T_r considered. As shown in Table 4.16, the percentage difference in surge ranges from 3.2 % to 11.4 % over all locations and return periods. The maximum difference is at location 1, for a T_r of 50 yr. At locations 3, 5 and 7, the maximum increase in surge is also seen for the 50-yr return period, thus the change in σ_θ impacts small storm events than it does more extreme events. It is observed in Figs. 4.118 through 4.121 that as σ_θ reduces, surge increases for the same return period. This observation suggests that storms with approach angle near shore-normal drive the highest surges in the θ scenarios of the surge matrix; it also suggests that as the standard deviation reduces, the surge values within the population approach the mean value of surges from storms with approach angles near shore-normal.

Table 4.16: Summary of differences in surge at specified return periods for $\overline{\sigma}$ and σ_θ sensitivity analysis.

Location	Return Period (yr)	$\zeta_{\bar{\theta}-base} - \zeta_{\bar{\theta}-sensitivity}$		$\zeta_{\sigma_\theta-base} - \zeta_{\sigma_\theta-sensitivity}$	
		Maximum Absolute difference (m)	% Difference using Maximum Absolute Difference	Maximum Absolute difference (m)	% Difference using Maximum Absolute Difference
1	50	0.07	**1.6**	0.48	**11.4**
	100	0.07	**1.4**	0.51	**10.0**
	500	0.09	**1.3**	0.59	**8.4**
	1000	0.09	**1.2**	0.58	**7.6**
3	50	0.05	**1.3**	0.41	**9.9**
	100	0.06	**1.1**	0.46	**8.6**
	500	0.08	**0.9**	0.55	**6.7**
	1000	0.08	**0.8**	0.59	**6.5**
5	50	0.06	**0.6**	0.41	**4.7**
	100	0.06	**0.5**	0.47	**4.1**
	500	0.05	**0.3**	0.59	**3.4**
	1000	0.07	**0.3**	0.63	**3.2**
7	50	0.05	**0.9**	0.38	**6.9**
	100	0.06	**0.9**	0.44	**6.3**
	500	0.07	**0.6**	0.56	**5.5**
	1000	0.08	**0.7**	0.58	**5.0**

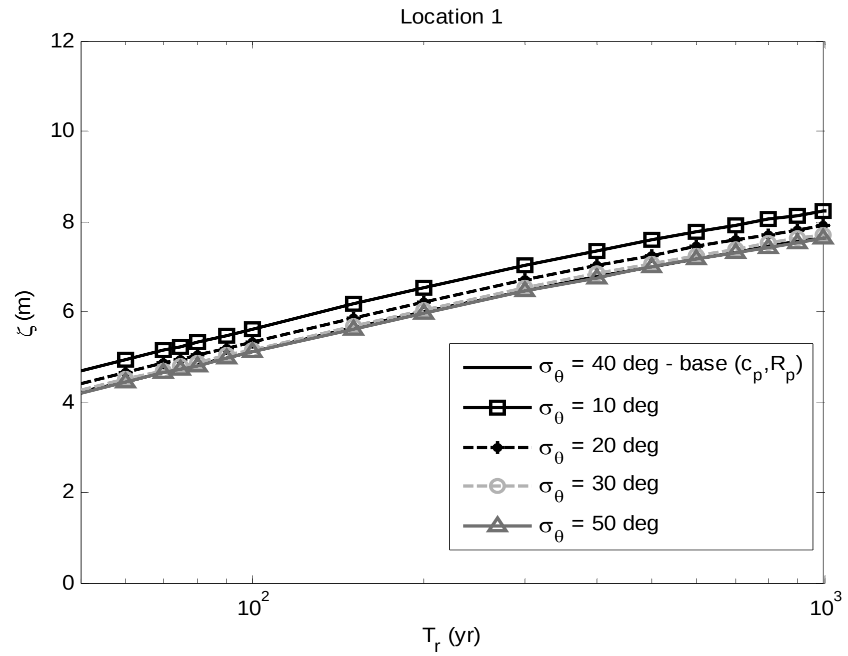

Figure 4.126: Sensitivity of σ_θ to ζ versus T_r trends at Location 1.

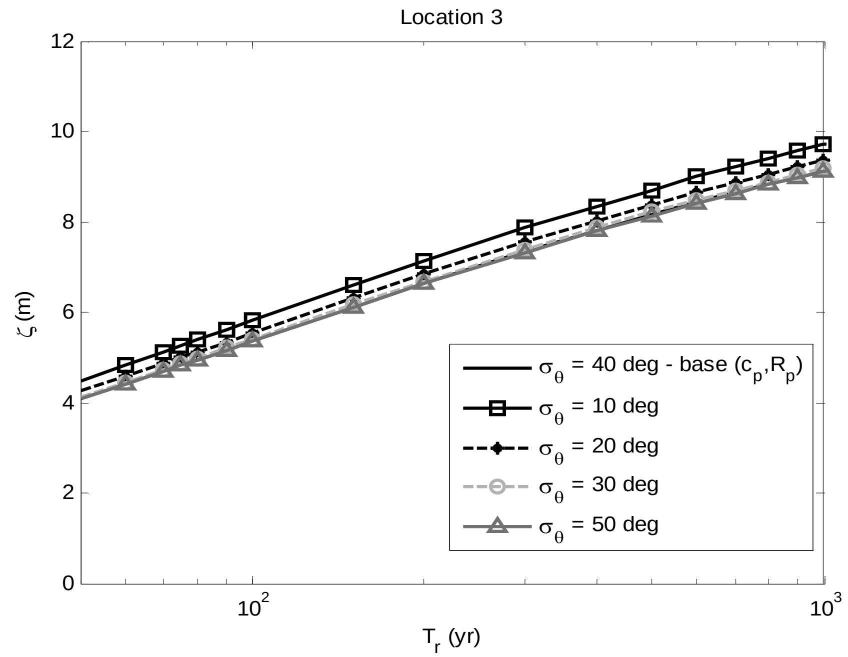

Figure 4.127: Sensitivity of σ_θ to ζ versus T_r trends at Location 3.

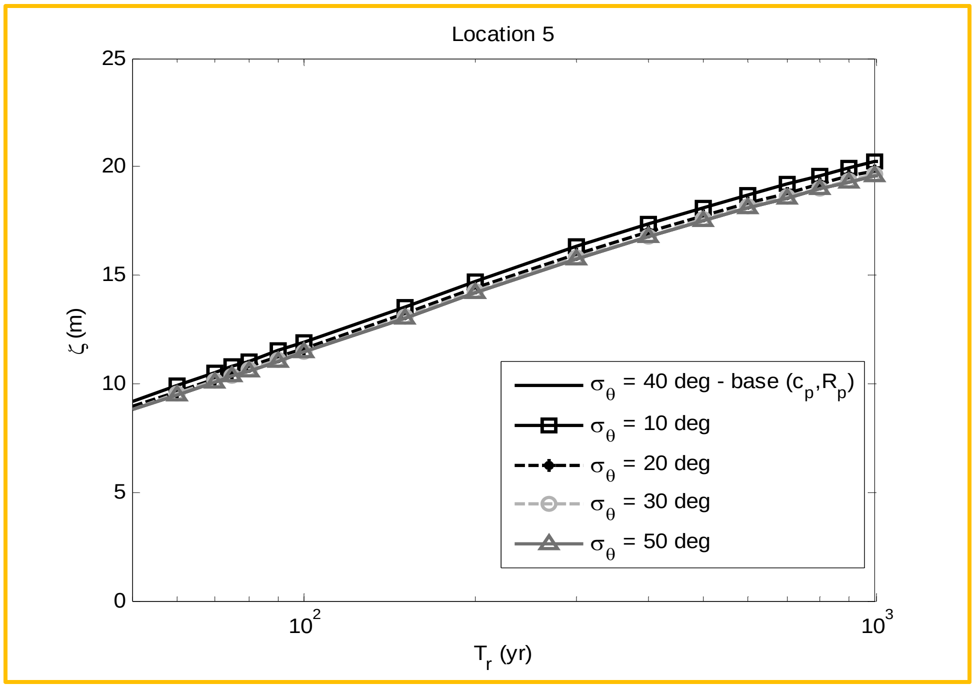

Figure 4.128: Sensitivity of σ_θ to ζ versus T_r trends at Location 5.

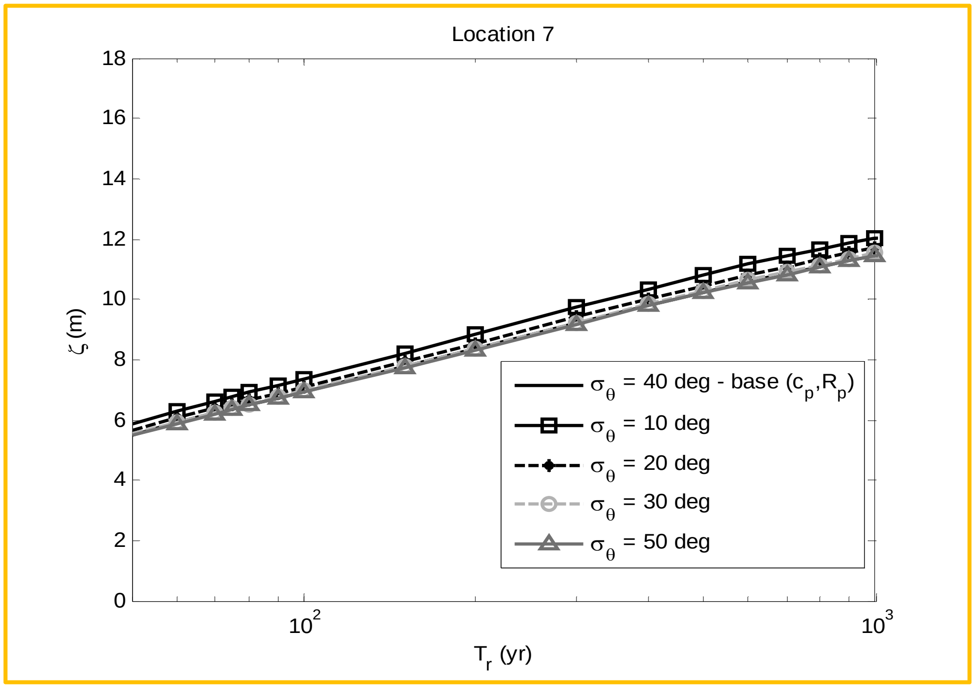

Figure 4.129: Sensitivity of σ_θ to ζ versus T_r trends at Location 7.

In the sensitivity analysis for the influence of $\overline{v_f}$ and σ_{v_f}, it is observed (Figs. 4.130 through 4.137) that an increase in both $\overline{v_f}$ and σ_{v_f} yields a positive response in surge consistently over all the return periods of interest. Table 4.17 shows the statistics for these sensitivity tests. While the variation in $\overline{v_f}$ yields maximum percentage differences at the relatively low-surge events (i.e. $T_r = 50$ yr) at all locations (up to 14.8 % at location 1), the maximum percentage differences due to an increase in σ_{v_f} are not consistently associated with either low or high T_r events. The observed increase in ζ over all return periods when $\overline{v_f}$ and σ_{v_f} increase suggests that in both cases, the probabilities of high surges are associated with the domain of the surge matrix populated by storms with high forward speed – storms with higher forward speeds generally produce higher surge values at the coast. For the $\overline{v_f}$ case, the percentage differences of 14.8 %, 12.4 %, 6.0 % and 8.0 % at locations 1, 3, 5 and 7 suggest that if the assumed value of $\overline{v_f}$ in Equation 4.39 deviated from the true value by up to 5.7 m/s, then the uncertainty in the T_r versus ζ curves could increase by these percentage differences at the respective locations. The percentage differences associated with the variation in σ_{v_f} are relatively smaller, suggesting a less significant impact on the T_r versus ζ curves if the true value deviated from the assumed within a 1.75 to 5.75 m/s range.

Table 4.17: A summary of differences in surge at specified return periods, for $\overline{v_f}$ and σ_{v_f} sensitivity analysis.

Location	Return Period (yr)	$\zeta_{\overline{v_f}-base} - \zeta_{\overline{v_f}-sensitivity}$		$\zeta_{\sigma_{v_f}-base} - \zeta_{\sigma_{v_f}-sensitivity}$	
		Maximum Absolute difference (m)	% Difference using Maximum Absolute Difference	Maximum Absolute difference (m)	% Difference using Maximum Absolute Difference
1	50	0.64	**14.8**	0.20	**4.7**
	100	0.71	**13.5**	0.25	**4.7**
	500	0.86	**11.8**	0.34	**4.7**
	1000	0.90	**11.3**	0.42	**5.2**
3	50	0.51	**12.4**	0.16	**3.8**
	100	0.60	**11.0**	0.15	**2.7**
	500	0.75	**9.1**	0.22	**2.6**
	1000	0.82	**8.8**	0.27	**2.9**
5	50	0.53	**6.0**	0.11	**1.2**
	100	0.59	**5.2**	0.11	**1.0**
	500	0.74	**4.2**	0.12	**0.7**
	1000	0.81	**4.1**	0.19	**1.0**
7	50	0.48	**8.8**	0.10	**1.8**
	100	0.56	**8.0**	0.13	**1.9**
	500	0.75	**7.3**	0.20	**1.9**
	1000	0.78	**6.7**	0.29	**2.5**

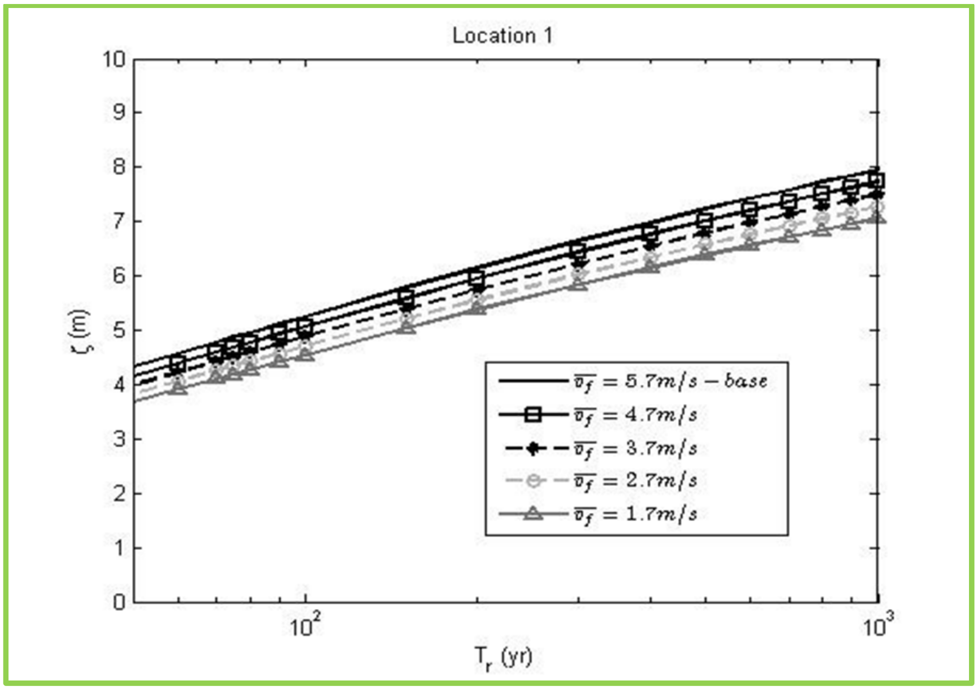

Figure 4.130: Sensitivity of $\overline{v_f}$ to ζ versus T_r trends at Location 1.

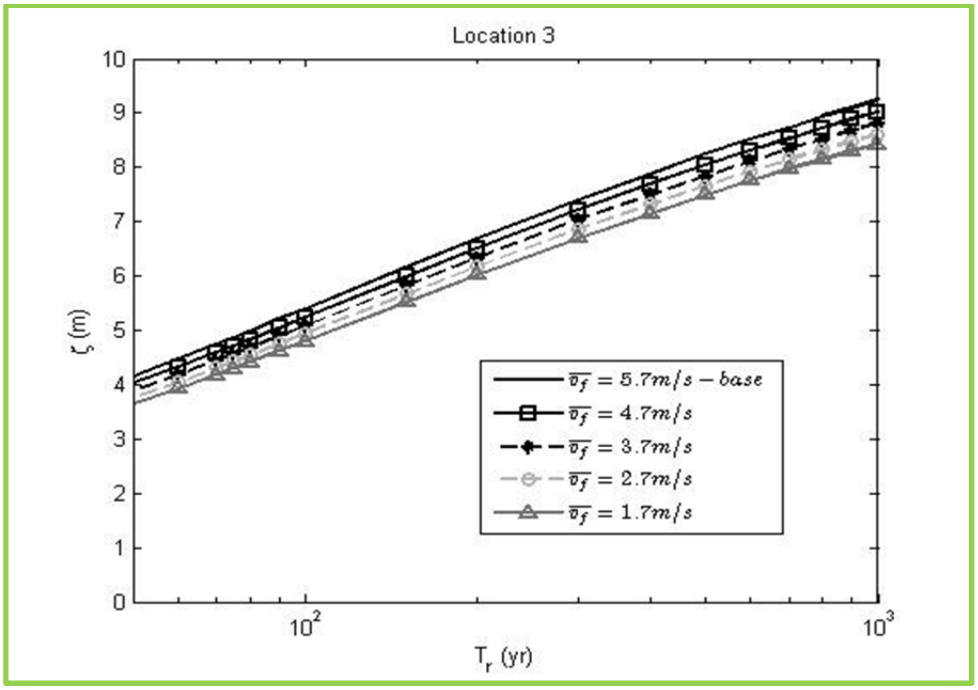

Figure 4.131: Sensitivity of $\overline{v_f}$ to ζ versus T_r trends at Location 3.

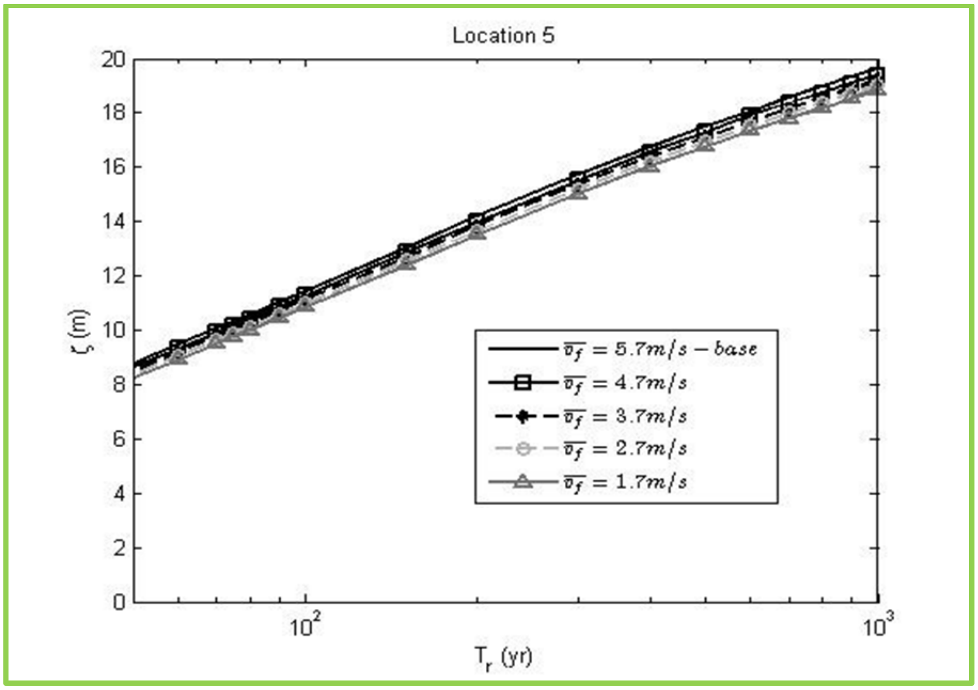

Figure 4.132: Sensitivity of $\overline{v_f}$ to ζ versus T_r trends at Location 5.

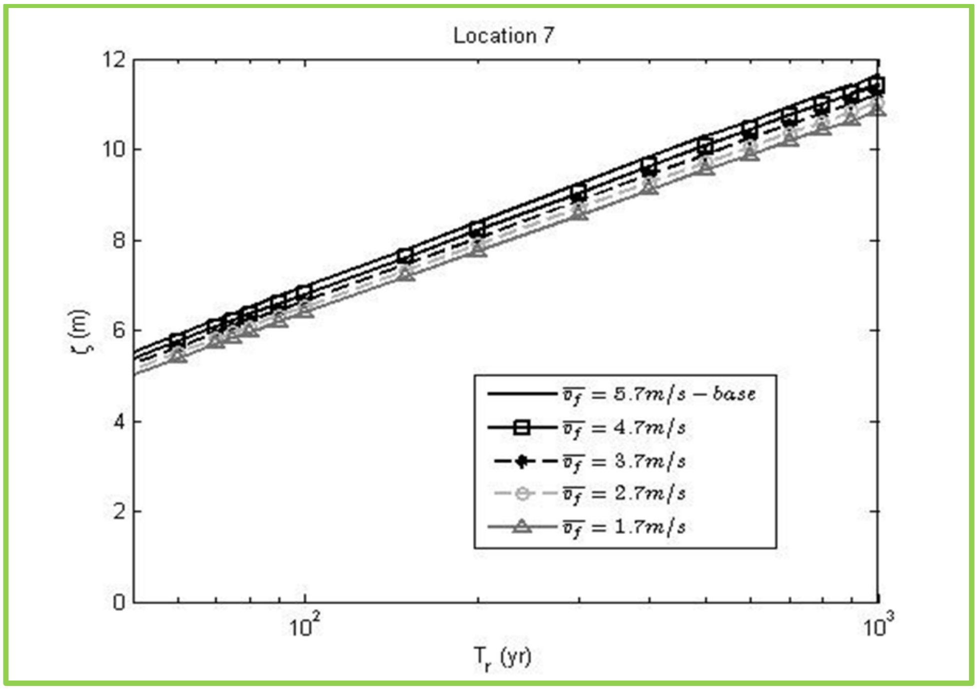

Figure 4.133: Sensitivity of $\overline{v_f}$ to ζ versus T_r trends at Location 7.

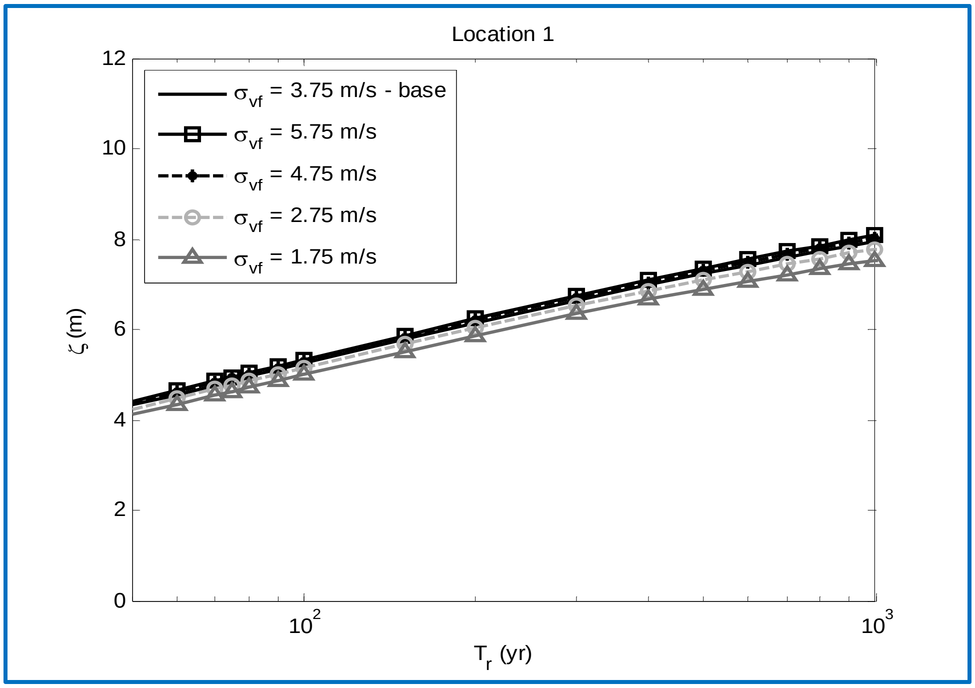

Figure 4.134: Sensitivity of σ_{v_f} to ζ versus T_r trends at Location 1.

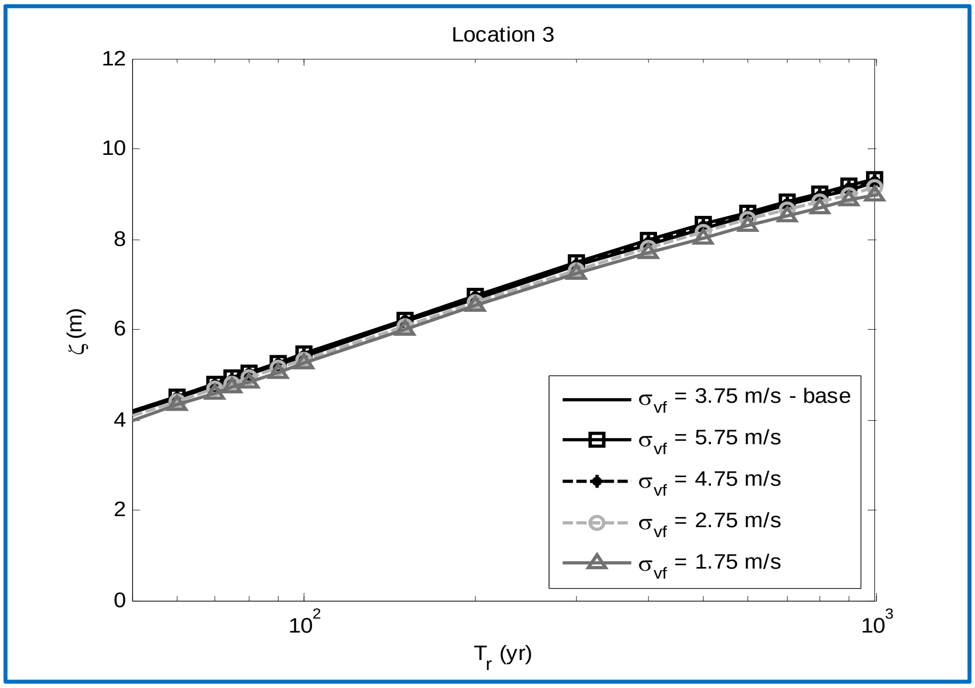

Figure 4.135: Sensitivity of σ_{v_f} to ζ versus T_r trends at Location 3.

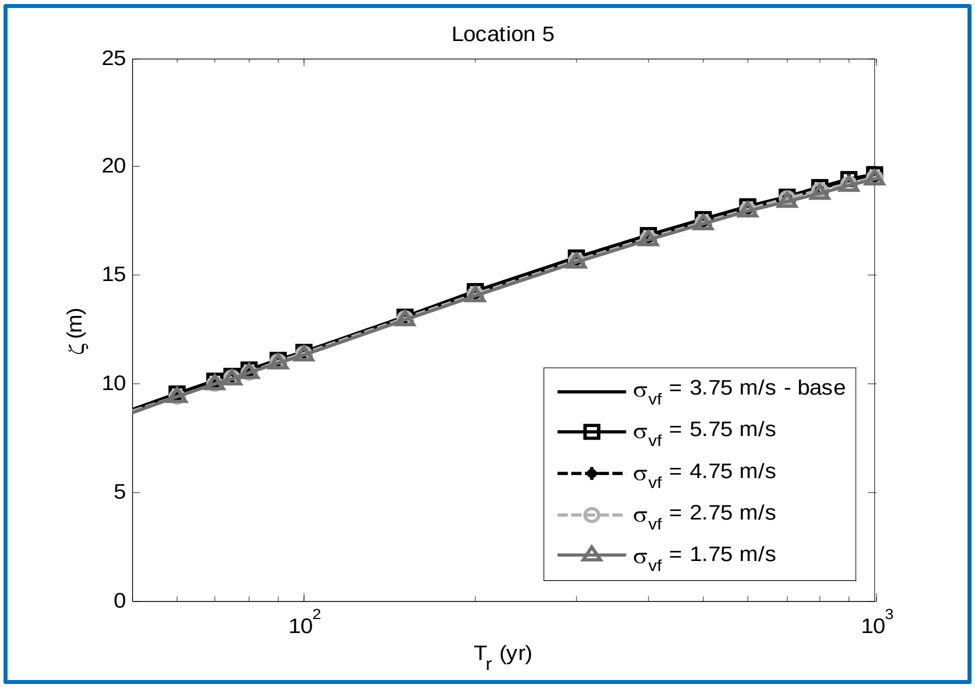

Figure 4.136: Sensitivity of σ_{v_f} to ζ versus T_r trends at Location 5.

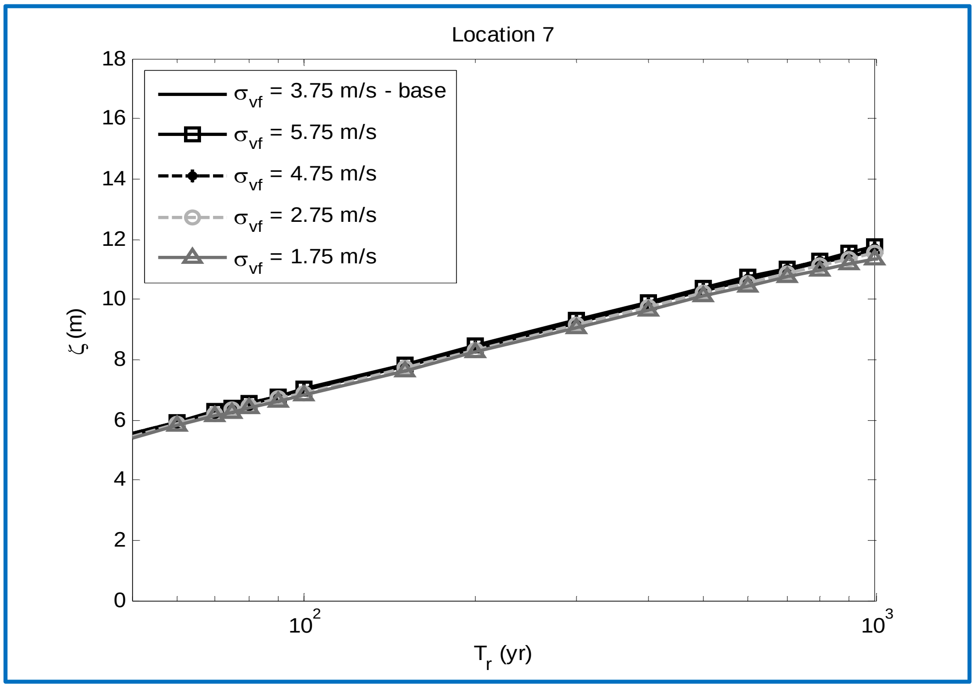

Figure 4.137: Sensitivity of σ_{v_f} to ζ versus T_r trends at Location 7.

4.5.3 Effect of Climate Change on the Surge versus Return Period Curves

Regarding SLR scenarios in the JPM-OS, only the scenarios for c_p and R_p were considered, along with the four SLR scenarios. To adjust the surge values in the surge matrix for SLR effects, a linear fit was applied to the data as described in section 4.3 of this dissertation. The resulting coefficients used in adjusting the surge values are presented in Table 4.18.

Table 4.18: Coefficients of linear fit used in adjustment of surge matrix for SLR effect.

Location	Slope	intercept
1	0.951	0.037
3	0.930	0.049
5	0.965	0.008
7	0.898	0.070

The results (Figs. 4.138 through 4.141) are not surprising, as the T_r versus ζ curves increase consistently with SLR; however, it can be observed that as T_r increases, the deviation of surge values for SLR higher than zero gradually reduces. For the maximum increase in SLR of 2.0 m, the percentage differences in surge are 41.3 %, 42.4 %, 13.9 % and 28.2 % at locations 1, 3, 5 and 7 respectively, and they correspond to the 50-yr return period. As the return periods increase, the percentage differences due to SLR variation reduce at all four locations; this is consistent with surge reducing at the coast with increase in SLR. The variation of these increments across the four locations indicates that SLR effects on the T_r versus ζ curves can vary significantly by location, emphasizing the importance of accounting for this influence with the approach used here.

On the impacts of hurricane intensification on surge in the JPM-OS, three scenarios were investigated using assumed values of change in sea surface temperature (dSST). The values used were 0.5^{o}C, 1.0^{o}C and 1.5^{o}C, and are representative of low, middle and high estimates of climate storylines in the literature (e.g. Irish et al., in press). Higher resolutions of landfall location and central pressure were used for this case (1 km and 1 mb, respectively). Figures 4.142 through 4.145 show the T_r versus ζ curves that delineate the effect of hurricane intensity on the extreme value probabilities. At all locations considered (1, 3, 5 and 7), the curves show that the impact of hurricane intensification on surge becomes increasingly important as return period increases. This finding is consistent with more intense hurricanes producing higher surge values. Table 4.19 summarizes the statistics for the T_r versus ζ curves.

Table 4.19: Summary of differences in surge at specified return periods, for JPM-OS climate change analysis.

Location	Return Period (yr)	$\zeta_{SLR_{base}} - \zeta_{SLR}$		$\zeta_{\Delta SST_{base}} - \zeta_{\Delta SST}$	
		Maximum Absolute difference (m)	% Difference using Maximum Absolute Difference	Maximum Absolute difference (m)	% Difference using Maximum Absolute Difference
1	50	1.66	**41.3**	0.21	**11.3**
	100	1.58	**32.5**	0.24	**11.1**
	500	1.39	**20.7**	0.29	**9.7**
	1000	1.33	**18.3**	0.30	**9.4**
3	50	1.66	**42.4**	0.15	**7.4**
	100	1.54	**29.7**	0.23	**9.2**
	500	1.25	**15.8**	0.33	**10.1**
	1000	1.19	**13.3**	0.37	**10.2**
5	50	1.20	**13.9**	0.37	**8.0**
	100	1.12	**9.9**	0.51	**9.1**
	500	0.90	**5.2**	0.72	**10.1**
	1000	0.81	**4.2**	0.77	**10.0**
7	50	1.52	**28.2**	0.21	**6.5**
	100	1.37	**20.3**	0.31	**7.9**
	500	1.15	**11.5**	0.42	**8.4**
	1000	1.13	**10.2**	0.47	**8.7**

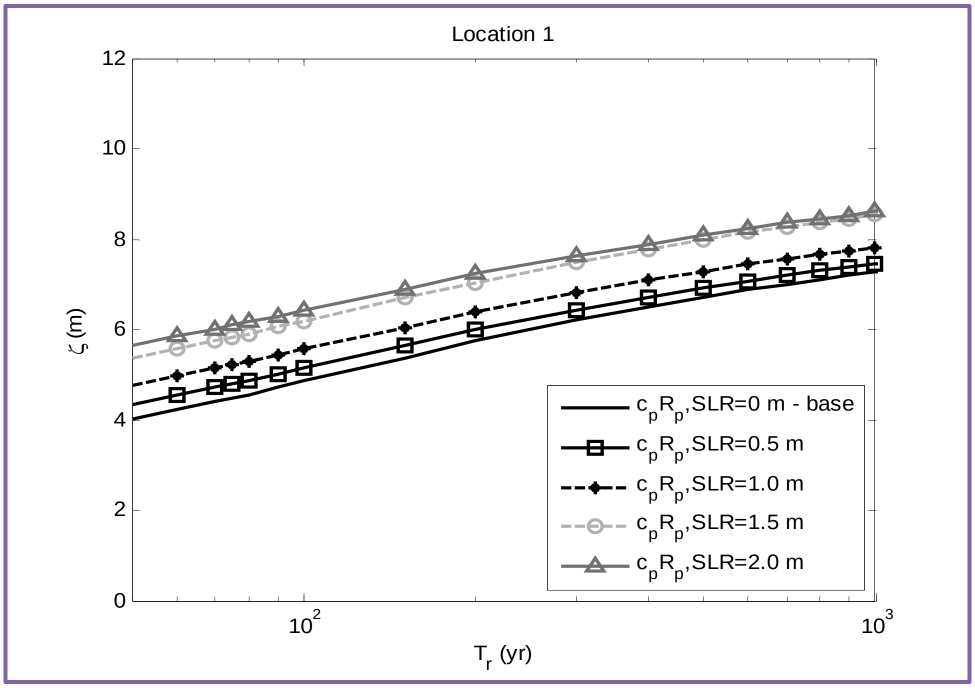

Figure 4.138: Effect of SLR on ζ versus T_r trends at Location 1.

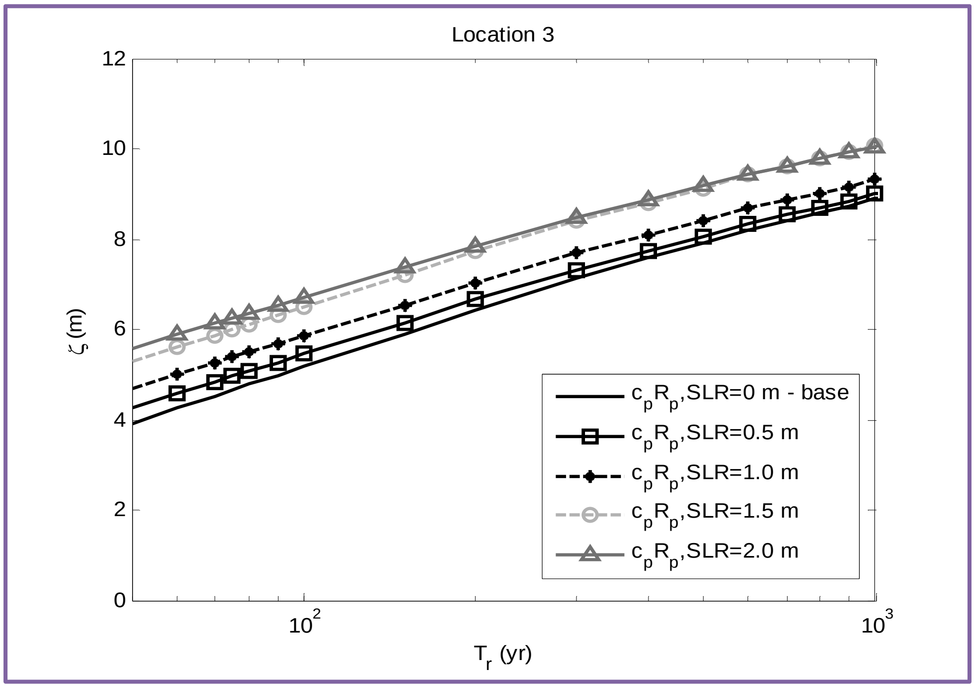

Figure 4.139: Effect of SLR on ζ versus T_r trends at Location 3.

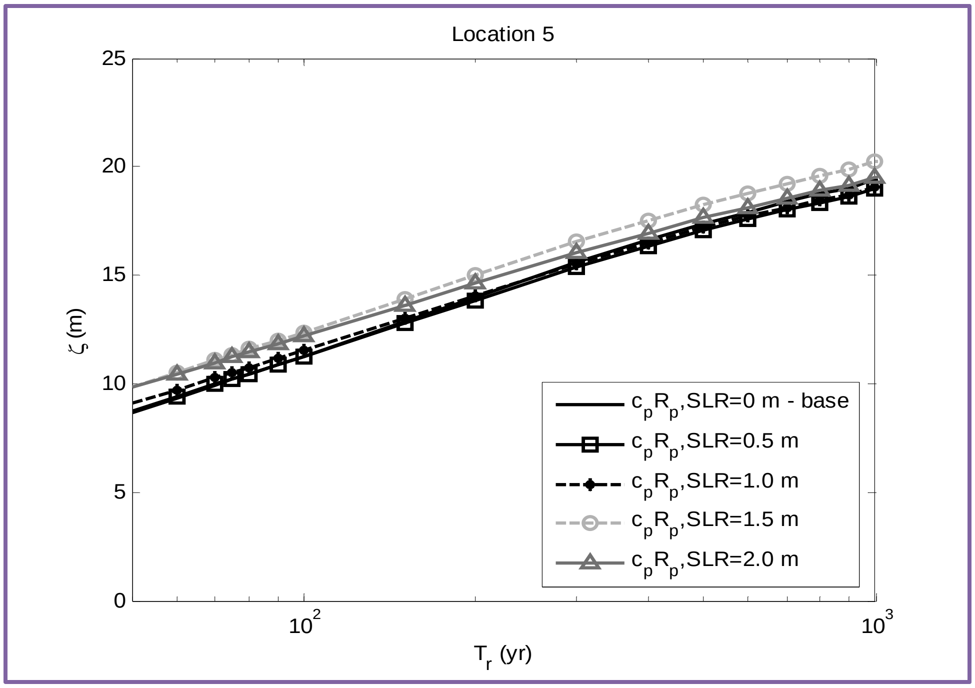

Figure 4.140: Effect of SLR on ζ versus T_r trends at Location 5.

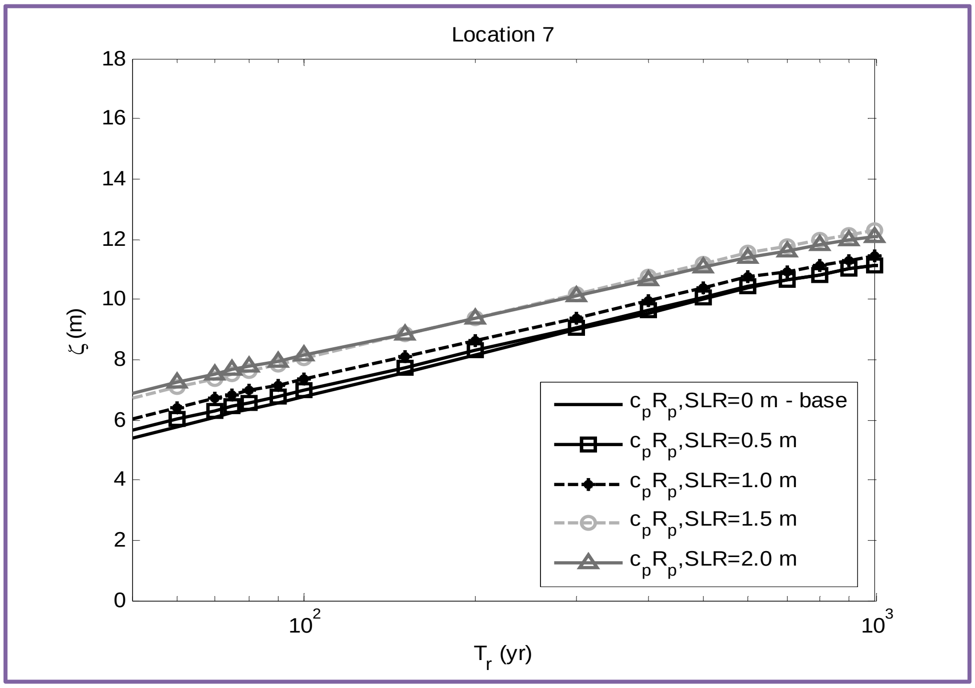

Figure 4.141: Effect of SLR on ζ versus T_r trends at Location 7.

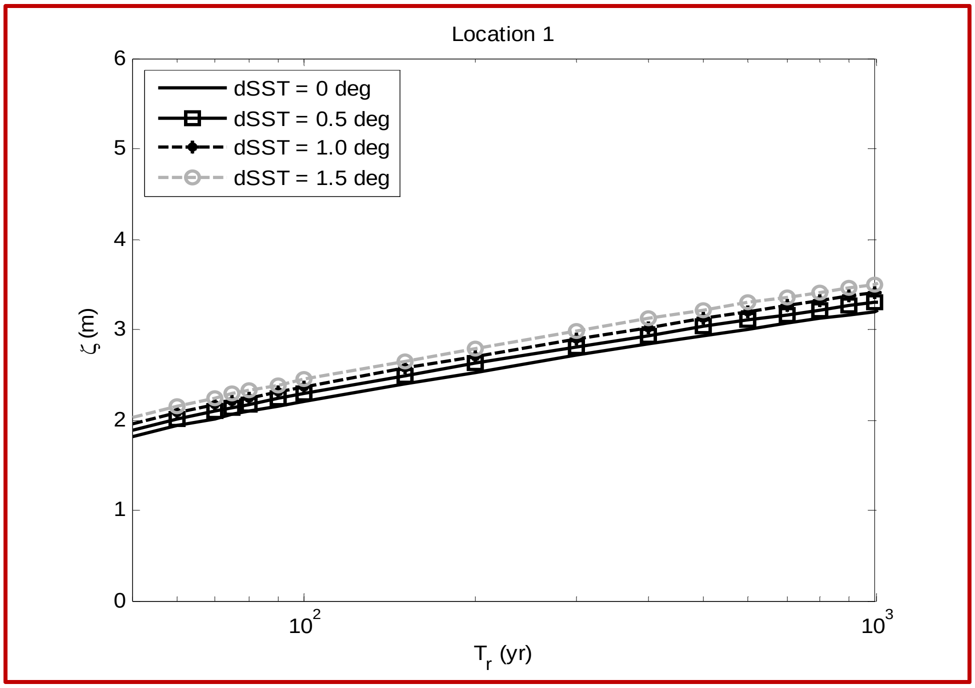

Figure 4.142: Effect of dSST on ζ versus T_r trends at Location 1.

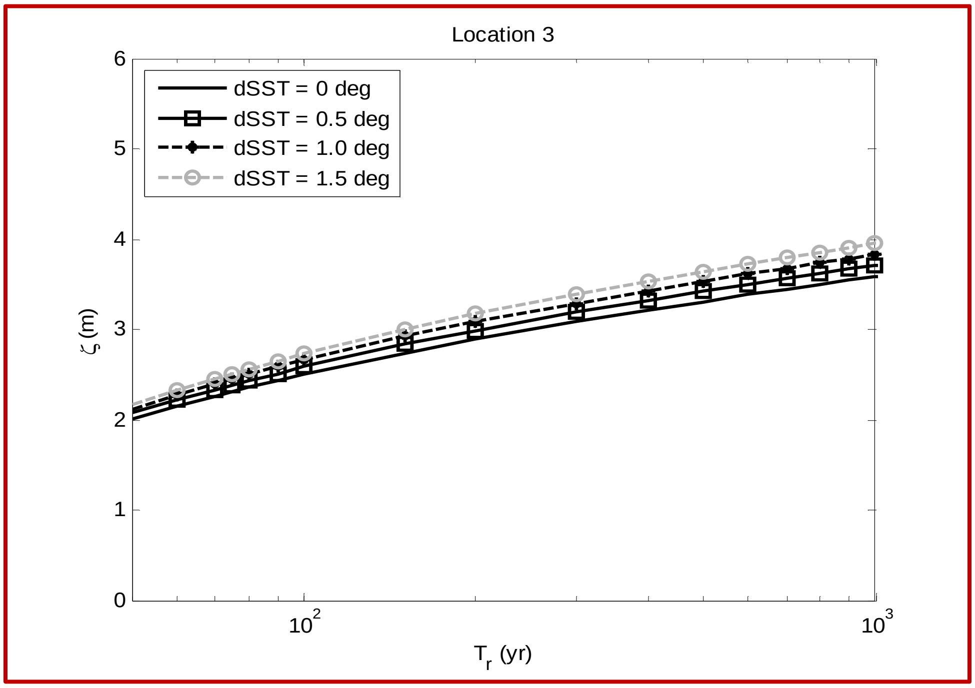

Figure 4.143: Effect of dSST on ζ versus T_r trends at Location 3.

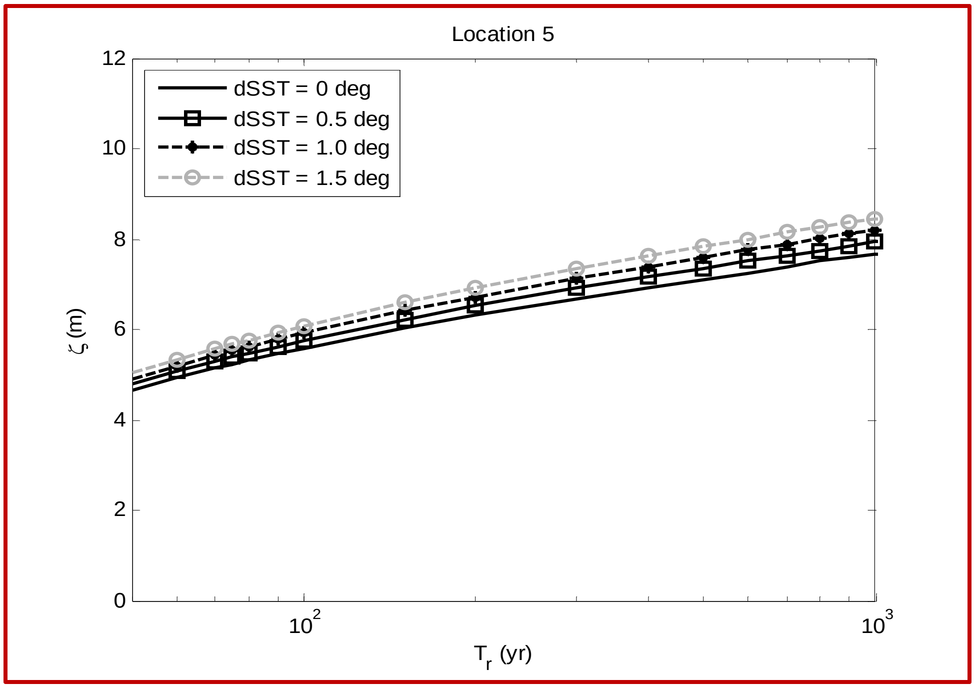

Figure 4.144 : Effect of dSST on ζ versus T_r trends at Location 5.

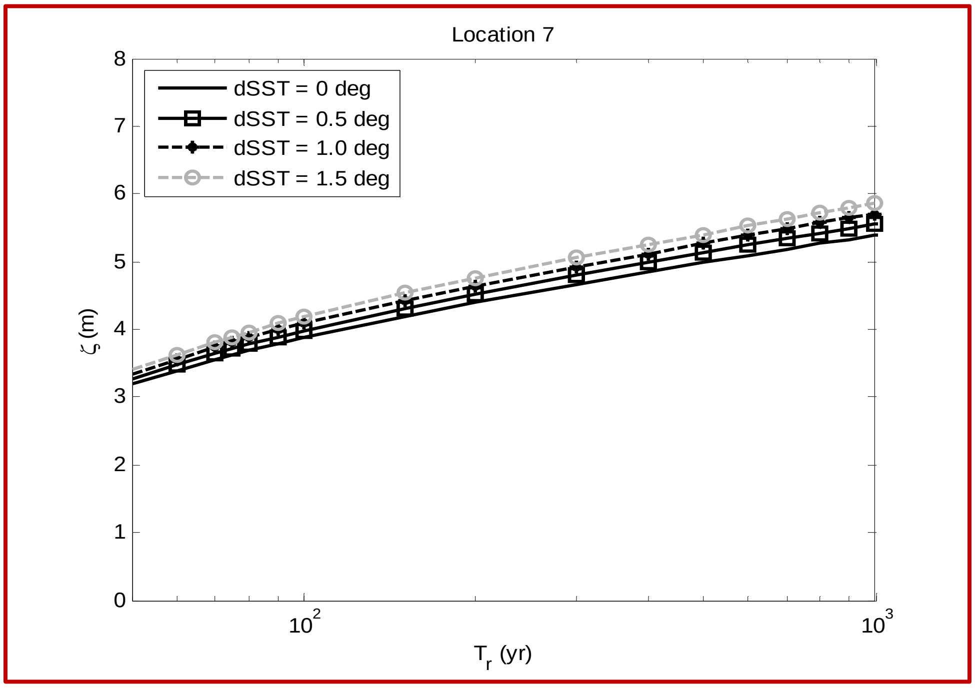

Figure 4.145: Effect of dSST on ζ versus T_r trends at Location 7.

At location 1, the highest percentage difference is associated with a return period of 50 yr - at this location, change in hurricane intensity has a greater impact on the smaller storm events, than it does on bigger events (i.e. those generating higher surge).

The hypothesis that including v_f and θ scenarios in the JPM-OS framework will yield significant changes in surge versus return period curves, does not hold true; as shown by the return period curves and the statistics, the increment in surge at each return period is very small - the maximum percentage increase in surge considering all locations is 6.7 %. Climate change however has a bigger impact on the JPM-OS results. Changes in SLR and hurricane intensification show percentage increments in surge of up to 42.4 % and 11.3 % respectively – these changes are very significant, and they emphasize the importance of accounting for climate change in extreme value analysis.

CHAPTER V

SUMMARY AND CONCLUSIONS

5.1 Research Summary

The need for assessment of coastal hazards and risk due to hurricane flooding is a fundamental one, and is getting significant attention in the field of coastal engineering. Amongst the available methods for risk analysis, the Joint Probability Method with Optimal Sampling (JPM-OS, Resio et al., 2009) has been shown to be an effective approach in estimating the probabilities associated with different levels of flooding due to storm surge. A critical part of the JPM-OS method is the estimation of surge heights for a large number of scenarios. Addressing this aspect of the method with high resolution numerical models is almost impracticable with the computing resources currently available for such storm surge modeling, and would require an enormous amount of time. Using Surge Response Functions (SRFs) to evaluate surge estimates for the required amount of storm scenarios in the JPM-OS framework is a much more effective approach. The robustness and reliability of such SRFs must then be ensured, through the incorporation of vital parameters that contribute to storm surge generation.

Review of literature (discussed in Chapter II) shows the relative importance of forward speed (v_f), approach angle (θ) and Sea Level Rise (SLR) on surge generation, at the open coast and in bays. Surge trends discussed in Chapter IV affirm the findings reported in literature, and also led to additional observations highlighted in section 5.2 of this dissertation. Essentially, surge varies with all three parameters to different degrees at different locations. Establishing this fact implied that to evaluate surge for different scenarios of v_f, θ and SLR within the JPM-OS framework, the previous versions of the SRFs (Song et al. 2012 for open coast locations, and Katyal, 2009 for bays) needed to account for the influences of these parameters to minimize the uncertainty in the surge estimates.

Having identified this need, our research has incorporated the influence of hurricane forward speed (v_f), approach angle (θ) and Sea Level Rise (SLR) into the response functions (for open coast locations and bays), and has addressed the influence of climate change on surge probabilities within the JPM analysis. This has been accomplished by first, investigating surge trends as a function of v_f, θ and SLR at the open coast and bays, to identify the parameters associated with surge generation at these locations. Parameters identified as essential to accounting for the effects of v_f, θ and SLR were then used to develop dimensionless scaling laws for onward incorporation into the original dimensionless SRFs. The adequacy of these scaling laws in capturing the influence of v_f, θ and SLR on surge, was judged by quantifying the errors (root-mean square and mean errors) in back-predicted surge using the SRFs. Errors associated with the SRFs obtained after including the effects of v_f and θ are of similar magnitudes to those of high-resolution numerical models discussed in Chapter III.

5.2 Major Research Findings

5.2.1 Major Contributions to the field knowledge

This work has advanced knowledge regarding the development of surge response functions for peak surge estimation in open coast locations and bays. Specifically, scaling laws have been developed to account for the influence of forward speed and approach angle in the SRFs for open coast locations and bays. The formulation to account for the influence of forward speed in the open coast response functions relates the time available for surge generation for a storm of given speed, to a characteristic time defined as the time it would take for a storm propagating at 5.7 m/s to generate surge over/across a continental shelf section with given width. This dimensionless term is weighted by a function of the continental shelf width. For the influence of approach angle, the dimensionless formulation developed in this research is derived by isolating the influence of rotating the hurricane wind field from a shore-normal direction. On application of these dimensionless terms in the SRFs, a general improvement is seen the potential of the SRFs to estimate peak surge with higher accuracy. The revised SRF formulation has the advantage of estimating at least 63 % of storm events with surge values of 2 m or greater along the Texas coast with better accuracy, when compared to the Song et al. (2012) version of the SRFs. With emphasis on the estimation of surges for extreme events in the JPM-OS framework, this represents a significant improvement in the SRFs, and thus a useful contribution to this field of knowledge. On a location-to-location basis, the maximum improvement seen in comparing the revised and previous open coast SRF forms is 12.5 %, with other locations showing an improvement in the range of 2.9 to 8.1 %.

In the bays, this work presents the incorporation of the influence of forward speed in the SRFs – the dimensionless scale comprises the time it takes for surge to fully develop in the bay, and a length scale – the length of the bay. The dimensionless surge equation has been modified such that storm size scales with the farthest distance through which water mass will move inside the bay from its center of gravity. This revision on how the influence of storm size is accounted for, has led to a better representation of surge data with varying sizes in dimensionless space, allowing better model fitting to the dimensionless surge data, and improved back-prediction of peak surge. For the influence of approach angle, the same formulation as in the open coast is applied to the bays. In comparison, the revised SRF for bays out-performs Katyal's (2009) formulation (by up to 54% in Matagorda Bay) – this represents a valuable improvement in the accuracy of the SRFs. In this work, not only have important parameters influencing surge generation in the bays been identified and discussed, the limitations in the revised SRFs have also been clearly outlined with possible steps to overcome them in further research. Regarding sea level rise, it is has been shown in this work that for open coast and bay locations, a linear model can be used to account for the influence of SLR on surge.

It is believed that some more improvement can be achieved in the open coast SRFs by further scaling the terms in a systematic way that accounts for local characteristics of the landfall location for the storms. The approach angle formulation for the open coast SRFs has been seen to worsen surge prediction at locations with relatively small shelf widths. Therefore, a more flexible scale of the θ term which is sensitive to geometric characteristics of the location of interest could improve the performance.

In the bays, it is more challenging to derive a universal parametric model of the SRFs, as many storms impact different bays with different surge magnitudes. Factors such as the shape, size and depth of the bays, as well as the presence or absence of adjoining water bodies add to the complications surrounding the derivation of a universal SRF model for the bays. It has been found in this research that for the same derived dimensionless function, storms which constitute scatter in dimensionless space in Corpus Christi Bay, do not necessarily constitute scatter in Matagorda Bay, and vice versa. To obtain a form of the SRFs that is truly general and applicable to any bay, further investigation to other factors that affect surge generation in the bays is required – recommended steps towards such investigation have been discussed in section 4.4 of this dissertation. However, the revised formulations for storm size, forward speed and approach angle have been shown to describe the physics associated with surge generation to a good extent – though not satisfactorily. The conditions applied in the model indicate that it has limitations, and further investigation is required to understand the effects that must be accounted for, in order to the reduce the dependency of the model on site-specific parameterizations.

Extreme value analysis using the developed surge response functions shows that incorporating varying v_f and θ scenarios in generating flood probabilities makes only a small difference in return periods. However, it is interesting to find that the T_r versus ζ curves are sensitive to the assumed mean and standard deviations of the probability distributions for the range of T_r typically considered in coastal engineering design projects. The sensitivity of these parameters to the return period curves are seen to be dependent on the deviation of the tested values from conditions of forward speed and approach angle that are known to produce high surge values; high forward speeds, and approach angles close to shore-normal are known to be associated with relatively high surge values, and the sensitivity tests show that if assumed values approach these conditions (higher forward speeds and small angles) then there is an increase in the observed surge trends with return periods. The changes in the return period curves with increase in SLR and increase in SSTs show that these parameters impact the JPM results significantly – by up to 41.3 % and up to 11.3 % respectively, for the range of values considered.

5.2.2 Observations Relating to Previous Research

On the influence of v_f on surge , findings in this research include that the continental shelf width affects the time available for surge generation, for a storm of given speed - this is in agreement with Irish and Resio (2010). Furthermore, Jelesnianski’s (1972) finding on the availability of critical forward speeds above which surge magnitudes do not increase, has also been seen in the v_f surge trends. In general, hurricane forward speeds are seen to have a positive effect on storm surge along the coast, similar to the results of Rego and Li (2009). The variation of surge with forward speed at a location of interest is dependent on the proximity of such a location to the landfall point, and on the side of the storm impacting the region – stronger positive trends of surge are observed to be associated with storms making landfall to the left of the location, such that sustained wind action over the region results in significant surge generation. In the bays, it has been observed that at very interior locations, storms traveling at slower speeds can generate higher surge than fast moving storms. This observation is in agreement with Weisberg and Zheng (2006), and is due to the slower storms allowing wind action over the bays for a longer time (than the faster storms), leading to higher surges. While none of the findings related to forward speed is new, these observations have significantly guided the analysis and development of the surge response functions.

Findings regarding the approach angle of the storm are somewhat interesting. Three primary effects were identified as being associated with the influence of hurricane approach angle on surge generation along the coast:

- first, the tendency for the strongest portion of the storm winds to push surge toward the location of interest, due to its orientation as it approaches the coast.
- second, the stretch of shelf length actually traversed by the storm; for a coast with varying continental shelf width, this effect is important as storms making landfall at a given point but with varying approach angles may have significantly varying shelf-crossing lengths.
- lastly, the proximity of the storm's path to the location of interest as it approaches the coast. Surge generated by a storm passing by a location (as against making landfall close to the location) could be more significant than that from a storm making landfall close to the location, but oriented away from the location of interest.

The surge trends showed that these effects have varying dominating potentials over each other along the Texas coast. In the bays, the influence of approach angle on surge magnitudes was seen to depend on:

- the proximity of the storm track to the entrance of the bay as the storm travels towards or across the coast, and
- the distance of the storm track to the location of interest inside the bay, as the storm traverses inland beyond the bay

Weisberg and Zheng (2006) discussed the influence of the storm proximity to the entrance of Tampa Bay. The authors noted that it is difficult to identify the worst-case approach angle for the bay, since the orientation that may present to be the worst case for one area of the bay may not be for another. Findings in the surge trends for Corpus Christi and Matagorda Bays presented in section 4.2 agree with Weisberg and Zheng (2006) – the track orientation producing the highest surge at one location, may not be the same one producing the highest surge at another location with the bays.

5.3 Future Research

Improvements in the current form of the Bay SRFs are required. Essentially, the ultimate goal is to achieve parameterized SRFs which can be applied for surge development in any bay. More investigation is needed to account for missing physics in the current form of the SRFs, and relieve the model of site-specific dependencies as much as possible. The open coast SRFs can be further improved by revising the formulation for approach angle, such that it includes the contribution of varying continental shelf widths for reasons mentioned earlier.

The current versions of the SRFs for the open coast and bays do not account for the influences of waves on surge. Preliminary findings from ongoing research related to this work suggest that the impact of waves on surge varies by location and storm characteristics. To fully account for the effects of waves in the SRFs, a sufficient amount of simulations needs to be performed to investigate the variation of surge. While the variations in surge may be small enough that a simplified correction could be applied to incorporate the influence of waves in some locations (such as open coast locations), explicit analysis may be needed in more complex regions like bays.

Further applications of the SRFs developed in this research are needed at locations different from the Texas coast. The performance of the formulations at such locations would further delineate the robustness of the SRFs. Even along the Texas coast, other relatively large estuaries such as Galveston Bay need to be considered for SRF analysis, as this location is very close to the Houston metropolis – a highly populated area with important infrastructure, hence under high risk of damage due to hurricanes. Given that Galveston Bay is a very irregularly shaped bay, it is important to assess the performance of the discussed formulations, and investigate any modifications that would be needed to ensure good results. Preliminary investigation of surge trends using five landfall points in Galveston Bay shows some similarity to Matagorda and Corpus Christi Bay trends. Other bays with different characteristics (e.g. bays with no barrier islands – like Bay St. Louis, Mississippi, USA, would also be important to study for the same purpose.

5.4 Conclusions

Scaling laws have been used to account for the influence of forward speed and approach angle in surge response functions for the open coast and bays. The formulations developed to account for these affects are informed by the mechanics of surge generation at the open coast and in the bays. The performance of the revised SRFs for the open coast has been shown to be significant, especially in the estimation of high-surge events which are important for extreme value analysis. For the bays, the revised SRFs have been shown to out-perform Katyal's (2009) version. A simple linear correction is shown to be sufficient in accounting for the influence of SLR on surge – this has been deduced by investigating surge trends with respect to SLR at open coast locations and in the bays (Corpus Christi and Matagorda Bays).

The hypotheses regarding the possibility of improving the accuracy of the SRFs by representing the influence of forward speed, approach angle and sea level rise using scaling laws and simplified corrections have held true. The hypothesis that including forward speed and approach angle in the JPM-OS analysis would make a difference in the probabilities and return periods is not so true, given that the differences seen in the T_r versus ζ curves are not too significant, at return periods typically considered in coastal engineering practice.

Comparatively, on including the forward speed and approach angle data, the previous version of the SRFs for bays (Katyal, 2009) indicated a weaker performance than the previous SRFs for the open coast locations (Song et al., 2012) in estimating peak surge. This is not surprising, given that the variability of surge with v_f and θ in the bays is higher than at open coast locations – it indicates that improvement in the SRFs for the bays by accounting for v_f and θ is likely to produce more significant differences in the JPM results (T_r versus ζ).

Overall, the primary objective of developing parameterizations to account for the influence of forward speed, approach angle and sea level rise in the SRFs for open coast locations and the bays has been achieved. Although the current form of these parameterizations could be improved, their performance at this point demonstrates a welcomed improvement in the potential of the SRFs to estimate peak surge with better accuracy. In demonstrating the application of the SRFs in to the JPM, the importance of climate change parameters on the surge estimates for considered return periods is shown to be higher than the impacts of hurricane forward speed and approach angle. In conclusion, all important meteoroidal parameters and relevant physics need to be accounted for, to attain the best possible accuracy in the SRFs.

REFERENCES

Bender, M. A., Knutson, T. R., Tuleya, R. E., Sirutis, J. J., Vecchi, G. A., Garner, S. T., and Held, I. M. (2010): Modeled impact of anthropogenic warming on the frequency of intense atlantic hurricanes. Science, 327(5964), 454-458.

Bengtsson, L., Hodges, K. I., Esch, M., Keenlyside, N., Kornblueh, L., Luo, J., and Yamagata, T. (2007): How may tropical cyclones change in a warmer climate. Tellus, 59A, 539–561.

Berg, R. (2006): Tropical cyclone report on hurricane Ike. Web link: www.nhc.noaa.gov/pdf/TCR-AL092008_Ike_3May10.pdf, 1 – 55.

Borgman, L.E, Miller, M., Butler, L. and Reinhard, R. (1992): Empirical simulation of future hurricane storm histories as a tool in engineering and economic analysis. Proceedings of the fifth international conference on civil engineering in the oceans v, College Station, Texas.

Bunya, S., Dietrich, J.C., Westerink, J.J., Ebersole, B.A., Smith, J.M., Atkinson, J.H., Jensen, R., Resio D.T., Luettich, R.A., Dawson, C., Cardone, V.J., Cox, A.T., Powell, M.D., Westerink, H.J. and Roberts H.J. (2009): A high resolution coupled riverine flow, tide, wind wave and storm surge model for southern Louisiana and Mississippi: Part I – model development and validation. Monthly Weather Review, 138, 345 –377.

Cazenave, A. and Nerem, R. S. (2004): Present-day sea level change: observations and causes. Reviews of Geophysics, 42, RG3001, 1 – 20.

Chen, C., H. Liu, and R. C. Beardsley (2003): An unstructured grid, finitevolume, three-dimensional, primitive equation ocean model: Application to coastal ocean and estuaries. Journal of Atmospheric and Oceanic Technology, 20, 159–186.

Church, J.A., and White, N.J. (2006): A 20th century acceleration in global sea-level rise. Geophysical Research Letters, 33: L01602.

Dietrich, J.C., Bunya, S., Westerink, J.J., Ebersole, B.A., Smith, J.M., Atkinson, J.H., Jensen, R., Resio D.T., Luettich, R.A., Dawson, C., Cardone, V.J., Cox, A.T., Powell, M.D., Westerink, H.J. and Roberts H.J. (2010): A high resolution coupled riverine flow, tide, wind wave and storm surge model for Southern Louisiana and Mississippi: Part II – Synoptic Description and Analyses of Hurricanes Katrina and Rita. Monthly Weather Review, 138, 378-404.

Elsner, J.B., Kossin, J.P. and Jagger, T.H. (2008): The increasing intensity of the strongest tropical cyclones. Nature, 455: 92-95.

Emanuel, K.A., Sundararajan, R. and Williams, J. (2008): Hurricanes and global warming: results from downscaling IPCC AR3 simulations. Bulletin of American Meteorological Society, 89, 347-367.

Federal Emergency Management Agency (2003): SLOSH – Sea, Lake, and Overland Surge from Hurricanes, SLOSH Display Training Document. Web link: http://www.nhc.noaa.gov/ssurge/ssurge_slosh.shtml#SDISPLAY, 3–95.

Frey, A.E., Olivera, F., Irish, J.L., Dunckin, L.M., Kaihatu, J.M., Ferreira, C.M. and Edge B.L. (2010): Potential impact of climate change and hurricane flooding inundation, population affected and property damages in Corpus Christi. Journal of the American Water Resources Association, 46, No. 5.

Gualdi, S., Scoccimarro, E. and Navarra, A. (2008): A. Changes in tropical cyclone activity due to global warming: results from a high-resolution coupled general circulation model. Journal of Climate, 21, 5204–5228.

Ho, F. P. and Myers, V. A. (1975): Joint probability method of tide frequency analysis applied to Apalachicola Bay and St. George Sound, Florida. NOAA Technical Report NWS 18, 43.

Ho, F.P., Su, J.C., Hanevich, K.L., Smith, R.J. and Richards, F.P. (1987): Hurricane Climatology for the Atlantic and Gulf Coasts of the United States. NOAA Technical Report NWS 38, completed under agreement EMW-84-E-1589 for FEMA, 194.

Horton, R., C. Herweijer, C. Rosenzweig, J. Liu, V. Gomitz, and Ruane, A. C. (2008): Sea level rise projections for current generation CGCMs based on the semi-empirical method. Geophysical Research Letters, 35. L02715.

Holland, G.J. (1980): An analytic model of the wind and pressure profiles in hurricanes. Monthly Weather Review, 108, 1213.

Holland, G.J., Webster, P.J. (2007): Heightened tropical cyclone activity in the North Atlantic: natural variability or climate trend? Philosophical Transactions of the Royal Society A, doi:10.1098/rsta.2007.2083, 1 – 22.

Holtcamp, W. (2006): The young Colorado river delta is a lush breeding ground for finfish, shrimp, crab – and controversy. Texas Parks and Wildlife Magazine. Web link: http://www.tpwmagazine.com/archive/2006/jul/ed_5/.

Intergovernmental Panel on Climate Change (2007): Climate change 2007 - The physical science basis summary for policymakers. Web link: http://www.ipcc.ch/publications_and_data/publications_and_data_reports.shtml#.UH3G5VHYEcs.

Irish, J.L., Resio, D.T., and Cialone, M.A. (2009): A surge response function approach to coastal hazard assessment, Part 2: Quantification of spatial attributes of response functions. Natural Hazards, doi:10.1007/s11069-009-0381-4, 183–205.

Irish, J.L. and Resio, D.T. (2010): A hydrodynamics-based surge scale for hurricanes. Ocean Engineering, doi:10.1016/j.oceaneng.2009.07.012, 69-81.

Irish, J.L. and Resio, D.T. (in press): A method for estimating future hurricane flood hazards and associated uncertainty.

Irish, J.L., Resio, D.T. and Ratcliff, J.J. (2008): The influence of Storm Size on Hurricane Surge. Journal of Physical Oceanography, 38, 2003-2013.

Irish, J.L., Frey, A.E., Rosati, J.D., Olivera, F., Dunckin, L.M., Kaihatu, J.M., Ferreira, C.M., Edge, B.L. (2010): Potential implications of global warming and barrier island degradation on future hurricane inundation, property damages, and population impacted. Ocean and Coastal Management, 53, 645-657.

Jarvinen, B.R., Neumann, C.J. and Davis, M.A.S. (1984): A tropical cyclone data tape for the North Atlantic Basin,1886–1983: contents, limitations, and uses. National Oceanic and Atmospheric Administration Technical Memorandum. NWSNHC-22, Coral Gables, FL, 21.

Jelesnianski, C. P. (1972): SPLASH (Special Program to List Amplitudes of Surges from Hurricanes) I. landfall storms: NOAA Technical Memorandum, Silver Spring, Maryland, NWS TDL-46, 56.

Jevrejeva, S., J. C. Moore, and Grinsted, A. (2010): How will sea level respond to changes in natural and anthropogenic forcings by 2100? Geophysical Research Letters, 37.

Katyal, R. (2009): Development of parameterized surge response functions for coastal bays. Master’s Degree Thesis, Texas A&M University.

Kennedy, A.B., Gravois, U., Zachry, B.C., Westerink, J.J., Hope, M.E., Dietrich, J.C., Powell, M.D., Cox, A.T., Luettich Jr, R. A., and Dean, R.G. (2011): Origin of the hurricane Ike forerunner surge. Geophysical Research Letters, 38, L08608, doi:10.1029/2011GL047090, 1-5.

Knabb, R.D., Brown, D.P. and Rhome, J.R. (2006): Tropical Cyclone Report on Hurricane Rita. Web link: www.nhc.noaa.gov/pdf/TCR-AL182005_Rita.pdf, 1 – 33.

Knutson, T.R. and Tuleya, R.E. (2008): Tropical cyclones and climate change: revisiting recent studies at GFDL, in climate extremes and society, Dias, H.F. and Murnane, R.J., Eds., New York, Cambridge University Press, 120-144.

Knutson, T.R. and Tulelya, R.E. (2004): Impact of CO_2-induced warming on simulated hurricane intensity and precipitation: sensitivity to the choice of climate model and convective parameterization. Journal of Climate 17(18), 3477-3495.

Knutson, T.R., Tulelya, R.E., 2000, Shen, W. and Ginis, I. (2000): Impact of CO_2-induced warming on simulated hurricane intensities as simulated in a hurricane model with Ocean Coupling. Journal of Climate, 14, 2458-2468.

Knutson, T. R., McBride, J. L., Chan, J., Emanuel, K., Holland, G., Landsea, C., Held, I., Kossin, J. P., Srivastava, A. K., and Sugi, M. (2010): Tropical cyclones and climate change. Nature Geoscience, 3(3), 157-163.

Levinson, D.H., Vickery, P.J. and Resio, D.T. (2010): A review of the climatological characteristics of landfalling Gulf hurricanes for wind, wave, and surge hazard estimation. Ocean Engineering, 37, 13-25.

Luettich, R., and Westerink, J. (2004): Formulation and numerical implementation of the 2D/3D ADCIRC finite element model version 44.XX. Web link: http://www.adcirc.org, 1-74.

Mann, M.E., Sabbetalli,T.A., and Neu, U. (2007): Evidence for a modest undercount bias in early historical Atlantic tropical cyclone counts. Geophysical Research Letters, 34, L22707, doi:10.1029/2007GL031781, 1-6.

Mayfield, M. (1995): Preliminary report on hurricane Opal. Web link: http://www.nhc.noaa.gov/1995opal.html.

Mousavi, M.E., Irish, J.L., Frey, A.E., Olivera, F., and Edge, B.L. (2009): Global warming and hurricanes: The potential impact of hurricane intensification and sea level rise on coastal flooding. Climate Change, DO1 10.1007/s10584-009-9790-0, 575-597.

Myers, V. A. (1975): Storm tide frequencies on the South Carolina Coast. NOAA Technical Report NWS 16, 79.

National Oceanic and Atmospheric Administration (2003): SLOSH – Sea, Lake, and Overland Surge from Hurricanes, SLOSH Display Training Document. Web link: http://www.nhc.noaa.gov/ssurge/ssurge_slosh.shtml#SDISPLAY, 3-95.

National Oceanic and Atmospheric Administration (1999): Hurricane Basics. Web link: hurricanes.noaa.gov/pdf/hurricanebook.pdf, 1-19.

Niedoroda, A.W., Resio, D.T., Toro, G., Divoky, D. and Reed, C., (2008): Efficient strategies for the joint probability evaluation of storm surge hazards. In: Proceedings of the ASCE conference on Solutions to Coastal Disasters, April 13–16, 2008, Turtle Bay, Hawaii, 242–255.

Oouchi, K., Yoshimura, J., Yoshimura, H., Kosunoki, S. and Noda, A. (2006): Tropical cyclone climatology in a global-warming climate as simulated in a 20km-mesh global atmospheric model: frequency and wind intensity analysis. Journal of Meteorological Society of Japan, 84, 2, 259–276 (2006).

Penland S., and Ramsey K.1(990): Relative sea level rise in Louisiana and the Gulf of Mexico: 1908-1988. Journal of Coastal Research, 6: 323-342.

Pfeffer, W. T., Harper, J. T., and O'Neel, S. (2008): Kinematic constraints on glacier contributions to 21st-century sea-level rise. Science, 321(5894), 1340-1343.

Powell, M.D. and Houston, S.H. (1998): Surface wind fields of 1995 Hurricanes Erin, Opal, Luis, Marilyn, and Roxanne at landfall. Monthly Weather Review, 126, 1259-1273.

Powell, M.D., Houston, S.H., Amat, L.R. and Morisseau-Leroy, N. (1998): The HRD real- time hurricane wind analysis system. Journal of Wind Engineering and Industrial Aerodynamics, 77 and 78, 53–64.

Rahmstorf, S. (2007): A semi-empirical approach to projecting future sea-level rise. Science 315: 368-370.

Rego, J.L. and Li, C. (2009): On the importance of forward speed of hurricanes in storm surge forecasting: a numerical study. Geophysical Research Letters, 36, L007609.

Resio, D.T., Irish, J.L., and Cialone, M.A. (2009): A surge response function approach to coastal hazard assessment. Part 1: Basic concepts. Natural Hazards, doi:10.1007/s11069-009-9379-y.

Resio, D.T., Boc, S. J., Borgman, L., Cardone, V. J., Cox, A., Dally, W. R., Dean, R. G., Divoky, D., Hirsh, E., Irish, J. L., Levinson, D., Alan Niedoroda, A., Mark D. Powell, M. D., Jay J. Ratcliff, J. J., Stutts, V., Suhada, J., Toro, G. R., Vickery, P. J. and Westerink, J. (2007): White Paper on Estimating Hurricane Inundation Probabilities. Web link: http://biotech.law.lsu.edu/katrina/ipet/IPET Vol VIII App 8_Jun 08.pdf, 1-146.

Scheffner, N., Borgman, L. and D. Mark (1996): Empirical simulation technique applications to a tropical storm surge frequency analysis for the coast of Delaware. Journal of Waterway, Port, Coastal and Ocean Engineering, doi http://dx.doi.org/10.1061/(ASCE)0733-950X(1996)122:2(93), 122, 2, 93-101,

Schwerdt, R.W., Ho, F.P., and Watkins, R.R. (1979): Meteorological criteria for standard project hurricane and probable maximum hurricane windfields, Gulf and East coasts of the United States. Technical Report, NOAA-TR-NWS-23, National Oceanic and Atmospheric Administration.

Signorini, S.R., Wei, J.S., and Miller, C.D. (1992): Hurricane-induced surge and currents on the Texas-Louisiana shelf. Journal of Geophysical Research, 97, C2, 2229-2242.

Simpson, R.H. (1974): The hurricane disaster-potential scale. Weatherwise, 27, 169 and 186.

Smith, J.M., Cialone, M.A., Wamsley, T.V. and McAlpin, T.O. (2009): Potential impact of sea level rise on coastal surges in southeast Louisiana. Ocean Engineering, 37, 37-47.

Song, Y.K., Irish, J.L., Udoh, I.E. (2012): Regional attributes of hurricane surge response functions for hazard assessment. Natural Hazards, 64:1475-1490.

Sorensen, R. M. (2003): Basic Coastal Engineering. Chapman and Hall, New York, USA.

Thompson, E.F. and Cardone, V.J. (1996): Practical modeling of hurricane surface wind fields. Journal of Waterway, Port, Coastal and Ocean Engineering, 122(4), 195-205.

Tonkin, H., Holland, G.J., Holbrook, N. and Henderson-Sellers, A. (2000): An evaluation of thermodynamic estimates of climatological maximum potential tropical cyclone intensity. Monthly Weather Review, 128, 746-762.

Toro, G.R., Resio, D.T., Divoky, D., Niedoroda, A.W. and Reed, C. (2010): Efficient joint-probability methods for hurricane surge frequency analysis. Ocean Engineering, 37, 125-134.

United States Army Corps of Engineers (2011): Report on sea-level change considerations for civil works programs. Web link: http://planning.usace.army.mil/toolbox/library/ECs/EC11652212Nov2011.pdf, 1-32.

Vecchi, G.A. and Soden, B.J. (2007): Effect of remote sea surface temperature change on tropical cyclones potential intensity. Nature, 450, 1066-1070.

Vecchi, G.A., Zhao, M., Wang, H., Villarini, G., Rosati, A., Kumar, A., Held, I. and Gudgel, R. (2011): Statistical–dynamical predictions of seasonal North Atlantic hurricane activity. Monthly Weather Review, 139, 1070-1082.

Vermeer, M. and Rahmstorf, S. (2009): Global sea level linked to global temperature. PNAS Early Edition. Web link: www.pnas.org_cgi_doi_10.1073_pnas.0907765106.

Vickery, P.J., Skerjl, P.F., and Twisdale, L.A. (2000): Simulation of hurricane risk in the U.S. using empirical track model. Journal of Structural Engineering, 126, 1222-1237.

Villarini, G., Vecchi, G.A., Knutson, T.R. and Smith, J.A. (2011): North Atlantic tropical storm frequency response to anthropogenic forcing: projections and sources of uncertainty. Journal of Climate, 24, 3224-3238.

Weaver, R. J., and Luettich, R.A., Jr. (2009): 2D vs. 3D storm surge sensitivity in ADCIRC: study of Hurricane Isabel. Eleventh Estuarine and Coastal Modeling Conference, Edited by Spaulding, M., American Society of Civil Engineers, 762-779.

Webster, P.J., Holland, G.J. and Curry, J.A. and Chang, H. R. (2005): Changes in tropical cyclone number, duration, and intensity in a warming environment. Science, 309, 1844-1846.

Weisberg R.H. and Zheng, L. (2006): Hurricane storm surge simulations for Tampa Bay. Estuaries and Coasts, 29, 6A, 909.

Westerink, J.J., Luettich, R.A., Feyen, J.C., Atkinson, J.H., Dawson, C., Roberts, H.J., Powell, M.D., Dunion., J.P., Kubatko, E.J. and Pourtaheri, H. (2008): A basin to channel scale unstructured grid hurricane storm surge model applied to southern Louisiana. Monthly Weather Review, 136, 833-864.

Zhao, M., Held, I., Lin, S-J. and Vecchi, G.A. (2009): Simulations of global hurricane climatology, interannual variability, and response to global warming using a 50 km resolution GCM. Journal of Climate, 22, 6653–6678.

APPENDIX A

SURGE RESPONSE FUNCTIONS RESULTS FOR OPEN COAST LOCATIONS

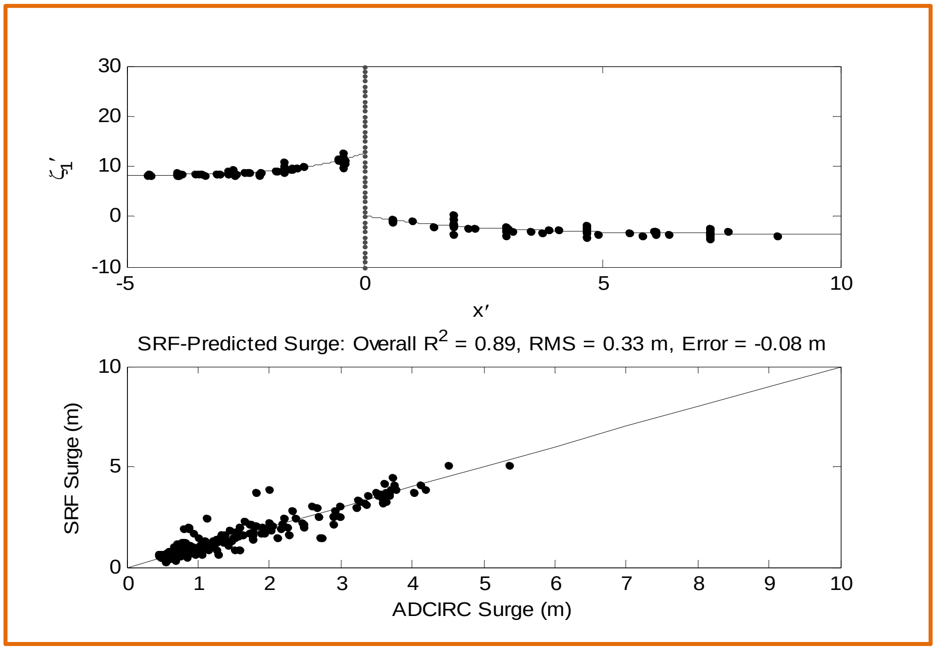

Figure A4.1: Performance of Song et al. (2102) SRFs at Location of 2 of Fig. 4.1. Top pane shows the plot of the dimensionless data using Equations 2.8 and 2.9. Bottom pane shows the back-prediction of surge using the dimensional SRFs.

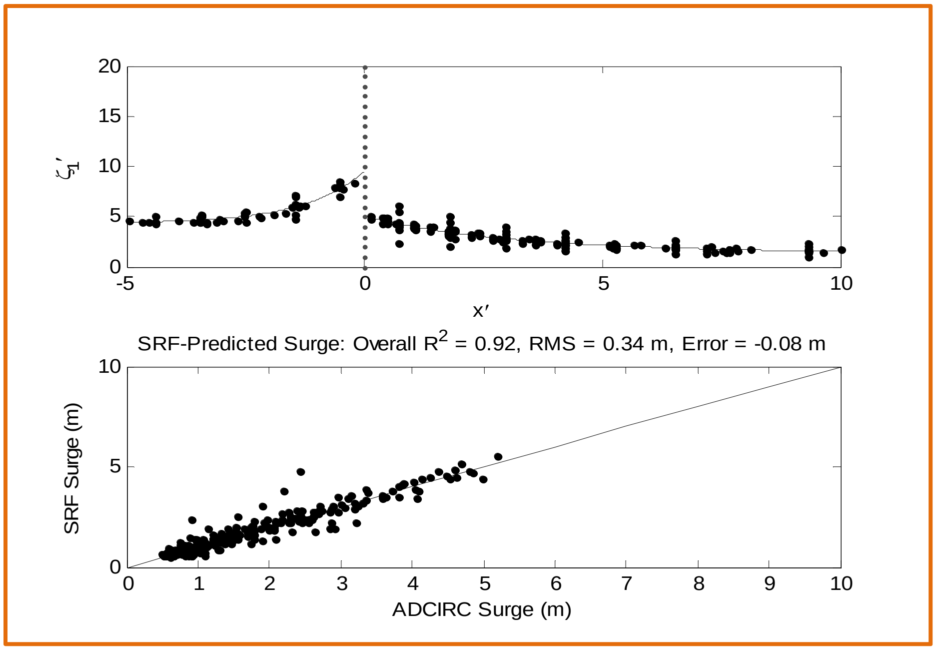

Figure A4.2: Performance of Song et al. (2102) SRFs at Location of 4 of Fig. 4.1. Top pane shows the plot of the dimensionless data using Equations 2.8 and 2.9. Bottom pane shows the back-prediction of surge using the dimensional SRFs.

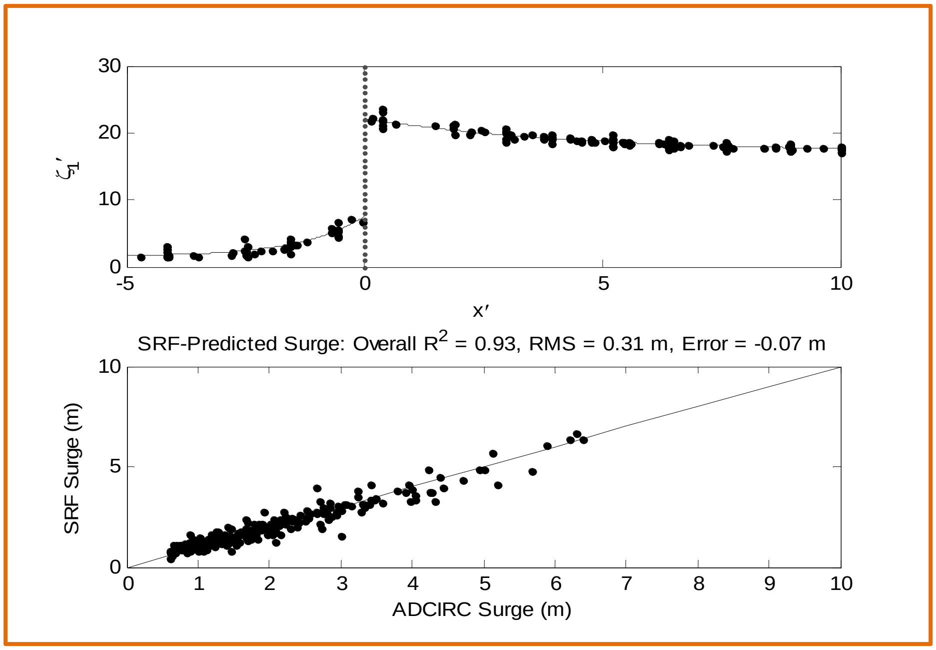

Figure A4.3: Performance of Song et al. (2102) SRFs at Location of 6 of Fig. 4.1. Top pane shows the plot of the dimensionless data using Equations 2.8 and 2.9. Bottom pane shows the back-prediction of surge using the dimensional SRFs.

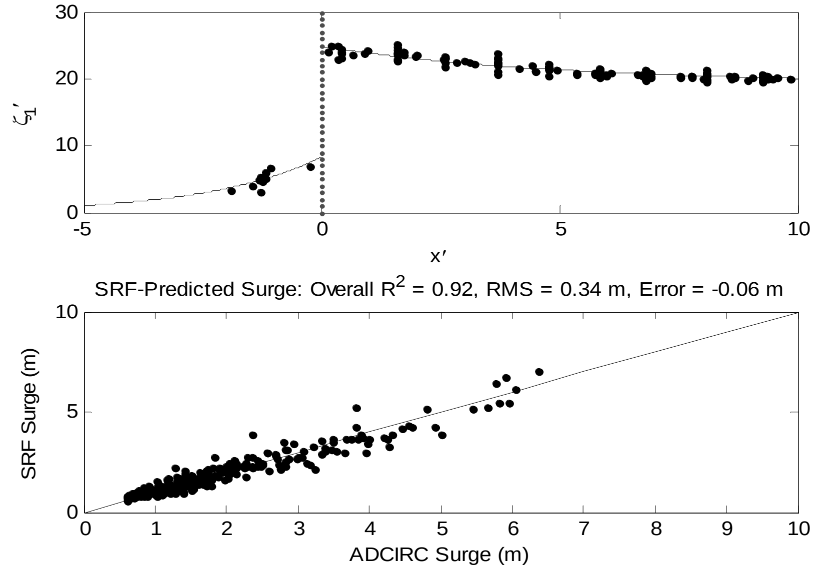

Figure A4.4: Performance of Song et al. (2102) SRFs at Location of 8 of Fig. 4.1. Top pane shows the plot of the dimensionless data using Equations 2.8 and 2.9. Bottom pane shows the back-prediction of surge using the dimensional SRFs.

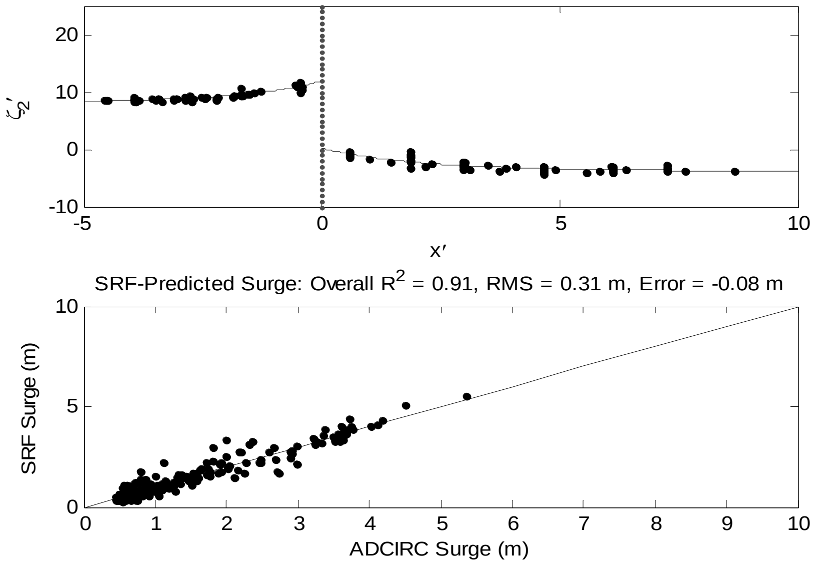

Figure A4.5: Performance of revised SRF at Location 2. Top pane shows the plot of the dimensionless data using Equations 4.7 and 4.8. Bottom pane shows the back-prediction of surge using the dimensional SRFs.

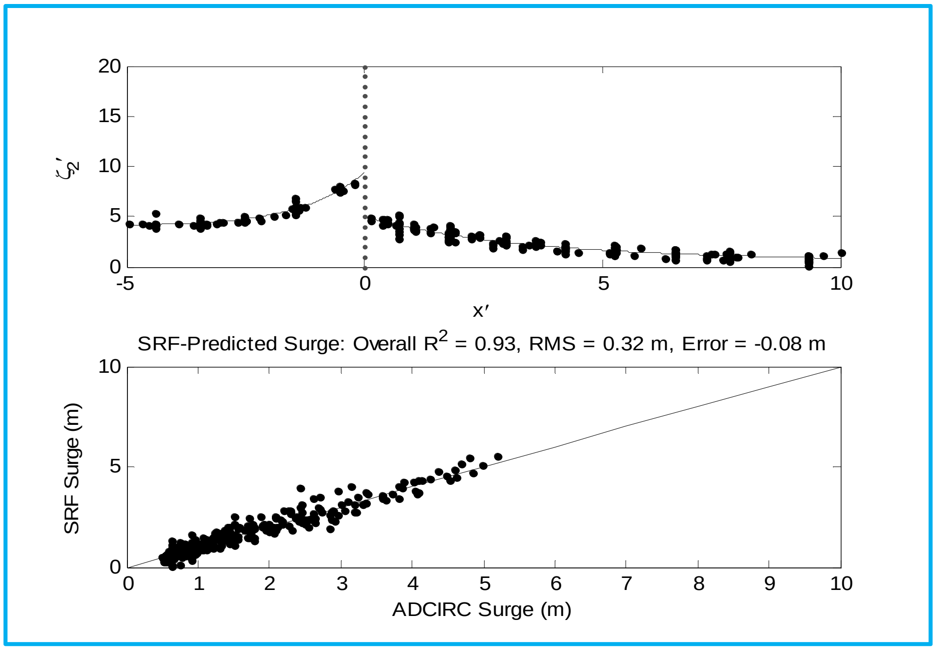

Figure A4.6: Performance of revised SRF at Location 4. Top pane shows the plot of the dimensionless data using Equations 4.7 and 4.8. Bottom pane shows the back-prediction of surge using the dimensional SRFs.

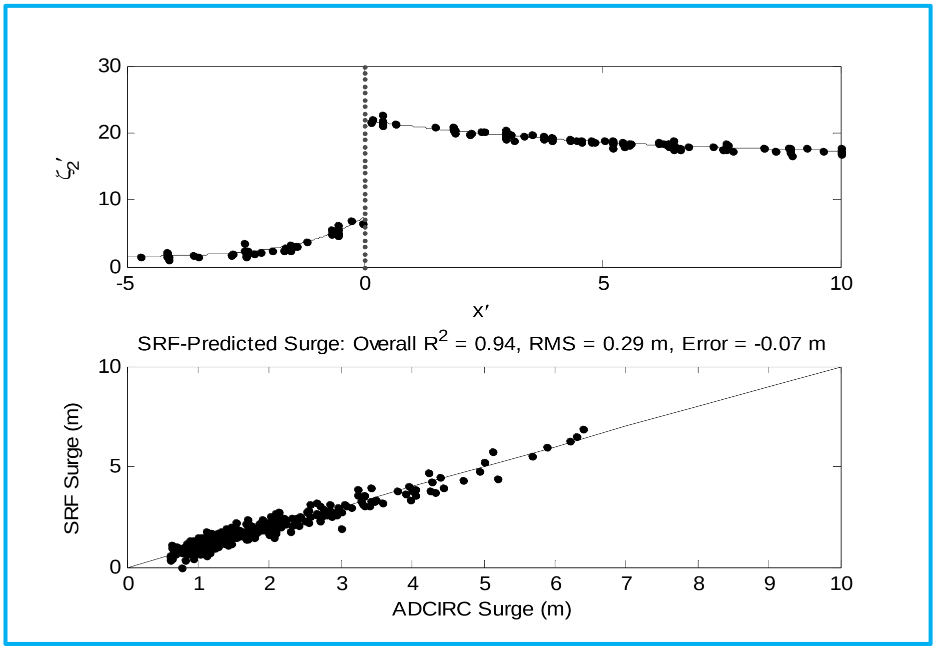

Figure A4.7: Performance of revised SRF at Location 6. Top pane shows the plot of the dimensionless data using Equations 4.7 and 4.8. Bottom pane shows the back-prediction of surge using the dimensional SRFs.

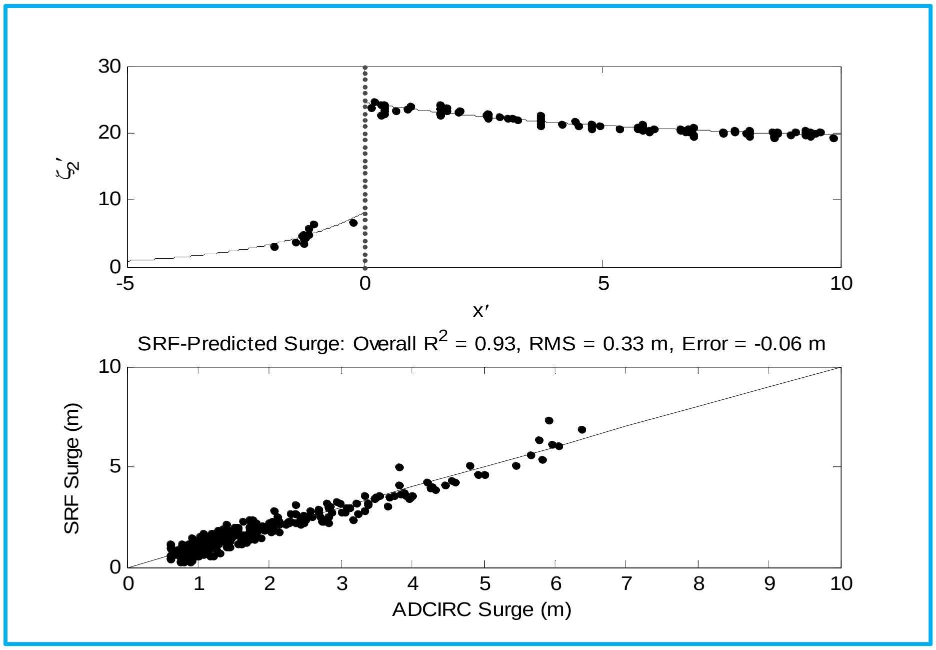

Figure A4.8: Performance of revised SRF at Location 8. Top pane shows the plot of the dimensionless data using Equations 4.7 and 4.8. Bottom pane shows the back-prediction of surge using the dimensional SRFs.

APPENDIX B

SURGE RESPONSE FUNCTIONS RESULTS FOR BAY LOCATIONS

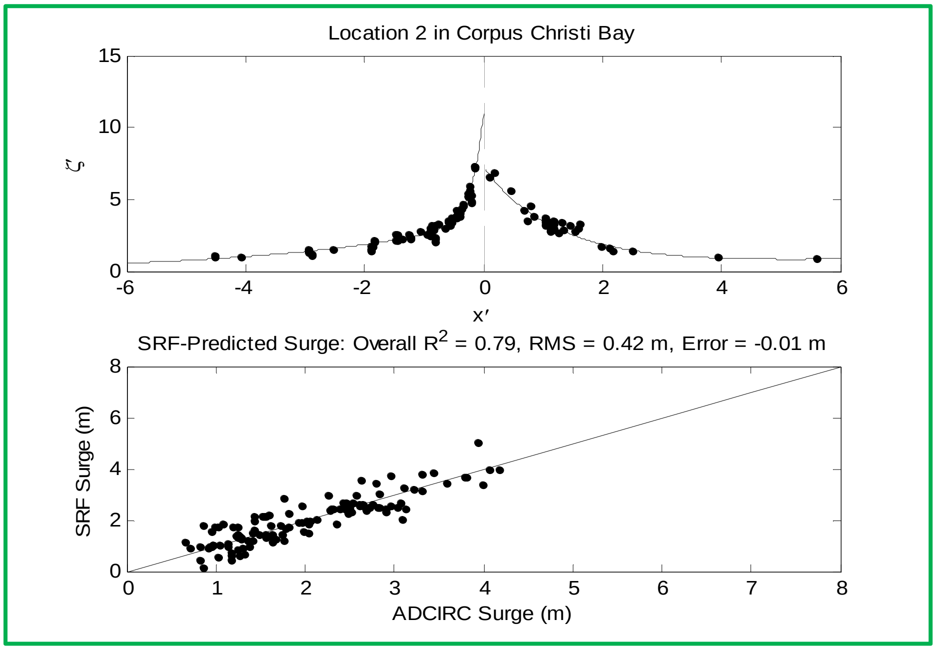

Figure B4.1: Performance of revised SRF formulation at Location 2 of Corpus Christi Bay, with v_f and θ correction. Top pane shows the plot of the dimensionless data using Equations 4.21 and 4.22. Bottom pane shows the back-prediction of surge using the dimensional SRFs.

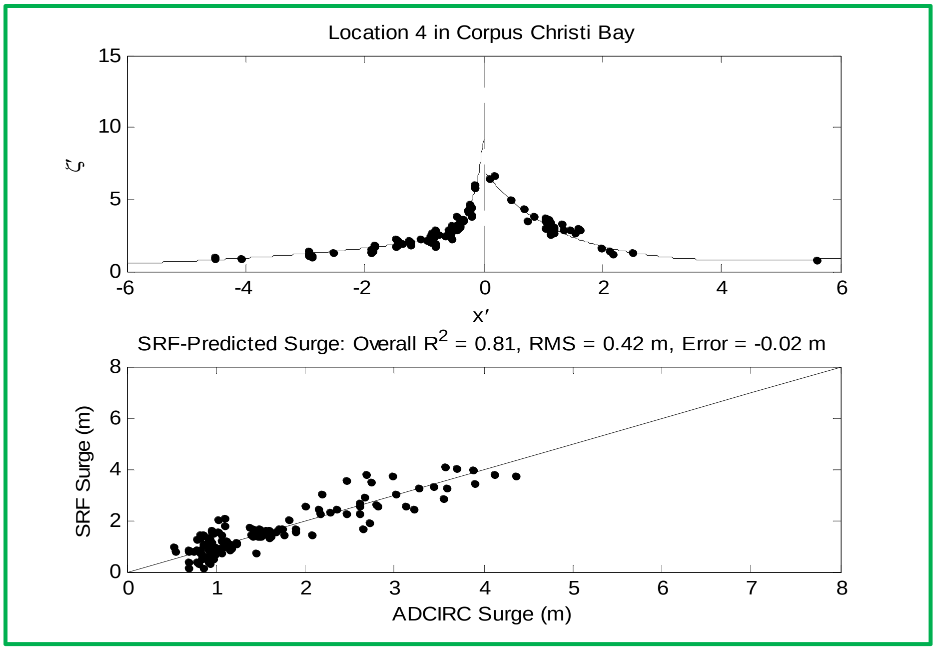

Figure B4.2: Performance of revised SRF formulation at Location 4 of Corpus Christi Bay, with v_f and θ correction. Top pane shows the plot of the dimensionless data using Equations 4.21 and 4.22. Bottom pane shows the back-prediction of surge using the dimensional SRFs.

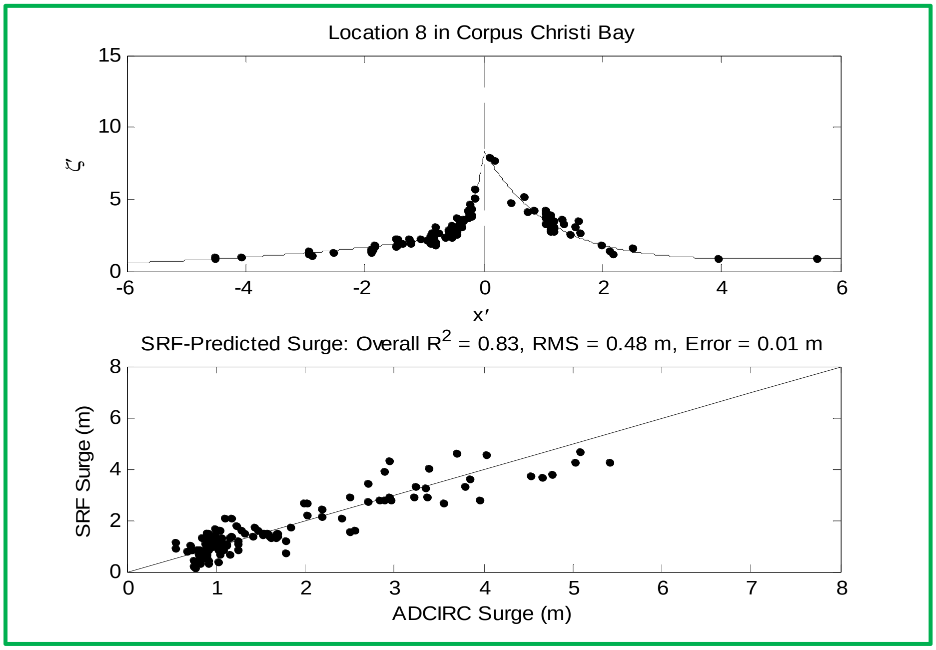

Figure B4.3: Performance of revised SRF formulation at Location 8 of Corpus Christi Bay, with v_f and θ correction. Top pane shows the plot of the dimensionless data using Equations 4.21 and 4.22. Bottom pane shows the back-prediction of surge using the dimensional SRFs.

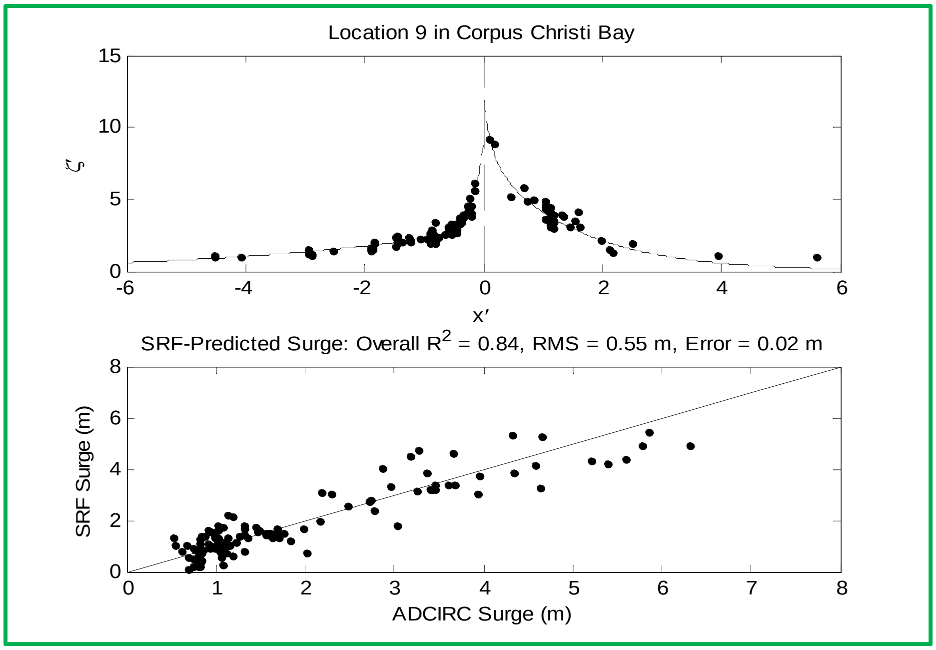

Figure B4.4: Performance of revised SRF formulation at Location 9 of Corpus Christi Bay, with v_f and θ correction. Top pane shows the plot of the dimensionless data using Equations 4.21 and 4.22. Bottom pane shows the back-prediction of surge using the dimensional SRFs.

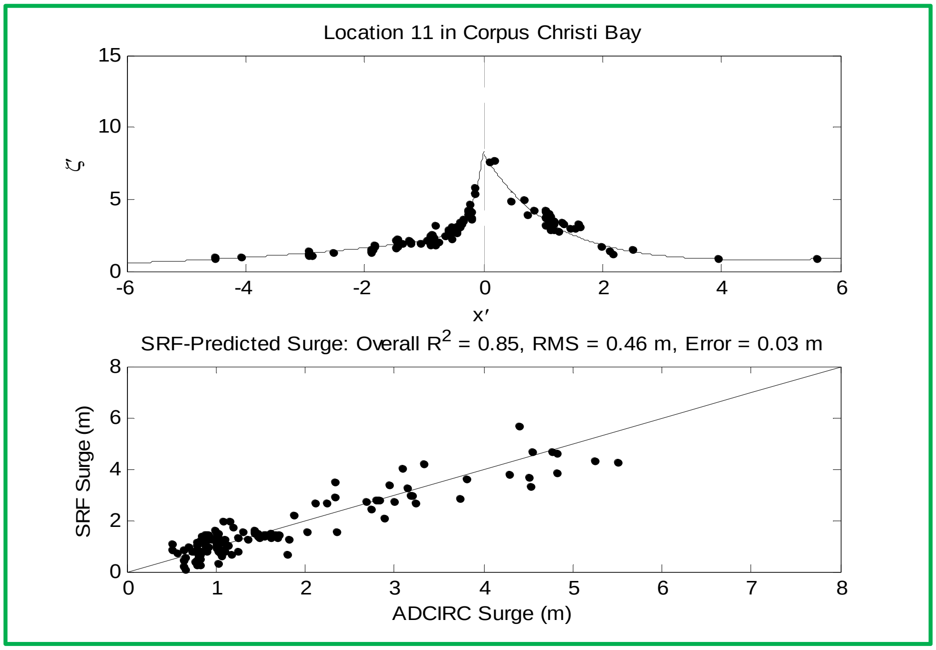

Figure B4.5: Performance of revised SRF formulation at Location 11 of Corpus Christi Bay, with v_f and θ correction. Top pane shows the plot of the dimensionless data using Equations 4.21 and 4.22. Bottom pane shows the back-prediction of surge using the dimensional SRFs.

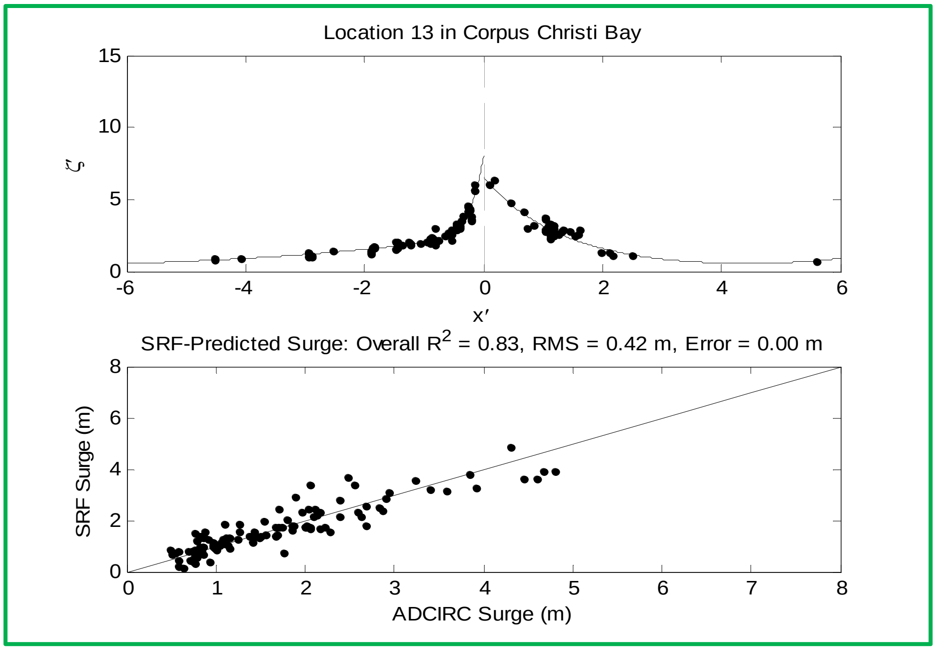

Figure B4.6: Performance of revised SRF formulation at Location 13 of Corpus Christi Bay, with v_f and θ correction. Top pane shows the plot of the dimensionless data using Equations 4.21 and 4.22. Bottom pane shows the back-prediction of surge using the dimensional SRFs.

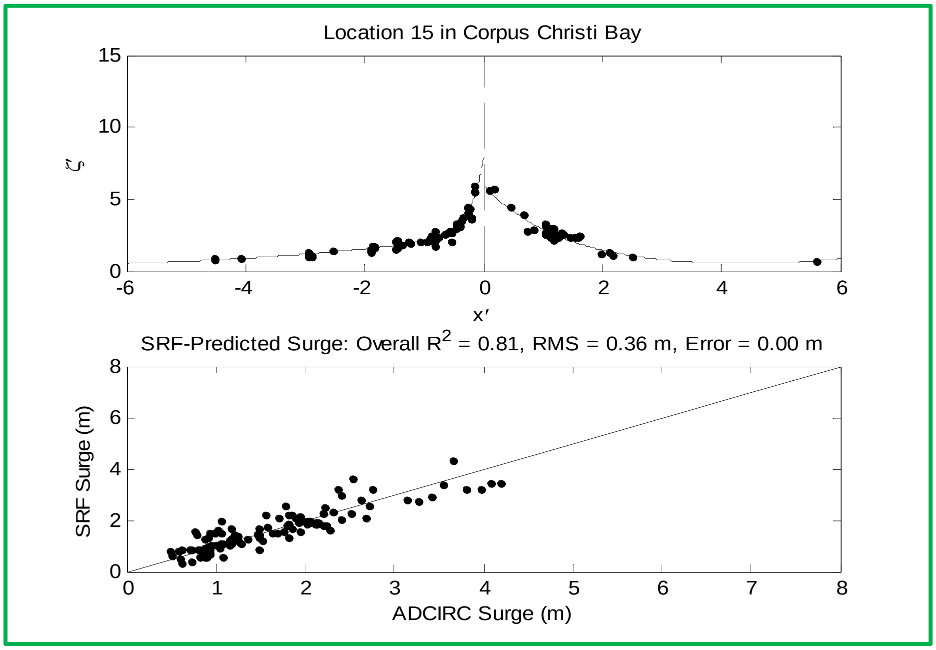

Figure B4.7: Performance of revised SRF formulation at Location 15 of Corpus Christi Bay, with v_f and θ correction. Top pane shows the plot of the dimensionless data using Equations 4.21 and 4.22. Bottom pane shows the back-prediction of surge using the dimensional SRFs.

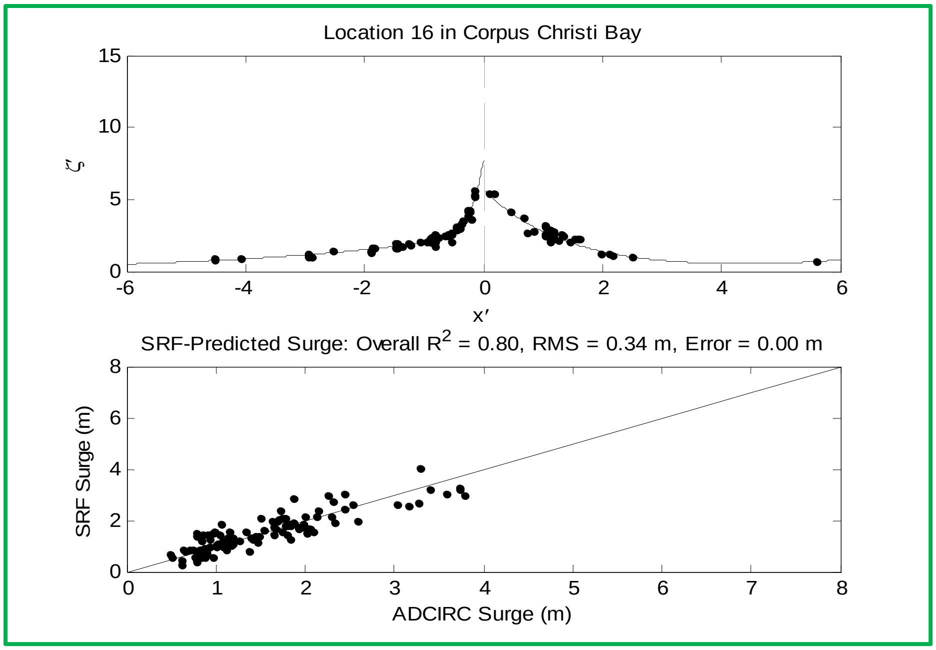

Figure B4.8: Performance of revised SRF formulation at Location 16 of Corpus Christi Bay, with v_f and θ correction. Top pane shows the plot of the dimensionless data using Equations 4.21 and 4.22. Bottom pane shows the back-prediction of surge using the dimensional SRFs.

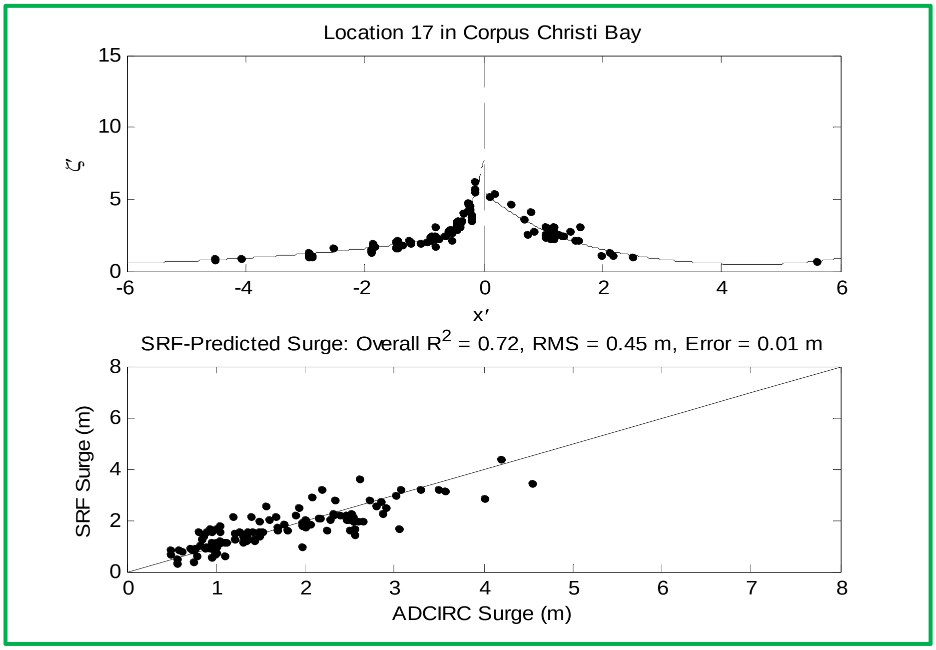

Figure B4.9: Performance of revised SRF formulation at Location 17 of Corpus Christi Bay, with v_f and θ correction. Top pane shows the plot of the dimensionless data using Equations 4.21 and 4.22. Bottom pane shows the back-prediction of surge using the dimensional SRFs.

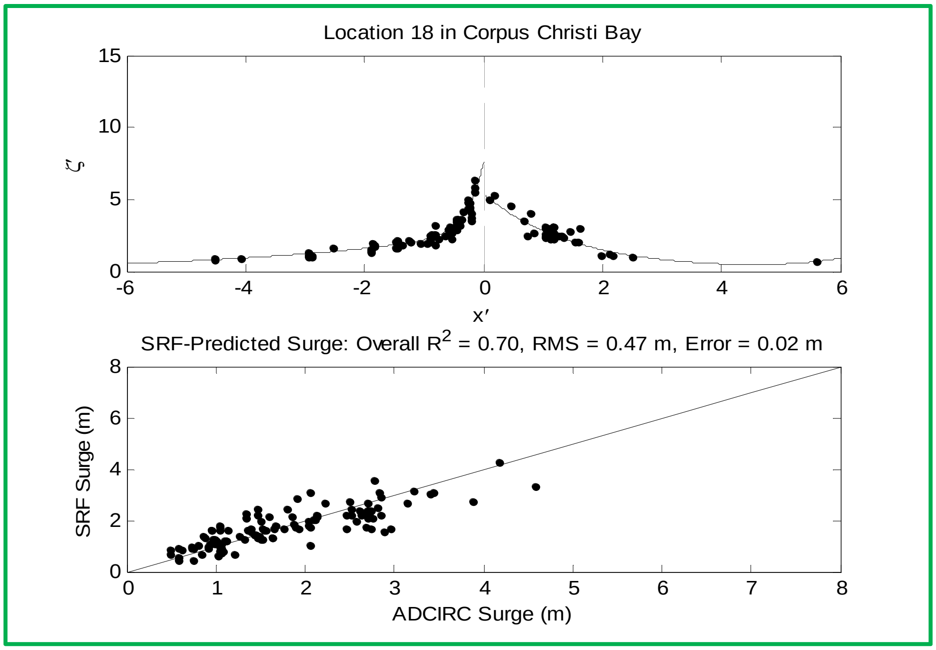

Figure B4.10: Performance of revised SRF formulation at Location 18 of Corpus Christi Bay, with v_f and θ correction. Top pane shows the plot of the dimensionless data using Equations 4.21 and 4.22. Bottom pane shows the back-prediction of surge using the dimensional SRFs.

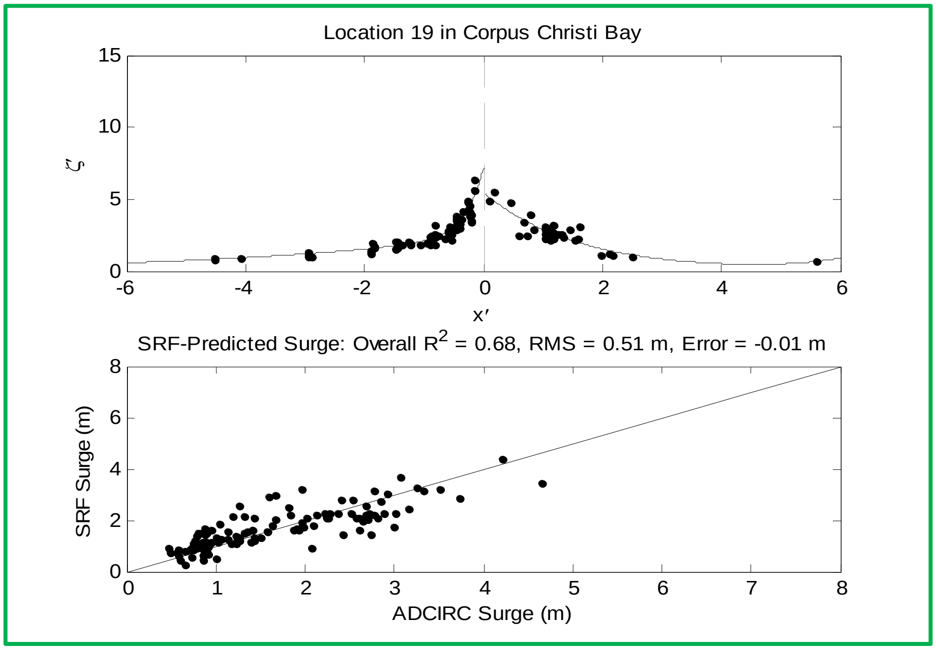

Figure B4.11: Performance of revised SRF formulation at Location 19 of Corpus Christi Bay, with v_f and θ correction. Top pane shows the plot of the dimensionless data using Equations 4.21 and 4.22. Bottom pane shows the back-prediction of surge using the dimensional SRFs.

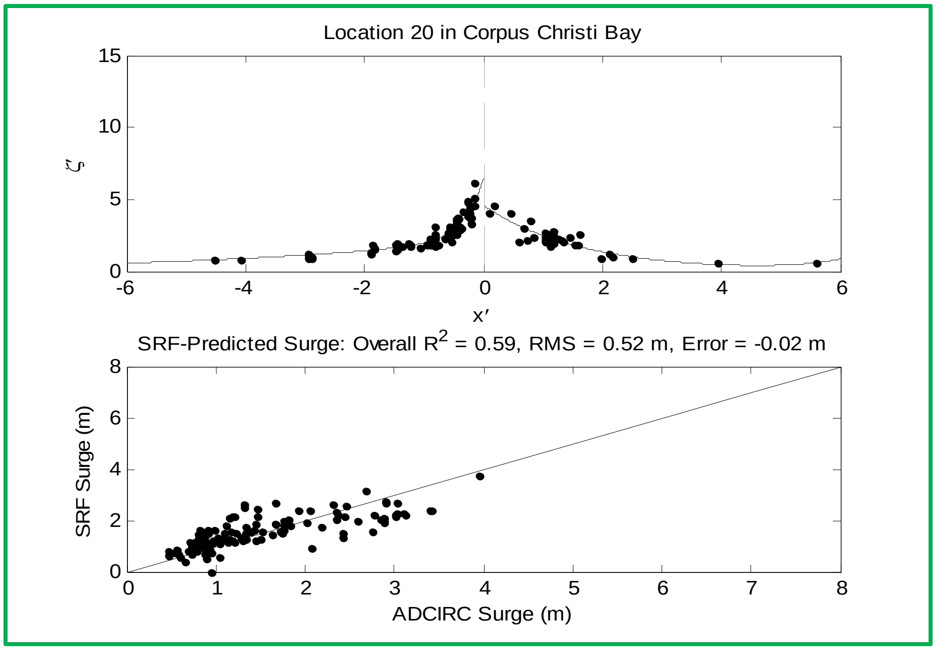

Figure B4.12: Performance of revised SRF formulation at Location 20 of Corpus Christi Bay, with v_f and θ correction. Top pane shows the plot of the dimensionless data using Equations 4.21 and 4.22. Bottom pane shows the back-prediction of surge using the dimensional SRFs.

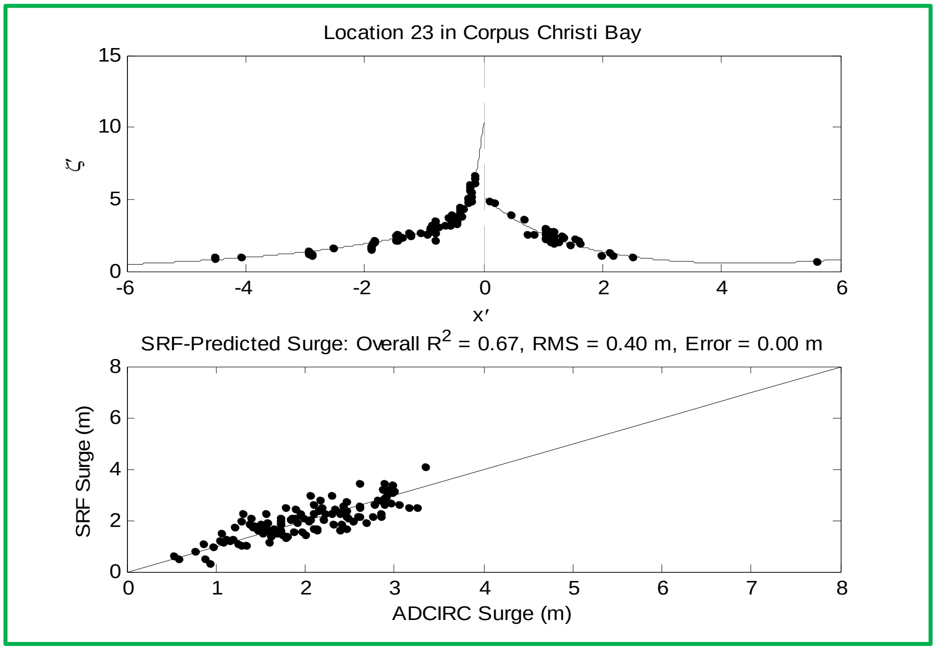

Figure B4.13: Performance of revised SRF formulation at Location 23 of Corpus Christi Bay, with v_f and θ correction. Top pane shows the plot of the dimensionless data using Equations 4.21 and 4.22. Bottom pane shows the back-prediction of surge using the dimensional SRFs.

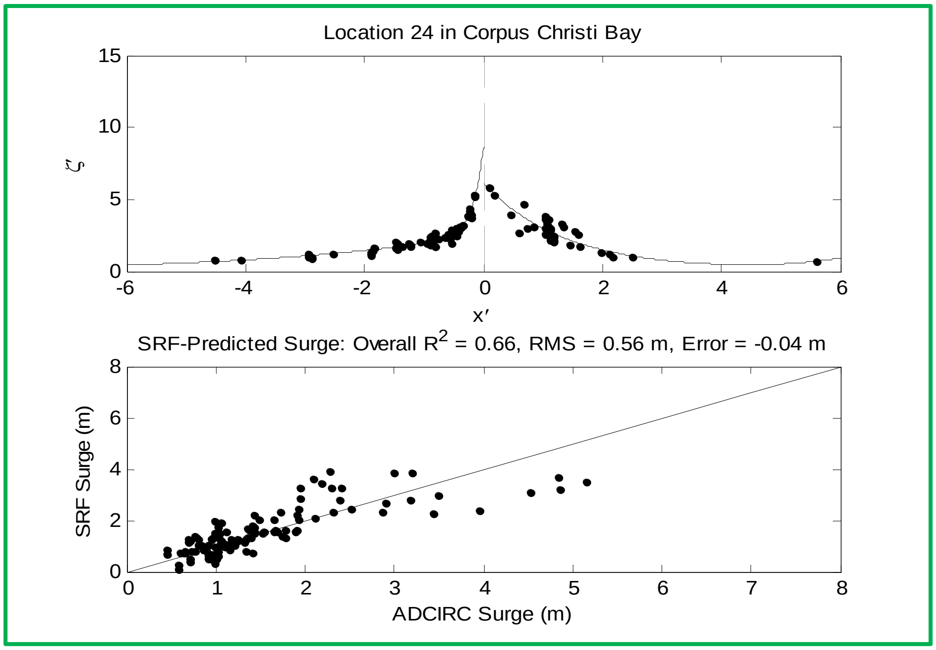

Figure B4.14: Performance of revised SRF formulation at Location 24 of Corpus Christi Bay, with v_f and θ correction. Top pane shows the plot of the dimensionless data using Equations 4.21 and 4.22. Bottom pane shows the back-prediction of surge using the dimensional SRFs.

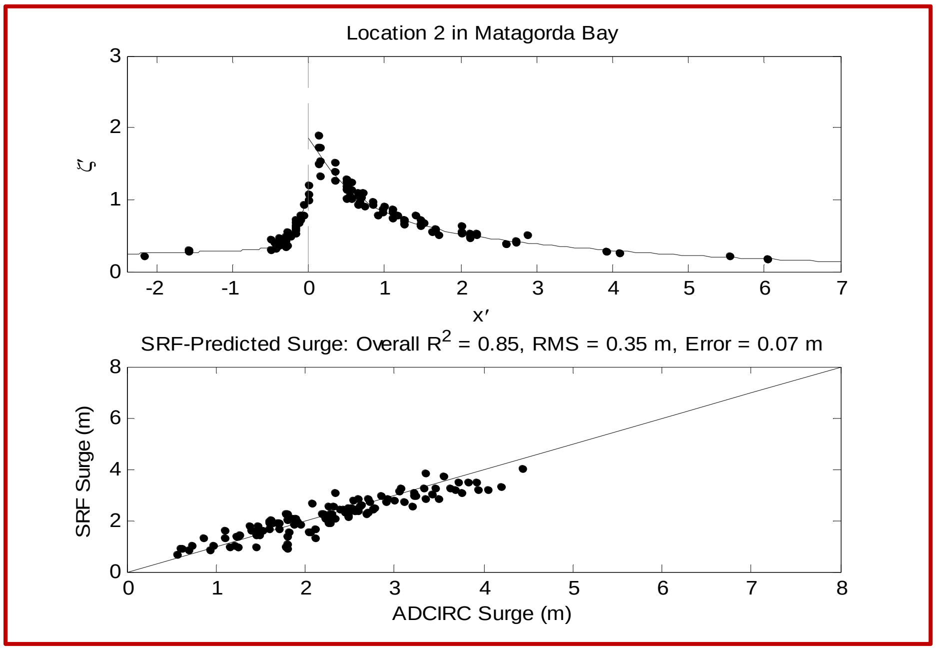

Figure B4.15: Performance of revised SRF formulation at Location 2 of Matagorda Bay, with v_f and θ correction. Top pane shows the plot of the dimensionless data using Equations 4.21 and 4.22. Bottom pane shows the back-prediction of surge using the dimensional SRFs.

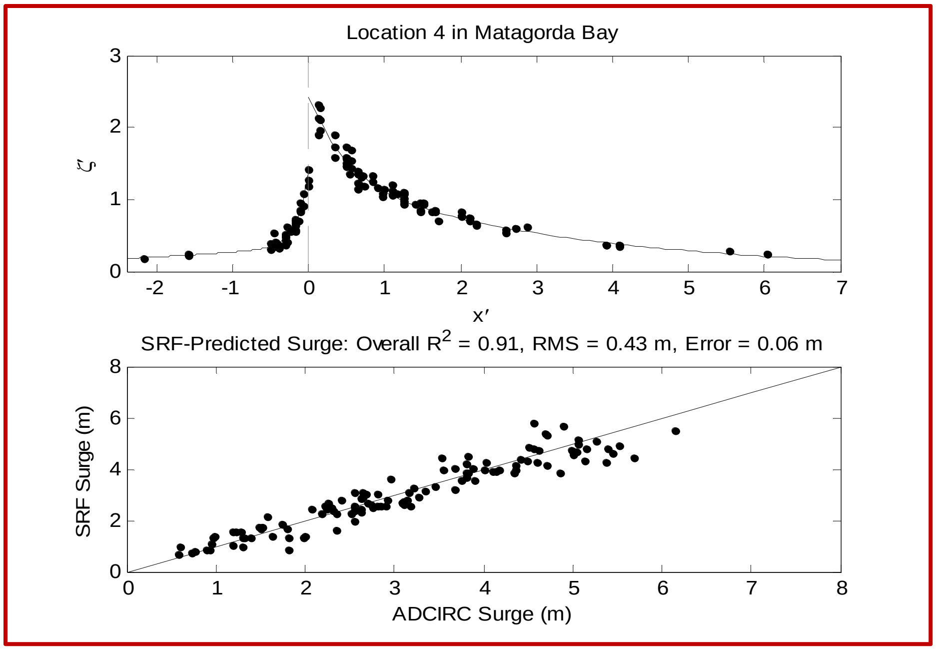

Figure B4.16: Performance of revised SRF formulation at Location 4 of Matagorda Bay, with v_f and θ correction. Top pane shows the plot of the dimensionless data using Equations 4.21 and 4.22. Bottom pane shows the back-prediction of surge using the dimensional SRFs.

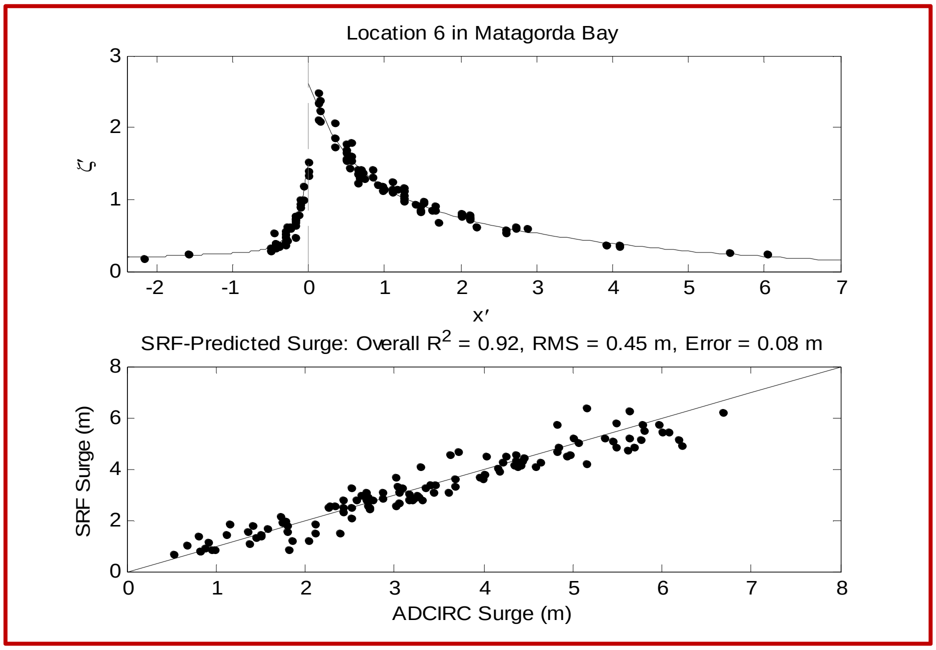

Figure B4.17: Performance of revised SRF formulation at Location 6 of Matagorda Bay, with v_f and θ correction. Top pane shows the plot of the dimensionless data using Equations 4.21 and 4.22. Bottom pane shows the back-prediction of surge using the dimensional SRFs.

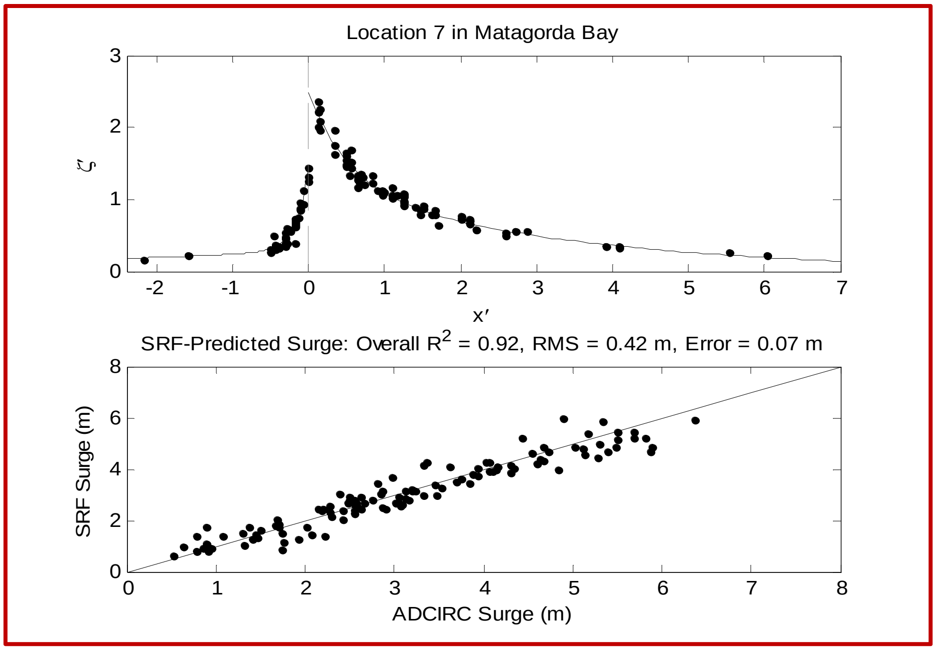

Figure B4.18: Performance of revised SRF formulation at Location 7 of Matagorda Bay, with v_f and θ correction. Top pane shows the plot of the dimensionless data using Equations 4.21 and 4.22. Bottom pane shows the back-prediction of surge using the dimensional SRFs.

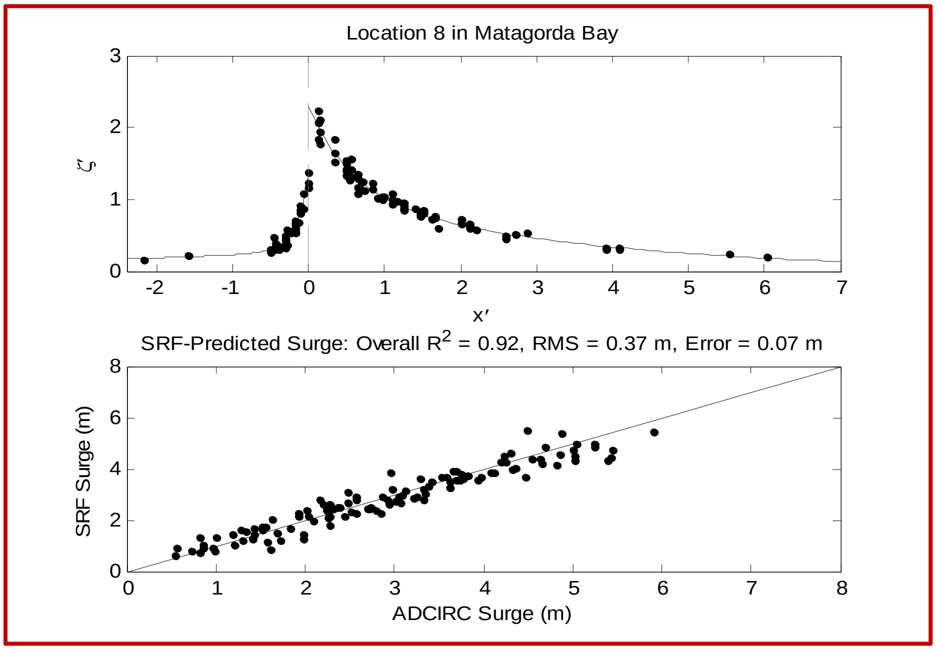

Figure B4.19: Performance of revised SRF formulation at Location 8 of Matagorda Bay, with v_f and θ correction. Top pane shows the plot of the dimensionless data using Equations 4.21 and 4.22. Bottom pane shows the back-prediction of surge using the dimensional SRFs.

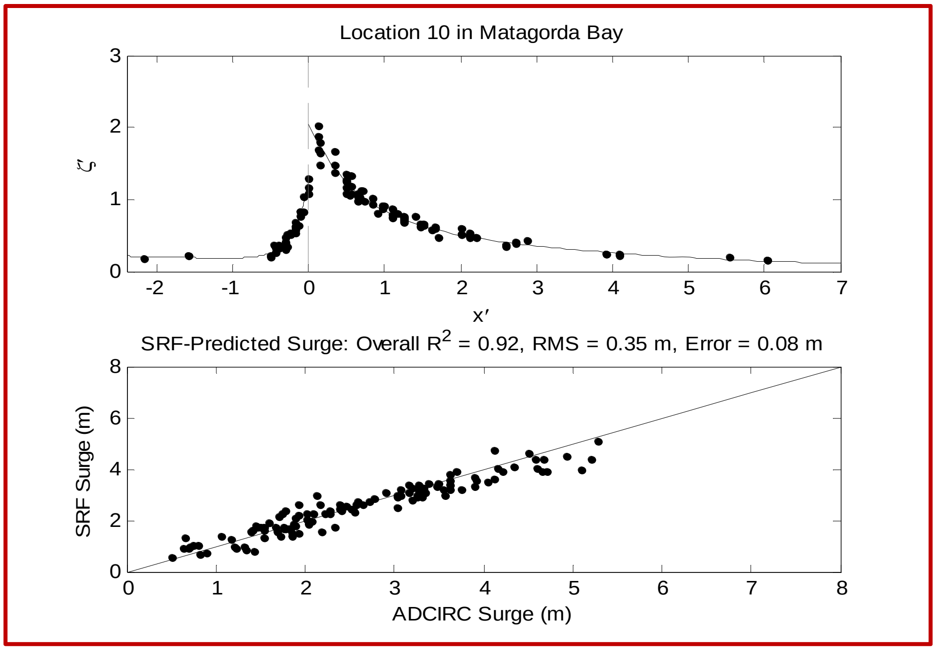

Figure B4.20: Performance of revised SRF formulation at Location 10 of Matagorda Bay, with v_f and θ correction. Top pane shows the plot of the dimensionless data using Equations 4.21 and 4.22. Bottom pane shows the back-prediction of surge using the dimensional SRFs.

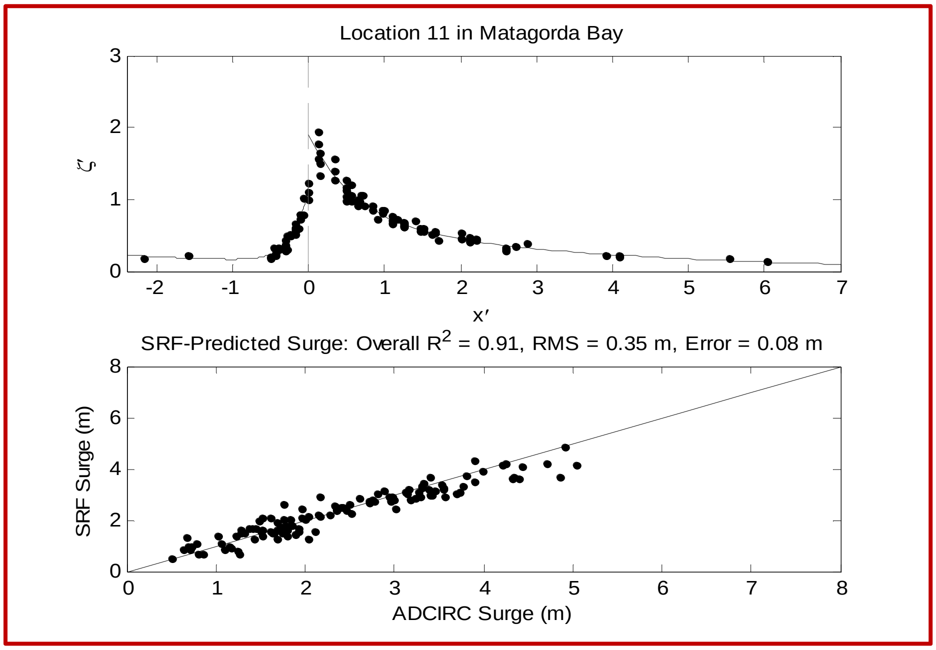

Figure B4.21: Performance of revised SRF formulation at Location 11 of Matagorda Bay, with v_f and θ correction. Top pane shows the plot of the dimensionless data using Equations 4.21 and 4.22. Bottom pane shows the back-prediction of surge using the dimensional SRFs.

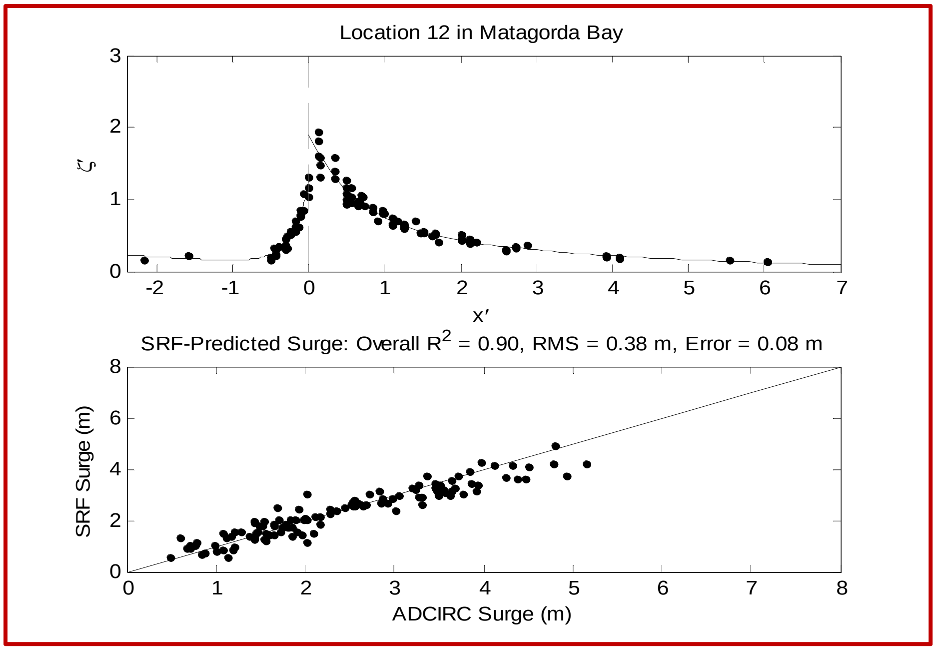

Figure B4.22: Performance of revised SRF formulation at Location 12 of Matagorda Bay, with v_f and θ correction. Top pane shows the plot of the dimensionless data using Equations 4.21 and 4.22. Bottom pane shows the back-prediction of surge using the dimensional SRFs.

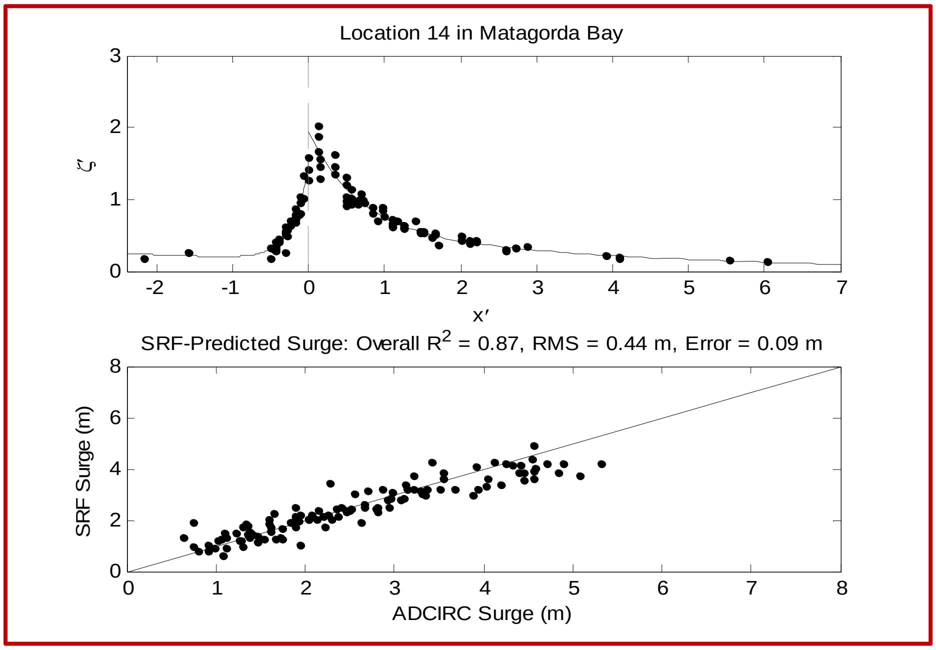

Figure B4.23: Performance of revised SRF formulation at Location 14 of Matagorda Bay, with v_f and θ correction. Top pane shows the plot of the dimensionless data using Equations 4.21 and 4.22. Bottom pane shows the back-prediction of surge using the dimensional SRFs.

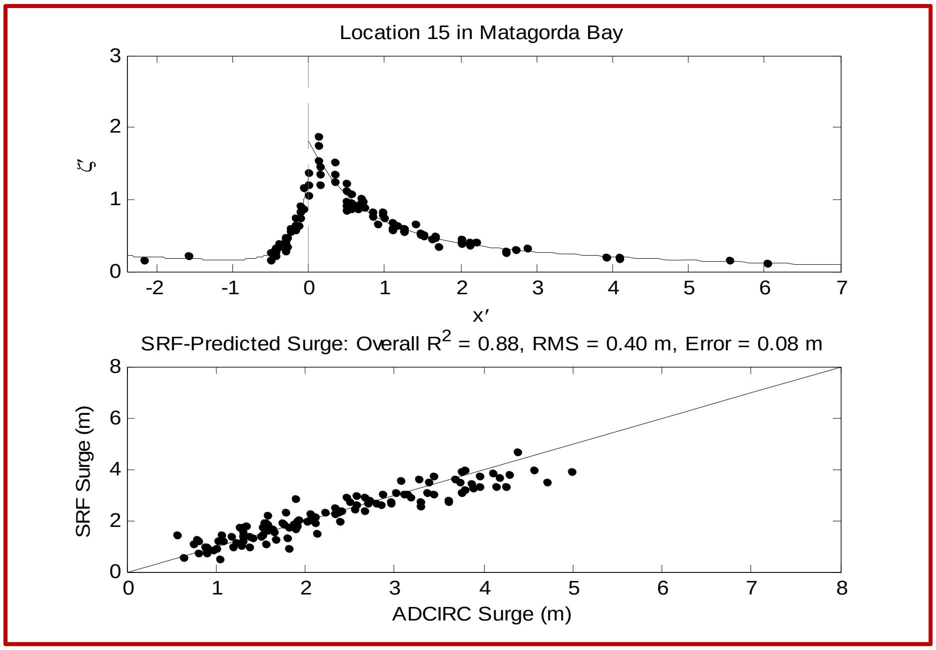

Figure B4.24: Performance of revised SRF formulation at Location 15 of Matagorda Bay, with v_f and θ correction. Top pane shows the plot of the dimensionless data using Equations 4.21 and 4.22. Bottom pane shows the back-prediction of surge using the dimensional SRFs.

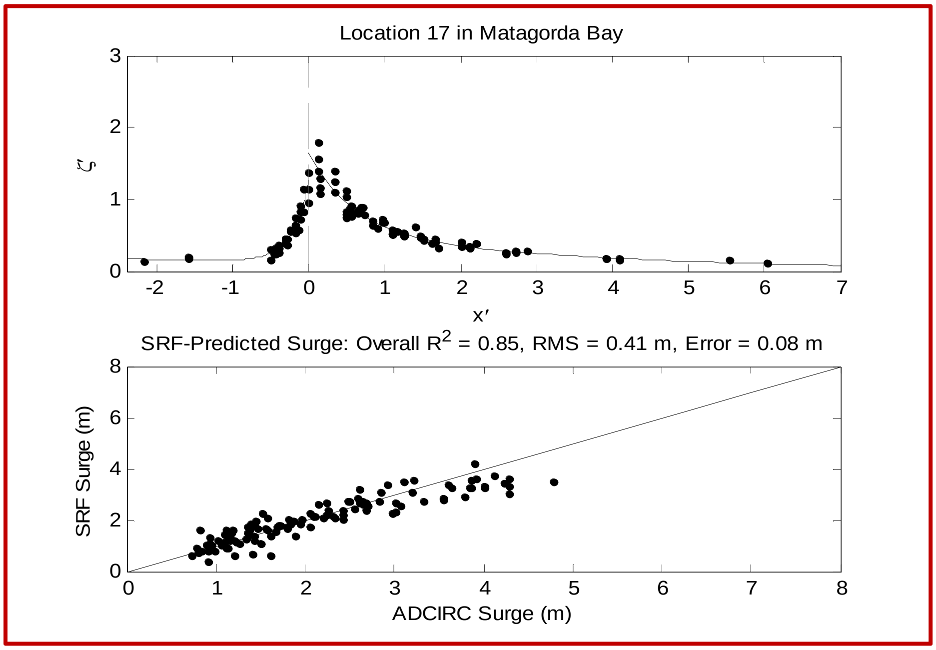

Figure B4.25: Performance of revised SRF formulation at Location 17 of Matagorda Bay, with v_f and θ correction. Top pane shows the plot of the dimensionless data using Equations 4.21 and 4.22. Bottom pane shows the back-prediction of surge using the dimensional SRFs.

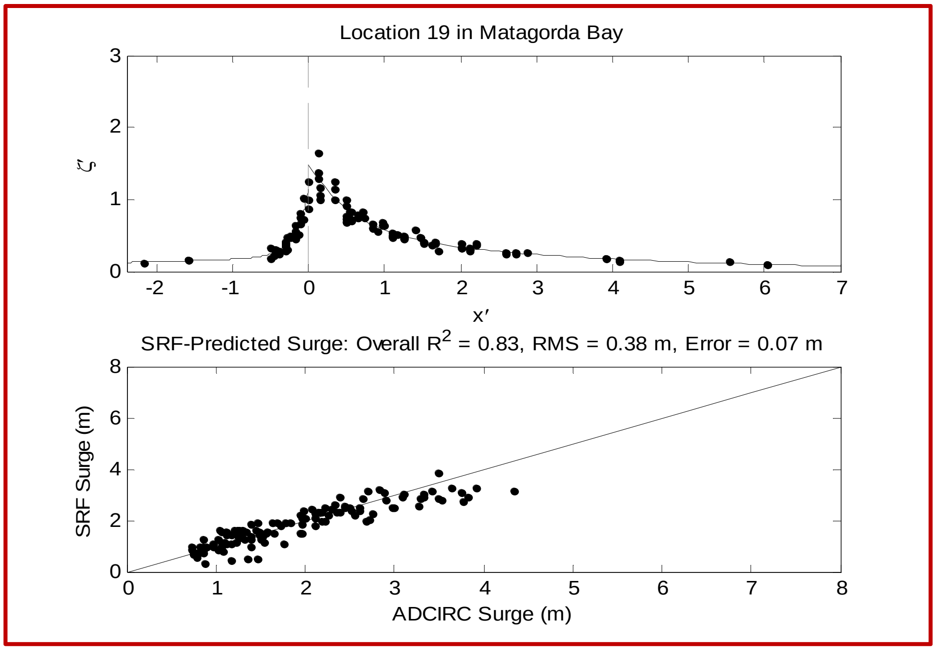

Figure B4.26: Performance of revised SRF formulation at Location 19 of Matagorda Bay, with v_f and θ correction. Top pane shows the plot of the dimensionless data using Equations 4.21 and 4.22. Bottom pane shows the back-prediction of surge using the dimensional SRFs.

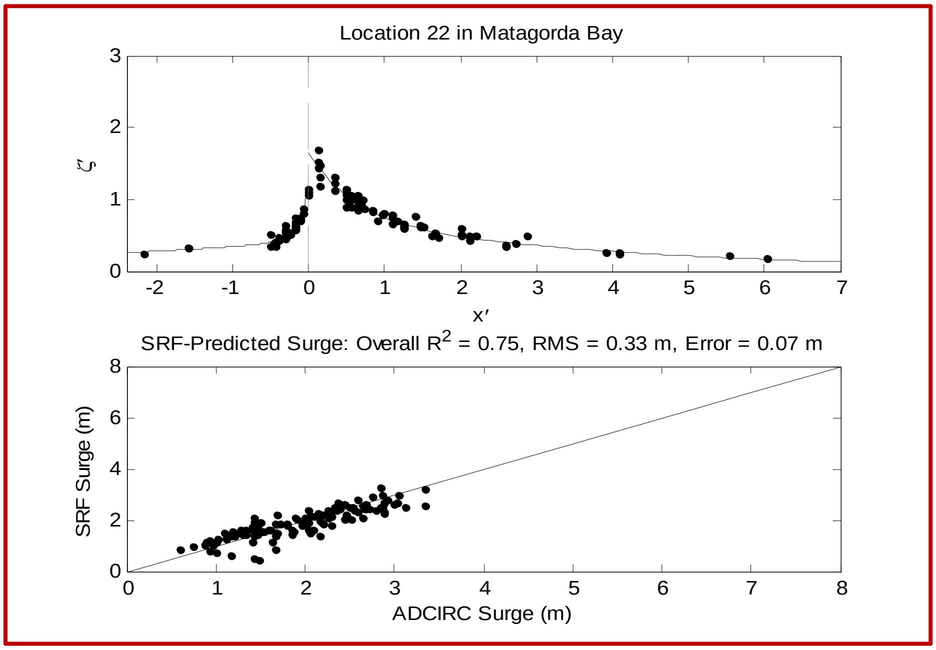

Figure B4.27: Performance of revised SRF formulation at Location 22 of Matagorda Bay, with v_f and θ correction. Top pane shows the plot of the dimensionless data using Equations 4.21 and 4.22. Bottom pane shows the back-prediction of surge using the dimensional SRFs.

APPENDIX C

COORDINATES OF OPEN COAST AND BAY SRF LOCATIONS

Table C1: Coordinates of open coast SRF locations

Open Coast Location	Latitude	Longitude
1	27.339	-97.329
2	27.893	-97.018
3	28.299	-96.486
4	28.683	-95.778
5	28.963	-95.268
6	29.318	-94.749
7	29.595	-94.281
8	29.688	-93.932

Table C2: Coordinates of SRF Locations in Corpus Christi Bay

Bay Location	Latitude	Longitude
1	27.704	-97.263
2	27.701	-97.324
3	27.726	-97.336
4	27.767	-97.383
5	27.805	-97.396
6	27.821	-97.390
7	27.833	-97.383
8	27.832	-97.469
9	27.886	-97.511
10	27.876	-97.490
11	27.872	-97.392
12	27.861	-97.344
13	27.875	-97.291
14	27.844	-97.230

Table C2 continued: Coordinates of SRF Locations in Corpus Christi Bay

Bay Location	Latitude	Longitude
15	27.831	-97.227
16	27.822	-97.213
17	27.871	-97.161
18	27.895	-97.136
19	27.929	-97.117
20	27.967	-97.089
21	27.877	-97.046
22	27.789	-97.114
23	27.682	-97.200
24	27.617	-97.292

Table C3: Coordinates of SRF Locations in Matagorda Bay

Bay Location	Latitude	Longitude
1	28.438	-96.394
2	28.505	-96.451
3	28.560	-96.522
4	28.621	-96.610
5	28.687	-96.641
6	28.712	-96.594
7	28.685	-96.559
8	28.636	-96.543
9	28.606	-96.499
10	28.614	-96.449
11	28.601	-96.406
12	28.621	-96.353
13	28.659	-96.292
14	28.690	-96.213
15	28.643	-96.237
16	28.580	-96.232
17	28.602	-96.152

Table C3 continued: Coordinates of SRF Locations in Matagorda Bay

Bay Location	Latitude	Longitude
18	28.608	-96.019
19	28.567	-96.117
20	28.534	-96.183
21	28.471	-96.302
22	-96.356	28.434